Nanoparticules et assemblages contrôlés pour la théranostique

Riya George

Riya George. Nanoparticules et assemblages contrôlés pour la théranostique. Coordination chemistry. Université Paris-Saclay, 2022. English. NNT : 2022UPASF086 . tel-04536606

Ultra-small theranostic nanoparticles and their controlled assemblies

Nanoparticules et assemblages contrôlés pour la théranostique

Thèse de doctorat de l'université Paris-Saclay

École doctorale n° 571,
Molécules, Matériaux, Instrumentation et Biosystèmes (2MIB)
Spécialité de doctorat: sciences chimiques
Graduate School : Chimie. Référent : Faculté des Sciences d'Orsay

Thèse préparée dans la unité de recherche **ECI, ICMMO**, sous la direction de **Laure CATALA**, Professeur, Université Paris-Saclay

Thèse soutenue à Paris-Saclay, le 16 Décembre 2022, par

Riya GEORGE

Composition du Jury

Nicolas TSAPIS Directeur de recherche, Université Paris Saclay	Président
Sylvie BEGIN-COLIN Professeur, Université de Strasbourg	Rapporteur
Francois LUX Maître de conférences, Université de Lyon	Rapporteur
Natividad GALVEZ RODRIGUEZ Professeur, Universidad de Granada	Examinatrice

THÈSE DE DOCTORAT

NNT : 2022UPASF086

Acknowledgement

As I am at the end of my doctoral studies, I would like to express my gratitude to the people who made this possible. First and foremost, Prof. Laure Catala for being an incredibly kind and brilliant thesis director. Her passion for doing thorough and in-depth research is inspiring and motivating. Her words of encouragement, especially when things were not working out, were priceless. It was incredible watching her balance so many responsibilities, and still make time to help out with the project. I will cherish our late-night/early-morning, weekend chats trying to find new solutions, calculating values and brainstorming possible mechanisms of action. We were a small team throughout these last 3.5 years and I am extremely grateful for that. Special thanks to Prof. Eddy Dumas, for being part of my thesis monitoring committee and providing interesting insights to the project. I would also like to thank professors Sylvie-Begin Colin, Francois Lux, Natividad Galvez Rodriguez and Nicolas Tsapis for agreeing to be part of my jury.

My heartfelt gratitude to Farah Savina and Erika Porcel for welcoming me to ISMO, helping with all the biological tests and giving me so much of your time. There were always many unexpected problems with the experiments, but you were always optimistic and ready to try out new methods. It was an honour to be a part of the diverse inorganic chemistry group at the Institute of Molecular Chemistry and Materials of Orsay, Université Paris-Saclay. My fellow PhD students, post-docs and professors made it a supportive and positive work environment, with their generous smiles and helpful attitude. Special thanks to Laura, Amanda, Flora and Abdoul for their care and help throughout. I am grateful to Claire Boulogne and Cynthia Gillet for training me to use the transmission electron microscope at I2BC, CNRS. Special thanks to Diana Dragoe for XPS measurements and tolerating my long discussions in deciphering the data. I am grateful to Francois Brisset and Alexandre Gloter for analyzing my samples using EDS, HR-TEM and STEM. I gratefully acknowledge the help from our collaborator Prof. Ruxandra Gref and her team from ISMO, specially Xue Li and Jingwen Qiu, for synthesizing the polymer CD-citrate. Thank you for allowing me to perform drug loading and release studies in your lab. It was a pleasure to work with Theotim Lucas and Prof. Florence Gazeau at Université de Paris for photothermal and photoacoustic measurements. Special thanks to Prof. Lucie Sancey at Université Grenoble Alpes for the *in vitro* studies. I am grateful to Prof. Sophie Laurent and Thomas Gevart at Université de Mons, Belgium for allowing me to visit and perform relaxivity measurements. I would like to thank DIM-Respore for funding my doctoral project. I am grateful to all the hardworking, curious interns: Marianne, Stella, Aurelia, Haziq and Andrea, who spent a few months working with me in the lab, helped us reach answers and provided fun company. I will be eternally grateful to all my amazing teachers in various high-schools, St. Stephen’s college, India, and Université Paris Saclay, France who were responsible for shaping my interest in science and making me believe it can change the world.

Words cannot adequately express my appreciation and gratitude to Davis who was there throughout the journey, always ready to help out. Thank you for your motivating words, making me laugh, and somehow managing to calm me down when I was at my most stressed, and sharing all my troubles. My heartfelt gratitude to Shreya, my dearest friend who was always just one call away. I loved every minute of our fun gaming sessions, one-day meetups in Prague as well as the super-long chats that always left me cheerful and happy. I was lucky to have a lovely, little family in Paris: Marija Knezevic and Rika Tandiana. From figuring out administrative hurdles, to paying taxes and venting our frustrations over so many voice messages, mid-day coffees and Indian restaurant lunches, we have grown up together. I could not imagine finishing my Masters and PhD here, without you.

I am deeply indebted to my family for nurturing me to be a confident, independent person and always supporting me. Thank you Roel for being such a fun, caring brother, Papa for your strong confidence in me and my dearest Amma for your infinite love and prayers. You have always believed I could do anything and this is for all of you.

Thank you!! धन्यवाद!! Merci beaucoup!! Danke Schön!! Хвала вам!! Terima kasih!! നന്ദി!!

Riya George

université PARIS-SACLAY

ÉCOLE DOCTORALE
Sciences Chimiques: Molécules,
Matériaux, Instrumentation
et Biosystèmes (2MIB)

Titre : Nanoparticules et assemblages contrôlés pour la théranostique

Mots clés : Nanoparticules, bleu de Prusse, nanomédecine, radiothérapie, thérapie photothermique, IRM

Résumé : Les nanoparticules théranostiques conçues pour détecter les tumeurs et les traiter avec des effets secondaires limités font partie d'une voie importante pour le développement pour la médecine personnalisée. Le bleu de Prusse (PB) est un réseau de coordination microporeux bien connu qui a récemment suscité l'intérêt en raison de son efficacité dans la thérapie photothermique (PTT) dans le domaine infrarouge ainsi que pour l'imagerie multimodale. Les objectifs de cette thèse étaient de développer des nano-agents pour la théranostique basés sur des structures de type PB et de former de nouvelles nano-plateformes auto-assemblées en utilisant des méthodes de synthèse vertes. La première partie du travail comprenait la formation et la caractérisation de nouvelles nanoparticules de type PB contenant des métaux lourds comme radio-sensibilisateurs pour la thérapie. Avec la combinaison or/platine, de nouvelles nanostructures originales d'or décorées de platine ont été obtenues. Les combinaisons Pt et Fe/Pt ont permis d'obtenir des particules de 1 à 5 nm contenant du platine, non-toxiques pour les cellules saines et capables de tuer efficacement les cellules cancéreuses sous rayonnement gamma. Il s'agit de la première indication que des nanostructures de type PB pourraient être utilisées comme radiosensibilisateurs pour la thérapie. L'un des principaux inconvénients de l'utilisation des nanoparticules en médecine est que les particules de moins de 10 nm sont éliminées prématurément, tandis que les plus grosses ne peuvent être éliminées par voie rénale. Pour surmonter ces difficultés, des assemblages activables de particules PB ultra-minces ont été conçus en combinant la chimie des polymères et la chimie de coordination. Les nanostructures 1D se sont avérées capables d'encapsuler des médicaments avec une grande efficacité et leur délivrance au site cible est déclenchée par des stimuli externes. Ainsi, une combinaison synergique de PTT et de chimiothérapie pourrait être réalisée. La formation de l'assemblage améliore également le contraste T1 en IRM , ce qui en fait un agent théranostique efficace.

Title : Ultra-small theranostic nanoparticles and their controlled assemblies

Keywords : Nanoparticles, Prussian Blue, nanomedicine, radiation therapy, photo thermal therapy, MRI

Abstract : Theranostic nanoparticles (NP) designed to both detect tumours and treat them with limited side effects are part of an important route for development of personalized medicines. Prussian Blue (PB) is a well-known microporous coordination network compound that has recently attracted interest because of its efficiency in photothermal therapy (PTT) in the infra-red domain as well as for enabling multimodal imaging. The objectives of this thesis were to develop ultrasmall nanoagents for theranostics based on PB like structures and form new self-assembled nano-platforms using green synthetic methods. The first part of the work included the formation and characterization of novel PB-like nanoparticles containing heavy metals as radio-enhancers for therapy. With gold/platinum combination, new and original platinum decorated-gold nanostructures were achieved. With Pt and Fe/Pt combinations 1-5 nm platinum containing particles were obtained, that were non-toxic to healthy cells while being capable of effectively killing cancer cells using a therapeutic dose of radiation. This is the first indication of PB-like nanostructures could be used as radio-enhancers for therapy. A major drawback of using NPs in medicine is that sub-10 nm particles are prematurely cleared out, while the larger ones cannot be renally eliminated. To overcome these challenges, activatable assemblies of ultrasmall PB particles were designed using a combination of polymer and coordination chemistry. 1D-nanostructures were evidenced capable of encapsulating drugs with high efficiency and their delivery to target site is triggered using external stimuli. So a synergistic combination of PTT and chemotherapy could be achieved. Assembly formation also improves the MRI contrast property of the NPs, making it an efficient theranostic agent.

List of Abbreviations

ALF- Artificial Lysosomal Fluid

CA- Contrast Agent

CD- Cyclodextrin

DLS- Dynamic Light Scattering

DOX- Doxorubicin

DSB- Double Strand Break

EB- Ethidium Bromide

EDS- Energy Dispersive Spectroscopy

EELS- Electron energy loss spectroscopy

EPR- Enhanced Permeability and Retention

FBS- Fetal Bovine Serum

FCC- Face Centred Cubic

FDA- Food and Drug Administration

GA- Gallic Acid

HAADF- High-angle annular dark- field

ICP- Inductively Coupled Plasma

IR- Infra Red

MRI- Magnetic Resonance Imaging

MW- Molecular Weight

NP- Nanoparticle

NIR- Near Infra Red

NO- Nitric Oxide

PAI- Photoacoustic Imaging

PB -Prussian Blue

PBA- Prussian Blue Analogue

PEG- Poly Ethylene Glycol

PET- Positron Emission Tomography

PTT- Photothermal Therapy

PVP- Poly Vinyl Pyrrolidone

ROS- Reactive Oxygen Species

SF- Sensitizing Factor

SER- Sentizer Enhancement Ratio

SSB- Single Strand Break

TE- Tris EDTA

TEM- Transmission Electron Microscopy

UF- Ultra Filtration

UV- Ultraviolet

XPS- X-ray Photoelectron Spectroscopy

XRD- X-ray Diffraction

Table of Contents

1 INTRODUCTION

1.1 NANOPARTICLES

A nanoparticle is essentially a particle of any shape with dimensions between 1 and 100 nm.[1] The nanoscale size of these particles lead to them having very specific and interesting physicochemical properties. Materials composed of nanoparticles have a large surface area when compared to the same volume of material made up of bigger particles. Hence, a nanomaterial has a higher percentage of its composite elements on the surface.[2] This enhances its chemical reactivity and opens up the door to many opportunities. They have unique mechanical, electrical, and optical properties which deviate from the respective bulk material. It has been a highly researched topic in the past few decades and new applications have been discovered. They are used for catalysis, as chemical sensors, in CO_2 capturing and even in the aerospace industry.[3]

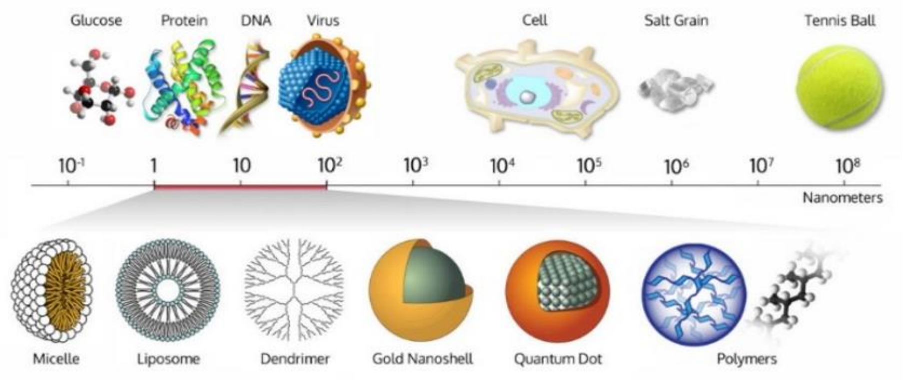

Figure 1. Size comparison of nanomaterials with respect to items used in daily life.[4]

Nanoparticles have made significant contributions to the medical and pharmaceutical industries. They provide enhanced biological mobility due to the size factor. They improve bioavailability by increasing the aqueous solubility and retention time within the body.[5] Some nanoparticles have characteristic properties because of their composition. Gold nanoparticles for example, are capable of absorbing light and efficiently converting it into heat. This localized heating can be used for selective elimination of cancerous tissues.[6] A1nti-microbial activity of silver nanoparticles have been well documented and they are widely used in wound dressings, household products and medicines.[7] Magnetic nanoparticles like superparamagnetic iron oxide also have diagnostic applications as they can act as MRI contrast agents.[8] The size of these single nanoparticles significantly influences the cellular uptake and bio-distribution. Particles with sizes over 100 nm are recognized by macrophages within the body and tend to accumulate in organs like the liver, spleen, lungs and lymph nodes. On the other hand, the nanoparticles smaller than 10 nm could be cleared by the kidney due to the pore size of the renal filtration system.[9] So depending on the required properties, the size as well as parameters like shape, charge and surface labelling can be done to target specific sites in the body. Additionally, having a large surface area enables the functionalization of these nanocomposites with drug moieties. Drugs could be loaded on to the particles and used to deliver it to the target site within the body by triggering the release with external/internal stimuli. This helps with optimizing the drug dosage and increases the therapeutic efficiency of the treatment.[10] The targeted release also reduces the noxious side effects which are generally observed with the conventional dosage forms. The therapeutic and diagnostic (theranostic) applications of nanoparticles will be the focus of this work.

1.2 CANCER

Cells in a human body grow and reproduce to replace old cells and to fix normal wear and tear or damages. However, when affected with cancer, the cells reproduce at a very fast rate and have no control over division. This excessive growth concentrated in a region of the body leads to formation of tumours. The earliest known description of this disease can be found in the Edwin Smith Papyrus dated 3000 BC[11] which illustrated a case of breast cancer. The cancer cells take up nutrients from the body and hinder the normal functioning of organs. It is a cause of a lot of suffering and leads to death of patients. Just in the year 2020, there were 19.3 million new cases of cancer and resulted in 10 million deaths all across the globe.[12] Huge amount of research has been dedicated to finding specifics on the cause and cure for this global disease. The anatomy and vasculature of solid tumours are fundamentally and morphologically different from the normal blood vessels. Under standard physiological conditions, the pH of blood is neutral and around 7.4. Lot of complex cellular mechanisms are triggered in the tumour micro-environment due to lack of oxygen. This renders the area acidic in nature with pH in the range of 5.5-6.8.[13,14] Poor lymphatic drainage from tumours and large pore sizes were demonstrated in 1986 by Matsumura and Maeda.[15] This led to the proposal of a mechanism called Enhanced Permeation and Retention (EPR).

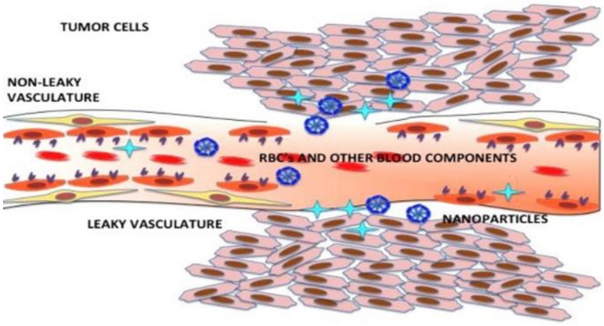

Figure 2. Schematic representation of EPR effect.[16]

During the growth of a tumour, disorganized networks are formed, with vessels being hyperpermeable, immature and leaky [17]. These characteristic traits of tumours can be used to our advantage. Small sized nanoparticles and macromolecular drugs are taken up to a larger extent within these diseased cells. The EPR effect shows that over time the drug concentration within the tumour builds up due to the lack of efficient lymphatic clearance. The increased uptake and retention of nanomaterials within tumours opened doors to new and efficient treatment strategies. EPR helps to passively target the nanoparticles and drug delivery systems (DDS) to tumour sites in the body and is the common route of administering drugs.[18] It has to be noted that a very low amount of the injected dose (~1%) accumulates in the target areas using EPR and it is also dependent on the degree of vascularization of the tumour. Therefore, other types of DDS following an active targeting path are being developed to improve drug delivery and increase its deposition. It relies on specific interactions between the carriers and tumour cells. Nanoparticle/ drug carrier surface is functionalized with ligands like monoclonal antibodies, tripeptide RGD, folic acid and transferrin.[19] Cancer cells have overexpression of specific receptors, for example, folate receptors are observed in fast-growing tumour cells of ovarian, breast, colon and lung cancers. So folic acid conjugated DDS undergo increased uptake in these tumour cells leading to better targeted therapies.[20,21]

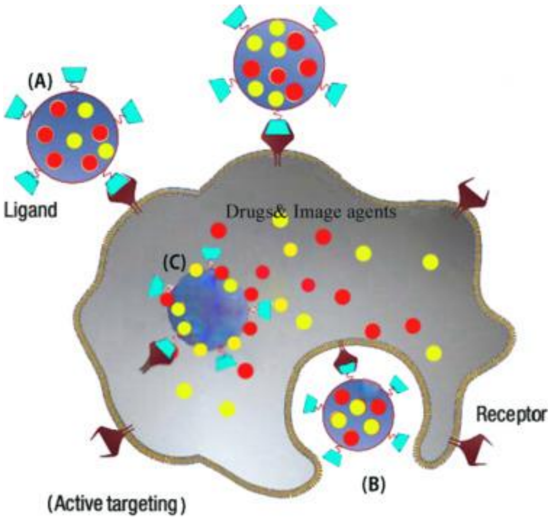

Figure 3. Schematic representation of active targeting mechanisms by which nanocarriers deliver drugs and imaging agents to target cells.[19]

There are many types of cancers and the treatment techniques vary accordingly. The traditional methods used are surgery, chemotherapy and radiation treatments. Novel strategies to reduce the side-effects, overcome drug resistance and improve the quality of life of the patients have come up in recent years.[22] Photodynamic therapy (PDT) is a widely used, non-invasive treatment involving the use of a photosensitizing drug that could be activated by specific wavelength of light, which can trigger killing of cancer cells.[23] Hyperthermia or thermal therapy is a clinically used treatment where cancer tissues are specifically exposed to high temperatures that cause their death. Photothermal therapy also involves increasing the local temperatures but through photothermal agents that convert light to heat. Some of these techniques are used in combination to generate a stronger effect.[24] Gene therapy involves modifying tumour cells with genetic materials. This can instigate a strong immune response and cause tumour suppression. New types of therapies involving stem cells, antibodies and cancer vaccines are being developed and are currently in different phases of clinical trial.[22,25]

Only few of these treatment methods that are directly related to the work in this thesis will be described in the following section.

1.2.1 Therapeutic methods

1.2.1.1 Chemotherapy

This treatment method utilises drugs to stop or slow down the growth of cancer cells. Standard medications include chemicals like paclitaxel, doxorubicin, gemcitabine, carboplatin, docetaxel and fluorouracil. They are marketed under different brand names and are sometimes given in combination to treat aggressive cancers. These drugs help with shrinking large tumours and lessen the chance of its return.

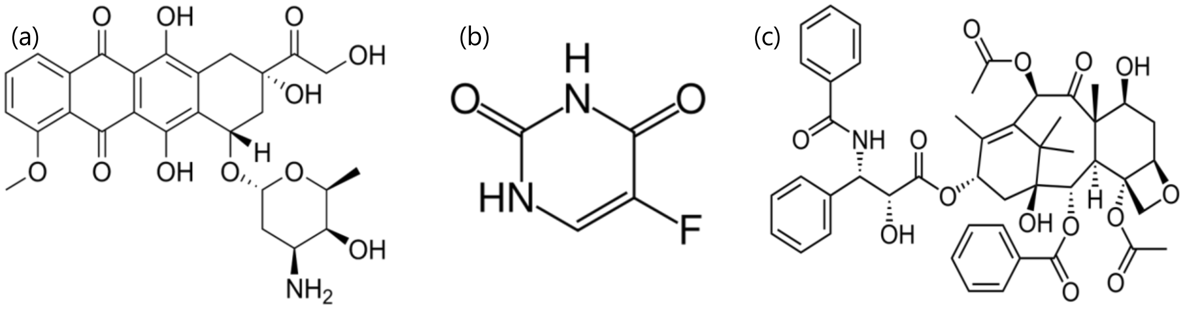

Figure 4. Chemical structure of (a) Doxorubicin (b) Fluorouracil (c) Paclitaxel

These medicines target rapidly dividing cells like the malignant cancerous ones, but this is also the cause of side-effects. Normal cells, present in blood, mouth, intestine and hair also divide rapidly and so the chemotherapy drugs affect them adversely.[26] This damage to healthy tissues cause intense fatigue, mouth sores, nausea and hair loss. Apart from these common side-effects, osteoporosis, vision, nerve and heart problems have also been observed in patients receiving such treatments. Hence, it is extremely essential to optimize the drugs used for therapy and increase its efficiency by targeting them to the required site of action. Strategies to deliver such drugs using nanoconjugates, to specific tumour sites while minimizing interactions with healthy cells is an important area of research.

A wide range of drug delivery systems (DDS) based on polymers, proteins, lipids, organic and inorganic nanoparticles have been developed in the past decade.[22,27] Carbon nanotubes, 2D layered double hydroxides, and mesoporous silica nanoparticles are some of the common inorganic nanocarriers.[28,29] Liposomes have been used to encapsulate hydrophilic drugs within their aqueous core and hydrophobic drugs in the lamellae. Polymeric nanoparticles made from synthetic polymers: poly(lactic acid), poly(ε-caprolactone), poly(lactic-co-glycolic acid), poly(styrene-maleic anhydride) copolymer, or from natural polymers: gelatin, dextran, chitosan, collagen etc. have been reported as efficient DDS.[27] Nanoscale metal organic frameworks (Nano-MOFs) have high specific surface area, adjustable pore size, and good biocompatibility. Therefore, a large variety of MOFs have been developed for drug-loading and combining different therapies.[30] Chemotherapy drugs paclitaxel, doxorubicin have also been incorporated within polymeric micelles, and a reduction in toxicity at high doses was observed.[31,32] Nanocarriers based on proteins (human/bovine serum albumins) have been developed and abraxane: a paclitaxel-albumin nanoparticle, is an FDA approved product.[33] Biocompatible 3D hydrogels have also been used for pH-sensitive controlled delivery of therapeutics.[34]

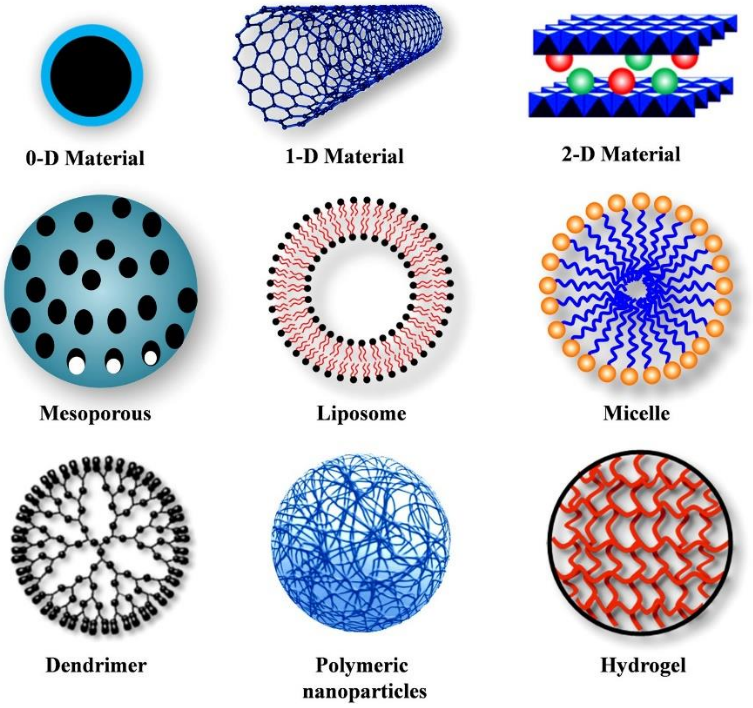

Figure 5. Different types of nanocarriers used as drug delivery vehicles for cancer treatment[27]

1.2.1.2 Radiation Therapy

Radiation therapy is one of the most common forms of treatment and it has been found that more than 50 % of cancer cases require this therapeutic method. High energy ionizing radiation (keV-MeV range) is used in this form of treatment. They can interact with the cancerous tissues in the body and cause damage to the genetic information of the cells. The main advantages of this procedure is non-invasiveness, quickness and localisation of treatment. The tumours located deep within the body could also be specifically targeted by tuning the source of radiation.[35] The mechanism of action is that when radiations pass through the water present in our body, it generates radicals. Radicals are chemical species that contain an unpaired electron and this makes it highly reactive. The radicals are capable of quickly generating Reactive Oxygen Species (ROS) like peroxide, superoxide, hydroxyl radicals and singlet oxygen[36]. They are capable of damaging biomolecules, breaking the strands of DNA in the cancer cells and cause mutations. These mutations in turn, halt the cell division process and eventually cause their death.

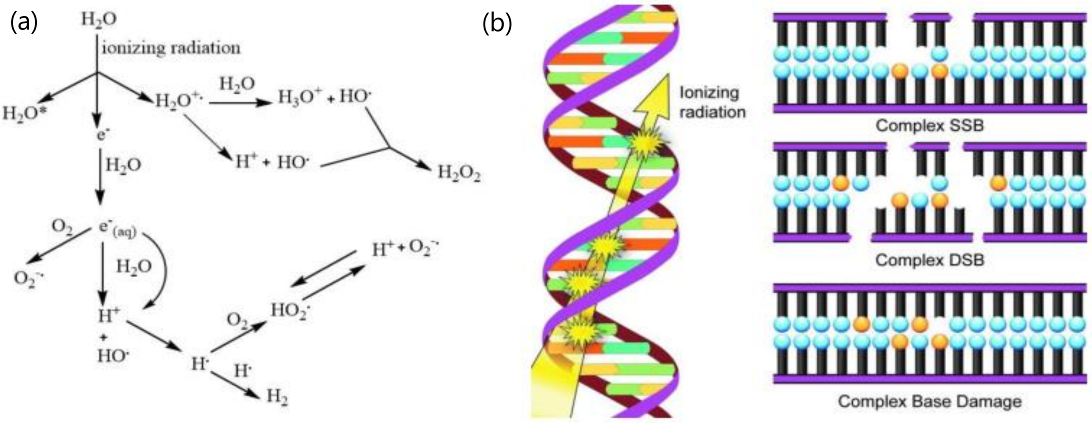

Figure 6. (a) Production of reactive oxygen species (ROS) on water radiolysis (b) Schematic representation of single and double strand breaks on DNA on exposure to ionizing radiation.[36]

It has also been observed that radiations can cause damage to the surrounding healthy organs, cause skin problems, fatigue and sometimes even long term side effects like a second cancer[37] due to the mutations. Hence, a certain safety limit to the amount of radiation applied to a patient was determined and enforced. This knowledge lead to the development of a new era of research to develop chemical agents called radio-sensitizers that could achieve targeted killing of tumours while being subjected to a therapeutic dose of radiation. In 1973, G.E Adams outlined the specific criteria that would be required for such sensitizers and stated that they should ideally be non-toxic to normal tissues and specifically sensitize cancer cells at therapeutic doses. The sensitizer also needs to be fairly resistant to metabolic breakdown, while being able to penetrate distances up to 150 μm from a blood capillary to reach the diseased tissues. [38]

Enhancement of radiation generated DNA damage by small bonded molecules, inhibition of cellular repair post-radiation, cell cycle dysregulation, and radiolysis of the sensitizer to form cytotoxic molecular fragments, were some of the common working theories behind developing new radio-sensitizers. Expanding on it, Fowler et.al [39] developed oxygen mimetic agents, studied their effects with clinical trials to specifically target hypoxic tumour cells which made them more vulnerable to high energy radiation. In 1980, the presence of high atomic number (Z) containing material like iodine within cells, was found to sensitize them towards X-rays [40] and this was attributed to photoelectric effect, causing increased dose absorption. Since a high-Z metal containing cisplatin obtained the FDA approval for chemotherapeutic treatments, its possible use as a radiosensitizer was widely investigated.[41] Additionally high-Z materials, especially chemically inert metals were the ideal choice for synthesizing the radio-sensitizers, as potential health hazards could be minimized. Thereafter, many more transition metal (Pt, Ru, Co, Fe, Rh, Gd etc.) [42–45] complexes were developed across the world, to further improve the properties, work against cisplatin-resistant models and to incorporate multi-functionalities like combining photo-sensitization or magnetic resonance imaging along with radiation effects.

More recently it was documented that irradiating cells internalized with high-Z elements, generated a cascade of Auger electrons. [46] These secondary electrons are brought about by inner shell ionization of heavy metal atoms and lead to a significant rise in the amount of reactive oxygen species (ROS) produced within the body, upon water radiolysis. When these radicals are generated in close proximity to the DNA of cancer cells, harmful single and double strand breaks occur. They are capable of stalling cell proliferation, causing apoptosis and subsequent elimination.[47] The nano-size has a wide range of advantages as described earlier. In 2004, J.F. Hainfield et.al provided the first proof of principle that gold nanoparticles (np) significantly improved the *in vivo* efficacy of radiation therapy. They demonstrated that the ultra-small size of these particles prove advantageous for bio-distribution and relatively high concentration of the heavy metal could be incorporated without toxicity. [48] The potential of metallic nps to enhance local dose deposition was soon identified, leading to an exponential increase in development of varied particles that could improve the performances of conventional radiation therapy.

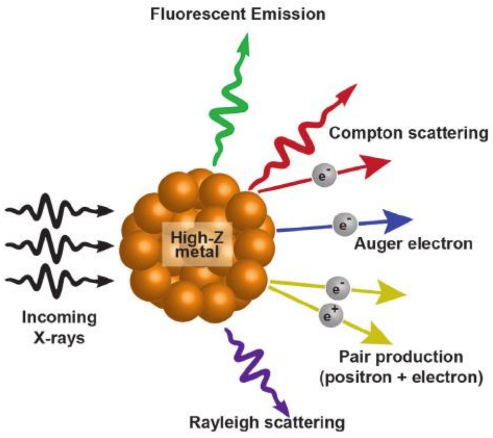

Figure 7. Production of secondary electrons upon irradiation of a high-Z metal. [49]

Additionally, nanoparticles provide a relatively large surface area and are flexible towards size, shape and charge modifications that prove advantageous for drug encapsulation and specific delivery to target sites. Gold (CYT-6091 CytImmune)[50], gadolinium (AGuiX, NHTheraguix) [51] and hafnium oxide-based (NBTXR3, Nanobiotix)[52] nanoparticles have even reached the clinical trial phase. Over the past few years, many physical and chemical techniques to produce such nano-agents have come into play.[53–56] However, most methods require multiple complicated steps for synthesis, use non-polar solvents, toxic reducing agents and organic surfactants for controlling the nanoparticle size. Subsequent functionalization with more chemical substituents is sometimes required to make them water-soluble and biocompatible.[57] Even after this painstaking process of development, long-term stability in physiological media and complete renal elimination, which is essential for nps developed for bio-medical processes remain questionable.

1.2.1.3 Photothermal Therapy

In this therapeutic technique, cancer cell death is induced by heating the tumour tissue. Localised temperature rise causes cell membrane collapse, protein denaturation and eventually apoptosis.[58,59] This form of treatment is minimally invasive as it can be achieved by exposing only the affected area to safe near-infrared (NIR: 650-1024 nm) light. This range of optical wavelength is called the biological window because skin, haemoglobin and tissues of the body have a minimal absorbance here.[60,61] So, the radiation can penetrate deeper than the other wavelengths. Specific material which can absorb NIR light and transform it to heat is essential for this process. A lot of research has been dedicated to develop such agents, in the past two decades. The photo-thermal agents need to have a large absorption cross-section in the biological window as well as a high light to heat conversion efficiency. As mentioned earlier, nanomaterials are a subject of interest in cancer therapy.[62] Carbon nanotubes, graphene based materials and quantum dots are shown to absorb light and cause ablation of tumour cells. Metallic nanostructures composed of gold (Au), silver (Ag), copper (Cu) and palladium (Pd) and have been widely studied for their photo-thermal properties.[63] AuroShell particles (PEGylated-silica cored Au nano-shells) have even advanced to the clinical trial stage due to their excellent preliminary results [64].

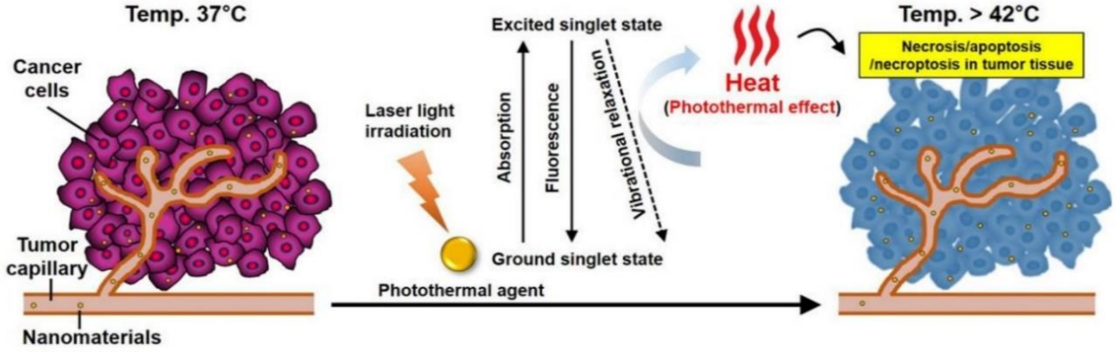

Figure 8. Mechanism of action of nanomaterial mediated PTT effects in tumour environment. For tumour ablation, the heat (> 42°C) generated during excited PTT agents' vibrational relaxation induces necrosis and apoptosis of the cancerous tissues.[65]

There are however some limitations to this method of treatment. It is possible to have some thermal damage to normal tissues during the course of PTT. The limited penetration depth of light and uneven heating is another disadvantage, especially for tumours located deep within the body.[66] This can lead to incomplete elimination of cancer cells which increases the chances of recurrence and metastasis. The combination of PTT with other treatments can help in improving the overall treatment efficacy.[67] For example, conjugating doxorubicin onto a nanocomposite made of Ag and graphene oxide improved the therapeutic index by a large extent. *In vivo* experiments performed on mice, revealed that the side-effects of the chemotherapeutic drug is drastically reduced, survival quality and prolongation of life time was observed.[68] Moreover NIR laser light aided in delivering the drug to the target site. The synergistic effect of combining chemotherapy and PTT have been well documented in literature.

Only a few cancer treatment techniques have been outlined above. Surgery is primarily used to remove large tumours. Immunotherapy, hormone and photodynamic therapy are also some of the methods which can be used to fight the growth of malignant tissues. Finding innovative, thorough, targeted and patient-specific type of treatment remains one of the main goals of research in this century.

1.2.2 Diagnostic Methods

It has to be noted that all these pharmaceutical therapies are highly dependent on clinical imaging. It is extremely important to visualize the diseased area in order to determine a treatment strategy. Only by constantly monitoring the tumour cell proliferation and migration within the body can the effectiveness of a therapeutic method be determined. Diagnostic imaging methods are necessary to formulate a plan, give early indications of treatment response and detect drug resistance. Also after the treatment is complete, patient monitoring is essential to check for recurrence[69]. All of these require advanced ways to look inside the body and many types of diagnostic methods have been developed.

X-rays have been used since the late 19th century to detect injuries, and it uses low dose of radiation to form images. Positron emission tomography (PET) is a popular diagnostic tool that generates 3-dimensional picture of areas within the body using radioactive (^{18}F, ^{11}C, ^{13}N, ^{15}O, ^{124}I, ^{64}Cu) tracers.[70] It is commonly used to detect cancer, because these cells take up more of the injected radioactive glucose compared to healthy cells. It can give insight into the tumour physiology, but cannot provide anatomical details as the spatial resolution is around 1-2 mm.[71] Computed Tomography (CT)-scan uses x-rays and is performed to obtain internal images of bones, muscles, organs and, blood vessels. Usually an iodine or barium sulphate based dye is introduced to enhance the contrast of this scan and extensive details like lesion location, size and morphology can be obtained, with resolution of 50-200 μm.[70,72] Only the diagnostic methods that are the focus of this thesis project: magnetic resonance and photoacoustic imaging are described in detail in the following section.

1.2.2.1 Magnetic Resonance Imaging

MRI is a non-invasive imaging procedure that can generate detailed, three dimensional anatomical images which can help in detection, diagnosis and treatment of different types of diseases. It uses strong magnetic fields and radio-waves to generate images of the organs in the body. This makes the technique very safe, especially compared to computed tomography (CT) scans and X-rays which use ionizing radiations. MRI provides a high spatial and temporal resolution, along with soft-tissue contrast. To put very simply, MRI works due to the fact that the nucleus of an atom behaves like a tiny magnet. So when a patient is placed inside a large magnet and a strong magnetic field is applied, the protons from the water in the body align with it. Then a radiofrequency (RF) pulse of the same frequency is passed through the system[73] which causes excitation and resonance of the protons. When this pulse is removed, the protons quickly try to relax and realign with the initial magnetic field. This relaxation leads to a release of energy which can be detected by sensors in the scanner.

Depending on the type of relaxation, longitudinal or transverse, different signals are released. They are represented by time constants and it determines the way an image appears. T_1 signal is dependent on the time taken for the system to return 63% toward thermal equilibrium after the RF pulse.[74] The faster the realignment occurs, brighter is the contrast in the picture. T_2 or transverse relaxation time relates to the speed of proton spin dephasing. A short T_2 relaxation time leads to a darker or negative contrast for the image. The physiological differences between the constituents of our body are capable of generating a MRI image with natural contrast. For example, the protons in fat can realign quickly, generate high energy and therefore a short T_1 value (260 ms).[75] So, a T_1-weighted MRI will display fatty tissue brightly whereas water will appear dark as it has a long T_1 (3000-5000 ms). But to improve the sensitivity of this diagnosis method and detect abnormal growth or diseases in the body, contrast agents (CA) are required.

1.2.2.1.1 MRI Contrast agents

Most common MRI contrast agents (MRCA) used clinically, work by shortening the T1 relaxation time of the protons. This was first practically demonstrated in 1981, by Young et.al [76] who showed that relaxation rate could be enhanced by using a paramagnetic contrast agent. They used iron chloride ($FeCl_3$) as CA to image the upper abdomen of adult volunteers and heightened contrast could be clearly seen. This was attributed to the change in mean T1 value, from 730 ms to 285 ms after ingestion of ferric chloride solution. A few years later, it was shown that chelates containing Gadolinium (Gd^{3+}) provide a significant contrast enhancement and can be even used to visualise tumours in the brain. The agent called Gd-DTPA (Gd-Diethylenetriaminepentaacetic acid), was intravenously injected in 12 patients suffering from different types of cancers. Cerebral tumours could be observed in all of the cases and additional lesions which could not be detected with CT were seen with Nuclear Magnetic Resonance (older name for MRI) imaging. As shown in Fig. 9(a) tumour and oedema is visible in the left frontal region, but after the Gd-DTPA administration a light ring of enhancement can be seen around the bulk of the tumour.[77] It was marketed as Magnevist and was a clinically approved CA. However, its usage has been suspended by European Medicines agency in 2017.[78]

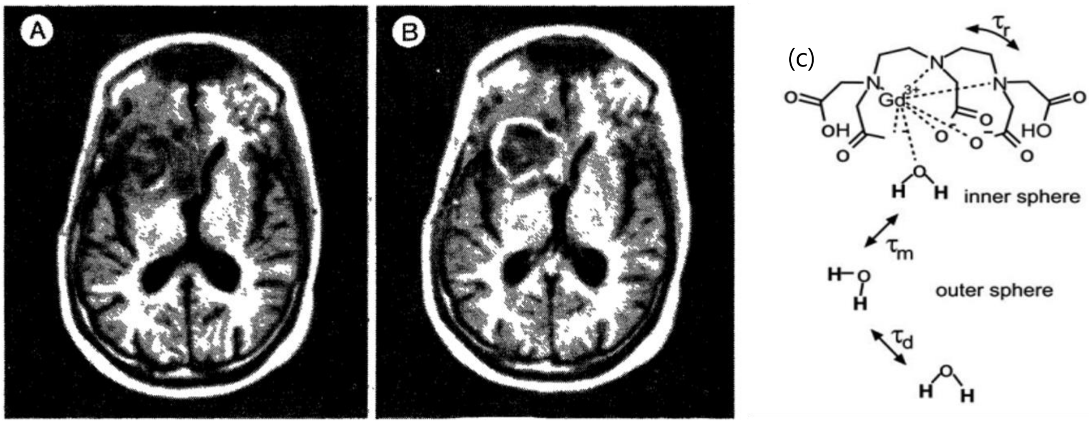

Figure 9. (a) Astrocytoma grade IV: transverse inversion-recovery (IR1500/500/44) scans before (A) and after (B) Gd-DTPA injection.[77] *(b) Working principle of a T_1 lowering agent, Gd-DTPA by coordination of water to the inner sphere of Gd^{3+} ion.*[79]

In the late 1980s, a new gadolinium complex: gadolinium tetraazacyclododecanetetraacetic acid (Gd-DOTA) was formulated. The T1 relaxivity was similar to Magnevist, but this cyclic complex had higher *in vitro* stability and better *in vivo* safety as compared to non-cyclic Gd-DTPA.[80] This led to further clinical studies and it was found that Gd-DOTA improves the anatomic definition of cerebral lesions and increases MR sensitivity and specificity.[81] This complex is sold under the brand name Dotarem and is one of the most widely used MRCA.

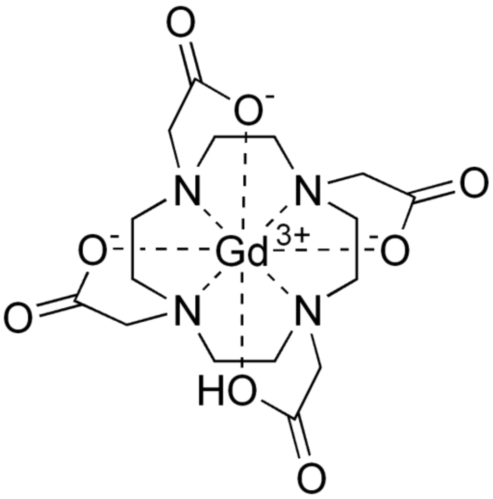

Figure 10. Structure of Gd-DOTA

The enhancement T_1 weighted contrast in presence of paramagnetic ions of Gd, Mn and Fe occurs because the unpaired electrons in them. Solomon-Bloembergen-Morgen theory gives details about interaction of electron-proton dipolar coupling. The effect of a T_1 CA can be described by understanding the Relaxation rate ($R_1=1/T_1$). It is the inverse of the relaxation time and in presence of a CA it is split into two: the intrinsic contribution from the tissue ($R_{1,tissue}$) that is being analysed and the paramagnetic contribution coming from the agent applied($R_{1,CA}$). [79] This $R_{1,CA}$ is dependent on the concentration of CA, as well as its relaxivity (r_1).

This parameter is characteristic to the CA used and depends on the solvent, temperature, field strength and the environment.

$$R_{1,\text{obsevered}} = R_{1,\text{tissue}} + R_{1,\text{CA}}$$

$$R_{1,\text{CA}} = r_1.\,[\text{CA}]$$

$$\text{Therefore,}\quad \frac{1}{T_{1,\text{obs}}} = \frac{1}{T_{1,\text{tissue}}} + r1.\,[\text{CA}]$$

So the overall relaxation rate can be increased by using an agent which has a high relaxivity value or increasing the physiological concentration of the CA. As shown in Fig.9 (c), Gd^{3+} ion coordinates directly with the water in the inner sphere and this can undergo fast exchange with the outer sphere. This exchange rate is dependent on the exchange correlation time (τ_m) and the number of coordinated water ligands to the paramagnetic ion . So, the paramagnetic ion is also indirectly connected to the bulk (second coordination sphere). The unpaired electrons in this paramagnetic agent create fluctuating local magnetic moment which provides the interacting water protons, with an alternate and quicker relaxation pathway.[79] There are other parameters like the rotational correlation time of the whole complex (τ_r) and diffusion correlation time (τ_d) that also influence the relaxation rate. With the relaxation time shortened, the protons are capable of quickly returning to equilibrium after the RF pulse, and this speed is translated to T1 contrast enhancement.

It was shown that small molecules, like Gd^{3+} complexes typically have an elimination half-life of 1.5 hours. This rapid clearance makes time-dependent MRI studies difficult and complicated. Additionally, the chelating agents have a high affinity for endogenous ions like Zn^{2+} and Ca^{2+} and subsequent transmetallation reactions can result in Gd^{3+} release from the complex. There is also a growing safety concern, as many Gd-based MRI CAs have been linked to development of nephrogenic systemic fibrosis in renally impaired patients.[82,83] Therefore a move from simple complexes to paramagnetic ion containing nanoparticles is highly favoured.

1.2.2.1.2 Nanoparticles for enhancing MRI contrast

As mentioned earlier nanoparticles have a tendency to accumulate in tumours because of the EPR effect. Formulating a contrast agent in nano-size provides an opportunity to diagnose them completely and follow their evolution with time. Multiple examples can be found in the literature where nanocomposites are synthesised with polymers or liposomes with gadolinium incorporated in the structure. There are also a lot of studies on grafting Gd^{3+} to other metallic nanoparticles, to provide a combined therapeutic and imaging modality.[84] Besides Gd^{3+}, manganese based contrast agents exist and they also work by shortening the T1. Mn^{2+} based nanoparticles have been used for tumour imaging, to follow the metastasis and monitor pH changes. [85] Ferric oxide based MRI contrast agents act as T_2 imaging agents. They shorten the T_2 relaxation time and provide a dark contrast for the images. This is due to its superparamagnetic nature. Many types of super paramagnetic iron oxide nanoparticles (SPION) have been synthesised over the past decade ranging from 2 nm to 35 μM in size.[86] These agents have been used for molecular imaging, gene monitoring and cancer diagnosis. But as with most T_2 agents, it is challenging to distinguish the darkened spots produced by accumulation of SPIOs and signals caused by bleeding, calcification, metallic deposits or artefacts from the background.[87]

The contrast efficacy and *in vivo* fate of magnetic and metallic nanoparticles rely heavily on physical and chemical features including shape, size, surface charge, chemical and colloidal stability. They play an important role in controlling the bio-distribution and blood circulation half-life of these particles. A long blood circulation of contrast agent is crucial for increasing the time window of imaging. MRCAs with large hydrodynamic size exhibit high uptake in reticuloendothelial system (RES) organs like spleen, liver, lymph nodes and lungs leading to accumulation or very slow elimination through hepatobiliary excretion. This can lead to *in vivo* toxicity and FDA approval for administering any imaging agent requires complete metabolization or excretion from the body once the goal is achieved.[88] Therefore large sizes hamper translation of nps into clinical medical agents. It has been shown that creating nanocomposites containing Gd complexes could prolong blood circulation. The pore size limit for glomerular filtration barrier (GFB) in the kidney is around 6 nm, to prevent excretion of useful proteins. But it has been demonstrated that some larger nanoparticles (> 6 nm) have bypassed the GFB and are successfully eliminated via urine.[89] This could be through the proximal convoluted tubules in the kidney and/or due to specific physico-chemical characteristics (charge, composition, density, shape etc.) of the nanoparticles.[90] Therefore, it is generally considered that sub-10 nm particles can be renally eliminated and safer for the body. Therefore many ultra-small Gd-based MOFs, carbon quantum dots and gold nanocomposites were synthesized to generate effective and multi-functional CAs. [91–94]

AGuIX® (Activation and Guidance of Irradiation by X-ray) nanoparticles developed by NH TherAguix (Lyon, France) is one of the most promising theranostic platforms ever developed. These sub-5 nm particles contain gadolinium cyclic chelates in a polysiloxane matrix.[95] Strong MRI contrast properties together with high radiosensitizing behaviour has been demonstrated with these nanoparticles, due to the presence of high-Z (Gd) metal in the structure. Biodistribution studies conducted on animal species (rodents, monkeys) proved they could be passively targeted to tumours via EPR and renal elimination is achieved after intravenous administration.[96,97] First in man studies demonstrated that AGuIX nanodrug is capable of crossing the blood brain barrier and detect metastases originating from lung, melanoma, colon and breast cancers.[98,99] Its safety and efficacy in patients have been tested and this theranostic nanoplatform is currently in phase-II clinical trials. [100]

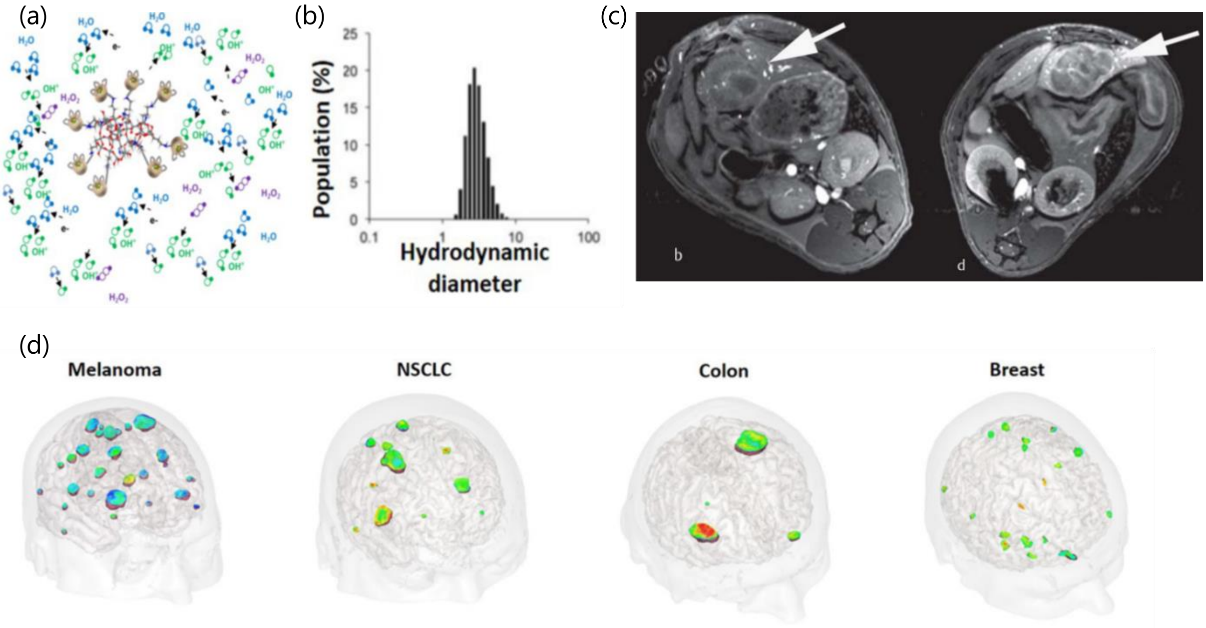

Figure 11. (a) Schematic representation of electron showers and ROS formation after irradiation with AGuIX (b) Hydrodynamic diameter of the nanoparticles (c) T1-weighted images of hepatic metastasis after application of Gd-DOTA (left) compared to AGuiX (right) (d) Illustration of 3D MRI of NanoRAD clinical trial obtained 2 h after intravenous administration of AGuIX nps.[96,99]

Various strategies to form Gd free CAs have also gained traction over the last decade to ensure maximum safety. Renally clearable iron nanodots have offered an attractive solution. Wang et.al developed a gram-scale synthetic route to form Fe^{3+} coordination polymer nanodots (Fe-CPNDs) by using polyvinylpyrrolidone (PVP) and Gallic Acid (GA). The nanodots are around 5 nm in size, display good photo thermal performance and act as pH activatable MRI imaging contrast agent (r_1= 1.9 $mM^{-1}.s^{-1}$ at pH= 5, 1.5 T).[101,102]

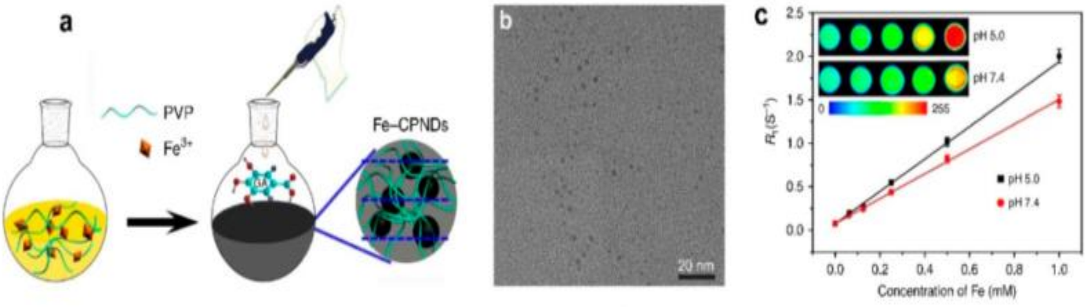

Figure 12. Fe-Coordination Polymer Nanodots synthetic scheme[101]

Shi and co-workers recently created a switchable T_1/T_2 CA by forming cross-linked Fe_3O_4 clusters using cystamine dihydrochloride. The ~135 nm nano cluster exhibits a dominant T_2 effect with r_2 of 26.4 $mM^{-1}.s^{-1}$ (0.5 T) and this cluster could be dissociated into 3.3 nm single nps in the reducing microenvironment of tumour(GSH= 10 mM). The disassembled ultra-small nps show a strong T_1-weighted MR effect with an r_1 of 3.9 $mM^{-1}.s^{-1}$(0.5 T).[103] It is a promising system with interesting properties and could aid precision imaging of cancer cells. It is critical to develop cost-effective strategies to produce CAs as they are generally administered in gram scale quantities. Agents with strong chelating properties must be developed to limit gadolinium leaking from the nanocomposites. Moreover, integrating two or more paramagnetic metallic ions into a single nanohybrid can be helpful in overcoming individual drawbacks and provide comprehensive imaging through T1/T2 weighted dual-mode MRI.[94]

1.2.2.2 Photoacoustic Imaging

Photoacoustic imaging (PAI) is a non-ionizing and non-invasive hybrid imaging technique that combines optical excitation and ultrasonic detection.[104,105] When laser light is shone on tissues, they absorb the energy, convert it to heat and undergo thermoelastic expansion.[106] This expansion generates ultrasound pressure waves which can be detected by sensors that transform the signal into images. This is a safe diagnostic tool, which can provide structural and functional information with high penetration depth. It is a convenient, comparatively cheap alternative and has near real-time imaging capability.[107] PAI could be used for lymph node detection, tumour microenvironment imaging and also cell tracking.[63]

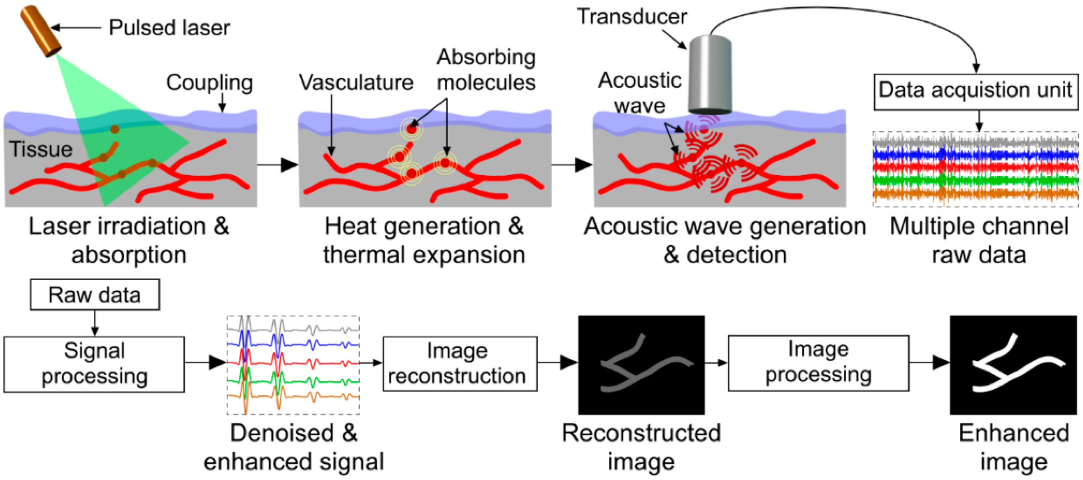

Figure 13. A conceptual flow of photoacoustic imaging working principle.[104]

Melanin, bilirubin, glucose, myoglobin, and haemoglobin in the blood act as natural photo acoustic agents.[105] However, an added exogenous light-absorbing material can improve the contrast obtained from PAI. Small molecule organic dyes such as methylene blue, indocyanine green and silicon naphthalocyanine have good tissue penetration and can generate acoustic waves after laser irradiation.[108] Their applications in vascular and tumour imaging as well as monitoring the blood-brain barrier function has been well documented.[9] The disadvantages of these molecules include low PA signal, poor photostability, fast clearance, and small optical absorption cross sections.[109,110]

Therefore, nanoparticles showing strong optical activity have been widely explored for these purposes. Many gold nanostructures (nanoshells, rods, cages, flowers etc.) with extinction coefficients in NIR range have been developed.[111,112] Carbon nanomaterials have excellent light absorption and low heat capacities which make them good photo acoustic contrast agents.[113,114]As local temperature rise is essential for the functioning of this procedure, PAI can work in synergy with photo thermal therapy. Photothermal agents such as the metallic nanoparticles (Au, Ag, and Cu) described earlier (section 1.2.1.2), have also been demonstrated to have PA properties. Photoacoustic imaging guided, *in-vivo* photothermal therapy for breast cancer has been recently demonstrated using FeOOH-polypyrrole nanorods.[115]

1.3 PRUSSIAN BLUE

Prussian Blue (PB) is an intense blue coloured pigment that was accidentally created in 1706. "*Preussisch-blau*" or "*Berlin Blau*" was first synthesized when Diesbach from Berlin, mixed potash contaminated with hexacyanoferrate into a solution which contained iron sulphate. Since its discovery, Prussian Blue was widely used by painters and also applied to dyeing of textiles due to its captivating colour. It is said that Vincent Van Gogh has used this colour to create his masterpiece: The Starry Night. The scientists of the time including Priestley, Berthollet, and Scheele were interested in finding the composition, stoichiometry and structure of Prussian Blue.[116] In 1811, Gay-Lussac revealed that Prussian Blue contained cyanide. Development of X-ray diffraction provided a greater insight into the structure of this compound. In 1936, Keggin and Miles reported that the ferrous and ferric atoms are arranged alternately and form the corners of a cubic lattice, while CN groups lie on the edges.[117] The first detailed structure and composition was confirmed as $Fe_4[Fe(CN)_6]_3.x\ H_2O$ (x=14-16) in 1977 by Buser, Schwarzenbach, Petter and Ludi.[118] They revealed that the cubic unit cell of PB has a lattice constant of 10.16 Å and density of 1.8 g/cm^3. The structure is porous with randomly distributed vacant sites. The distances between the individual atoms in PB were reported as: Fe(II)–C=1.92 Å, Fe(III)–N=2.02 Å, and C-N=1.13 Å. The distance between the two iron species Fe(II)–Fe(III) was approximately 5.1 Å. [117] The cubic cell is made up of four such cubes, resulting in a lattice length of about 10.2 Å. This corresponds to the distance between two consecutive FeII–FeII.

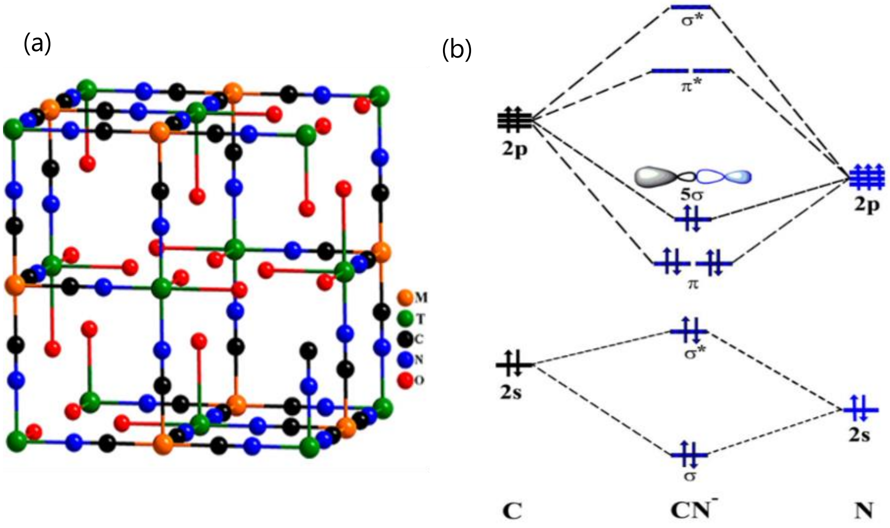

Figure 14. (a) Structure of Prussian Blue and analogues. M and T represent the two composite

metals linked through a cyanide bridge. In case of PB, M and T are Fe^{II} and Fe^{III} respectively. (b) Molecular orbital diagram of CN linker in PBA.[119]

Figure 14 represents the structure of Prussian Blue. By changing the constituent metal ions, PB analogues (PBA) could be formed. CN^- generates a strong ligand field at the carbon end and thereby locking M (or Fe^{II}) in a low spin (LS) electronic configuration. In these coordination polymers, hexacyanometallate $[M^m(CN)_6]^{(m-6)-}$ complex ion and the other metal (T) remain strongly linked through the CN bridge due to an overlap of their electron clouds caused by CN^- π back-donation ability. As shown in orbital diagram, the highest occupied molecular orbital (HOMO) of the ligand is 5σ which contributes to the electrophilic attack of the complex. The electron density from M is subtracted, located on to the N end of 5σ and donated onto the second metal (T) leading to formation of the coordination bond. This metal to metal charge transfer is responsible for the intense blue colour and strong absorption of pure PB around 700 nm. The strong bonds with metal at both C and N end of the cyanide bridge, confers high insolubility in aqueous medium to the formed polymers. The stability of PB in neutral and acidic conditions also arises from the CN^- bonding properties.[119,120]

The arrangement of atoms allows the accommodation of water molecules and cations within the tetrahedral vacancies of the Prussian Blue network. This characteristic property makes PB act as a chelating agent and absorbent. It can act as an ion-exchanger and trap toxic radioactive and non-radioactive ions. Despite being made out of cyanide salts, PB is non-toxic because CN groups are tightly bound to the iron. It is a Food and Drug Administration (FDA) approved drug for this reason and used as an antidote for heavy metal poisoning.[121] It was determined that a concentration of up to 500 mg of PB is safe for consumption and was administered to individuals exposed to radioactive 137-Cs^+ during the Goiania accident in Brazil in 1987.[122] Surface adsorption, proton exchange and mechanical trapping of ions within the crystal structure are the primary mechanisms of decontamination.[123] This versatile compound has many significant scientific and industrial applications apart from the ones mentioned above. They can be used as electrocatalysts, photomagnets, batteries, super capacitors, ion-sensors, in electrochromic displays and also for hydrogen storage.[124] The bio-medical applications of Prussian Blue will be described in this thesis.

1.3.1 Synthesis of Prussian Blue and analogue nanoparticles

Many synthetic strategies have been developed to expand the application, enhance the performance and facilitate the clinical applications of PB nanomaterials. The most simple and conventional method to prepare pure PB is one-step mixing process of the precursors i.e. alkali hexacyanoferrate $[Fe(CN)_6]^{4-}$/ $[(Fe(CN)_6]^{3-}$ with corresponding iron salt (Fe^{3+}/Fe^{2+}). The analogues could also be synthesised with ease using this co-precipitation method by replacing one or both of the precursors with other required metal salts. A variant to this process is reacting Fe^{2+} salt with hexacyanoferrate (II) forming Berlin white and then oxidizing it with agents like hydrogen peroxide to form PB.[124] However preventing PB nanoparticles from coagulating or aggregating when administered to a living organism was a challenge. Different methods of surface functionalization were developed involving polymers (PVP, PAH, PEG), biomolecules (RBCs, albumin, avidin, gelatin), organic acids and oleylamines.[125] In 2010, Shoukimehr et.al showed that biocompatible and water dispersible PB nps could be synthesised by using citric acid to cap the surface.[127] The reaction could be carried out at 60°C or room temperature and yielded 25 nm cubic nanoparticles. This synthetic procedure was adapted by many groups to synthesize PB for varied applications.

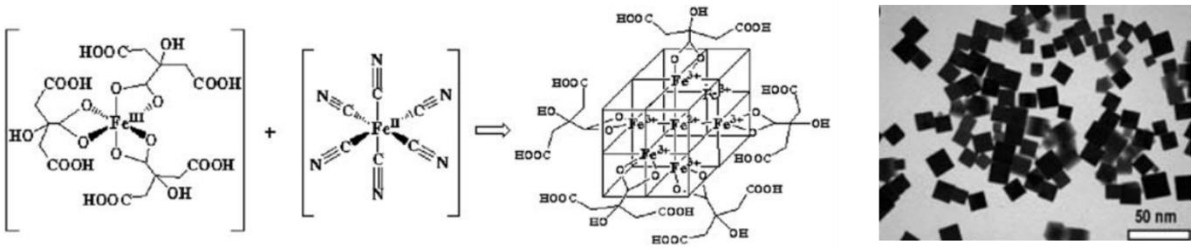

Figure 15. Citrate mediated growth of PB nanocrystals and their TEM image.[127]

The hydrothermal method utilizes an autoclave reactor, involves dispersion of the reactants in water, and subjecting them to high temperatures (>100°C) and pressure. PB mesocrystals were formed by reacting potassium hexacyanoferrate(III) and PEG 4000 in acidic conditions for 20 h at 120°C. Hollow Prussian Blue nps were developed by controlled chemical etching in the presence of a polymer. Large PB nps (110-190 nm) were used as starting material and treated with hydrochloric acid at 140°C for 4 h in the presence of PVP to create hollow interiors that could be used to load drug molecules.[128]

A single precursor method to form PB also exists and it involves slow oxidation or reduction of either $[Fe(CN)_6]^{4-}$/ $[(Fe(CN)_6]^{3-}$ in an acidic environment. The formed iron ions then react with undecomposed hexacyanometallate to form well controlled and monodisperse PB. In addition to being a slow reaction process, traces of hydrogen cyanide are released which is not ideal.[129] Using microemulsions to control the growth of nanoparticles have also been explored. Anionic surfactants like bis(2-ethylhexyl) sulfosuccinate were used to encapsulate iron precursor complexes and then a slow reaction was induced to produce numerous nuclei and clusters within the water droplets in reverse microemulsion method.[130] Soluble PB and analogue nano-worms were synthesized by Roy et. al using metal organic block ionomers in THF -water emulsion. [131] Although it is an interesting route, microemulsions are hard to scale-up, require organic solvents and involve tedious recovery processes. Uniform PB nanomaterials of desired sizes and morphology could be synthesized by template-assisted methods. Based on the type of template used, the synthetic method could be distinguished into three types: sacrificial, soft and hard template. Many varieties of hollow PB materials can be precisely prepared using sacrificial templates. For example, based on the geometrical shape of silver template PB nanotubes and nanospheres could be formed. The synthesis occurs on the surface of the template which is gradually consumed, resulting in a hollow interior. [132]

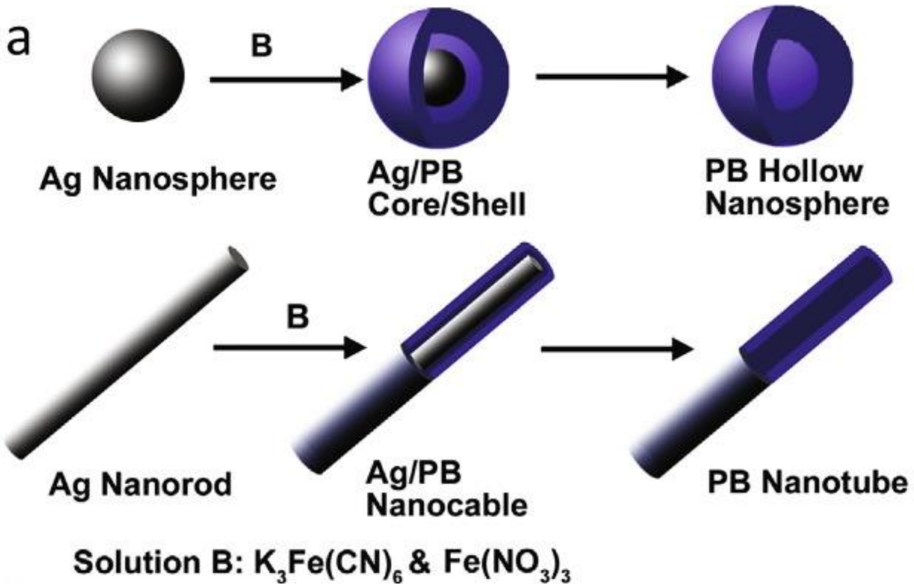

Figure 16. PB hollow spheres and hollow tubes synthesized using sacrificial-template method.[132]

Soft templates like non-RNA cowpea green spot virus (CCMV) capsids are used to encapsulate iron precursors. By modulating the pH, the capsid could be assembled or disassembled to obtain PB nanomaterials.[133] CoFe analogue of PB was the first example of successful entrapment of nanomaterial within amorphous silica gel. G.Fornasieri et.al showed 5-6 nm PBA nanoparticles could be obtained by confining the growth to the porosity of silica monoliths used as a template for synthesis.[134] The monoliths are thermally treated with hexaaqua Co(II) complex and then impregnated with aqueous acidic solution of ferricyanide to form photomagnetic CoFe nps and other PBA. Anodized alumina, polystyrene nanospheres, alginate beads, inverse opals, carbon nanotubes and apoferritin are some of the other widely used hard templates to form PB nanomaterials. [135,136]

Since 2005, our group has focussed on developing a method to form self-standing, ***individualized*** nanoparticles in the colloidal form without using surfactants. By controlling the physico-chemical parameters (temperature, concentration of precursors, presence of alkali etc.), PB and PBA nps could be obtained using a green process with high yield. Ultra-small particles containing Cr, Fe, Co and Ni could be prepared with hydrodynamic diameter of 5-7 nm. These charged nps are stable over long periods of time and since the surface is free of any organic moiety, facile post-coating with polymers and ligands can be achieved.[135] Prussian Blue nanoparticles have been widely studied for applications in the medical field. These water-dispersible compounds are safe and have a good biocompatibility. PB has a strong optical absorption in the NIR region and has a porous structure as described earlier. This makes it an ideal host for ions and small molecules that can impart special properties. Also since nps have larger specific surface area, nanosized PB demonstrates faster kinetics and larger capacity to trap and eliminate radioactive ions compared to commercially used bulk PB.[137] On top of this, PB can be oxidised and reduced and the redox potentials can lead to enzyme-like activities. [124]

These physicochemical characteristics transform PB into a unique and impressive pharmaceutical agent.

1.3.2 Prussian Blue nanoparticles for therapy

In photo-thermal therapy, the malignant tissue is heated to a temperature above 43°C to non-invasively kill the target cells. Light in the near infra-red range is used to trigger cell death. Owing to the charge transfer phenomenon between Fe^{II} and Fe^{III} in Prussian Blue, it has a strong absorption around 700 nm and a large tail in the NIR range. Fu et al.[138] , showed for the first time in 2012 that PB nanoparticles can operate as a photothermal ablation agent. They demonstrated the molar extinction coefficient of PB (1.09×10^9 M^{-1} cm^{-1} at 808 nm) was higher than carbon nanotubes and comparable to that of gold nanorods, which were traditionally used for the PTT. It quickly reached the required temperature of 43°C with the laser and remained stable over multiple cycles. This photostability of PB was a huge advantage over the Au agents that underwent deterioration with every cycle of heating. In-vitro experiments done by the group also showed that PB nanoparticles were safe for the cells but on combining with laser radiation lead to severe cytotoxicity. This was the first proof-of-concept that PB could be used as a PTT agent.

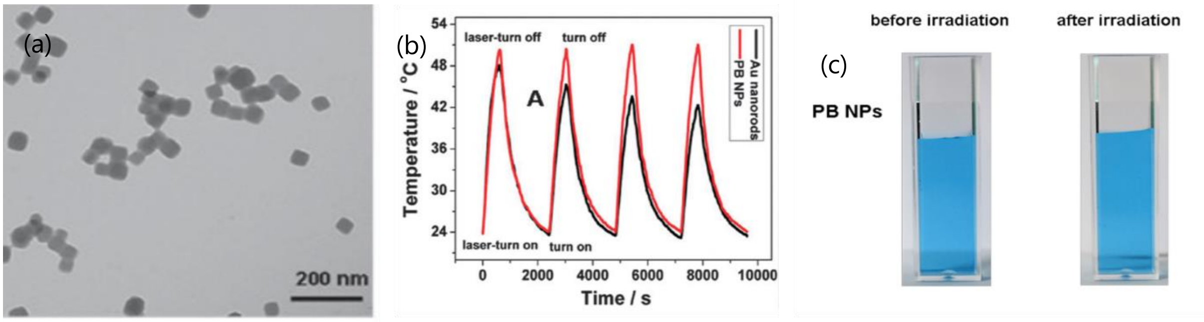

Figure 17. (a)TEM micrograph of PB nanoparticles (b) Proof of their photothermal stability in comparison to gold nanorods and (c) photographs of PB aqueous solution before and after 4 cycles of heating.[138]

Later, *in-vivo* trials were performed that indicated that photo-thermal ablation with PB led to debulking and decreasing the tumour growth in mice.[139] Since then, there have been many groups working with PB to improve this property. The chemical composition, size, shape, charge and surface modification largely influences the photothermal performance of any nanomaterial. [140] Cai et. al showed that by incorporating Gadolinium ions in the PB lattice, the maximum NIR absorbance can be shifted from 710 to 910 nm. The replacement of Fe^{3+} with Gd^{3+} causes a shift in maximum absorption due to changes in electron density, transitions and orbital energies of the CN bond. This optimization helps enhance the PTT capabilities as the maxima is closer to the applied wavelength of the IR laser (usually 808 nm). [141] However these nanoparticles have large sizes with hydration diameters ranging ~345 nm while also requiring highly acidic conditions for synthesis. The large size could prove detrimental for *in-vivo* circulation, biodistribution as well as elimination from the body.

Along with PTT, it has been demonstrated that Prussian Blue nanomaterials can aid Photo Dynamic (PDT) and Sono Dynamic Therapy (SDT). It is a non-invasive, efficient and selective treatment strategy that uses photosensitizers/ sonosensitizers to produce ROS upon laser radiation. These radical species are capable of destroying cancer cells. But the formation of ROS is highly dependent on the presence of oxygen. This is scarce in the hypoxic tumour microenvironment (TME), where hydrogen peroxide (H_2O_2) occurs in abundance. Fortunately PB has the ability to act as a catalyst and promote H_2O_2 conversion to O_2. Integrated nanoplatform were created by loading a photosensitizers like chlorin e6 and different metallo-porphyrins into mesoporous PB.[142,143] These nanosystems improved the therapeutic efficiency of PDT by delivering the sensitizer to target site, while simultaneously enriching the TME with O_2. Similar work has been done by combining PB with non-toxic sonosensitizers[144] to target deep-seated tumours.

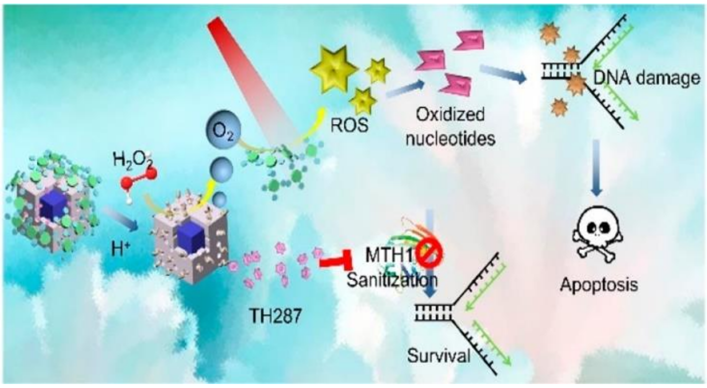

Figure 18. Schematic representation of oxidative damage with photodynamic process using Prussian Blue nanoplatform.

PB has an impressive range of applicability for therapy; however preclinical and clinical trials have revealed that a single therapeutic method is not enough to achieve complete cure. In the case of PTT, heat shock proteins are expressed at high temperature and some NIR laser light is always scattered and absorbed by tissues in the body.[136] Therefore complete elimination of tumours and malignant cancerous cells might not occur, leading to a possibility of recurrence. Other reasons for the failure of monotherapy are tumour metastasis and development of drug resistance over prolonged usage.[145] This is especially seen with chemotherapy, which is the most used treatment method across the world. Widespread research is being conducted to overcome these problems.

Combining two or more therapeutic methods turned out to be a good strategy to get desired results. It has been observed that this combination treatment has synergistic anti-cancer effects revealing better and improved result compared to even the sum of individual methods.[146] For example, several studies successfully showed that hyperthermia caused by photothermal effect, increases the sensitivity of cancer cells and leads to an improved uptake of drugs. This helps overcome drug resistance and increases its accumulation in tumour cells. Moreover, the heating leads to reduction in p-glycoprotein expression in multidrug resistant

(MDR) cells, increasing its toxicity and making it possible to challenge the most difficult type of cancers.[147,148] Some teams working on gold[149] and Fe_3O_4[150] were able to show that forming vesicles and clusters of these nps tremendously improve the therapeutic efficiency. This inspired us to move towards forming assemblies of ultra-small PB to increase PTT effect and incorporate other properties like loading chemotherapeutic drugs to obtain synergistic effect.

1.3.3 Prussian Blue nanoparticles and drug encapsulation

Metal organic frameworks (MOF) have been some of the most focussed inorganic systems to encapsulate drug molecules since early 2000s, when the Ferey group reported that ibuprofen could be loaded and released using chromium MIL-100 and 101.[151] Later on, it was demonstrated in Institut Gallien and Institut Lavoisier, that iron-based MOFs provide a non-toxic alternative and encapsulates anti-cancer and anti-viral drugs efficiently, while also providing an imaging modality with good relaxivities owed to the Fe-based cores.[152] The FDA approved, porous, iron coordinated structure of Prussian Blue, with a large surface area satisfied all the conditions and could act as an excellent agent for loading chemotherapeutic drugs. The Yamauchi team from Japan synthesised highly crystalline hollow, homogenous PB nanoparticles in 2012. The 110 nm particles were chemically etched with the help of strong acid at high temperature (1M HCl, 140°C) in the presence of PVP. [153] Together with the Wu team, they showed for the first time, that PB can act as an intracellular drug delivery system (DDS) for cisplatin.

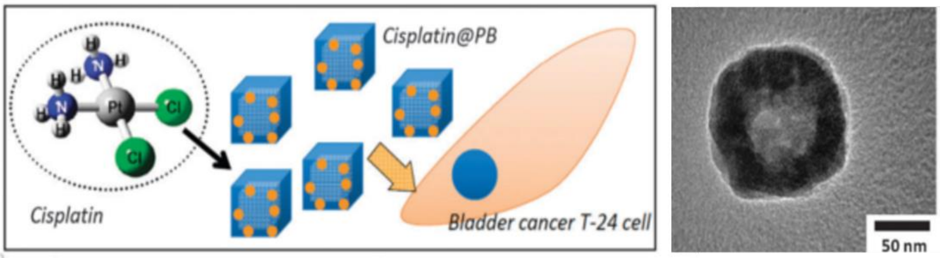

Figure 19. Hollow PB nanoparticles loaded with cisplatin.[154]

A high loading efficacy of ~100% could be achieved at a short time owing to the hollow interior and suitable pore size of PB and it provided a 5% release at neutral pH conditions.[154] Around the same time, hollow gold nps loaded with doxorubicin (Dox)[155] and CuS nps loaded with Camptothecin (Cpt)[156] were developed. Both these systems displayed significantly enhanced drug release at high temperatures achieved as a result of NIR laser radiation. The "two-punch approach" combining photothermal ablation and controlled release of drug, increased the cell killing efficiency. In 2014, multifunctional PB nps stabilised using gelatin conjugated with Dox was prepared.[157] The drug was covalently bonded to gelatin before linking it to citrate capped normal PB nps. As a result, the Dox loading percentage was low but it was done to minimize non-specific release and to target deposition only at gelatinase enzyme rich tumour environment. They displayed synergistic cell destruction by combining chemo and photothermal treatments but Dox release was only studied as a function of enzyme concentration.

Wu et.al used larger hollow PB nps and attained 88.4% encapsulation efficiency (EE) using nanoprecipitation with Dox.[158] This high EE is attributed to hydrophobic interactions and π-π stacking of the drug within the cavity. The loaded Dox could also be released using this PB Nano Cage (PBNC) system. At simulated physiological conditions, the highest percentage of release (~25% in 15h) was observed at the acidic pH of 4.8 while only 10% was released at a pH of 7.4. It indicated that the drug release will occur at the acidic tumour site while healthy cells might remain unaffected. The reason for this difference in release percentages is attributed to protonation of amino group in Dox and its increased solubility at low pH. Irradiating 100 µg/mL PBNCs with 808 nm laser, temperatures up to 80°C could be obtained and the required temperature could be tuned by adjusting the concentration of this photothermal agent. NIR laser driven drug release behaviour was also demonstrated *in-vitro* using hepatocellular carcinoma cells (HepG2) and the cell killing was much amplified compared to PB+NIR or free Dox alone. This was conclusive proof that PB acts as an efficient drug carrier and the heat produced with PTT would trigger cell death while also providing an added advantage of increasing drug release at heated sites.

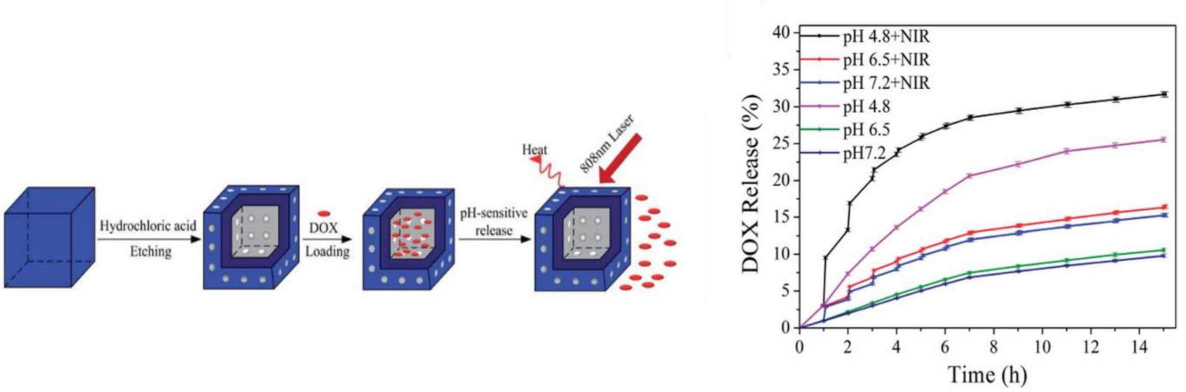

Figure 20. Schematic view of the synthesis procedure of PBNC-Dox nanocomposites and the observed drug release with NIR laser and pH effect.[158]

More systems were developed in the following years to improve the drug loading and release profiles while also incorporating other properties.[159,160] For example, a smart pH responsive hollow mesoporous PB with manganese-PBA coating was synthesised using a multi-step synthetic route. It demonstrated a high EE with controlled pH dependent release while also acting as a T1-weighted MRI CA due to the presence of Mn.[161] Without appropriate surface modifications, HPB nps tend to be removed by the immune system or prematurely leak drugs causing side effects. Spherical and cubic hollow mesoporous PB were synthesised to act as a carrier for Dox. They were coated with folic acid (FA) and erythrocyte membrane (EM) to improve targeting and escape the immune system to achieve precise and controllable release specifically at the target site. [162] Other such systems are summarized in the table below.

Prussian Blue system	**Average Size**	**Synthetic route**	**Drug**	**EE**	**Payload (wt.%)**
Hollow PB (HPB)[154]	110 nm	Etching HCl (1.0 M), PVP, 140°C	Cisplatin	100 %	-
Gelatin-Dox PB[157]	53.5 nm	Green synthesis in water, Citric acid, 60°C, Gelatin-dox complex using periodate oxidation	Doxorubicin	-	18.5 %
HPB nanocage[158]	80 nm	Etched with HCl, 80°C	Doxorubicin	88.4 %	33.0%
HMPB-Mn[161]	290 nm	HCl, PVP, 80°C, $Mn(CH_3\ COO)_2$, $Na_3C_6H_5O_7$	Doxorubicin	97.5 %	62.3 %
PEGylated PB-Dox nps[159]	119 nm	Oleylamine modification in toluene, lipid PEGylation	Doxorubicin	98.0 %	9.2 %
Hyaluronic Acid-PEG modified HPBNs[160]	120 nm	HCl etching, PVP, 140°C, HA, PEG, PAA and PAH	10-hydroxy Camptothecin	52 %	10.4 %
SCPB coated with Erythrocyte Membrane and Folic Acid [162]	185 nm	Synthesis in HCl, PVP, 80°C, hemolysis of blood for EM and then FA coating	Doxorubicin	~45%	131 % for 3:1 ratio

PAH-PAA-PEG conjugated PB[163]	128 nm	HCl, PVP, 80°C, Ethanol, PAH, PAA and PEG polymers	CO and Dox co-delivery	-	14.5 %
HMPB with phase change material (PCM)[164]	98 nm	HCl, PVP, 140°C, 1-tetradecanol (PCM), methanol	Camptothecin and Dox	-	Cpt: 1.6% (3.21/200 µg) Dox: 2.2% (4.42/200 µg)
Nanococktail PLGA shell-PB core with PEG + FA targeting [165]	237 nm	Citric acid PB synthesis, 60°C, PLGA shell double emulsion process, PVA alcohol, dichloromethane	Paclitaxel	77.8 %	7.2 %
Mesoporous-PB@ CaP shell[166]	160 nm	$Ca(OH)_2$, PAA, alcohol micro-emulsion, $(NH_4)_2HPO_4$, NaOH for etching	Doxorubicin	100.0 %	-
Mn-doped PB[167]	55 nm	Green synthesis in water, room temperature	Doxorubicin	-	7.6 %
HMPB with mesoporous SiO_2 shell[168]	150 nm	HCl, PVP, 140°C, CTAB, TEOS, ammonia	Doxorubicin	-	86.8 % (868.27µg/mg of carrier)

Table 1. Summary of sizes and synthetic strategies applied to form PB nps in the last 10 years and their corresponding efficiency in loading various anti-cancer drugs

All of the PB systems displaying a good EE are made of hollow nanoparticles, synthesized with complicated synthetic routes while using harsh and toxic chemicals for etching. They also are huge particles ranging between 100-300 nm and there is no information available on the fate of these particles once therapy is achieved. It would be tough to attain renal clearance with such sizes and it would probably lead to accumulation within the body. So far, there has not been any significant research utilizing ultra-small PB nanoparticles for drug encapsulation and delivery. Recently, comparatively smaller (~55 nm) Mn-doped PB were synthesised in water and they displayed an improvement in PTT effect by using a two-photon laser instead of a single wavelength NIR laser.[167] However as expected, these nps have a low encapsulation efficiency of 7.6 wt.%. since the drug is physisorbed and loaded in the double lacunas in the structure. Inspired by the innovative methods found in the state of art we wanted to improve the treatment capabilities of combining PTT and chemotherapy with ultra-small nps. The aim of this thesis project was to use sub-10 nm, renally clearable PB nps synthesized in green manner to carry drug molecules with high efficacy and possibly attain controlled release at target site.

1.3.4 Prussian Blue nanoparticles for imaging

The unique structure and properties of Prussian Blue nanomaterials have made them a useful tool for diagnosis. Prussian Blue contains low-spin Fe^{2+} (S=0) bound to C and high spin Fe^{3+} (S=5/2) linked to N of the cyanide group. It could behave as a T_1-weighted MRI contrast agent as water molecules are bound to $Fe^{3+}$and can diffuse out of the structure. Shokouhimehr and co-workers were the first to demonstrate potential utility of PB nps as MRI contrast agent.[127] Their 25 nm citrate coated PB particles produced a positive contrast with low relaxivity (r_2/r_1) ratio of 6.1 at 1.5 T. The typical r_2/r_1 for other iron systems, especially the oxides (SPIO) are greater than 10 as these particles have dense solid-state structure. So the metal centres are completely inaccessible to water coordination and only the outer-sphere relaxation mechanism helps generate the contrast. Since the structure of insoluble PB has many vacant sites it was proposed that inner-sphere relaxation plays a role in generating a T1 contrast with these nanoparticles.[127] Liang et.al demonstrated for the first time that high molar extinction coefficient of PB, its photothermal efficiency and photostability could be used to improve the contrast of photoacoustic imaging (PAI). Clear cerebrovascular images were obtained after intravenous injection of these nanoparticles.[169] Therefore, PB has promising applications as a multimodal (MR-PA) imaging agent.

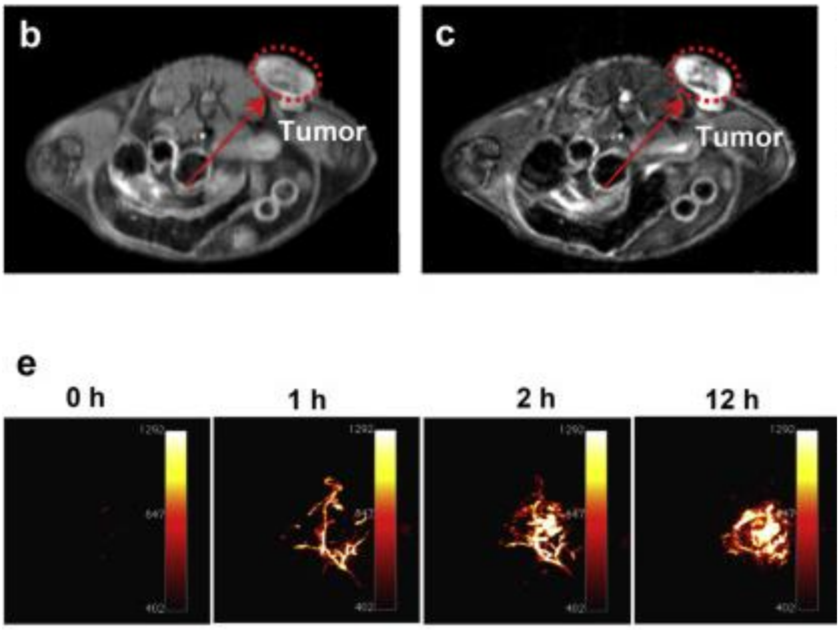

Figure 21. T_1 MR images of tumour on mice taken pre-injection and 12 h post intravenous injection of PB-PEG nanocubes (top) and PA images taken at different time points after injection (bottom).[170]

The longitudinal and transverse relaxivities of the bare PB nps were much weaker than commercially used MRCAs. Different strategies were employed to compensate for this difference. Introducing Gd^{3+} in the interstices of PB lattice showed a 9-fold increase in MRI signal intensity[171] and doping hollow mesoporous PB nanocrystal (290 nm) with high-spin Mn^{2+} increased the r_1 from 0.14 to 7.43 $mM^{-1}.s^{-1}$ (7.0 T) in acidic environment.[161] Doping with gadolinium ions caused a red-shift in the absorption peak, which also significantly enhanced the photoacoustic signal obtained using PB nanoparticles.[172] More recently, Wu and co-authors demonstrated a method to form ~4 nm PB by doping Zn (10%) ions in the structure. The particles display a transverse relaxivity of 17.70 $mM^{-1}.s^{-1}$ and longitudinal relaxivity of 11.94 $mM^{-1}.s^{-1}$ at 0.5 T. This was much higher than that of Gd-DTPA, the most commercially used contrast agent which has an r_1 of 3.24 $mM^{-1}.s^{-1}$.[173]

SPECT (single-photon emission computed tomography) is a powerful diagnostic tool with high sensitivity and PB nanoparticles labelled with radioactive thallium ($^{201}Tl^{+}$) could be used for the same. [174,175] The applicability of these nanomaterials in ultrasound (US) imaging has also been reported. Perfluoropentane (PFP) encapsulated within hollow mesoporous PB, undergoes liquid-to-gas phase change upon heating. Since NIR laser radiation on PB can cause a local temperature rise, a large number of bubbles could be released, which aids US imaging. [176]

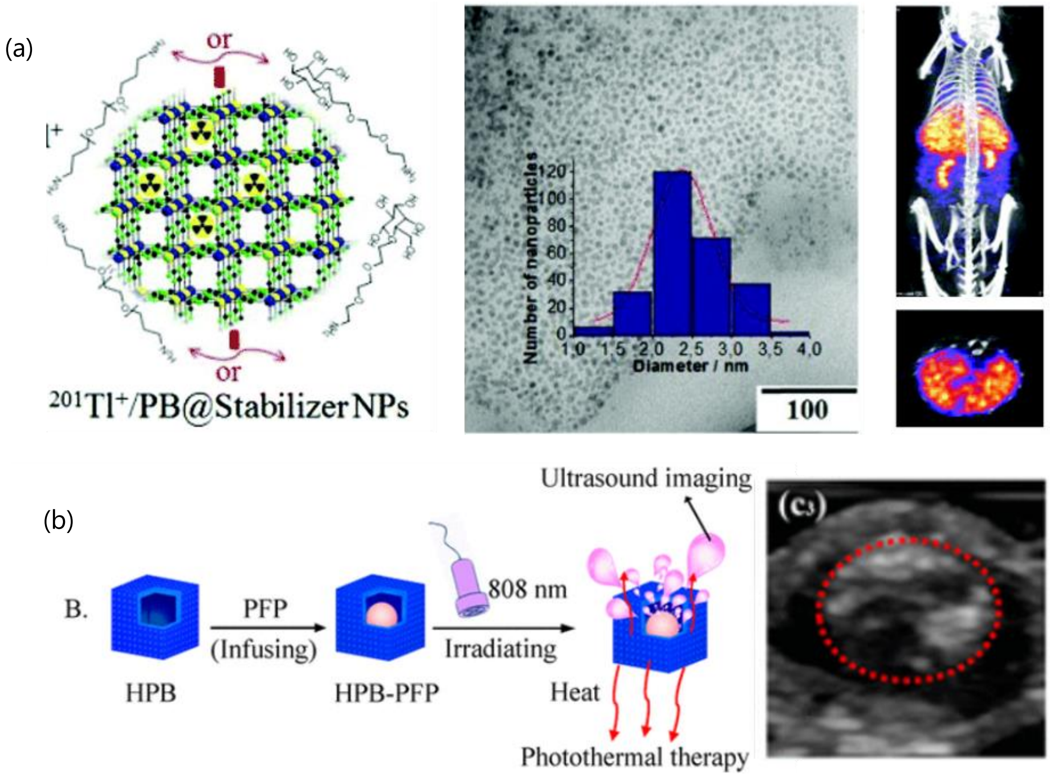

Figure 22. (a)Schematic representation of $^{201}Tl^+$*-PB nanoparticles, TEM image and SPECT/CT image obtained after 3.5 hrs of injection.*[174] *(b) Schematic representation of HPB-PFP formation and in-vivo US image of tumour site after 808 nm laser irradiation*[176]

In 2019, our group reported a one-step, green synthetic procedure of forming sub-5 nm PB particles.[177] The size remained almost constant with varying percentages of Gd doping. The ultra-small 5% Gd-PB displayed an unprecedentedly high longitudinal relaxivity value of 40 $mM^{-1}.s^{-1}$ per Gd^{3+} ion and is an efficient T_1 contrast agent with r_2/r_1 below 2 . The extraordinary r_1 results were 10 times higher than the commercial agents and four times that of similar sized Gd_2O_3 nps. This is attributed to the presence of maximum paramagnetic ions at the surface of the nanostructure as opposed to the core. Therefore, by applying our methodology, a low concentration of Gd (0.2 mM) would be sufficient to perform efficient MRI imaging and the comparative contrast results are indicated below. Leaching of Gd ion was negligible as it is strongly conjugated through cyanide linkage in the PB structure and these ultra-small nps had low toxicity. Additionally, Gd-PB (5%) remains useful *in vivo* for photoacoustic imaging, is capable of efficient photo thermal conversion and aids in reduction of tumour volume with a radiation of 808 nm laser.

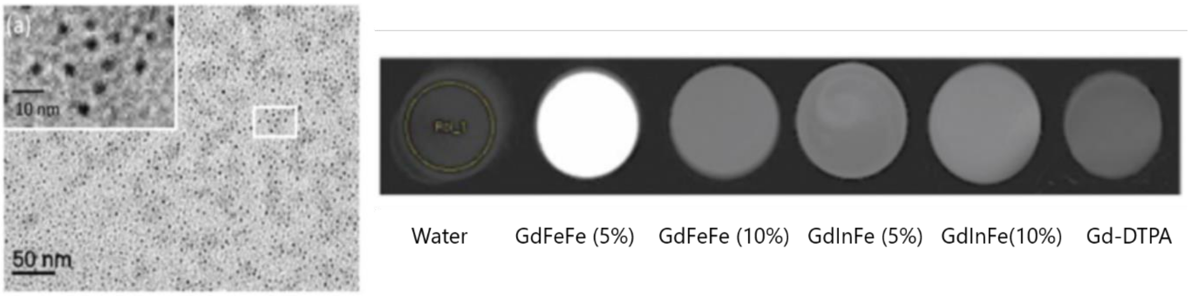

Figure 23. (a) TEM image of sub-5 nm Gd-PB nanoparticles (b) T_1-weighted MR images recorded under 7T at Gd^{III} concentration of 0.2 mM.[177]

1.4 OBJECTIVE OF THE THESIS

The main aim of this thesis project was to improve the therapeutic and diagnostic functions of these ultrasmall, biocompatible Prussian Blue nanoparticles. As seen from the examples described above, PB and its analogues are well-established agents for photothermal, photodynamic and sonodynamic therapy, but its applicability in radiation treatment of cancers has been left unexplored. Creation of PB-like, porous nanoparticles by substituting one or both of the constituent Fe^{II}/Fe^{III} with heavy metal ions, could lead to a new family of compounds with radio-enhancing capabilities. It would increase the versatility of these nanomaterials but the challenge is to obtain stable, ultra-small particles using a cost-effective procedure, while maintaining a green synthetic manner. This work was done in collaboration with Erika Porcel and Sandrine Lacombe from the NanoBio team at Institute of Molecular Sciences Orsay (ISMO), University Paris-Saclay.

A major obstacle in using nanoparticles for medical applications is that sub-10 nm particles are quickly and prematurely cleared out of the body due to their size.[178] So even if they are effective therapeutic agents, the overall efficiency drops because of the low circulation time. Large nanoparticles, although beneficial for EPR targeting, endure a high uptake by the reticuloendothelial system (RES) organs, undergo slow elimination and could prove potentially toxic due to accumulation. Therefore, acquiring the FDA approval and translation to clinical use is difficult. This thesis project was dedicated to finding a way to overcome both these issues and obtain a safe, multifunctional and efficient theranostic platform. A possible solution was creating supramolecular assemblies of ultra-small PB nanoparticles which could improve its circulation time within the body, and once the therapeutic/diagnostic functions are fulfilled, be disassembled with time.

Over the past decades, multiple strategies to assemble functional nanoparticles into superstructures have been reported. These assembled nano-structures are scientifically attractive, enable multi-functionalities, increase diversity and have been used to develop better sensor devices, optoelectronic materials and drug delivery vehicles.[179] An oligonucleotide based method was developed to control and form a reversible assembly of gold nps.[180]

Bioconjugation using antigen-antibody coupling and external magnetic field manipulations were few of the other strategies employed to form np assemblies.[181,182] Literature also showed that the assembly formation leads to higher loading of drugs compared to its composite single np, and the stability and biocompatibility of the system could be improved.[183]

Nanogels combine nanoparticles with polymeric biomaterials and is an area of research that has attracted a lot of interest in the past few years. Nagasaki and co-workers have been pioneers in developing hybrid, pH-sensitive nanogels incorporating gold nps.[184,185] It has been shown that 2 nm gold nps could form 100-150 nm spherical clusters by combining with cationic poly(allyl amine hydrochloride) polymer and they can load peptides and antibodies.[186] Most nanogels that have been developed for drug delivery have been formed via self-assembly. Self-assembly is usually triggered by non-covalent interactions like hydrogen bond formation, hydrophobic, electrostatic and host-guest interactions. Depending on the required stability, stronger covalent bonds, click chemistry or specific reactive groups could also be utilised to link the nanoparticles. Cyclodextrins (CD) offer attractive pathways to form supramolecular nanoparticles for biomedical applications.[70] When gold nps functionalized with β-CD, were mixed with adamantly-terminated dendrimers of poly(propyleneimine) (AD-PPI), size-controlled nanoparticle clusters were formed.[187]

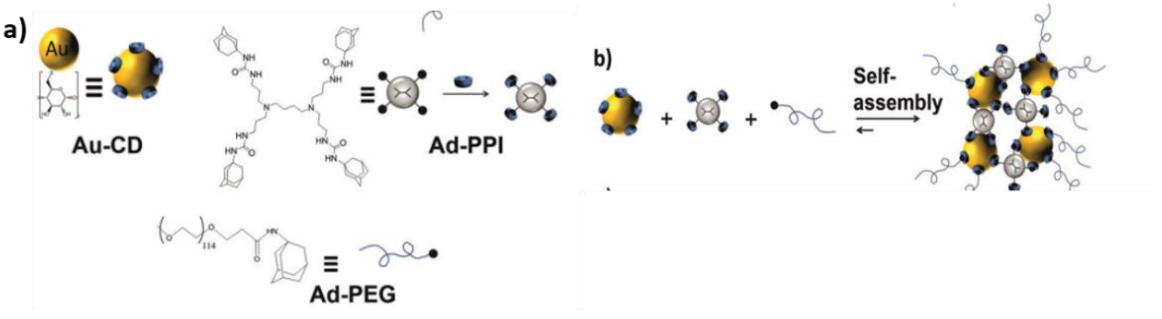

Figure 24. (a) Functionalization of gold nanoparticle surface with CD and (b) their self-assembly with AD-PPI.[187]

Another interesting system involving host-guest interactions, was developed by S.Engel et.al where three types of CD decorated nanoparticles were linked through light sensitive arylazo pyrazoles (AAP). The linker causes the nanoparticles to aggregate under visible light radiation, while UV and NIR light disassembles the structure as the linker undergoes E to Z conversion.[188] Nanogels have also been fabricated using functionalized polymers (PAMAM, PPEGMA, PADMA) to encapsulate doxorubicin and indocyanine green to combine photothermal and chemotherapy (Fig.25).[189]

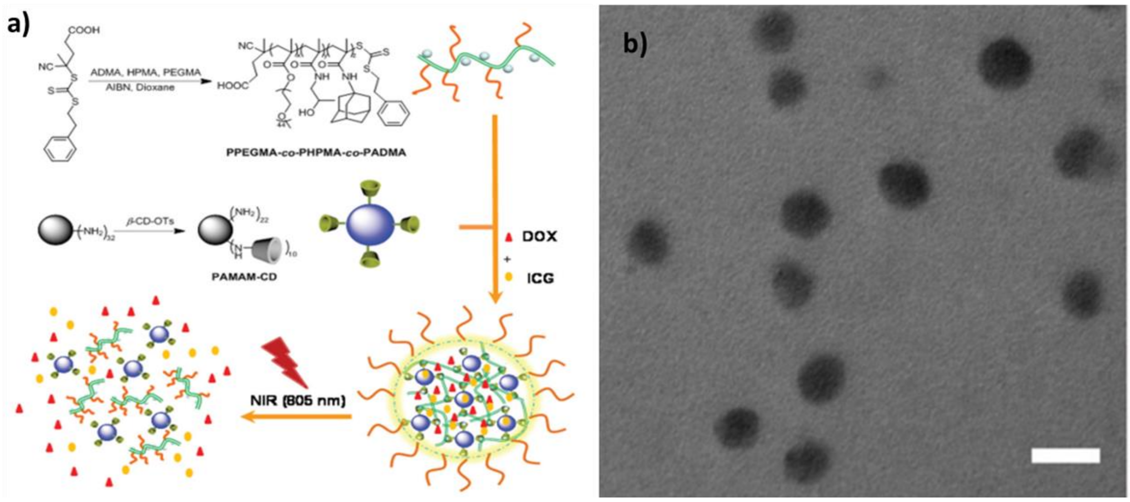

Figure 25. (a) Schematic representation of nanogel encapsulating ICG and DOX and their release with NIR laser irradiation and (b) corresponding TEM image (scale bar 100 nm)[189]

Using stimuli-responsive polymers in formulating nanogels have been extensively studied, not only for drug loading/release but also to improve diagnosis. Multifunctional, degradable, 110 nm zwitterionic nanogels were synthesized using 9 nm Fe_3O_4 nps to enhance T_2 MR imaging contrast (Fig. 26).[190] Inverse microemulsion with poly carboxybetaine methacrylate (pCBMA) and di-sulphide cross linkers were used. It was seen that upon exposure to a reducing environment, the sensitive linker degrades leading to drug release and renal clearance of constituent nps. The same group has reported that while uncoated gold nanoparticles are quickly cleared out, forming 250 nm soft nanogels with the nps increase their *in-vivo* circulation half-life (10-19 hrs).[191]

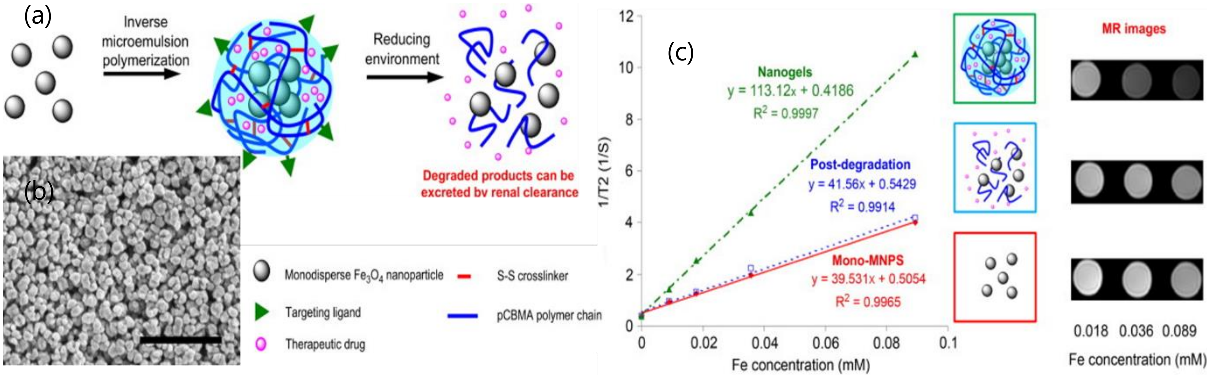

Figure 26.(a) Schematic representation of pCBMA – Fe_3O_4 nanogel formation and degradation. (b) SEM image of the nanogel with scale bar 1µm. (c) Enhanced T2 contrast observed with aggregates and the effect of degradation.[190]

Only one such example of Prussian Blue nanoparticle assembly has been demonstrated so far. Yang Sun and team designed an elaborate "nanococktail" containing PB nps encapsulated within a shell of PLGA (poly lactic-co-glycolic acid) using a double emulsion (water/oil/water) evaporation strategy.[165] This composite could load paclitaxel, an anti-cancer drug and the polymer shell was functionalized with PEG and folic acid (FA) for targeting breast cancer cells (Figure 27). This nanocomposite was 236.6 ± 55.0 nm in size and contained ~ 40 nm PB nps. While they demonstrated good photothermal conversion, photoacoustic and MRI contrast with 20 mg/mL of PLGA-PB-PTX-PEG-FA, only a low drug loading of 7.2 wt % could be achieved. The nanocomposite could be retained *in vivo* for longer than 24 hours but there is no information on the fate of the particles.

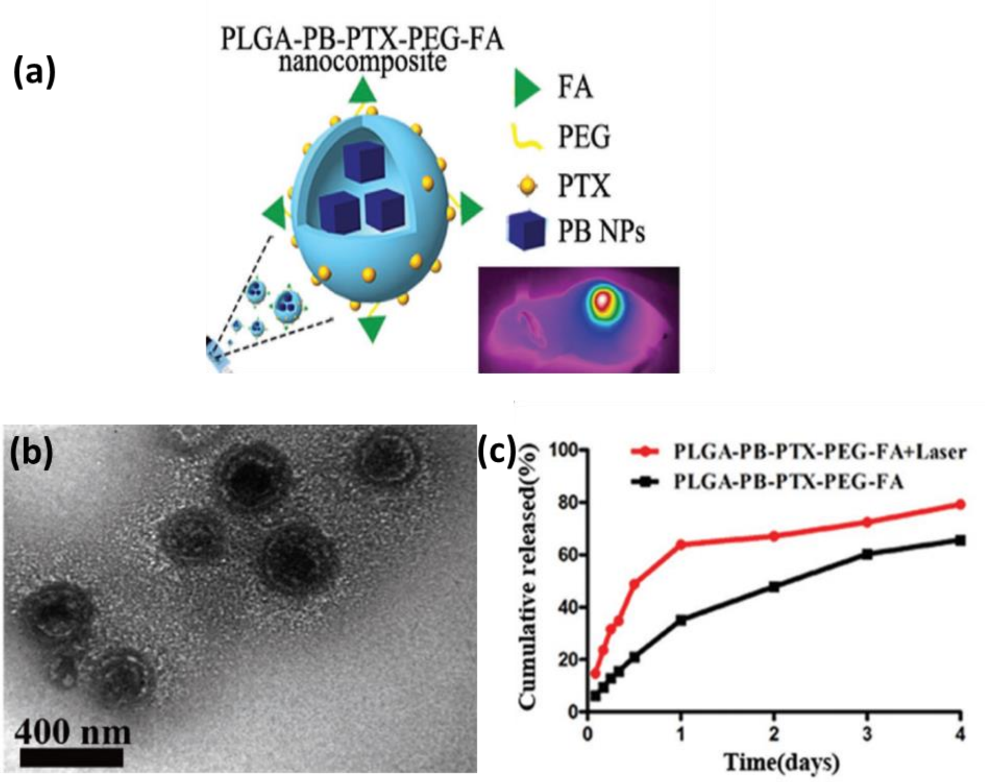

Figure 27. (a) Schematic depiction of PLGA coated Prussian Blue nano-cocktail. (b) TEM image of ~ 250 nm PLGA-PB-PTX-PEG-FA nanoparticles (c) Release of Paclitaxel from the PB nano-cocktail and improvement on laser radiation. [165]

Inspired by the work of many groups over the past years, our objective was to create assemblies incorporating sub-10 nm Prussian Blue nanoparticles with cyclodextrin containing polymers. The project involved strong collaboration with Ruxandra Gref and team at ISMO and was supported by DIM-Respore grant. It has been demonstrated that poly(γ-CD citrate) enhances the drug loading efficiency of MOFs due to the available cage-like structures.[192] So, in principle this nano-structure containing the polymer and PB nps could have improved chemotherapeutic drug encapsulation properties. Also, due to the larger hydrodynamic diameter, the *in-vivo* circulation time could be improved and the challenge of fast, premature clearance could be overcome. As the retention time in the body is increased, the nanoassembly could reach the target tumour site through EPR and may also perform as better MRI contrast agents due to larger correlation time.

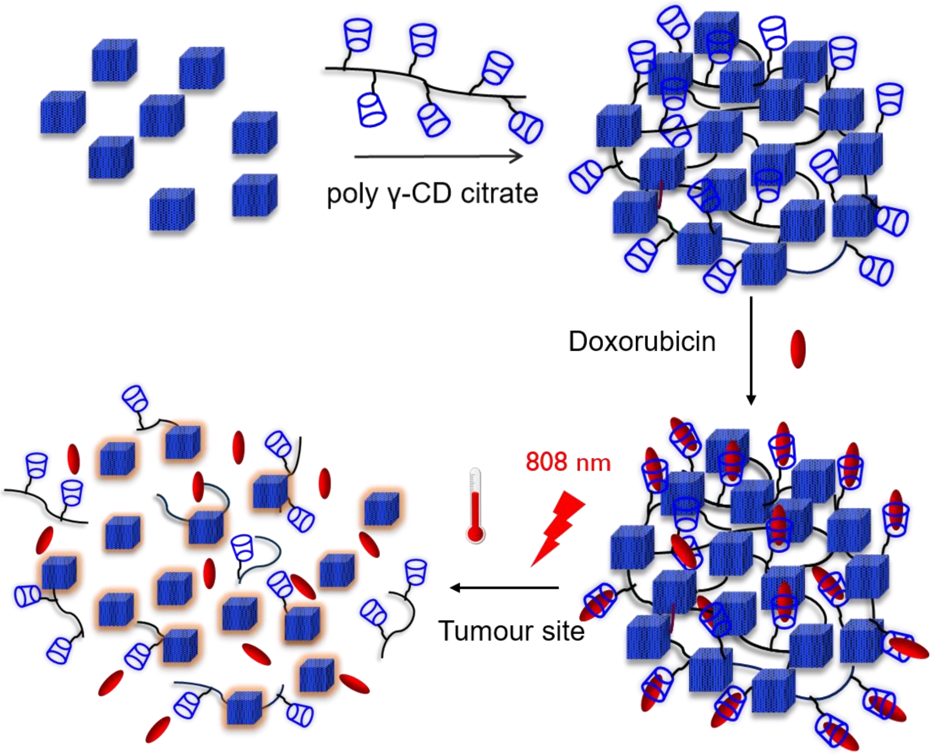

Figure 28. Schematic depiction of the aim of the original project: forming theranostic PB nano-assembly

Then, once the PB nano-assembly reaches the tumour micro-environment, irradiation with NIR laser would trigger photothermal therapy. The temperature rise could lead to expulsion of the loaded drug and breakdown of the structure to its constituents. Since the individual particles are sub-10 nm in size, there is strong possibility of renal clearance out of the body, thereby minimizing accumulation and side-effects. The aim was to form a flexible and biocompatible nanosystem using Prussian Blue using a completely green synthetic method. We wanted to avoid trapping it within a shell or liposome, and have the surface of PB available for water exchange, in order to maximize its diagnostic performance. Improving drug loading of PB nanoparticles, without using hollowed out structures formed in harsh conditions was another important target. The ultimate aim was to develop a safe theranostic nanoplatform capable of performing image-guided, photothermal-chemotherapy with high efficiency.

CHAPTER II

2 PRUSSIAN BLUE ANALOGUE NANOPARTICLES FOR RADIATION THERAPY

2.1 INTRODUCTION

Our aim was to produce new varieties of self-standing PB-like nanoparticles in aqueous medium using a green synthetic pathway. We sought to prepare PB analogues by incorporating at least one heavy metal, while avoiding the use of any surfactants or stabilizing agents. As discussed in chapter I, ionizing radiation passing through water in the body, generate radicals called reactive oxygen species. They are capable of causing damages to the biomolecules and kill cells. Controlling the dose of applied radiation and targeting it specifically to the diseased area provides a competent way to arrest tumour growth and eliminate cancerous tissues. High-atomic number (Z) elements undergo inner shell ionization, upon radiation and a cascade of secondary Auger electrons are generated. This amplifies the number of radicals formed, which in turn improve the efficacy of treatment. Therefore, incorporating a high-Z metal within PBA can provide radio-enhancing properties and add a new perspective to this interesting field of research.

The main advantage of porous nanoparticles is that the proportion of atoms available at the surface is much larger than typical dense metal particles. For example a 3 nm PBA has 64% of its constituent atoms on the surface, which is almost twice when compared to an iron np of the same size.[177] This is very beneficial in achieving larger relaxivities and better MRI diagnosis. The nanoparticles formed using coordination chemistry have an added advantage of being easily functionalizable. Moreover, we expect the content of zeolitic water, coordinated water and porosity of the nanostructure to affect the radio-enhancing efficiency in a positive way. Therefore our objective was to develop a simple, safe and scalable method of synthesizing mono and bi-metallic PBAs for radiation therapy under the framework of IRS NanoTheRad with a collaboration between institutes (ICMMO, ISMO and ICP) of Université Paris Saclay. This chapter begins with the state of the art prior to this work and a short description of synthesis technique used to obtain ultra-small PB. The method developed in our group, is varied to obtain 3 new analogues of PB and the optimization methods are explained in detail. These novel co-ordination nanoparticles are completely characterized and stability in physiological medium is assessed. The final section describes their toxicity to living cells and possible applications of this heavy-metal containing particles in radiation therapy.

2.2 STATE OF THE ART

Analogues of Prussian Blue could be formed by substituting one or both of the constituent ions (Fe^{II} or Fe^{III}) with other di- and tri-valent ions. In 1992, a team from Princeton university showed that inorganic hydrogels could be formed purely using co-ordination chemistry.[193] They formed analogues of PB by combining different cyanometallates (Fe^{III}, Fe^{II}, Pt^{II}, Ru^{III}, Ru^{II}, Os^{II} and Co^{III}) with chloride salt of palladium (PdCl$_4^{2-}$). The Cl ligand is substituted with the N terminus of the bridging cyanide in aqueous solution and long polymeric chains are formed. They grow along in multiple directions and depending on the reaction conditions, a gel-like material containing more than 95% water could be fashioned. The Bocarsly group further developed this system and named them cyanogels as they undergo true sol-gel phase transition. By raising the temperature, the cyanogel could be converted to respective transition-metal alloys in a few minutes as opposed the hours required to form alloys in traditional furnace.[194] Platinum-Cobalt cyanogel was modified to form an alloy network that exhibited high electrochemical activity and could be used for methanol oxidation electrocatalysis.[195] Later on, cyanogel hybrid nanoflowers composed of Pd-Co were prepared, which demonstrated excellent catalytic activity and durability towards reduction of Rhodamine B. [196] A recent review summarizes the various applications of cyanogel and derivatives, its use in water splitting electrolysers, fuel cells and for energy storage due to their porous structure, 3D interconnected backbone and uniform distribution of metals at an atomic level.[197]

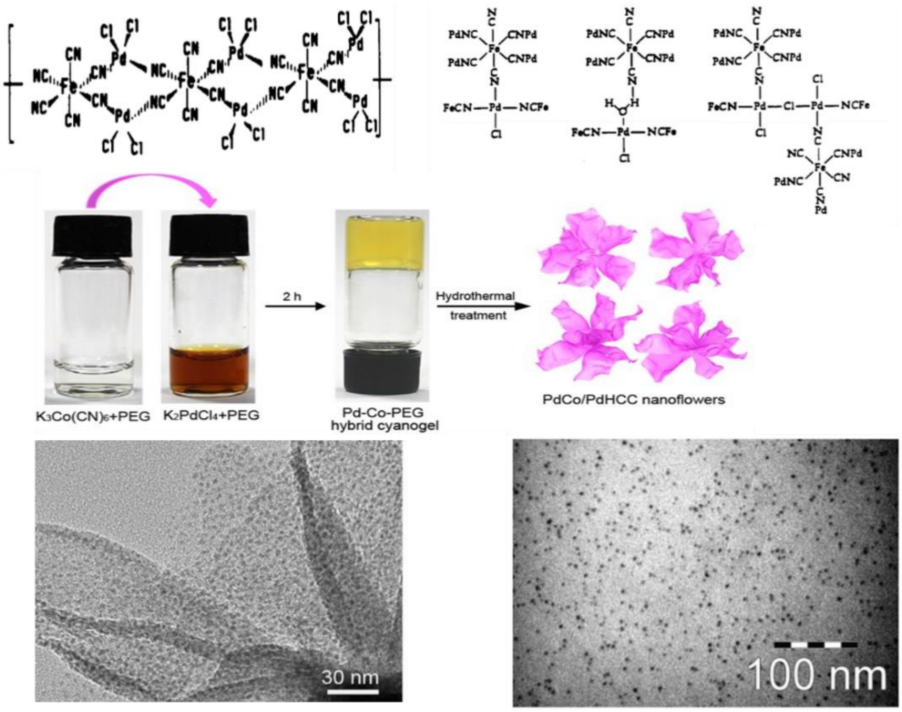

Figure 29. Co-ordination structure involved in forming Pd/Fe polymeric gel by substitution of 2 Cl ligands to form cis isomer and possible interchain cross-links when substitution is trans at Pd center (top). Cyanogel hybrid nanogel and nanoflower formation and TEM image. TEM image of Pd: Co stabilised cyanosols.[196,198]

Burgess et.al reported that Pd/Co cyanogels can also be chemically altered and a bulky cation when used as a stabilizing agent (CTAB) could isolate nanoparticles that are stable in the solution form. These nps called "cyanosols", were around 4 nm in size and soluble in organic solvents. Depending on the time of addition of CTAB, nano-agglomerates could also be formed.[198] Different combinations of metals were used to create a family of versatile nps for a variety of applications. A copper analogue of PB was designed to encapsulate DOX and achieve sustained release over time.[199] More recently, a multifunctional silver PBA np was developed as nanomedicine that has anti-cancer as well as anti-bacterial properties.[200] However, most PBAs used for medical applications are focussed only on photothermal treatment and combining it with drug delivery. The possibility to expand it to radiation therapy has not been explored. This chapter is devoted to the development of such Prussian Blue analogue nanoparticles (cyanosols) that remain stable in water without adding stabilizing agents.

2.3 PRUSSIAN BLUE NANOPARTICLES

2.3.1 Synthesis and characterization

As discussed in section 1.3.1, our group had developed a method to synthesize stable colloids of individualized Prussian Blue and its analogues in a template and surfactant free manner. The process optimization involved tuning the concentrations of both metal precursors, alkali cations and maintaining the temperature of the aqueous solutions during synthesis. The general route followed for obtaining ultra-small Prussian Blue nanoparticles is a fast mixture of Fe^{III} salt (0.50 mM) solution into an aqueous hexacyanoferrate (0.50 mM) at 2°C with constant stirring. The colloidal solution undergoes an immediate colour change to intense blue, which is characteristic of the metal-to-metal charge transfer in PB. The reaction is carried out for 30 minutes while maintaining the low temperature. The reaction conditions ensure controlled nucleation and leads to formation of sub-10 nm homogenous Prussian Blue nanoparticles. The solution remains stable, without evolution over the many months due to the inherent negative charge over the surface of each nanoparticle. During the course of the thesis of Dr.Gabriella Paul and Dr.Lucile Fétiveau, many types of ultrasmall PB nanoparticles containing varying proportions of Mn^{II}, Gd^{III} and In^{III} have been developed for a medical imaging purposes. Only a brief summary of characterization of bare PB is provided here as it has been widely reported elsewhere.

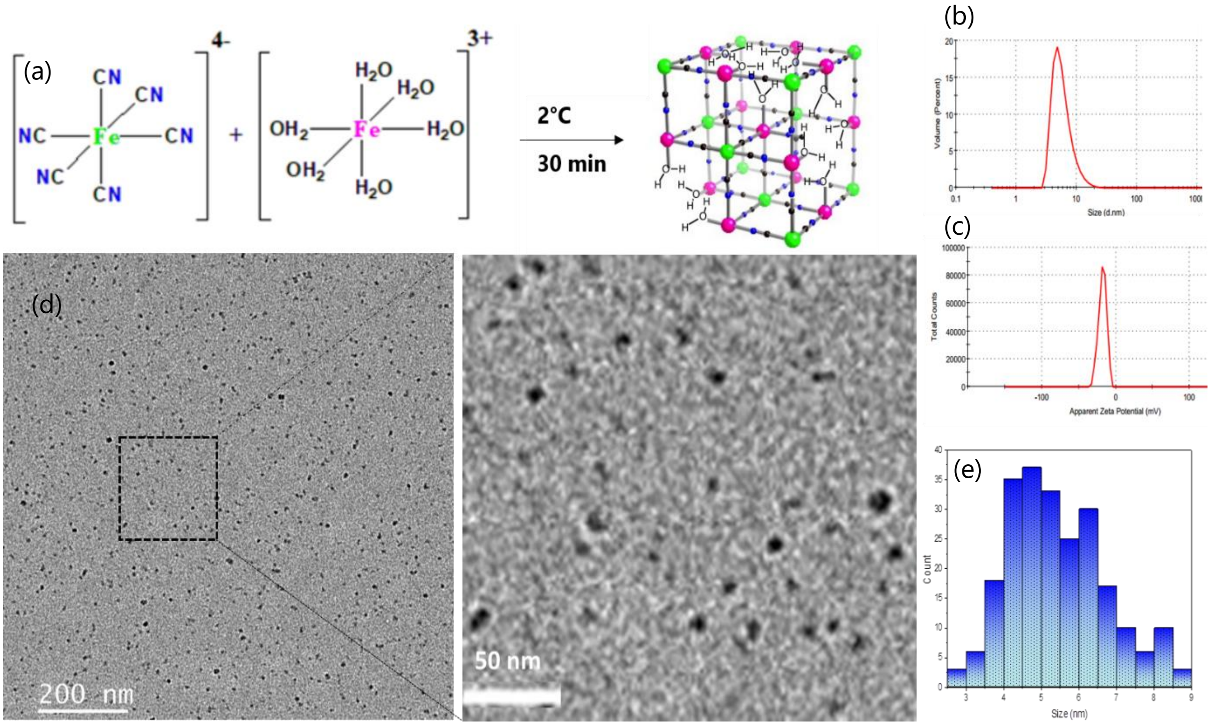

Figure 30. Schematic representation of the synthesis of Prussian Blue nanoparticles in water. (b) DLS and (c) zeta potential measurement results (d) TEM image PB at different magnifications and (e) the corresponding size distribution chart

Dynamic Light Scattering (DLS) experiments reveals the hydrodynamic diameter of the nps including the surrounding solvation shell. It is crucial to study this overall size as renal clearance through the kidney would only be possible for sub-10 nm particles. Multiple batches of PB were made over the past three years using the above mentioned procedure and the DLS measurements indicated the particle size between 5.5-8.3 nm. After coating the PB nps with polymers of interest for bio-medical applications, the sub-10 nm size is maintained. The measurement of zeta potential makes it possible to determine the sign of the surface charge of nanoparticles in solution. The pure PB nanoparticles display a potential around -25 mV which is a strong indication of stability. The electrostatic repulsions between the particles ensure that no aggregation or precipitation occurs and therefore the particles are capable of maintaining colloidal stability over time. Transmission electron microscopy (TEM) makes it possible to clearly visualize the nanoparticles. TEM analysis of PB nps revealed the actual dimensions of the synthesized particles and the lay in the range of 5.3± 1.6 nm. One of the main focus of this doctoral project was to form similar ultra-small analogues of Prussian Blue containing a heavy-metal in a green manner and study its applications in cancer treatment. Cyanometallate building blocks $[M(CN)_x]^{n-}$ are utilized as they can generally form multi-dimensional networks as the carbon and nitrogen ends of CN ion can act as Lewis bases that coordinate two different metal cations. To incorporate at least one heavy metal the cyanosol syntheses were attempted with potassium tetrachloroplatinate ($K_2[PtCl_4]$) salt. The Pt salt is kept constant, while the corresponding metal could be changed to obtain a new family of compounds with interesting properties.

2.4 GOLD-PLATINUM PB ANALOGUE NANOPARTICLES

The aim was to prepare novel cyanide-bridged nanoparticles containing useful metals like gold (Au) and platinum (Pt). Special attention was given to obtain individualized particles stable in solution. A non-toxic process of synthesis was essential for the targeted applications. Also, for use as biomedical agents, it is essential that the nanoparticles do not aggregate or coagulate in the physiological environment. It has been shown previously that coating the surface with certain biocompatible polymers help prevent this effect and therefore polyvinylpyrrolidone (PVP) is utilized in our experiments. As mentioned earlier, one of the precursors used was a tetrachloro salt of platinum and the idea was to form nanoparticles by exchanging the Cl in the complex with a CN linked to the other metal (M). This substitution should result in formation of an analogue of Prussian Blue with M-CN-Pt linkage. However the ligand exchange in a Pt complex is very slow, due to inert Pt(II) and the kinetics of formation of the inorganic polymer has to be assisted with temperature. Various optimization techniques were employed to obtain pure and stable AuPt cyanosols and is discussed in detail in the coming section.

2.4.1 Synthetic strategies

The precursors used for this synthesis were potassium di-cyanoaurate ($K[Au(CN)_2]$) and potassium tetrachloroplatinate ($K_2[PtCl_4]$). Previous experiments explored different stoichiometries between reactants and the results indicated that the most stable nanoparticles with best size distribution were obtained with the ratio of 2:1 between Au and Pt salts.[201] Hence this ratio of starting material would be maintained throughout all the experiments. The strong inert character of platinum required an energy contribution in the form of heat to induce nucleation. Solutions of $K [Au (CN)_2]$ (20mM) and $K_2 [PtCl_4]$ (10mM) were prepared in distilled water and heated to 85°C using a water bath. Once the required temperature was reached, fast addition of the platinum (II) complex into the gold cyanide solution was performed, under constant stirring. The reaction was carried out for 1 hour while maintaining the temperature. The solution turned bright yellow and then slightly turbid. The mixture was cooled down to room temperature. Then 30 equivalents of PVP, a biocompatible polymer was added to coat the surface of the nanoparticles. This sample would be referred as AuPt+ PVP from hereon. The turbidity of the solution was an indication of evolving size and was corroborated with characterization techniques. Therefore, the method had to be changed and further attempts were made to attain smaller sized AuPt nanoparticles that remained stable over time.

2.4.1.1 PVP assisted Au-Pt cyanosol synthesis

Solution of $K [Au (CN)_2]$ (20mM) was first mixed together with PVP 40,000 (0.6 M) solution and heated to 85°C. $K_2 [PtCl_4]$ (10mM) solution was heated separately to the same temperature and added to the mixture with vigorous stirring. The reaction was carried out for 1 hour while maintaining the temperature. The solution appeared bright yellow at the end of the reaction with no turbidity. The sample referred as (Au+PVP)-Pt was analyzed by DLS and TEM to understand their size and structure. Precipitation was induced by addition of 3 volume equivalents of acetone. The compound was collected by centrifugation (8000 rpm, 2°C, 45 minutes), washed well with water and acetone. The bright yellow powder could be obtained by drying under vacuum for 2 hours and used for chemical characterization. The powder was finely ground for IR, EDS and X-Ray diffraction studies.

DLS analysis revealed size of AuPt+ PVP nanoparticle to be around 80 nm. The sample was not very stable as ultra-filtration (UF) led to precipitation. The precipitate could be re-dispersed back into water but the hydrodynamic diameter of the particles in solution had evolved to 150 nm. Addition of PVP further lead to an increase in size of the particles to 200 nm (Fig. 31(a)). These particles were observed by TEM and appeared to be nano-spindles of 150 nm (Fig. 31(c)). They were hard to disperse back after their recovery as powders. So the PVP assisted synthesis route was adopted for further experiments. The hydrodynamic diameter of (Au+PVP)-Pt was significantly smaller at 55 nm and it did not evolve with time. Moreover, the microscopy results showed that this synthetic procedure formed thin, uniform rods containing gold and platinum.

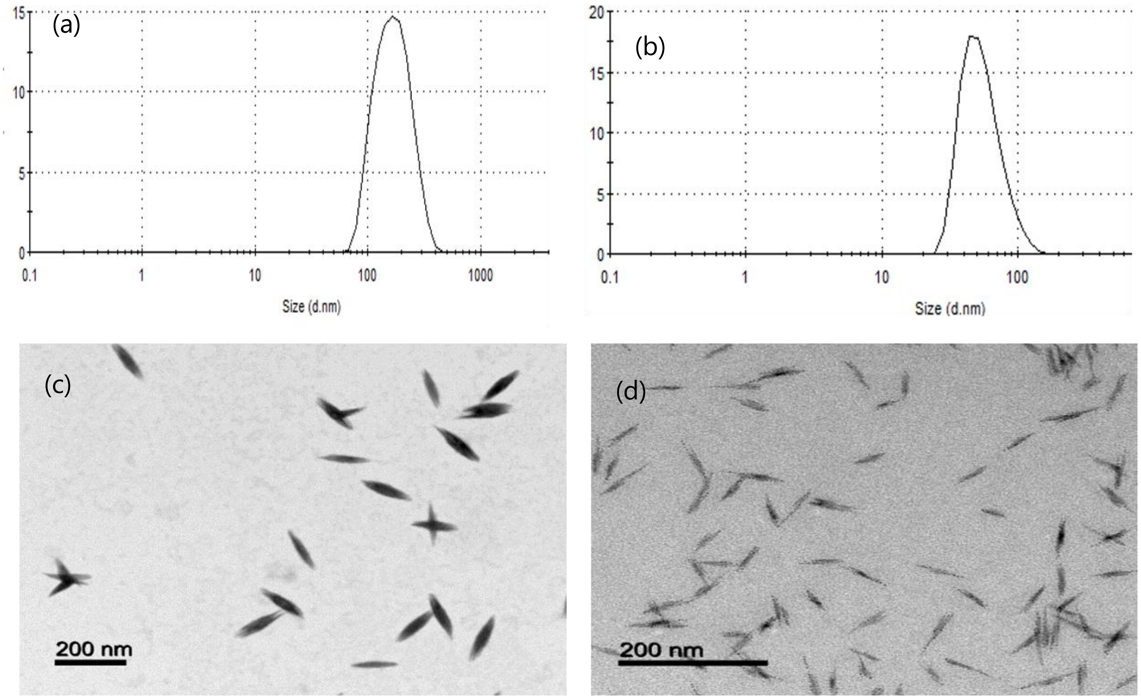

Figure 31. Hydrodynamic diameter and TEM image of (AuPt)+PVP(a, c) and (Au+PVP)-Pt (b, d)

The AuPt nanoparticles had thin rod-like structure but careful study of the images revealed that the samples also contained some percentage of spherical 3 nm pure gold nanoparticles. UV-Vis spectra proved that the nps were indeed gold as the characteristic surface plasmon resonance band around 540 nm (Fig.33) could be observed. The reaction conditions must have resulted in partial reduction of Au(I) and different methods were employed to eliminate this phenomenon so as to obtain a solution containing pure AuPt nanorods.

2.4.1.2 Optimization of the synthesis

i) Reaction time variation: Precursor solutions (K [Au (CN)$_2$], PVP 3500, K$_2$[PtCl$_4$]) were heated to 85°C and mixed together with vigorous stirring. The reaction time was limited for 15 minutes and the solution was brought down to room temperature. Smaller Au-Pt nanorods of size around 25 nm were formed even under this reduced time of reaction. This sample is named (Au+PVP)-Pt-85°-15min but as shown in Figure 32(a), spherical nps of Au could still be observed.

ii) Reaction temperature variation: The reduction of Au^I to metallic Au was then attributed to the temperature of the reaction. Therefore, the synthesis was tried at 50°C and run for 60 minutes. Slightly bigger nanorods of size 30 nm were obtained with traces of pure gold nanoparticles. In order to eliminate this side-product completely, reaction was performed at 50°C but stopped after 15 minutes. These conditions led to formation of Au-Pt nanorods without the interference of pure gold nanospheres. This sample would be called (Au+PVP)-Pt-50°C-15min.

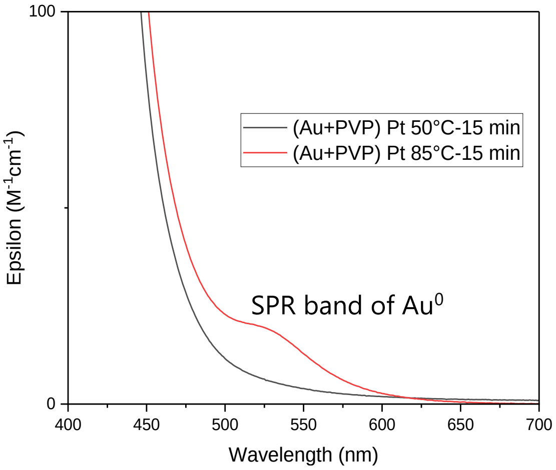

Figure 32. Changes in absorption of AuPt cyanosol upon optimization of reaction conditions

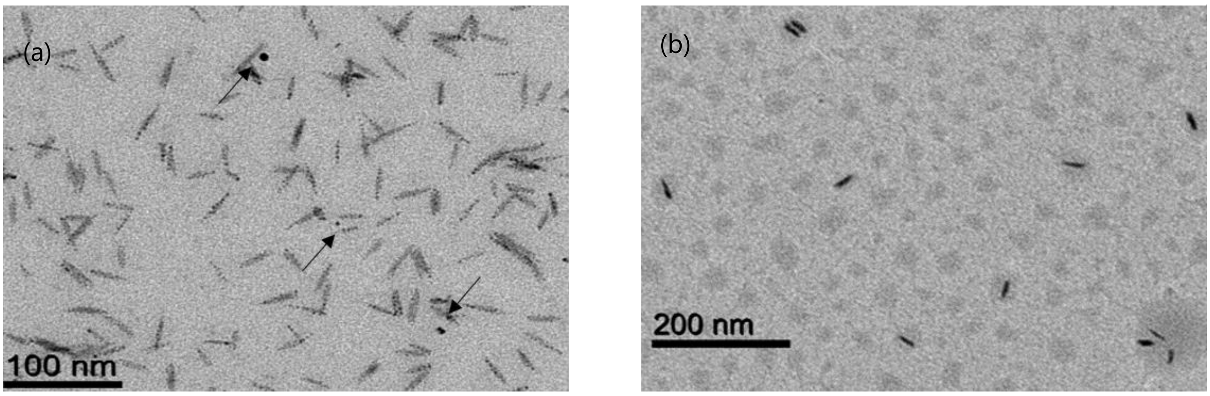

Figure 33. (a) 25 nm rods of (Au+PVP)-Pt-85°C-15 min; spherical Au np also seen (arrows). (b) 30 nm rods of (Au+PVP)-Pt-50°C-15 min. Au np eliminated

iii) Precursor concentration variation: Once the method of synthesis was optimized to remove pure Au contamination, the effect of change in the concentration of reactants was studied. An attempt was made by doubling the initial concentration of each precursor- $K_2[PtCl_4]$ (20mM) solution and the mixture of $K[Au(CN)_2]$ (40mM) + PVP (1.2M) were heated in a water bath until the temperature of 50°C was attained. Then the Pt salt solution was added in one go into the gold complex solution under constant stirring while maintaining the temperature. The solution turned bright yellow with no indication of turbidity. After 15 minutes, the reaction was stopped and the solution was cooled down to room temperature. UV-Visible spectroscopic analysis makes it clear that there is no Au nps interference as the SPR band is not observed even though a higher concentration of Au precursor is used. Hence, this method of preparation was employed as standard and the solution was used for further experiments. This sample is (Au+PVP)-Pt (40:20mM)-50°-15min and will hereafter be referred to as **AuPt cyanosol**.

2.4.2 Characterization

The optimized AuPt cyanosol solution was stable with no visible turbidity. It could be ultra-filtered without the occurrence of deposition. So the sample could be easily purified and washed with water to remove excess salts. The sample could also be concentrated to the desired concentration for further experiments using the ultrafiltration technique. The aqueous solution was used for structural characterization. Precipitation was induced by adding acetone and centrifugation at 2°C. The precipitate obtained after separating the supernatant was dried under vacuum. A bright yellow powder composed of AuPt was obtained and used for chemical characterization.

2.4.2.1 Dynamic light scattering and zeta potential measurements

The hydrodynamic diameter of AuPt nanoparticles in solution was observed to be between 40 to 45 nm. There is no significant change in the size of nanoparticles over time. The solution does not become turbid or deposit when PVP was added during the synthesis. Zeta potential measurements revealed that the nanoparticle surface is highly negatively charged with a potential around -47mV. This explains the long-term stability of cyanosol solution due to electrostatic repulsions.

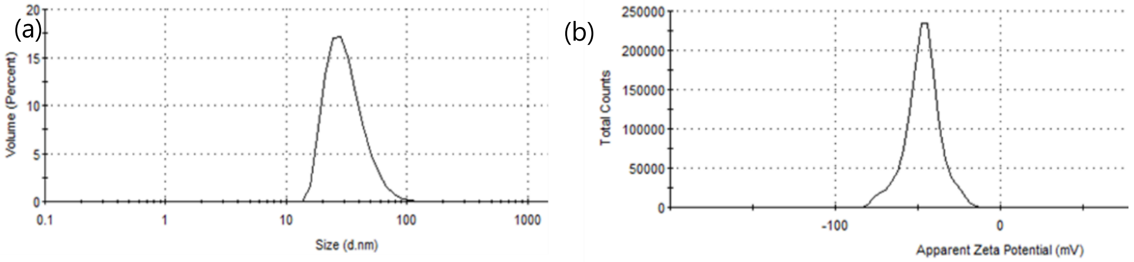

Figure 32. (a) DLS measurement-40 nm and (b) zeta potential result -47mV of AuPt cyanosol

2.4.2.2 Transmission Electron Microscopy Imaging

TEM analysis showed that the AuPt nanoparticles have a rod-like shape. The size and thickness varied according to the method of synthesis. Much thinner nanorods were obtained under these optimized reaction conditions as compared to the first synthesized 150 nm spindles. The absence of pure gold 3 nm spherical particles underlined that this synthetic route was clean. The TEM images also prove that the nanorods are fairly homogenous with respect to both shape and size. The statistics on TEM micrographs indicated that the AuPt cyanosol is composed of 28 ± 4.5 nm long and 5.1 ±0.7 nm wide nanoparticles.

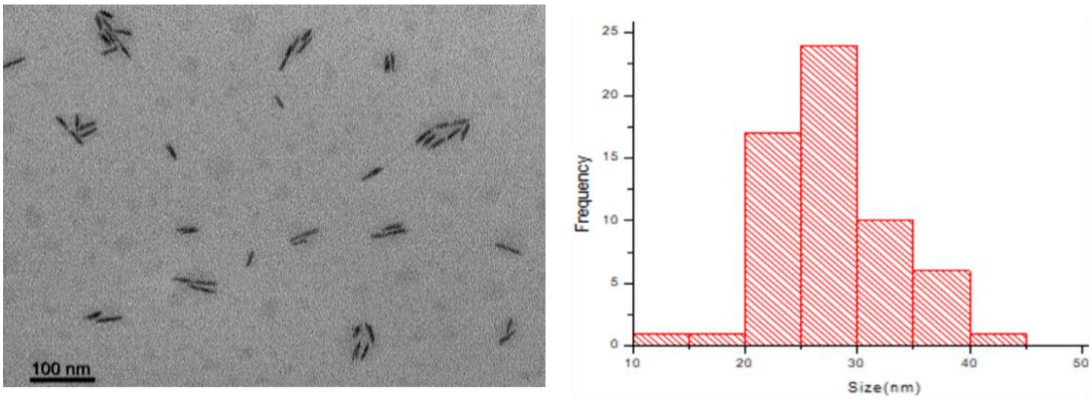

Figure 33. Thin nanorods of optimised AuPt cyanosol and corresponding size distribution chart.

2.4.2.3 Optical Properties

AuPt cyanosol is a bright yellow-coloured solution. Fluorescence studies on the cyanosol indicated that the nanoparticles are not very photo-luminescent. The maximum emission around 492 nm is obtained when excited at a wavelength ($\lambda_{exc.}$) of 355 nm.

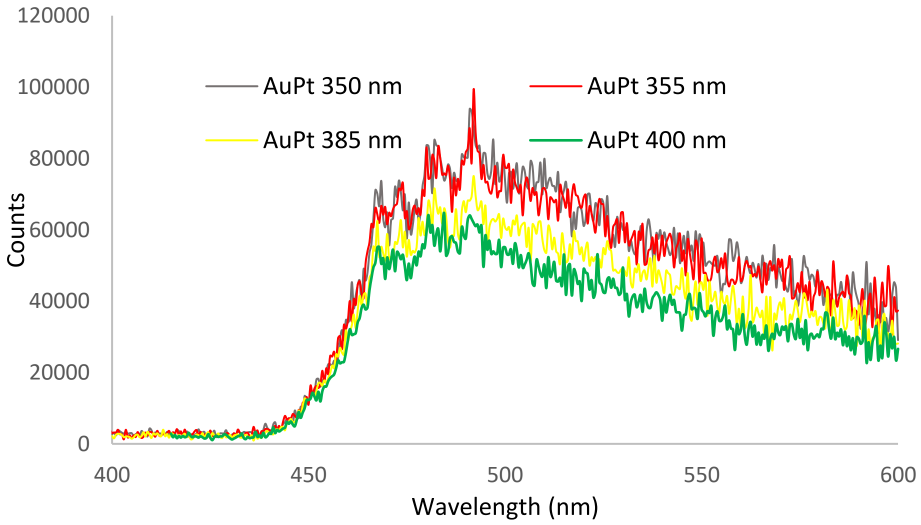

Figure 34. Fluorescence measurement results of AuPt cyanosol

2.4.2.4 X-Ray Diffraction studies:

The AuPt powder obtained by precipitating the cyanosol was used for XRD analysis and the result is displayed in Figure 37. The pattern shows crystalline composition in AuPt. Comparison to the available literature indicated that Bragg peaks corresponded to AuCN structure which was not the initially targeted coordination polymer. The organisation of atoms was deduced to be hexagonal with a space group of P6mm[202] with a=b=3.396 Å and c=5.092 Å, with α=β= 90° and γ=120°.

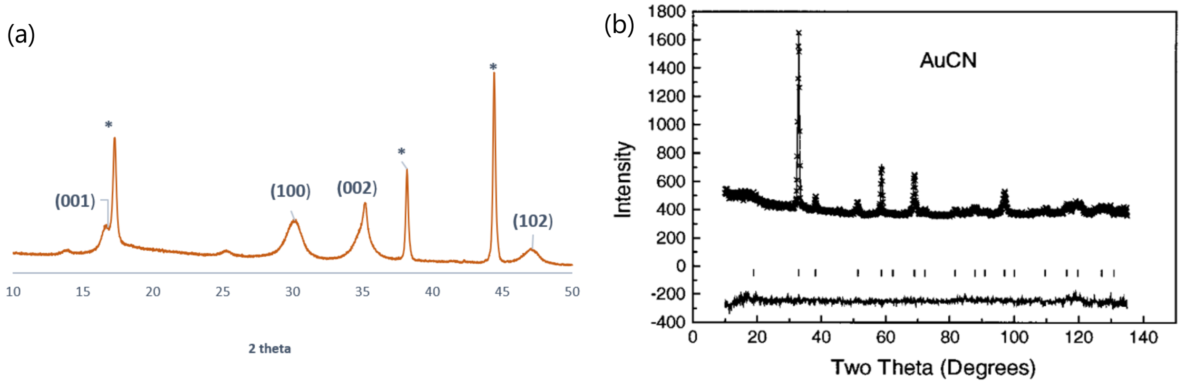

Figure 35. (a) XRD recorded for AuPt powder, (*) marked peaks come from aluminium sample holder. (b) Observed and calculated profiles for AuCN[205]

Peak	**(100)**	**(002)**	**(102)**
Size (nm)	5.8	8.0	4.9

Table 2. Size of crystalline domains calculated along each plane

This formed compound could be described as gold (Au-Au) planes linked through Au-CN-Au chains.[203] The sizes of crystalline domains were calculated using the Scherrer formula and are tabulated above. The size of crystalline domains attained from XRD are significantly smaller than those from TEM analysis. The peak along (100) can be associated to the width of the nanoparticle. The peak along (001) could have given an idea of the crystallinity along c-axis, but it suffered interference from the reflections of the aluminium plate. Hence, only incomplete information could be extracted from the X-Ray diffraction pattern.

2.4.2.5 *Energy Dispersive Spectroscopy*

Once the synthesis method was optimised to attain pure AuPt nanorods without the presence of reduced Au^0, the exact elemental composition was investigated using EDS analysis. The results obtained by varying precursor concentrations is displayed below. Although the Au:Pt starting precursor ratio is maintained at 2:1 and the reaction conditions are the same, we observed a difference of thickness in the nano-rods with TEM imaging.

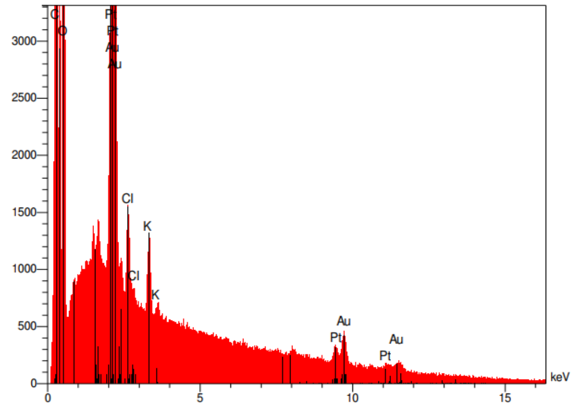

Sample	Au/Pt	Cl/Pt	K/Pt
AuPt (20:10mM) 50°C-15min	5.2	2.2	1.4
AuPt (40:20mM) 50°C-15min	2.0	0.4	0.4

Figure 36. Energy dispersive spectra of AuPt and calculated elemental ratios

Following the results of EDS it is clear that upon using 20 mM of K [Au $(CN)_2$] and 10 mM $K_2[PtCl_4]$, lesser amount of Platinum is incorporated in the nanoparticle and is only equal to 1/5th of the gold content. However, using the precursor ratios of 40mM Au^I and 20mM Pt^{II}, the ratio of Au/Pt is 2. This demonstrates that the amount of reagents put into the reaction is completely accounted for in the product. Moreover, with this synthetic procedure the amount of Cl retained in the nanoparticle is much lower, indicating an almost complete exchange of ligands. Therefore it is further proof that this synthesis technique is very reliable and the optimisation was thorough. The formula unit of AuPt nanoparticle is **$K_{0.4}Cl_{0.4}Pt_1[Au(CN)]_2$@(PVP)**.

2.4.2.6 *Infra-Red Spectroscopy*

Infra-Red spectroscopy is a powerful characterization technique for our samples containing CN bridges. This is because the cyanide bond stretch region of 2000-2250 cm^{-1} are extremely sensitive to the bonding environment and the variations indicate differences in metal-CN bond. It is well-established that formation of strong σ bonds results in increased ν_{CN}, while decrease in electronegativity or oxidation state of the metal tends to decrease the stretching frequency. If the metal co-ordination number is increased, ν_{CN} typically decreases by 20-40 cm^{-1} depending on the number of added ligands. On the other hand when metals are added to the nitrogen end of a coordinated CN, the ν_{CN} is increased by 20-40 cm^{-1}.[204] AuPt nanoparticles synthesised by different techniques were analysed using the IR spectrophotometer and the result of the most optimized sample is displayed below. The vibrations of CN region is focussed on and the two sharp peaks and one broad band can be assigned as follows:

-2235 cm^{-1}: CN triple bond stretch in Au^{I}-CN [205]

-2153 cm^{-1}: vibration of terminal cyanide of Pt^{II}-CN[206]

The broad band around 2216 cm^{-1} is not well defined and probably due to an overlap of several vibrations in the region. Therefore it is attributed to a combination of bridging cyanide in Pt^{II}-CN-Pt^{II} /Au (as 2208 cis-CN bridge between Pt and Cu[207]) together with the terminal -CN vibration in AuCN.

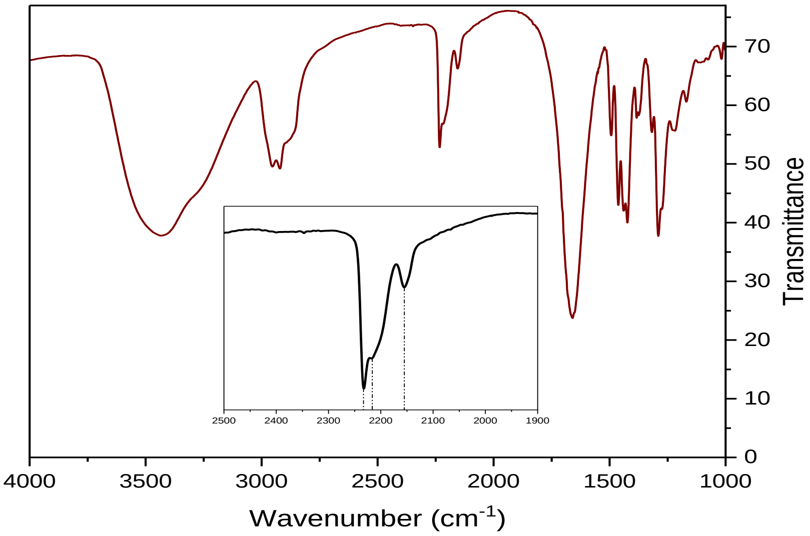

Figure 37. IR spectra of Au-Pt cyanosol

The spectroscopy results also prove the presence of polymer coating in the nanoparticle. The absorption band at 1272 cm^{-1} is related to C-N bending vibration of pyrrolidone. The large band centered around 1660 cm^{-1} rises from the C=O stretch of the PVP. It is blue-shifted compared to that of pure PVP (1644 cm^{-1}) signifying coordination of PVP with metal. The vibrations of CN (2854 cm^{-1}), symmetric CH$_2$ stretching of the ring at 2886 cm^{-1} and chain at 2919 cm^{-1} is clearly visible in the spectra along with the asymmetric CH$_2$ stretch of the ring at 2954 cm^{-1}. [208] IR spectroscopy thus gave a direct confirmation of the formation of AuCN, and also indicated the presence of Pt-CN nanostructures

2.4.2.7 X-ray Photoelectron Spectroscopy

XPS studies allowed us to detect the elements that exist within the nanoparticle and provided information regarding the oxidation states of the metal in the sample. It is a surface sensitive spectroscopic technique that detects electrons that escape from the sample after irradiation with X-rays. The binding energy (BE) of the emitted electrons is calculated to provide information of the chemical state of elements. The complete survey over multiple points were performed. Extensive literature review and study of reference compounds (annex 6.2.4) helped assign the peaks of this novel compound. The BE peaks of 85.1 and 88.8 eV was attributed to gold in Au^{I} state[209] and the ones at 73.8 and 77.0 eV, indicated the existence of platinum as

Pt^{II}. The C 1s XP spectrum exhibits a strong emission around 285.2 eV with a shoulder~287.9 eV. Deconvolution of the peak reveals contribution of CN molecules together with C-C and N-C=O from PVP. The large N 1s peak at 399.7 eV with a FWHM of 1.75 eV could be ascribed to N atom in the pyrrolidone group of the polymer. This signal is shifted to a higher binding energy (~1 eV) compared to pure PVP (398.8 eV)[208] suggesting changes in PVP during the synthesis at 50°C. XPS analysis helped prove that Pt is indeed incorporated into the sample, even if the structure was not in the expected form.

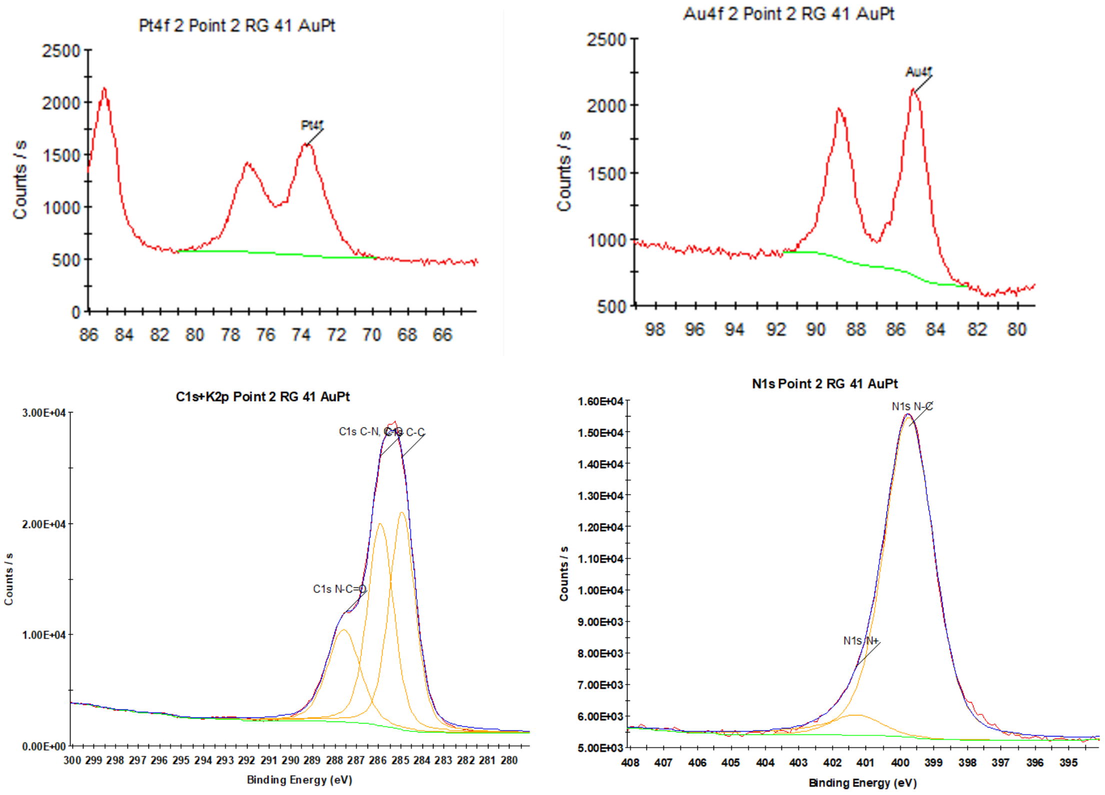

Figure 38. XPS spectra of AuPt cyanosol

2.4.2.8 High resolution transmission electron microscopy

The sample was studied at higher magnification and resolution with HR-TEM by Alexandre Gloter at Laboratory of Solid Physics (LPS, Orsay). This imaging technique was employed to observe the local structure and crystallinity of our sample. Interesting new features were revealed and as seen in Figure 41, the rod contains ordered planes that taper towards the end. The surface of the nanorod is decorated with 1 nm spherical nps. The distances were calculated to be (001) = 0.5029 nm, (100) = 0.294 nm, (101) = 0.253 nm and the rods could be indexed with P6mm space group.

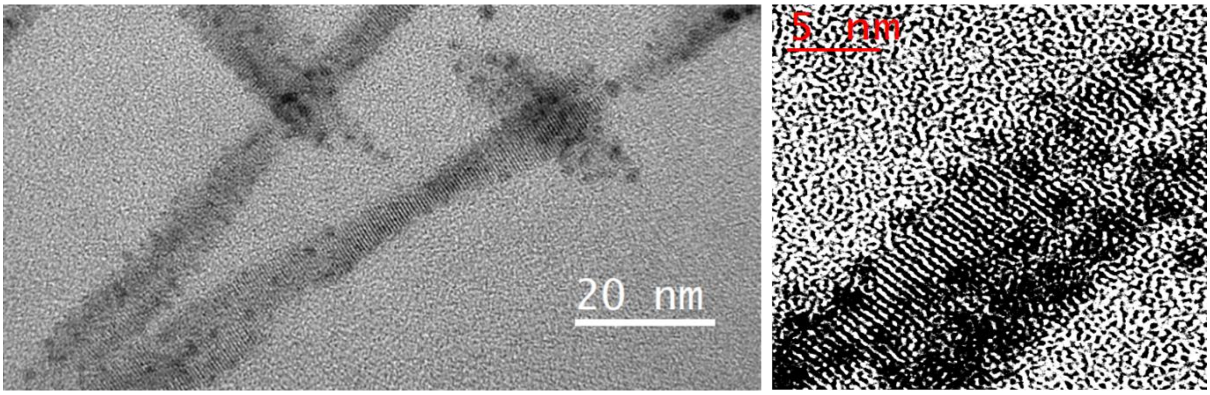

Figure 39. High resolution TEM images at 200 kEV of AuPt cyanosol nanoparticles.

2.4.3 Discussion

It is well documented that the cyanoaurate precursor used in our synthetic procedure can be used as a building block to manufacture novel porous and conducting materials. Gold has special chemical properties and the propensity of d^{10} Au^{I} ions to attract each other is one of them. These *aurophilic interactions* are strong and responsible for the formation of gold planes or sheets as seen in Figure 42. The Au atom forming the sheet are bonded to 6 other Au atoms at a distance of 3.396 A. It is connected to another Au^{I} through a cyanide bridge forming a stable structure with $k_f = 10^{37}$ M^{-2}. It has to be noted that this AuCN structure is usually formed using the Elsner reaction in highly acidic conditions that can lead to poisonous side products or via a radical-involved multi-step photochemical cyanidation of Au nanoparticles using acetonitrile.[209]

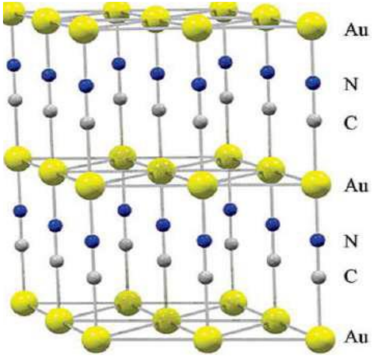

Figure 40. Solid state structure of AuCN.[209]

Here, we have demonstrated the formation of such a structure in water using a green process. Combining the information obtained from the above mentioned characterization techniques, a hypothesis on the formation of this unique AuPt structure is proposed. Our synthesis conditions involves conversion of $Au(CN)_2^-$ into AuCN with the loss of one cyanide molecule. In the presence of PVP and the activated Pt^{II} complex, a ligand exchange takes place leading to the formation of Pt-CN-Pt bridges. These cyanide bridges lead to formation of 1 nm spherical Prussian Blue analogue (PtPt) nanoparticles that decorate the surface of gold nanorod. As far as we know this is the first reported formation of such AuPt alloy nanoparticles where the constituent metals retain their original oxidation states. They do not need to undergo reduction to a purely metallic (Au^0 or Pt^0) in order to form nanoparticles and remain stable in solution. Photoluminescence originating from short Au-Au distances were expected, but it is possible that incorporation of PVP within the structure during synthesis is responsible for some quenching and would be investigated in the future.

2.5 IRON-PLATINUM PB ANALOGUE NANOPARTICLES

The iron-platinum (FePt) nanoparticles were synthesized in a single step using pure water as the solvent. Various experimental conditions were explored and effect of parameters such as concentration of precursors, temperature and time of reaction were investigated during the thesis of Dr.Fetiveau. The aim was to achieve stable and self-standing solutions containing nanoparticles of a controlled size. The optimised and most stable configuration required for obtaining FePt cyanosol is described below.

2.5.1 Synthesis of FePt cyanosol

Potassium ferrocyanide ($K_4[Fe(CN)_6]$)(10mM) and potassium tetrachloroplatinate ($K_2[PtCl_4]$) (10mM) solutions were prepared in water. Each solution was heated to 55°C as previous studies indicated that this temperature was required for thermal activation. Once a homogenous solution was obtained, $K_2[PtCl_4]$ was added to the metal cyanide solution in one go, under constant stirring. The mixture turned yellow in colour and the reaction was run for 60 minutes while maintaining the temperature. The solution was cooled down to room temperature and turned dark green in colour. 30 equivalents of PVP monomer (0.15 M) with respect to Pt(II), was introduced to the aqueous solution under constant stirring. The solution remained unchanged in colour and was stable at room temperature. This sample would hereafter be referred to as FePt cyanosol. It was ultra-filtered to remove unreacted precursors and washed twice with water. This solution was analyzed regularly to investigate the evolution and for biological tests. Addition of 9 volumes of acetone (with respect to 1 volume of colloidal solution) led to a slightly turbid solution. Upon centrifugation at 8000rpm, 2°C for 90 minutes a dark green precipitate could be obtained. It was dried under vacuum for many hours and finely ground to get a homogenous powder that was used for chemical characterizations.

2.5.2 Characterization

2.5.2.1 Dynamic Light Scattering and Zeta potential

DLS experiments were effective in following the evolution of nanoparticles during synthesis. FePt nanoparticles before the addition of PVP were around 150 nm in size. A drastic reduction to around 2.5 nm was observed when the polymer was added indicating that aggregates of nanoparticles were formed initially which could be disassembled by the addition of PVP.

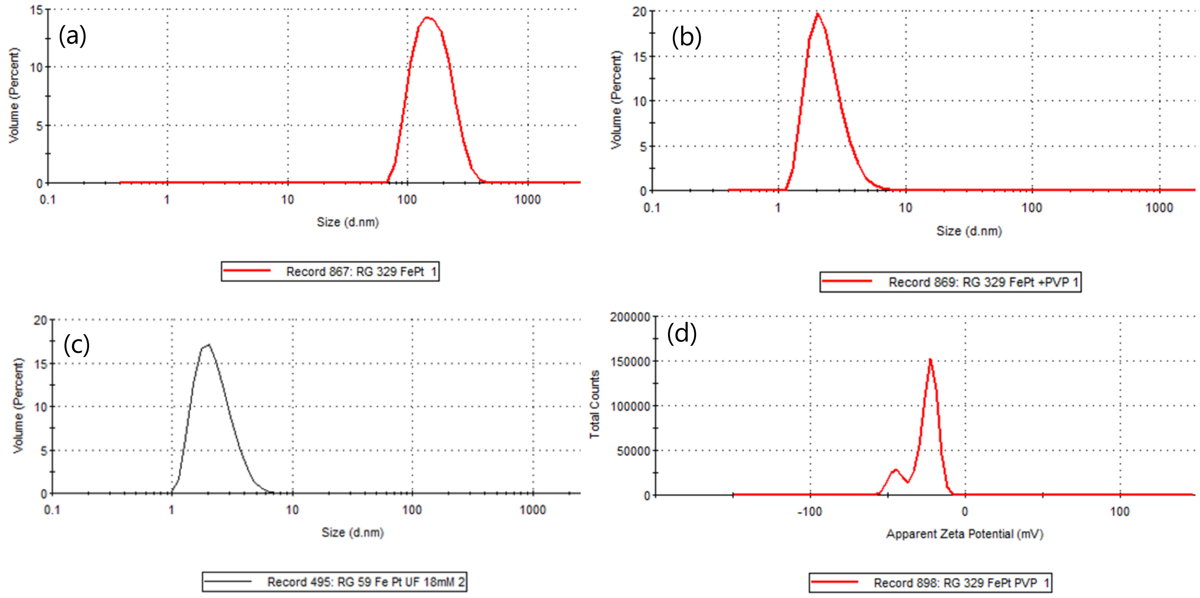

Figure 41. Hydrodynamic diameter measured (a) before (b) after PVP addition and (c) after UF and concentration (d) zeta potential result of Fe-Pt cyanosol

Ultra-filtration of the solution (MWCO 3000) could be done without any flocculation which is a further proof of small size and high stability of these nanoparticles. The filtrate was colourless indicating no particles were passing through the membrane. Zeta potential measurements of the cyanosol solution showed peaks at -23.5 mV with a shoulder around -45 mV. This is an indication of stability as the negatively coated surface of nanoparticles would prevent their aggregation over time.

2.5.2.2 Transmission Electron Microscopy

The particles in the colloidal solution could be visualized using TEM. The grid was pre-treated with glow-discharge to make the surface hydrophilic and uniformly charged. The analysis revealed well-individualised nanoparticles of FePt with an average size of 5.0 ± 0.9 nm. There is no significant difference in the size of the particle upon coating with PVP polymer. In this case, DLS measurements under-estimate the real size of the particles.

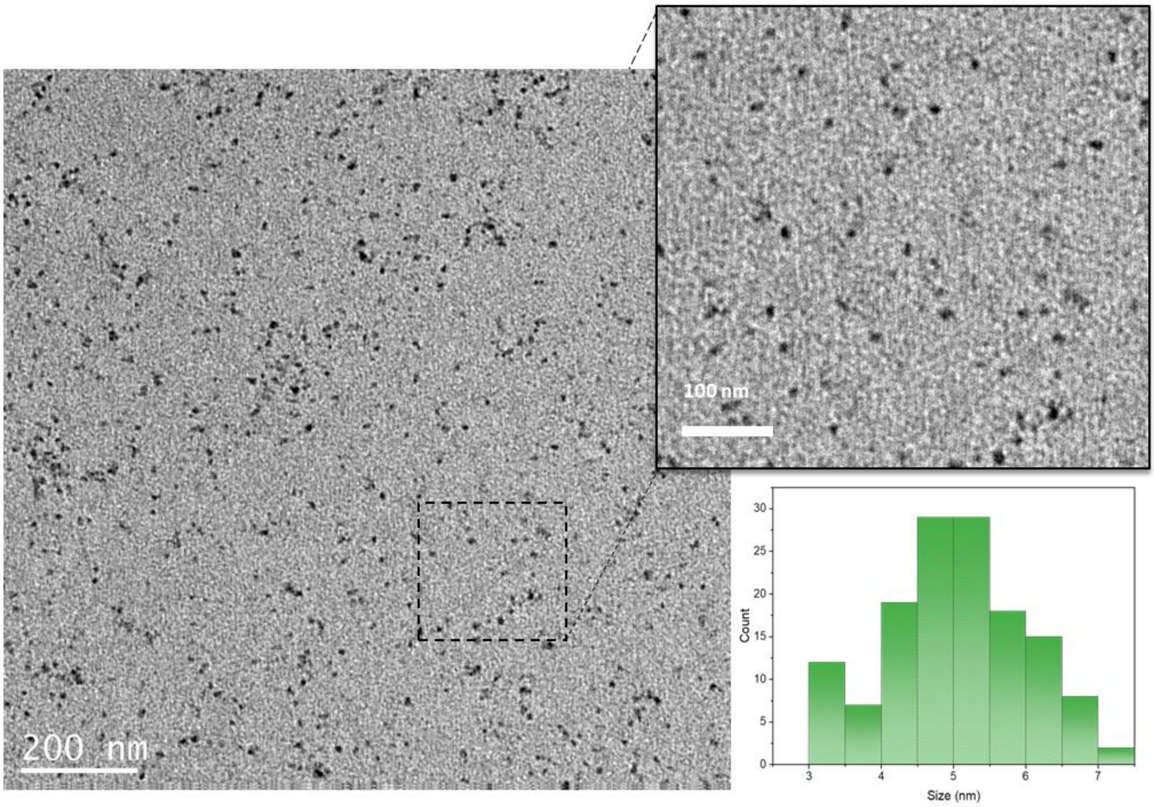

Figure 42. TEM image of Fe-Pt nanoparticles with corresponding size distribution chart

2.5.2.3 Energy Dispersive Spectroscopy

The EDS analysis was done in order to estimate the composition of Fe-Pt cyanosol powder. This provided us with the amount of various elements like K, Cl, Pt and Fe in the sample and each ratio was calculated from the atomic percentages. The formula unit of this compound is $\mathbf{K_{1.2}PtCl_{0.4}[Fe(CN)_6]_{0.7}@(PVP)}$. We can consider that almost all chlorides have been exchanged around the Pt, and that the remaining chloride are probably located at the surface of the particles.

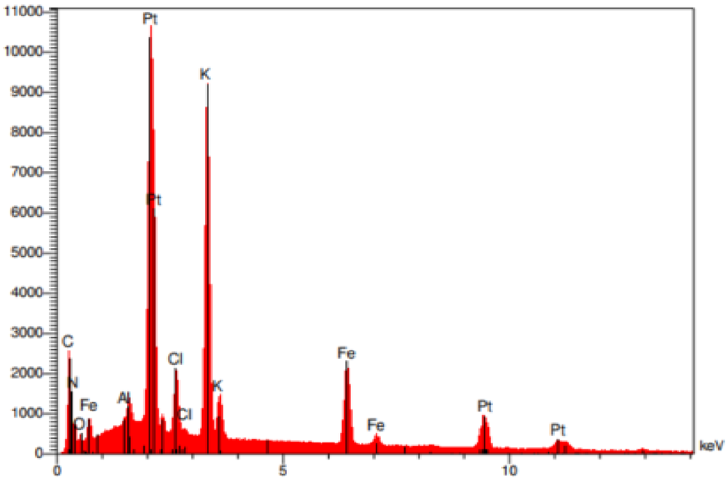

Figure 43. Results of EDS analysis on FePt nanoparticles

2.5.2.4 Infra-Red Spectroscopy

The different bonds present in the sample could be characterised by IR spectroscopy. The vibrations of cyanide functional group usually fall in the range of 2000-2200 cm^{-1}. Depending on the type of bond the peak shifts to higher or lower energies. In this compound three significant peaks can be observed in this range.

-2072 cm^{-1}: vibration of cyanide of Fe^{II}-CN-Fe^{III}

-2109 cm^{-1}: vibration of bridging cyanide of Fe^{II}-CN-Pt^{II}

-2130 cm^{-1}: vibration of cyanide linked to Fe^{III}-CN [210]

It was expected that a small amount of Fe^{II} would undergo oxidation during the synthesis process to form the highly stable Prussian Blue and its characteristic peak at 2072 cm^{-1} is observed, in addition to the terminal Fe^{II}-CN. The typical peaks of polyvinylpyrrolidone are discussed in detail in section 2.4.2.6 and they are also observed together with the FePt signals in the IR spectrum.

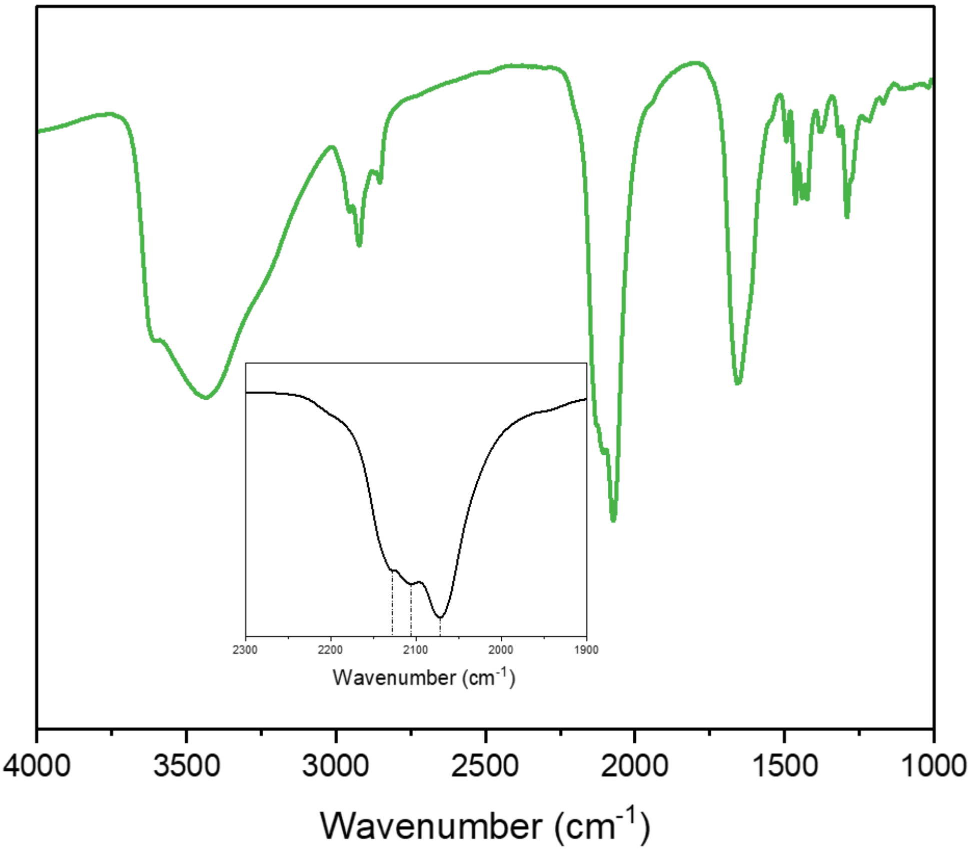

Figure 44. IR spectra of FePt cyanosol with inset zoom on cyanide region

2.5.2.5 X-ray Photoelectron Spectroscopy

The XPS analysis of deposited iron-platinum powder provides clear indication of iron in Fe^{II} state with Fe 2p edge located at 708.3 eV. It is characteristic of Fe^{II} bound to CN. The Pt binding energy has shifted to slightly lower values of 73.5 eV which could be attributed to Pt^{II} linked to the N end of the cyanide bridge. As shown in Figure 47, the C 1s and N 1s peaks obtained in the survey could be assigned to the cyanide bonds coming from the ferrocyanide and the C-N and C=O found in PVP polymer.

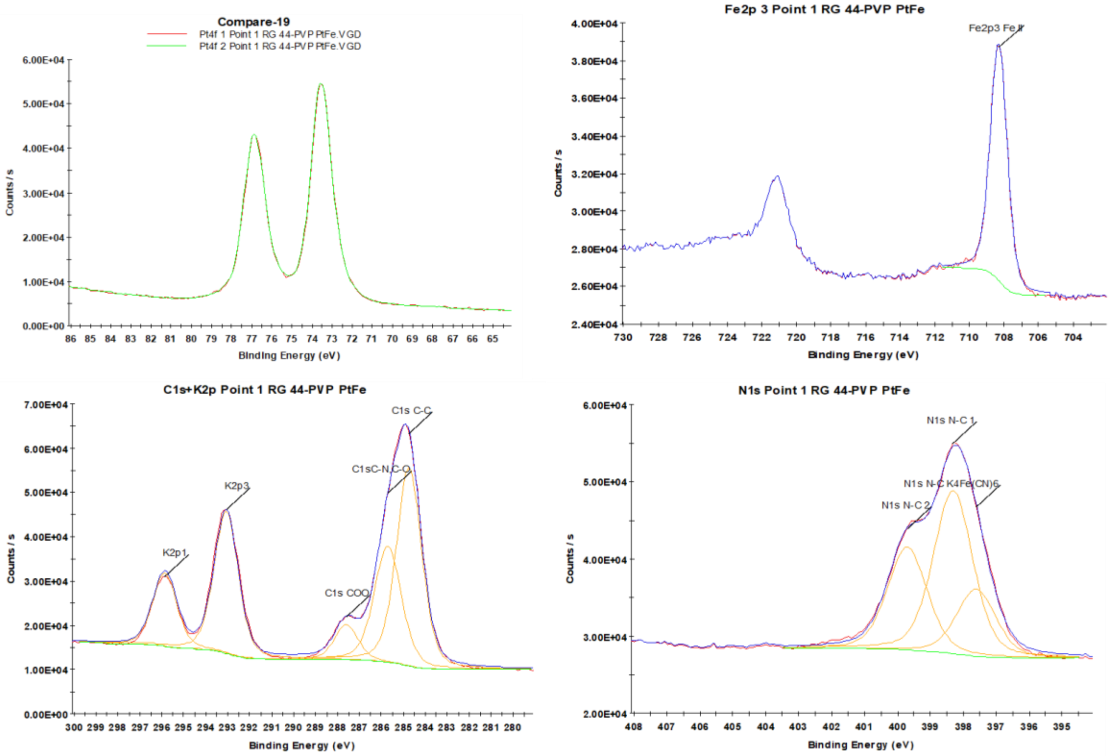

Figure 45. XPS survey results of FePt nanoparticles

2.5.2.6 X-Ray Diffraction

XRD studies were performed in order to probe the crystallinity of the FePt nanoparticles. A diffractogram of Prussian Blue nanoparticles of 3-5nm size would clearly reflect peaks related to the FCC structure of the lattice[201]. Such peaks are not observed for FePt structures. The obtained diffractogram is a characteristic of an amorphous compound. In the case of this type of coordination polymer, defects are expected in the fcc structure due to partial chloride replacement. The absence of crystallinity is probably due to these defects within the network in addition to the minimal number of atoms being probed in such small particles.

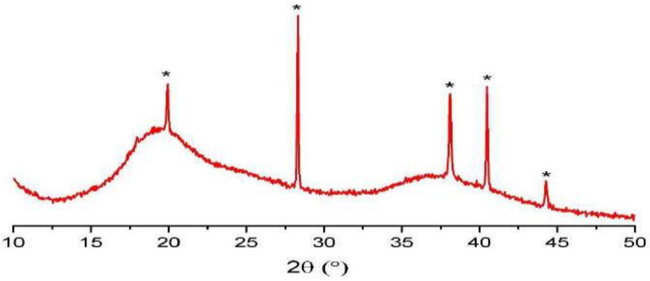

Figure 46. XRD results of FePt nanoparticles (*) indicates peak due to aluminium sample holder

2.5.2.7 UV-Visible Spectroscopy

UV-Visible spectroscopy provided further information about the constituents of the green coloured FePt cyanosol. The spectra of the ultra-filtered cyanosol solution was recorded in the 300-1200 nm range. There are two significant absorptions : the intense peak in the ultra-violet region, around 310 nm could be assigned to the metal to metal charge transfer between Fe^{II}-CN-Pt^{II} pairs in the coordination network and broad band around 760- 820 nm. This confirms the presence of a few Prussian blue (Fe^{II}-CN-Fe^{III}) pairs. The number of PB pairs formed are extremely small (<5 %) because its molar absorption coefficient is usually around 7000 M^{-1} cm^{-1} and plot shows ε (800 nm) = 245 $M^{-1}cm^{-1}$. Therefore, the oxidation of Fe^{II} to Fe^{III} during the synthesis is very minimal. The formation still occurred due to the high stability of Prussian Blue complexes.

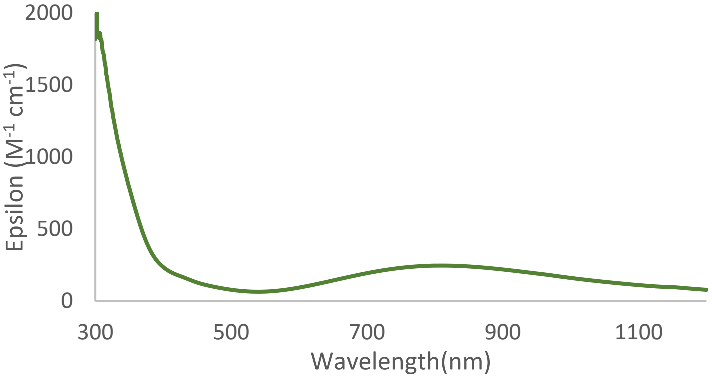

Figure 47. UV-Visible spectra of Fe-Pt cyanosol solution

Characterization results indicate that the chloride ligands from the tetrachloroplatinate precursor are exchanged by the CN ligands from ferrocyanide to form FePt nanoparticles. The iron (Fe^{II}) in octahedral geometry bridges through a cyanide linkage to platinum ions. But since Pt^{II} exists in a square planar configuration, 1:1 cyanide bridging between composite metal ions would not be possible. Four Fe^{II}-CN would surround 1 Pt^{II} ion if all Cl are removed and 6 Pt^{II} would envelop 1 Fe^{II} ion. It explains the low Fe/Pt ratio in EDS. This Fe^{II}-CN-Pt^{II} coordination network formed is full of defects compared to the fcc structure of Prussian Blue, as clarified by XRD. Therefore, a roughly PB-like structure with vacancies and defects, is formed in this FePt cyanosol.

2.6 PLATINUM-PLATINUM CYANOSOLS

Inspired by the above results, attempts were made to synthesise cyanosols comprised of purely platinum metal centres. Such coordination nanoparticles had never been synthesised or studied previously. Higher temperature of activation was necessary to form these cyanosol particles to induce ligand exchange between inert Pt(II) complexes. Experiments were conducted to obtain self-standing nanoparticles of a controlled size. The results obtained are described below.

2.6.1 Synthesis of PtPt cyanosol

Potassium tetracyanoplatinate ($K_2[Pt(CN)_4].3H_2O$) (10mM) and $K_2[PtCl_4]$ (10mM) solutions were prepared in water and heated to 85°C. Once both the solutions were at the required temperatures, platinum chloride was quickly added to the metal cyanide solution under vigorous stirring. The mixture turned brown upon mixing but slowly changed to almost colourless over the duration of 1 hour. The solution was cooled down to room temperature. PVP monomer (0.15M) solution was added to the cyanosol with constant stirring at room temperature. It was ultra-filtered and washed with water twice to remove all unreacted precursors. The final solution was stored in a refrigerator at 4°C for further characterisation. This solution would hereafter be known as PtPt cyanosol. Cetyltrimethyl ammonium bromide (CTAB) (5mM) in methanol was added to induced flocculation. The mixture was centrifuged (8000 rpm, 2°C) and pellet was formed. It was dried under vacuum for several hours and white coloured powder was obtained for characterisation.

2.6.2 Characterization

2.6.2.1 Dynamic Light Scattering and Zeta potential

Hydrodynamic diameter of the synthesised Pt-Pt nanoparticles was measured using DLS. The size of Pt-Pt particles was found to lie between 3-7 nm. Addition 30 equivalents of PVP led to a shift to higher values of 8-10 nm. This was attributed to polymer coating and solvation shells. Zeta potential of the solution was observed to be around -27 mV. These measurements provide proof that the nanoparticle solution which could be synthesized at high concentrations, are quite stable and no significant changes occur after ultra-filtration and washing steps. Additionally concentrating the sample further for biological experiments did not cause any deposition.

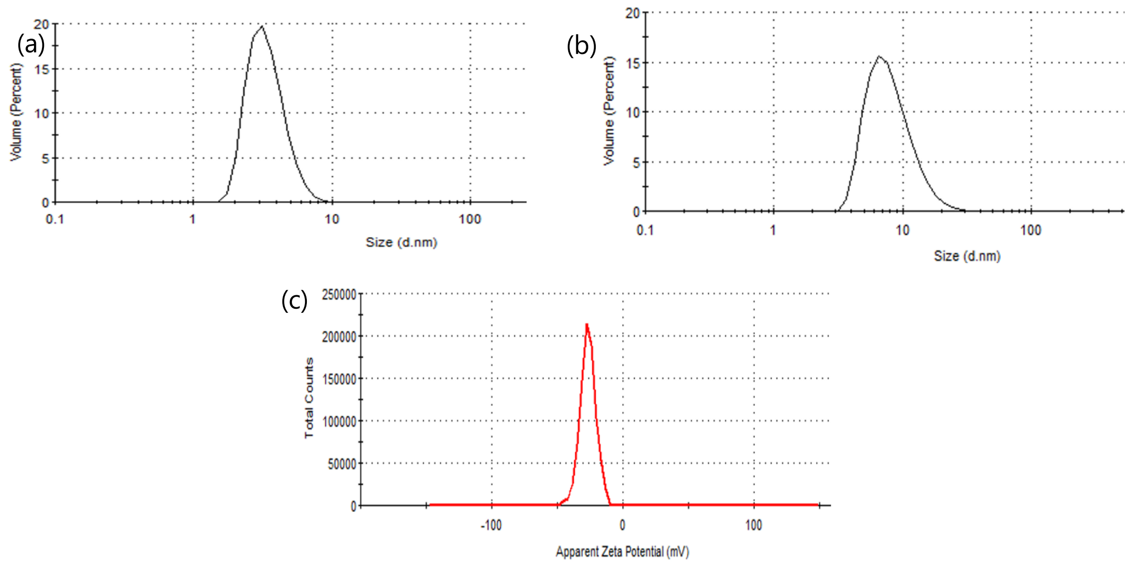

Figure 48. Hydrodynamic diameter (top-left), after addition of PVP and UF (top-right) and zeta potential (centre) of Pt-Pt nanoparticles

2.6.2.2 High Resolution Transmission Electron Microscopy

It was hard to detect PtPt nanoparticles with a good contrast using the normal electron microscope. Therefore we resorted to HRTEM for the synthesised particles and this study was performed by Francois Brisset at ICMMO, Université Paris-Saclay. The analysis revealed that PtPt nanoparticles are spherical in shape and much smaller in size compared to its FePt counterpart. Majority of the nanoparticles lie in the range of 1.7 ± 0.3 nm. This size is much smaller than the hydrodynamic diameter obtained from DLS results, probably due to the solvation shell and polymer coating. These results advocate that ultra-small nanoparticles of controlled sizes could be obtained from this method of synthesis in pure water. This surfactant-free method of forming cyanosols is simple and extremely efficient.

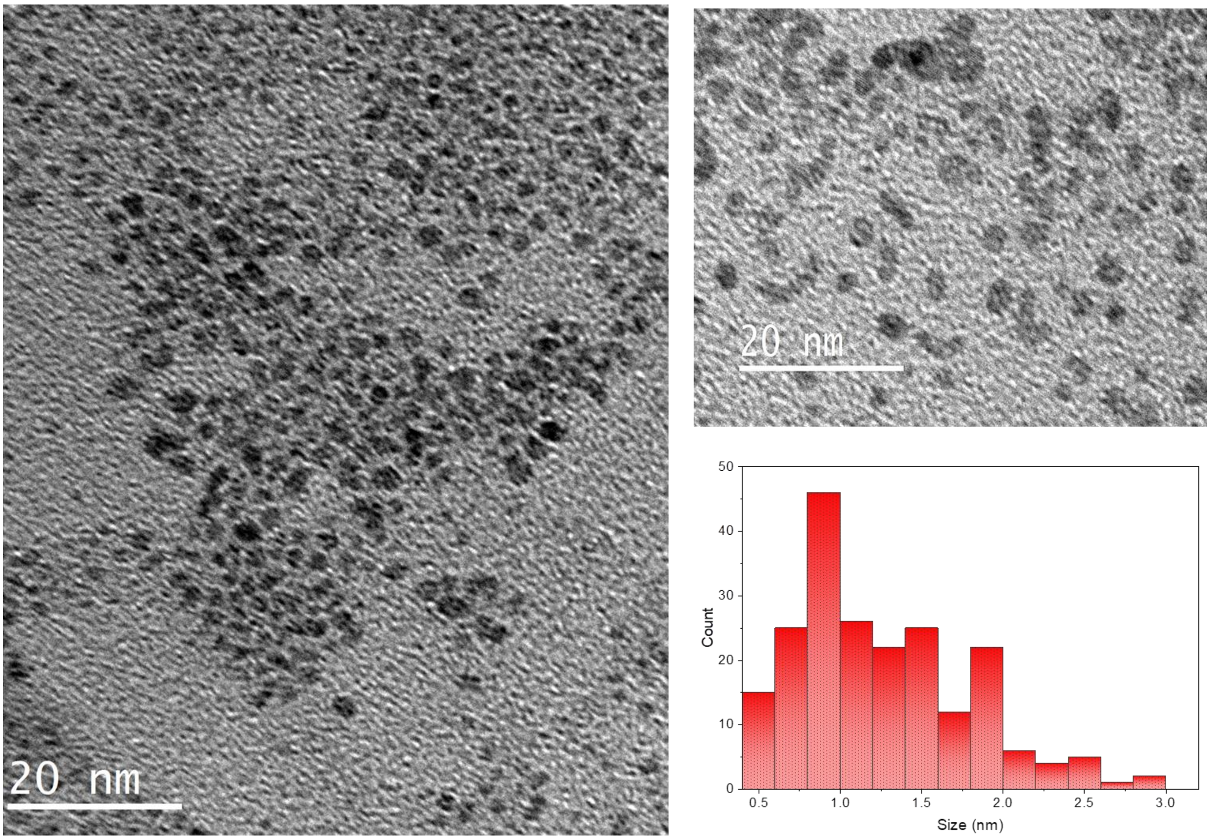

Figure 49. HR-TEM images of PtPt cyanosol nanoparticles with corresponding size distribution chart

2.6.2.3 X-ray Diffraction

Diffractogram of PtPt powder from 2θ= 10 to 50° were studied to check crystallinity of the sample. The peaks characteristic of an FCC lattice of PBA were not found even with long accumulation time. The only peaks obtained were that of the aluminium sample holder. This is an indication that the nanoparticle size is too small or including defects, and thus cannot be probed using XRD.

2.6.2.4 Energy Dispersive Spectroscopy

Elemental analysis indicated that the final compound was mostly composed of platinum (89 A%) with very little amounts of potassium and chlorine remaining within. Therefore almost all chloride of K_2PtCl_4 has been replaced by nitrogen of cyanide around the Pt atoms. The formula unit of the compound is **$K_{0.1}PtCl_{0.1}[Pt(CN)_4]$@PVP**. A small amount of chloride atoms that are present that may be located at the periphery of the particle.

2.6.2.5 Infra-Red Spectroscopy

The IR spectra (Fig.52 b) show peaks characteristic to the PVP coating at 2920, 2854 and 1660 cm^{-1} in PtPt powder. There were two intense peaks in the cyanide region of spectra: 2150 cm^{-}

^{1} arising from the terminal cyanide vibration of Pt^{II}-CN while the 2201 cm^{-1} could be assigned to the higher energy vibrations of cyanide bridge between two Pt ions.

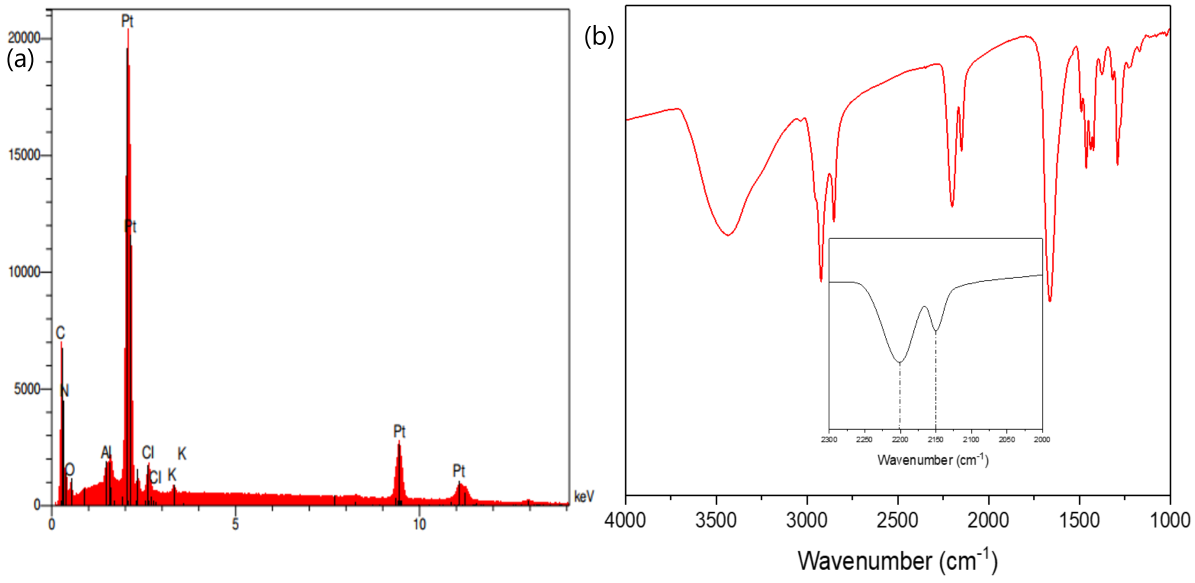

Figure 50. (a) EDS analysis and (b) IR spectroscopy results of PtPt nanoparticles.

2.6.2.6 X-ray Photoelectron Spectroscopy

As mentioned earlier, XPS is a surface sensitive technique that helps detect the various ions present in the synthesised compound by irradiating it with X-rays. The analysis results are displayed in Fig. 53. The Pt^{II} presence is clearly depicted by their binding energy peaks centered at 73.8 and 77.1 eV. The C 1s spectral region show contributions of C-C, C-O and C-N from the polymer. Potassium is not detected in this analysis, since CTAB was used to precipitate these ultra-small nanoparticles from its solution form. So the CTA^{+} ions exchange with the K^{+}, which are then removed. The deconvolution of N 1s core level peaks suggests the presence of cyanide bound to Pt^{II} together with C-N originating from pyrrolidone moiety in the PVP.

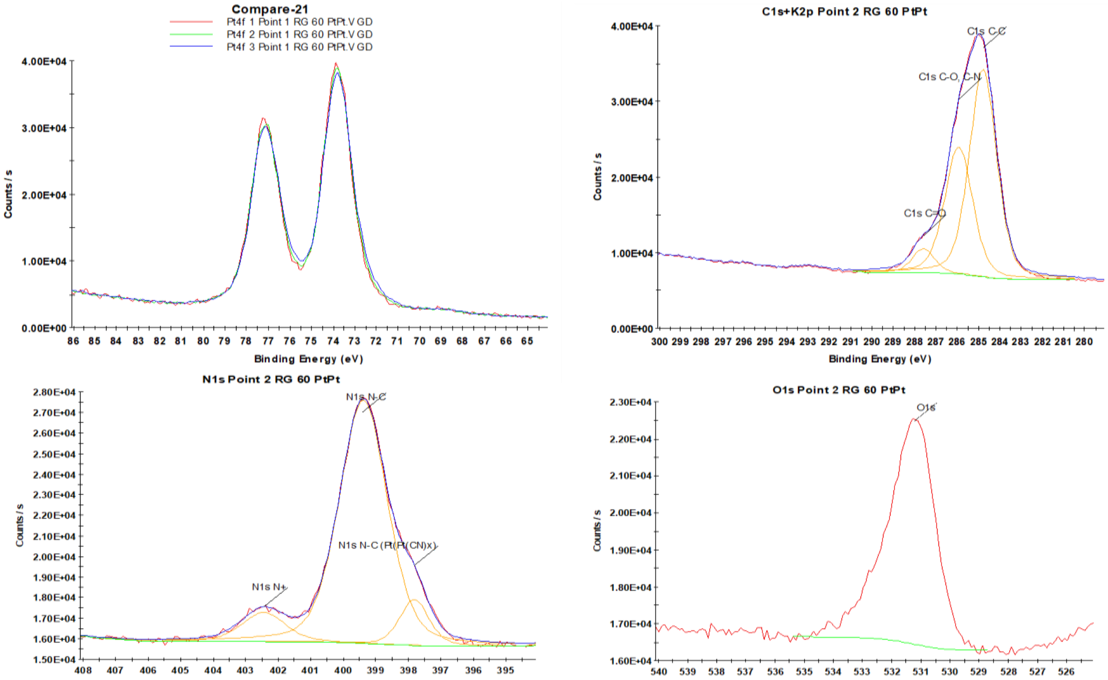

Figure 51. XPS survey results of PtPt nanoparticles

Altogether, the data suggest that PtPt nanoparticles are formed by exchange of Cl ligands with cyanide coming from $Pt(CN)_4^{2-}$. Square planar Pt^{II} complexes would organize into lamellar, 2 dimensional sheets composed of platinum separated by regular distances. The inorganic core of PtPt nanoparticles is thus made of sheets of Pt^{II}-CN-Pt^{II} bridges that are held together by other types of interactions (Pt-Pt, VdW). A 1.5 nm particle would contain sheets of 16 Pt atoms.

2.6.2.7 Optical properties

PtPt cyanosol is a colourless solution and as expected, the absorption spectra displayed one intense band in the UV region, between 250-350 nm. However, fluorescence spectroscopy provided some interesting results. These cyanide bridged Pt^{II} containing nanoparticles are highly photo-luminescent. As shown in Fig. 54 the maximum emission could be obtained upon using the excitation wavelength ($\lambda_{exc.}$) of 390 nm. The broad fluorescence band is centered around 487 nm. Diluting the sample brings down the emission. A drastic decrease is observed upon addition of PVP to the cyanosol. At the same Pt concentration, introduction of PVP led to a 68 % decrease in the observed emission (green dotted arrow, Figure 54 b). A small blue shift can also be seen in this case. The maxima for PtPt@PVP is obtained at a λ_{exc} of 380 nm and consequently the emission band is centered around 466 nm. It was verified that the signal was not coming from the Pt precursors used in the synthesis. Some studies done on metallic Pt^0 nanoparticles show photoluminescence properties but as far as we know this is the first report on Prussian Blue analogue nanoparticles exhibiting strong emission in the visible spectrum.

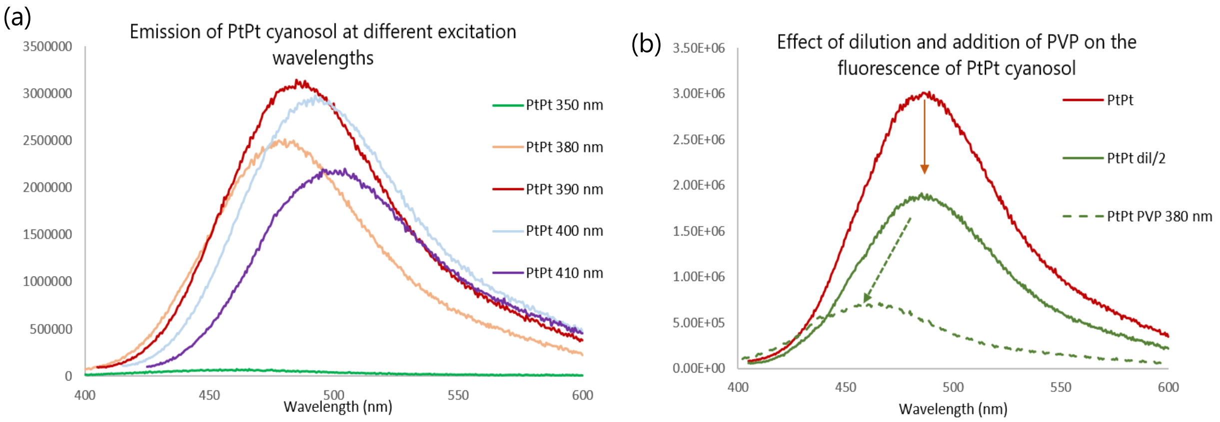

Figure 52. (a)Summary of fluorescence studies on PtPt cyanosol and (b) effect of dilution and PVP addition on emission maxima

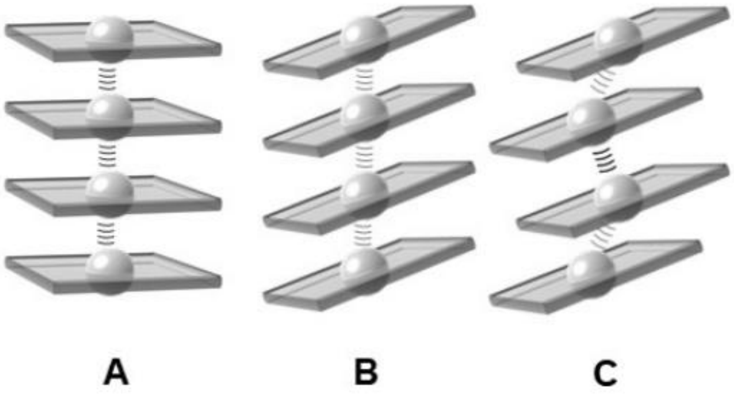

Figure 53. Stacking features for infinite chains of Pt^{II} complexes that affect the Pt--Pt interactions: a) parallel stack b) oblique stack with equivalent distances and (c) oblique stack with non-equivalent Pt-- Pt distances[211]

This fascinating property could be attributed to the close Pt--Pt distances between the sheets that are below 3.5 Angströms (twice the vDW radius of Pt) as reported in the literature for Pt^{II} complexes.[211,212] The 2D planes composed of Pt^{II} can interact and give rise to the strong fluorescence properties. In analogy to studies on molecular complexes that show a direct dependence (in the solid state) [213–215] of the emission wavelength with the Pt-Pt distance, we think the Pt-Pt distances are between 3.3 and 3.4 Angströms. The dramatic decrease in emission and shift to a lower wavelength could be due to a looser and less rigid structure, with slightly larger Pt-Pt distances in the presence of PVP. A possible justification is that the polymer may insert partly between the planes, having kind of an exfoliating effect or just exert some strain on the surface sites of the particles. Some experiments have been tried to evidence this (HRTEM and STEM with A.Gloter), but without success due to the ultrasmall size of the particles.

As time was lacking, a complete study of the fluorescence properties will be done in collaboration to determine the quantum yield and emission lifetimes, The influence of the nature of the polymer on the emission will be checked in close future and may open interesting ways to tune the emission. Fluorescence imaging will be performed once the particles are internalised in cells to check if they retain their photoluminescence, which would be an important result in our quest for theranostic nanoparticles.

2.7 STABILITY OF CYANOSOLS IN PHYSIOLOGICAL MEDIA

Regular monitoring via UV-Visible spectroscopic and DLS studies proved that all three cyanosols were stable at room temperature in water and their composition did not change with time. These nanoparticles were synthesised to act as radio-enhancing agents for cancer therapy. So, they would have to be internalised into the cells of human body to play their role as therapeutic agents. But in order to proceed further, we needed to investigate their behaviour in the biological environment. Therefore, once the chemical synthesis and purification of nanoparticles was done, the effect of two different physiological media on the nanoparticle solution were studied. We could analyse the behaviour of particles during their transport into the tumour and after internalisation in a cell. Very few studies report such analysis but we wanted to know the complete effect in the media before moving on to experiments with DNA and cells.

2.7.1 Fetal Bovine Serum

Fetal Bovine Serum (FBS) is used as a substitute that accounts for the environment of blood in the body. It is mainly composed of bovine albumin, proteins, insulin, cortisol, hormones and ions of sodium, potassium, calcium and most importantly phosphate. It is the closest available substitute for studying the behaviour of nanoparticles during their transport to the site of tumour. The nanoparticle solutions were exposed to the serum and their evolution was studied at 37°C, to mimic the body temperature. UV-Visible spectroscopy was a convenient method to follow the changes and kinetic studies were performed in the 300-1200 nm wavelength range. Each solution was studied for 15 hours in the medium. It is assumed that within this time the nanoparticles would be assimilated into the cancer cells. In the most ideal case, the properties of cyanosol should remain unchanged over the first few hours of introduction into the body. Results of the experiment are displayed in Figure 56 and changes observed in the intensity of each peak over time is specified.

The iron platinum cyanosol underwent minimal change over the course of 15 hours in FBS medium. There are 3 significant bands :

- at 772 nm contribution of Prussian blue pairs (Fe^{II}-CN-Fe^{III}) which is at much lower energy due to the effect of Pt^{II} in the vicinity, as reported with Mn^{II}
- at 410 nm due to LMCT of some Fe^{III}-CN moeties due to a tiny amount of ferrocyanide

oxidation to ferricyanide

- at 305 nm intense band related to Fe^{II}-CN-Pt^{II} pairs of the cyanosol.

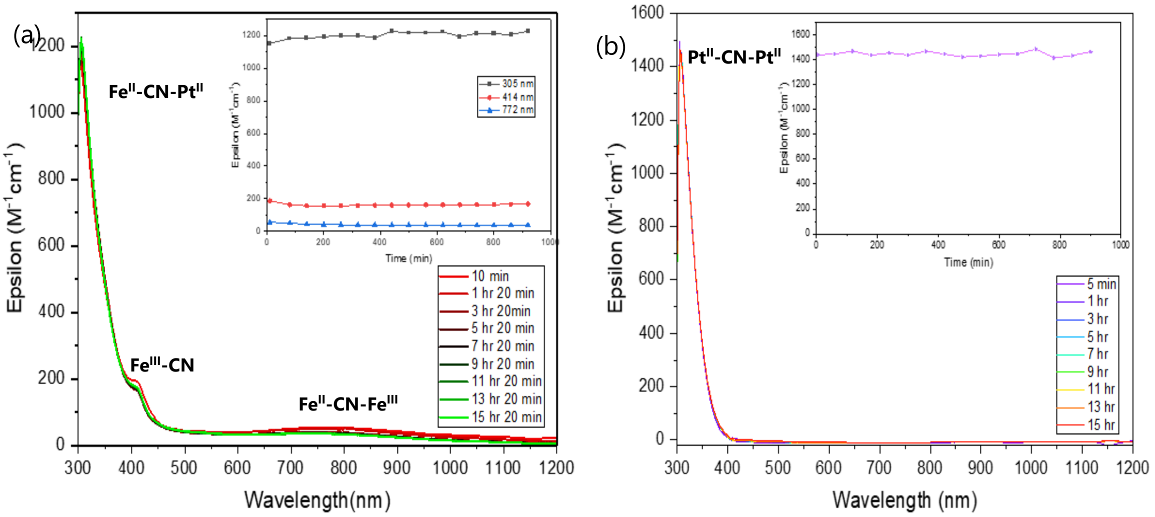

Figure 54. (a)Study of FePt cyanosol stability (b) PtPt cyanosol stability in FBS at 37°C in 15 hrs. Inset- Plot of evolution of different peaks with time.

It is well established that phosphate ions have a special affinity towards ferric ions. The PO_4^{3-} present in FBS attack the Fe^{III} ion containing pairs and reduce their numbers causing a slight decline in the intensity of the peaks at 414 and 772 nm. This phenomenon is also commonly observed in Prussian Blue -FBS experiments. However, the FePt characteristic peak around 305 nm does not undergo any deterioration over the course of 15 hours at 37°C.

The PtPt cyanosol has only one major peak around 300 nm which corresponds to Pt^{II}-CN-Pt^{II} charge transfer band. The experimental results indicate that the composition of this nanoparticle does not change in biological media (Figure 56 b). The peak remains almost constant even after 15 hours of exposure to the serum. These experiments provided an indication that these nanoparticles would remain unaffected and stable during its transport within the human body. The gold platinum cyanosol has intense bands between 300 and 415 nm. The impression of hypsochromic shift is indeed related to the saturation of the band around 350 nm. A decrease in intensity upon increasing incubation time in the serum at 37°C is observed, although it is very slight. The much larger size of these nano-objects may be less stable in the presence of proteins over long times, and we attributed this decrease to a slight deposition.

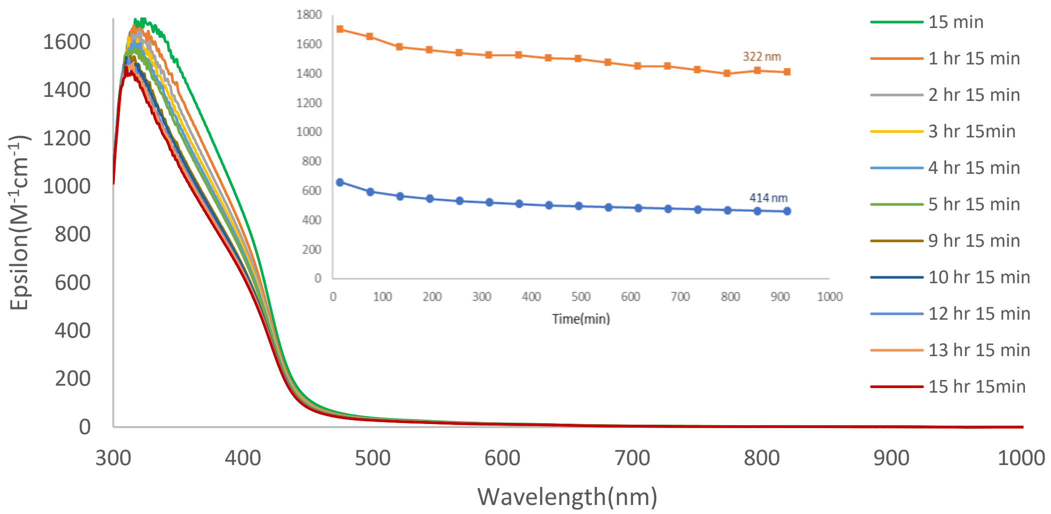

Figure 55. Result of Au-Pt stability in FBS study. Inset: evolution of major peaks with time.

2.7.2 Artificial Lysosomal Fluid

Nanoparticle-cell interactions have to be studied prior to their use in biomedical applications. It is a known fact that when NPs are taken up by the cells, they get localised in lysosomes. These organelles contain hydrolytic enzymes that are capable of digesting biomolecules and foreign materials. Hence, if the synthesised cyanosols can survive the lysosomal fluid they could remain stable inside cells in the body. The environment of lysosome can be mimicked chemically by using Artificial Lysosomal Fluid (ALF). ALF is an acidic solution containing many chelating and reducing agents and was prepared in the lab using citric acid, sodium hydroxide and various proportions of different chloride, sulphate, tartarate, lactate and pyruvate salts. Each of the cyanosol solutions were exposed to ALF and monitored for 6 hours at 37°C. The evolution of their signals with time is demonstrated in Figure 58.

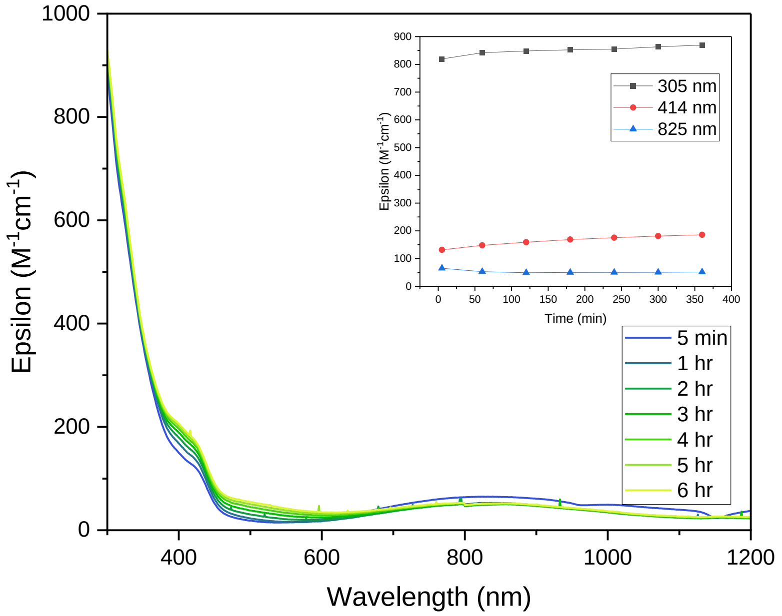

Figure 56. Evolution of major peaks of Fe-Pt in the presence of Artificial Lysosomal Fluid

The charge transfer band of FePt cyanosol at 305nm remains unchanged over this duration. This is an indication that the Fe-CN-Pt composition of the nanoparticle does not undergo any change in the acidic ALF. The peak at 414 nm displays a minor increase in intensity suggesting a slight oxidation of Fe^{II} to Fe^{III} with time. The intensity of Fe^{II}-CN-Fe^{III} peak (825 nm) decreases to the same extent due to the same reason. The PtPt cyanosol remained extremely stable in ALF showed no evolution with time. The signal saturates in the UV region of 240-300 nm. But the evaluation at 316 nm proved that there was very minimal change over 6 hours. Gold platinum cyanosol also gave similar results (plots in annex 6.2.5). There was no decay in the characteristic band indicating that these nanoparticles remain stable even in this highly acidic medium. Therefore, it can be asserted that all three novel, coordination nanoparticles of Fe-Pt, Pt-Pt and Au-Pt do not experience any significant damage in the lysosomal fluid. In conclusion, the cyanosols synthesized using a green process in water did not suffer any major change or decomposition in the physiological medium and could be used for further biological tests.

2.8 IRRADIATION EXPERIMENTS

The nanoparticles were synthesised for use as enhancers for radiation therapy, so the next step was check if they remain intact when irradiated with high energy γ-rays. The experiment was conducted in collaboration with Prof. Hynd Remita at Institut Chimie Physique (ICP), Orsay. The Cobalt-60 gamma source at ICP was utilised as the radiation source. As discussed in chapter 1, the idea behind using high-Z metallic nanoparticles as radioenhancers is to increase the amount of radicals formed upon radiation. These generated reactive oxygen species (ROS) can cause damages to the DNA of diseased tumour cells which could lead to their death and elimination. So it is important that the nanoparticles used for such processes remain intact and maximize the amount of radicals formed upon irradiation with high energy beams. The formation of radicals could be detected in an indirect manner using one of the precursors: potassium ferrocyanide. Spectral study of radiated ferrocyanide solution shows an LMCT band of ferricyanide appearing around 400 nm. This oxidation of Fe^{II} into Fe^{III} is triggered by the ROS generated upon water radiolysis. So control experiments were done simultaneously using all precursor solutions ($K_4[Fe(CN)_6]$, $K_2[Pt(CN)_4]$ and $K[Au(CN)_2]$) and the effect of the presence of PVP was investigated. Cyanosol and control solutions (2.5mM) were first degassed with N_2O and irradiated for 1 hour under the dose rate of 4kGy/hour. UV-Visible spectroscopy was employed to study the changes before and after radiation.

Similar experiments were performed during the doctoral thesis of Dr.Fetiveau. The nanoparticles synthesized involved coating with dextran and hence the control experiments involved studying the precursor in presence of this polymer. As demonstrated in Fig.59 (a) an LMCT band appears on irradiation of Fe^{II} solution, but the band vanishes and no ferricyanide is produced when dextran is present in the sample. This indicated that the radicals generated during the process were scavenged by the dextran. It was an unfortunate result and this is one of the main reasons we resorted to evaluating other polymer coatings to make the nanoparticles more biocompatible. While maintaining comparable conditions, a mixture of precursors with and without PVP were irradiated for 1 hour and the obtained results are described in Figure 59 (b). It can be clearly seen that presence of PVP yields the exact same signal in the visible region as the control solution. Sufficient ferricyanide (Fe^{III}) is formed due to the radicals and the PVP present in the solution does not hinder this oxidation process. Thus, the problem of radical scavenging could be rectified and nanoparticles coated with PVP could be effectively used as radioenhancers.

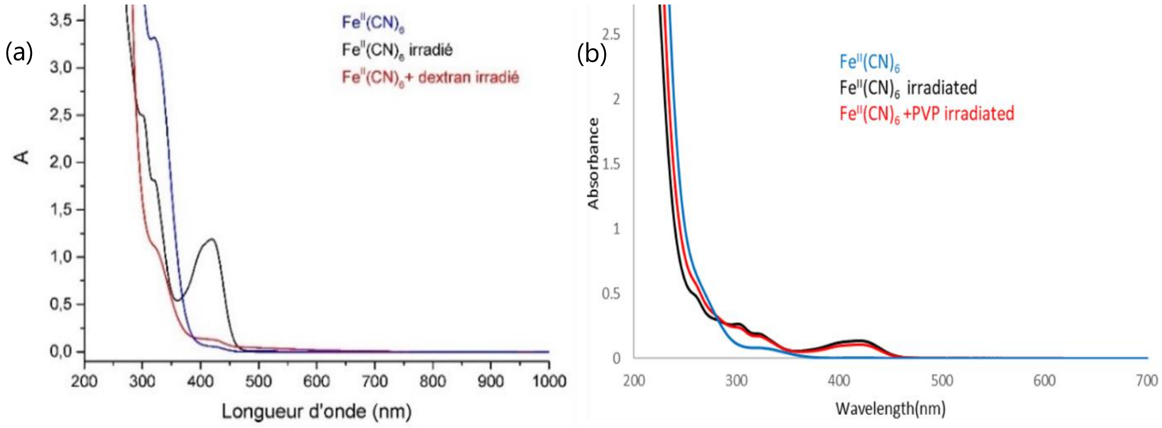

Figure 57. Spectra denoting changes in solution upon irradiation of ferrocyanide precursor with (a) dextran polymer and (b) PVP

Once it was determined that the polymer coating would not cause issues with the radical scavenging, the next step was to verify if the Pt containing nanoparticles would remain intact upon radiation exposure. UV-Visible spectra of nanoparticle solutions before and after radiation revealed that no significant changes occurred in FePt and PtPt cyanosols. However, in the case of AuPt cyanosol, a band around 540 nm appeared post irradiation (Figure 60). This is due to surface plasmon resonance in pure gold nanoparticles. They could be formed by reduction of some Au^{I} from the nanorods to Au^{0} due to the applied gamma radiation of 4000 Gy. TEM and DLS analysis were also used to verify the results. The size of all nanoparticles remained almost the same before and after radiation. TEM images revealed that irradiated AuPt cyanosol contained 2nm spheres along with approximately 30 nm nanorods. It has to be noted that in medical applications, heavy dose of 4000Gy would never be applied. Therefore, our cyanosols would not change in composition and remain stable during the course of radiation treatment.

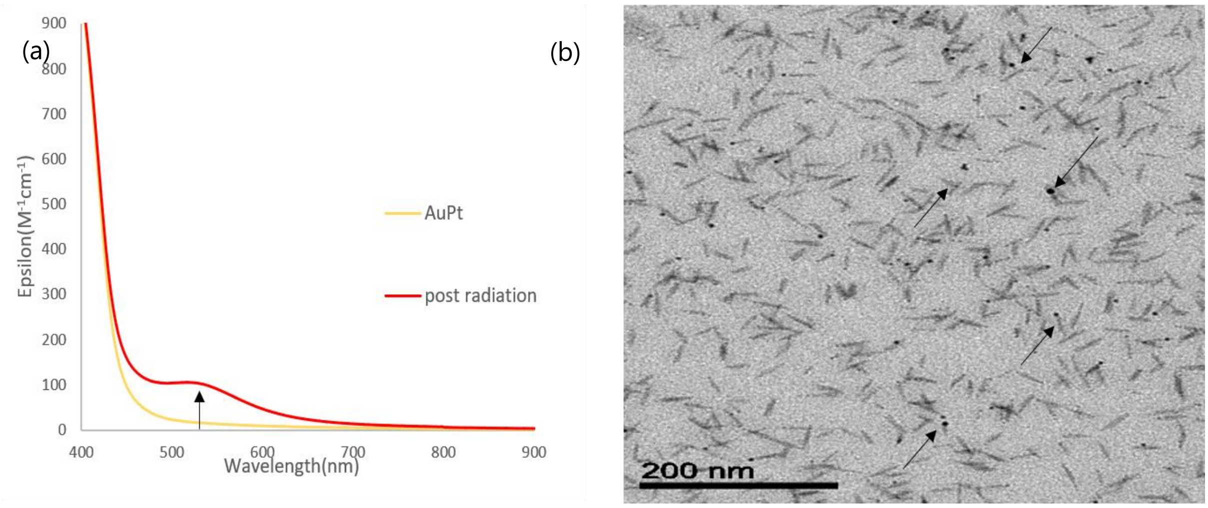

Figure 58. Effect of radiation on AuPt cyanosol observed via (a) UV-Vis spectra and (b) TEM analysis. SPR band indicates generation of pure Au nps, verified by TEM (arrows).

2.9 EVALUATION OF THERAPEUTIC ACTIVITY

The nanoparticles discussed in this chapter were developed with high-Z metals for application in radiation treatment of tumours. It is known that DNA molecules are critical structures responsible for proliferating the overall population of diseased cells and ionizing radiation can induce many changes within the nucleotides. A first indication of the therapeutic efficiency of these radioenhancers could be obtained by studying its effect on similar biomolecules. Plasmids are commonly used for such experiments. Bollivar and Rodrigues pBR322 is a double stranded circular plasmid containing more than 4000 base pairs. When the strands that make up the DNA structure are broken by radiation, cell death is induced. Ideally the presence of a high-Z enhancer amplifies the damaging effect, leading to single and double strand breaks in the plasmid (chapter 1, section 1.3). This could be quantified experimentally and is discussed in this section. Another important factor pertaining to use of nanoparticles for biomedical applications is their safety. In order to be used as therapeutic agents the additives need to be non-toxic to the healthy cells of the body. Cytotoxicity studies were also performed using the synthesized cyanosols. The experiments were performed at Institute of Molecular Sciences, Orsay (ISMO) under the guidance of Erika Porcel and Sandrine Lacombe. The protocol was developed by their Nanomedicine and Hadrontherapy team and involves multiple steps which are described in the next section.

2.9.1 Radiation response of cyanosols

2.9.1.1 Sample preparation

The ultra-filtered and washed nanoparticle colloidal solutions were diluted to a total metal concentration of 4×10^{-5}M before conducting the experiments. The nanoparticles had to be combined with plasmid prior to irradiation. Plasmid pBR322 and Tris-EDTA (TE) buffer was used for this purpose. The specific amounts of each additive are tabulated in annex 6.2.6. The mixture was incubated for 1 hour to ensure binding of nanoparticles to the plasmid. Each solution was split into 6 aliquots of 20µL to be irradiated with different doses of radiation. The experiment was performed using the Cobalt-60 gamma source in ICP, University Paris-Saclay. The energy of radiation is 1.25 MeV and dose rate supplied to the solutions was 3.96 Gy/min. Depending on the duration of radiation, dose supplied to each aliquot of NP+plasmid solution would be different. This was done so as to follow the trend of DNA damage with the amount of radiation (0-160 Gy).

2.9.1.2 Gel Electrophoresis

Two 14 well gels were prepared using Agarose D5 in Tris-Acetate EDTA (TAE,1x). The gels were introduced into the electrophoresis tank and covered with TAE solution. Once the irradiation was complete, DNA loading dye (blue R0611) was added to each of the samples. 9 µL of this blue mixture was carefully deposited inside the wells of the gel in increasing order of dose supplied. The gel was placed in a refrigerator at 4°C. Voltage of 80V was applied to the system and ran for three hours. DNA was stained using Ethidium Bromide (EB) solution to make it visible under UV light. The gel was washed with water before transferring it into the Transilluminator. The separated fractions could be visualised by exposing each gel for 3 seconds under UV light and a CCD camera was used to capture the image. It could be observed that the plasmid separated into three bands after migration depending on their size. The supercoiled form (S) is the original form of plasmid and represents the undamaged DNA. It migrates the farthest distance from the wells because it occupies the smallest diameter. When DNA undergoes a single strand break (SSB), the structure is unwound and the relaxed conformation (R) is formed. It occupies a large volume, thereby travelling the slowest upon gel electrophoresis. Its presence is recorded closest to the well. The intermediate band originates from the linear conformation (L), which only arises when a double strand break (DSB) occurs.

Obtaining large amounts of the L form is rare because the lesions need to be well orchestrated for a DSB to occur. These breaks are infrequent but highly lethal and cytotoxic for the cancer cells. The objective of using radioenhancers is to maximize these DSBs, since it is an irreparable type of damage. As shown in Figure 61, increasing the dose of radiation leads to a marked increase in the amount of L and R conformers and with image analysis the yield of SSB and DSBs could be calculated.

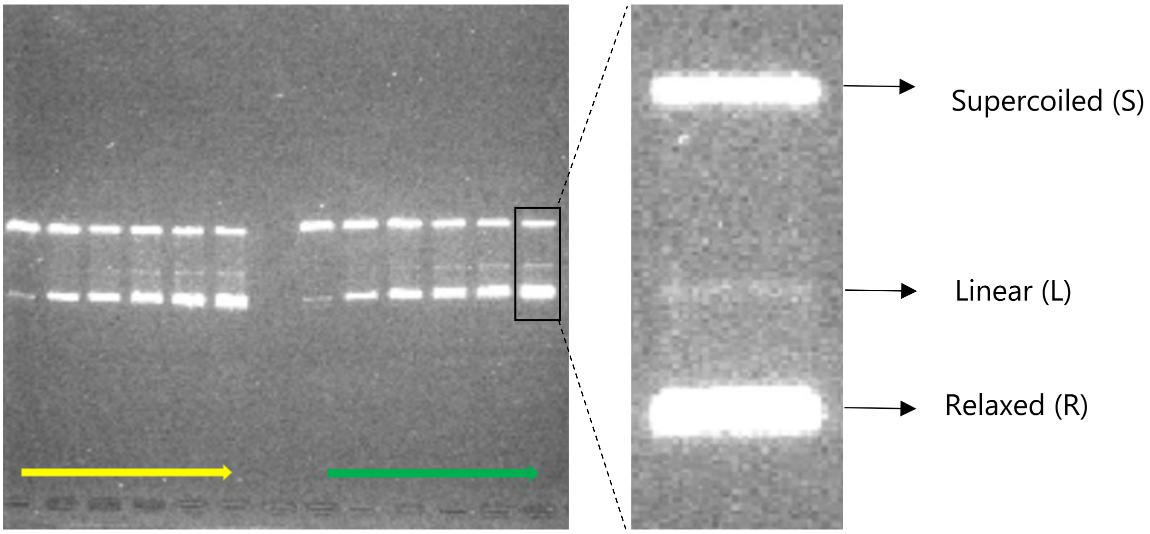

Figure 59. Gel electrophoresis results of 2 sets of nanoparticle+plasmid solutions. Direction of arrow indicates increasing dose of radiation. Zoomed view of irradiated DNA separated into 3 constituents depending on type of strand break

2.9.1.3 Results and discussion

The images obtained were analysed using ImageJ software. The intensity of a band corresponded to the amount of that particular conformation of DNA. Normalisation is done to take into account the fact that Ethidium Bromide binds 1.47 times less with the supercoiled form. Single and double strand breaks could be quantified by using these mathematical formulae:[216]

$$\text{Normalisation Constant (N)} = 1.47 \times S + R + L$$

$$S' = 1.47 \times S/N;\ R' = 1.47 \times R/N;\ L' = 1.47 \times L/\text{total}$$

$$\text{SSB per plasmid} = \ln[(1 - L')/S]$$

$$\text{DSB per plasmid} = L'/1 - L'$$

Control experiments (plasmid without nanoparticles) were also performed simultaneously. It represents radiation treatment in the absence of radioenhancers and the amount of damage that can cause to the cancer cells. Experiments were repeated multiple times to ensure reproducibility of results. It has to be noted that some variations in the environmental conditions and power of Co-60 radiation source occur over time and it can affect the final result. Sensitizing factor (SF) is the quantitative measure of efficiency of nanoparticles for the treatment. It is the ratio of strand breaks per plasmid per Gray induced in the DNA loaded with nanoparticles, compared to the control. SF of each nanoparticle could be calculated from the slope (m) of the curve (linear fitting) in the following manner:

$$SF_{SSB,DSB} = \frac{m(SSB, DSB)_{NP}}{m_{Control}}$$

Results obtained over the span of 3 years indicate that all of the synthesized cyanosols amplify the damage on DNA upon radiation. It was observed that AuPt, FePt and PtPt (5.3 ×10^{-6} M) improve the number of single strand breaks and display an SF_{SSB} value between 1.2 and 1.5. However, double strand breaks are of higher significance as it causes multiple mutations and cell death. The number of lethal nanometric DSBs generated, are presented in Figure 62 as a function of radiation dose.

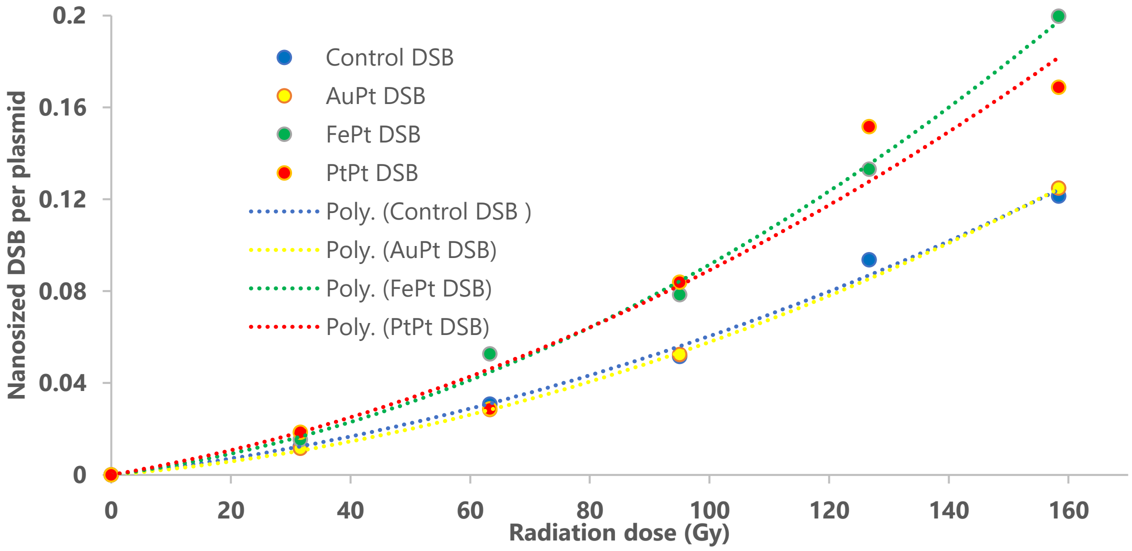

Figure 60. Nanometric double strand breaks induced by γ-radiation in plasmid nanoprobes in presence of FePt (green), PtPt (red) and AuPt (yellow) and their respective fitted curves

Quantifying the DSBs for each cyanosol revealed that AuPt nanoparticles (nps) are not as efficient as FePt and PtPt. However, it has to be noted that the AuPt nps are 6-7 times larger than FePt, and have a different elongated shape. Some studies on gold nanoparticles have shown that both size and shape significantly affect the binding and uptake of particles which drastically change the radiosensitivity.[217,218] Also, since the size of gold-platinum nps are big, the number of atoms available on the surface are much lower as compared to a 1 or 5 nm particle. This could possibly be a cause of lower number of interactions with the radiation, thereby reducing the DSBs. Therefore, changing the experimental conditions or using a higher concentration of AuPt cyanosol might improve the performance of these nanoparticles.

The results also indicate that FePt and PtPt nanoparticles behave quite similarly. It was found that the obtained data aligns better using a polynomial fitting curve (R^2 between 0.96-0.99). This is an indication that the complex damages occur as a result of single ionizing events coupled with secondary effects rising from the presence of radicals. The number of nanosized breaks/plasmid/ Gy was calculated for both cyanosols and is tabulated in the annex 6.2.6, table

12. The sensitizer enhancing ratio (SER) was calculated at each dose to quantify the amplifying effect of FePt and PtPt nps using the equation:

$$SER = DSB_{cyanosol} / DSB_{control}$$

here, $DSB_{control}$ corresponds to the number of nanoscale damages per plasmid upon a certain dose of radiation while $DSB_{cyanosol}$ indicates the same in presence of plasmid loaded with nanoparticles.

Table 3. Sensitizer enhancing ratio (SER) of FePt and PtPt nanoparticles at different radiation doses

Dose (Gy)	**SER FePt**	**SER PtPt**
30	1.34	1.49
65	1.44	1.48
95	1.51	1.48
125	1.55	1.47
160	1.59	1.46

It is interesting to see that with PtPt cyanosol, irrespective of the dose supplied, an almost constant enhancement in double strand breaks in the range of 46-49% is obtained. On the other hand, FePt nanoparticles produce a comparatively smaller effect at low doses (SER 1.34 at 30 Gy) and sequentially intensifies its damage to the DNA with increasing dose of radiation (1.59 at 160 Gy). Therefore, even at a minimal concentration of 5.3×10^{-6} $mol.L^{-1}$, both nanoparticles amplified the effect of radiation on plasmids, indicating that they act as radiation-enhancing agents. These experiments help in understanding the molecular mechanisms behind radiation treatment. The aim is to maximize the amount of damages to the cancerous cells, instigate quick apoptosis and minimize the possibility of regeneration while applying a safe dosage of radiation. Therefore, even the lowest ~30 % amplification in DSBs in the presence of these porous coordination nanoparticles, synthesized in a green and inexpensive manner is very significant.

2.9.2 In-vitro studies

Once it was established that cyanosols are capable of producing a amplified effect on plasmid damage, it was necessary to verify if they are safe and non-toxic for medical applications. The first step was to know the effect of nanoparticles on the cells. The *in-vitro* cytotoxicity studies were performed using FePt and PtPt nanoparticles on fibroblast, HeLa (cervical cancer) and PC3 (prostate cancer) cell lines. The experiments were performed in the biological L2 laboratories of ISMO, Université Paris-Saclay by Farah Savina and Erika Porcel. Two types of studies were done and the results are discussed in this section. The results of AuPt cyanosols are not presented here as they were found to be toxic, maybe due to some release of cyanides. They were also found not to be very efficient as radio-enhancers for double strand breaks.

2.9.2.1 MTT assays

MTT cell-proliferation assay is a colorimetric method to determine cell viability. It utilizes 3-(4,5-dimethylthiazol-2-yl)-2,5-diphenyltetrazolium bromide dye (MTT-yellow colour) that interacts with mitochondrial reductase enzyme from live cells and undergoes conversion to formazan. Formazan has a purple colour and the absorbance could be recorded with a spectrophotometer. The signal intensity depends on the concentration of formazan in the cell, which is directly proportional to the amount of cells alive after incubation with nanoparticles. It is a rapid and convenient technique to determine the toxicity of a certain reagent. The assay involves multiple preparation steps for different solutions (MTT dye, lysis buffer, menadione negative control etc.) that is described in the annex 6.2.7.

Cyanosol solutions were ultra-filtered and washed twice with water before being frozen and converted to a powdered form using lyophilisation. The green (FePt) and white (PtPt) powders obtained were dissolved in 500 µL of sterile water to make a concentrated mother solution (25 mM). Depending on the cell lines used for the experiment, these NP solutions are dispersed in the complete medium containing 10% FBS, 1% P/S (penicillin-streptomycin) or S/S, 1% L-glu and RPMI or DMEM. The cells are plated in 11 columns of a 96-well plate and four concentrations (1 mM, 0.5 mM, 0.25 mM and 0.10 mM) of each cyanosol were studied simultaneously with the control. The remaining column contains the medium for a blank measurement. Optimization of several experimental conditions, including incubation time were necessary. It was determined that a total of 6 hr incubation for nanoparticles with cells, at 37°C gave the best results. One of the columns is reserved for a negative control experiment and menadione solution is added to each of the wells. Once the allotted time ends, the medium is removed from each well and replaced with MTT solution. The well plate is incubated at 37°C for 4 hr to allow the dye to interact with the cells that remain alive after interaction with the nanoparticles. Then, a previously prepared lysis buffer containing acidified isopropanol is added to the MTT containing cell plates. This is done to dissolve the insoluble formazan crystals before analysing the plate under Glomax spectrophotometer. The absorbance at 560 nm is recorded over a period of 9 hrs and the signal of the treated cells are compared against the control samples. After correcting the absorption contribution from the medium, the obtained results are plotted as a function of time (Figure 63) . The time point where the curve appears linear is considered for calculating cytotoxicity.

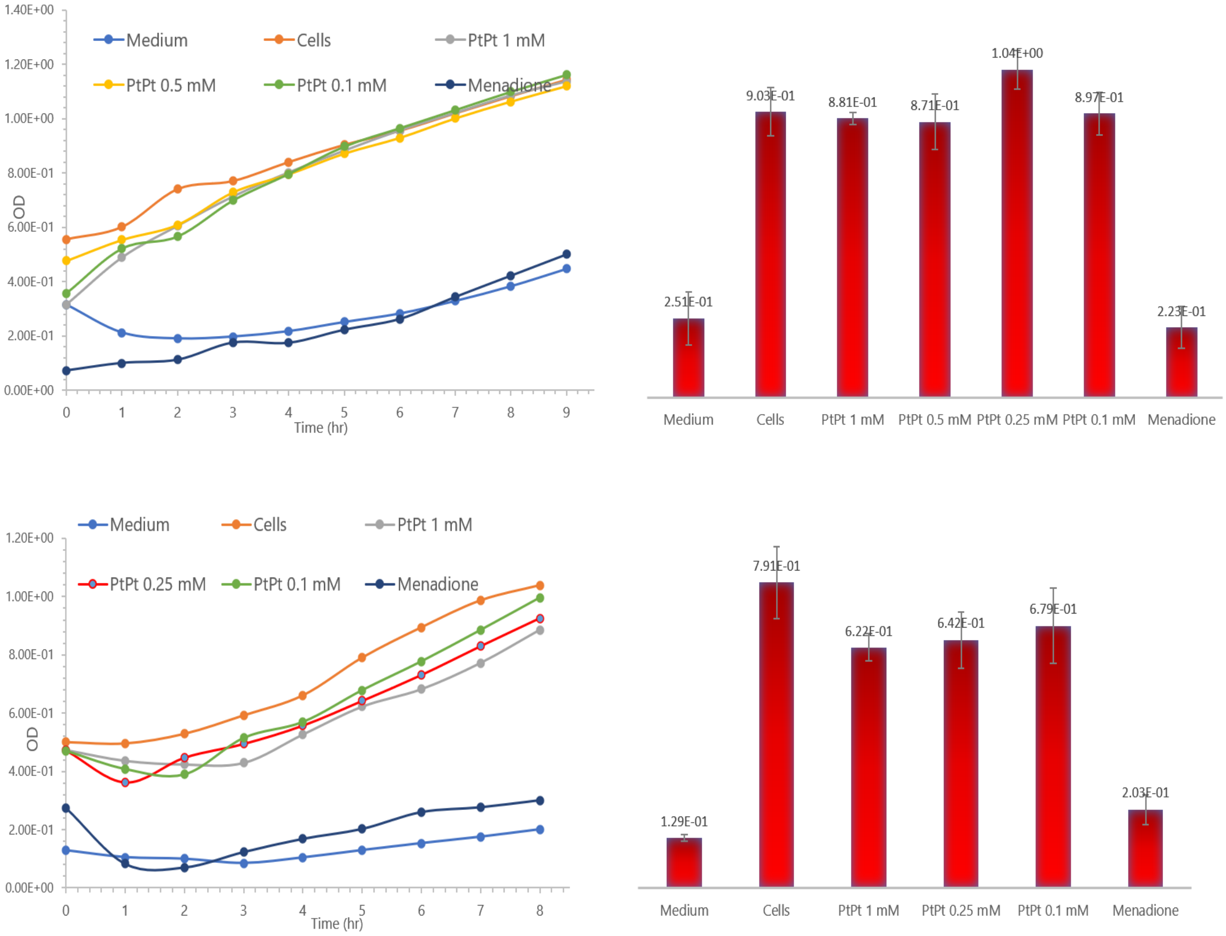

Figure 61. MTT assay results of PtPt nanoparticles on healthy fibroblast cells (top) and prostate cancer cell lines(bottom) and corresponding cytotoxicity plots expanding on the 5 hr time point.

The effect of PtPt cyanosol on two types of cell lines is demonstrated in the figure 63. It can be clearly seen that these Pt containing nanoparticles do not harm the healthy, primary fibroblast cells, as 97.5% cells survive even at the highest concentration of 1 mM. Its interaction with prostate cancer cells appear more toxic as the cell survival falls to 78% at the same concentration. The values obtained at each concentration for both cyanosols is reported in the table 13, annex 6.2.7.

Since the final result of this assay relies strongly on the absorption values ($A_{560\ nm}$), there were some complications to gather reliable data for iron-platinum cyanosol. This is because the coloured FePt solution also absorbs in the same region and leads to an over-estimation of cell survival especially at the highest concentration. Various experiments with FePt controls were performed to rectify this issue but the final results were not consistent. Other limitations to the MTT assay have also been reported, for example a decrease in the D-glucose or NADPH in the culture medium could decrease the formazan production from the dye leading to lower OD values even if the added NP is non-toxic.[219] On the other hand, cells undergoing apoptosis could reduce MTT in the early stages as the mitochondria still remains intact. This assay indicated that PtPt is primarily non-toxic but to obtain better and precise results for each cyanosol, clonogenic experiments were conducted.

2.9.2.2 Clonogenic Assay

Clonogenic assay evaluates the ability of cells to divide and proliferate after being introduced to an external factor. It is also called a colony formation assay as it relies on the ability of a single cell to grow into a colony. The number of colonies formed after incubation with nano-agents determine their survival rate, which in turn provides information on its toxicity. The effect of concentrations (0.1-1.0 mM) for each cyanosol was studied. This was done to attain the most optimum concentration for further experiments. It is a multi-step experiment spanning over 2 weeks. Concentrated mother solution with total metal concentration of 25 mM was prepared in the lab by ultra-filtration. They were dispersed into the required physiological medium (DMEM or RPMI with 10% FBS and 1% P/S). Depending on the number of samples to be analysed, cells were prepared in 6-well plates (seeded ~160,000 cells per well). They were incubated with different concentrations of FePt and PtPt nanoparticles for a 6 hr duration. Then the medium containing nanoparticles are removed and washed with PBS. After trypsinization, the cells are transferred into petri-dishes (~400 cells per dish, 3 dishes per concentration). They are incubated at 37°C under 5% CO_2 for 14 days. The cells that survive after exposure to NPs would divide several times and form colonies. Control samples (no cyanosol) are also prepared simultaneously. At the end of incubation time, the cells are killed using methanol and stained with methylene blue. The cleaning and staining process is performed carefully under a fume-hood. Once the washing is complete, stained colonies are clearly visible. Each petri-dish is then manually counted to determine the cell viability. The fraction of cells alive in presence of nanoparticles with respect to the control gave an estimate of toxicity of our samples. Each measurement was triplicated to obtain an average value within a margin of error. The experiments were repeated multiple times with different cell lines to ensure reproducibility.

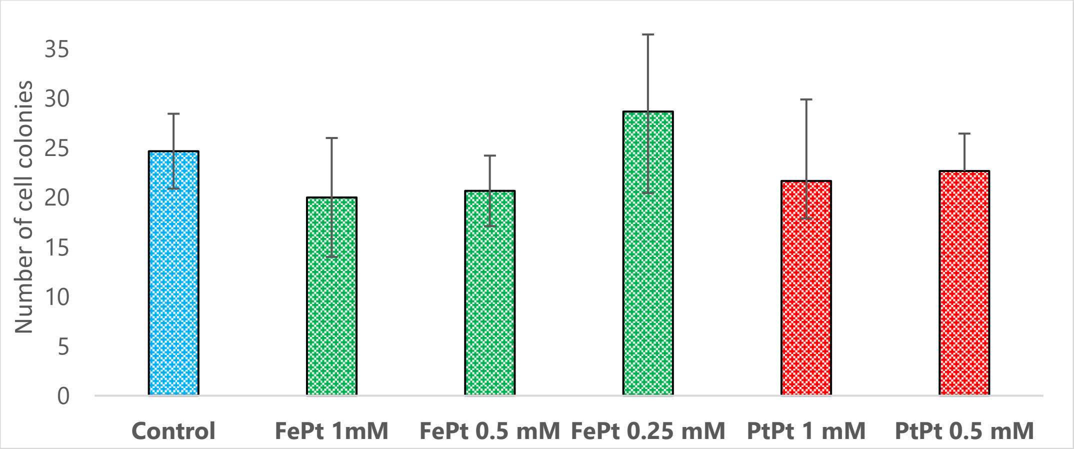

Figure 62. Results of PC3 cells clonogenic assay.

Some of the results were inconclusive, for example a study done using PC3 cells (results: Fig 64). Although the margin of error is high, it could be seen that FePt (0.25 mM) and PtPt (0.50 mM) are non-toxic, as the number of cells that survive in these conditions are comparable to that of the control. However, these results cannot be used as this set of experiments displayed an extremely low plating efficiency. Instead of the 25% cell plating expected for PC3 cells, only 6% of the seeded cells were attached to the petri dish surface, even in the control sample. This is a clear indication that small differences in the environmental/ experimental conditions (here new batch of serum used) can drastically affect the final result.

Results of *in-vitro* studies performed with Fibroblast and HeLa cells displayed a clear trend of toxicity with increasing total metal concentration in the nanoparticles. The primary fibroblasts are biologically relevant tools for measuring toxicity of nanoparticles towards healthy cells, while HeLa can provide an indication of their behaviour towards cancerous cells. It has to be noted that fibroblasts are much more sensitive cells as compared to HeLa and therefore the expected survival percentage is slightly lower in their case. According to the international standard for biological evaluation of medical devices, a sample is considered non-cytotoxic when even the highest concentration provides 70% cell-survival.[220] The fibroblast cell viability is close to 80% at the highest [metal] of 1×10^{-3} M for both nanoparticles indicating their safety for medical applications. HeLa cells appear more sensitive to the presence of nanoparticles as they reach the same limit at 0.5×10^{-3} M concentration. So, both FePt and PtPt nanoparticles are safe for HeLa cells upto a concentration of 0.25 mM. This concentration was used for further experiments for estimating cell survival on exposure to ionizing radiation.

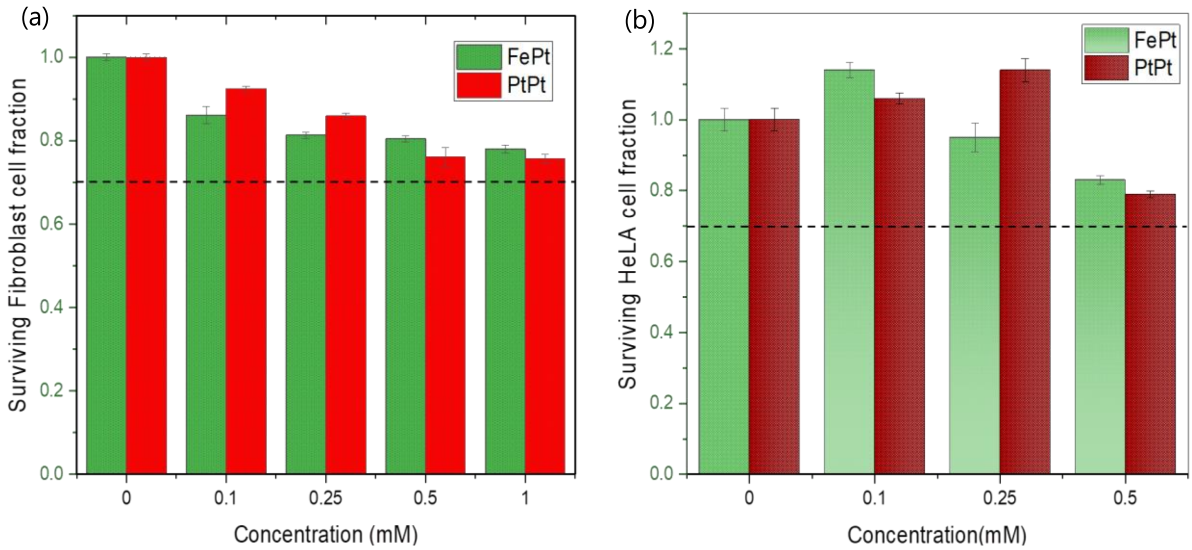

Figure 63. Survival ratio of cells incubated with FePt and PtPt nanoparticles evaluated in (a) Fibroblast and (b) HeLa cell lines

2.9.3 Radiation response of cyanosol on cells

The impact of radiation on cell survival in the presence of prepared cyanosols was also evaluated using a clonogenic assay. HeLa cells were cultured in T25 flasks and maintained at

37°C overnight, in a humidified 95% air-5% CO_2 atmosphere. They were then incubated for 6 hours with enriched culture medium containing FePt and PtPt nps at 0.25 mM total metal concentration. The cells with the nanoparticles, as well as the control containing an equivalent amount of water were irradiated using ^{137}Cs-radiation source, Institute Curie at room temperature. The dose supplied ranges between 0 and 7.5 Gy. After the exposure, the cells were seeded onto petri-dishes to start the standard 14 days culture. The colonies formed were fixed and stained using 0.5% methylene blue 50% (v/v) methanol solution and counted manually. Survival fractions (SF) at each dose were calculated and the data obtained was normalized against the corresponding control. Each measurement was performed in triplicate and the average was used to determine the efficiency of the synthesized nanoparticles. The obtained SF results are plotted in Figure 66. The percentage of surviving cells sequentially decreased as a result of radiation, but this decline is significantly amplified in the presence of FePt and PtPt nanoparticles.

The colony count data was fit using a linear-quadratic model (LQM) on a logarithmic scale (SF vs dose) using equation:

$$SF(D) = e^{-(\alpha D+\beta D^2)}$$

here D corresponds to dose supplied, while parameters α and β describe the cell's radiosensitivity. α represent directly lethal damage whereas β term corresponds to additive sub-lethal lesions, ultimately causing cell death[221] and the values obtained are reported in Table 4.

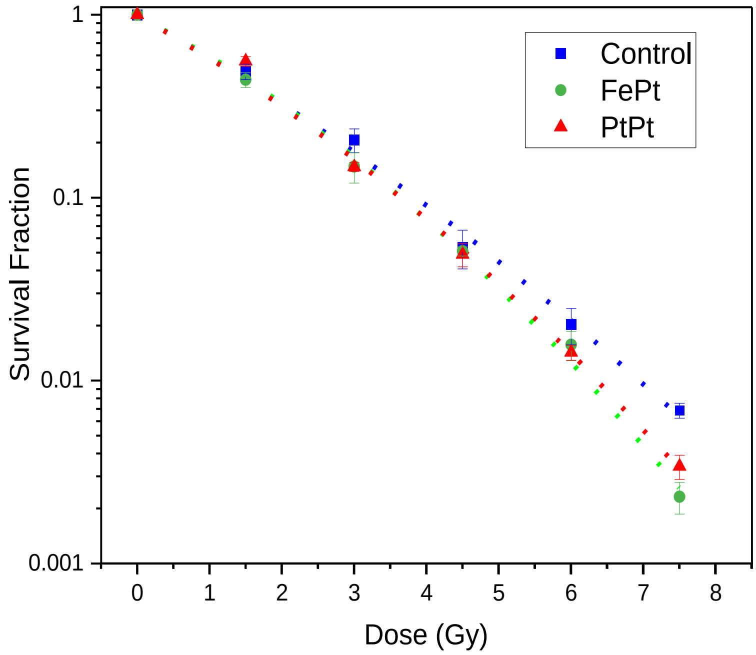

Figure 64. Survival fraction of HeLa cells with 0.25 mM nps : FePt and PtPt compared to the control on increasing dose of radiation. The fit of data obtained using LQM (dotted lines)

Table 4. Values of α and β obtained through the fitting curve for cyanosols and control experiment in HeLa cells in the presence of radiation.

Sample	α (Gy^{-1})	β (Gy^{-2})	α /β (Gy)
Control	0.515 ± 0.050	0.021 ± 0.007	24.30 ± 9.44
FePt	0.464 ±0.050	0.044 ± 0.008	10.57 ± 2.21
PtPt	0.500 ±0.049	0.034 ±0.007	14.38 ± 3.56

The α /β provides the dose (Gy) at which 50% of the damages caused to the cells are due to directly lethal effect of radiation while the rest are a result of additive damages, triggering a lethal consequence. The alpha values are quite similar for the control and cyanosol containing cells, indicating that the number of directly lethal damages produced as an effect of radiation does not vary. However, the β shifts from 2.1×10^{-2} Gy^{-2} for the control to significantly high values for PtPt (3.4×10^{-2} Gy^{-2}). In case of FePt nanoparticles the β is more than double the control at 4.4×10^{-2} Gy^{-2}. Once the α and β values were determined, SF values at each dose point could be accurately calculated. The effectiveness of these nanoparticles as radio-enhancing agents could be quantified by means of SER, calculated using equation 2:

$$SER = SF_{control,\ fit} / SF_{cyanosol,\ fit} \qquad (2)$$

here, $SF_{control}$ and $SF_{cyanosol}$ correspond to the respective survival fractions from the fitted curve at the same dose of radiation.

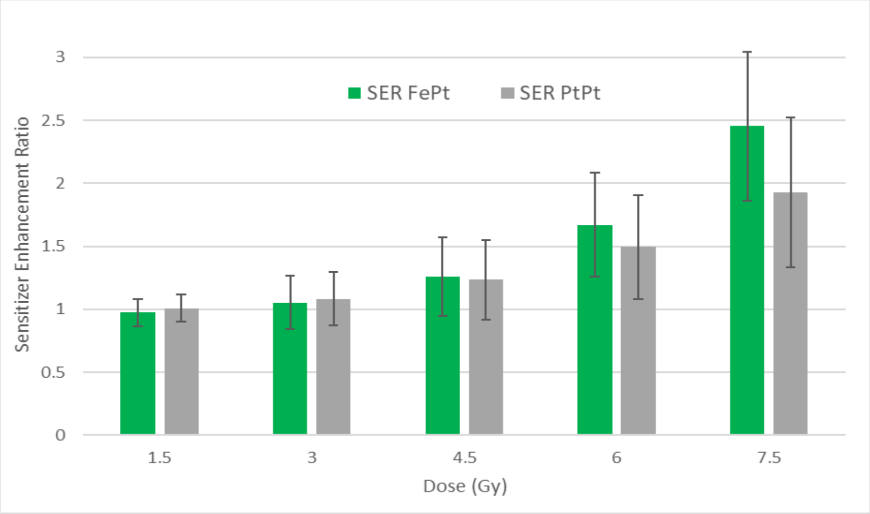

Figure 65. SER calculated for FePt and PtPt nanoparticles at each radiation dose.

Results suggest that a dose of 3 Gy is essential to observe the enhancement effect in presence of these nanoparticles. At 4.5 Gy, both nanoparticles improve the cell death by approximately

20 % (SER 1.25). As the dose supplied to the sample increases, high SERs of 1.92 for PtPt and 2.45 for FePt could be observed. It indicates that 2.5×10^{-4} $mol.L^{-1}$ concentration of the cyanosols is capable of amplifying the cell death by 48 % (PtPt) and 59 % (FePt). This is a very positive result as the cyanosols could be synthesized in a green and surfactant-free manner in pure water without the use of expensive reagents or experimental conditions and they are still able to perform as excellent radio-enhancers.

2.10 CONCLUSION AND PERSPECTIVES

This chapter summarizes the work carried out during this doctoral project on developing new Prussian Blue analogue nanoparticles with a heavy metal. The focus was on achieving stable, self-standing particles in water using a green synthetic process. Various methods were employed and three novel, well-individualized porous nanoparticles composed of iron-platinum, platinum-platinum and gold-platinum were obtained. Synthesis and complete characterization of these negatively charged PBA is reported above. They possess interesting nanostructures. Original platinum decorated AuCN nanorods could be obtained without the use of harsh experimental conditions. High concentrations of the ultra-small FePt (5 nm) and PtPt (1 nm) coordination nanoparticles were synthesized in standard laboratory conditions in pure water. These newly synthesized "cyanosols" were post-coated with polyvinylpyrrolidone, a biocompatible polymer. Experiments were conducted to evaluate the stability of these nanoparticles in physiological media like FBS and ALF, which yielded positive results. Then, the possible applications were studied. A high magnitude of gamma radiation did not cause any damages to the composition of the nanoparticles indicating that they could be used as enhancing agents for radiation treatment of cancers. Tests conducted on plasmids revealed that these nanoparticles demonstrate a marked increase in the number of lethal double strand breaks which could lead to death of cancerous cells.

The *in vitro* tests revealed that FePt and PtPt nanoparticles were safe for healthy primary fibroblast cells even at high concentrations. In the presence of an ionizing radiation beam, strong cytotoxicity towards cancerous HeLa cells could be observed with the cyanosols. The α and β values obtained suggests that the mechanism of action is different as compared to usual dense metallic nanoparticles used. It can be hypothesized that water molecules coordinated to the surface of the nanoparticle as well the ones constantly diffusing through the porous network are available for conversion to ROS. The Auger electrons generated as a result of high energy radiation on Pt-containing nanoparticles form a higher number of radicals that could be quickly dispersed through the system due to porosity of the nanoparticle. This maybe the cause of markedly high amount of sub-lethal damages that is transformed to a final lethal effect in the cell. The pure Pt coordinated, 1 nm particles amplify cancer cell killing to 48 %, while 5 nm FePt nanoparticles show a 59 % enhancement in cell death at high doses. The possibility that these iron containing nanoparticles are better internalized within the cells is currently being investigated using ICP measurements. A recent work has shown that bi-metallic, dense gold-platinum core shell nps induces higher number of nanosized breaks when compared to pure gold nps.[222] Our results with porous bimetallic iron-platinum nanoparticles line up with this established phenomenon and the combination of two metals maybe the reason for the enhanced activity.

The chemical design of these Prussian Blue-like nps allow for easy modification of the structure through coordination networks. Doping with paramagnetic gadolinium ions could impart strong MRI contrast properties and lead to image-guided treatments. Anti-cancer drugs could be encapsulated to facilitate synergistic chemo-radiotherapy. Importantly, PtPt nanoparticles are photo-luminescent and this opens the door to many new possibilities. Tuning of the emission wavelength with the nature of the coating is expected. Fluorescence lifetime imaging experiments have been planned for the future. The potential of such highly stable coordination network-based nanoparticles will be further developed to obtain multimodal theranostic platforms.

CHAPTER III

3 ASSEMBLIES OF ULTRA-SMALL THERANOSTIC NANOPARTICLES

3.1 INTRODUCTION

Nanoparticles display many interesting and unique behaviours due to their small size and large surface area. These physicochemical parameters lead to them having a wide-range of applications ranging from catalysis, sensors, batteries to imaging and disease treatments. Creating assemblies of such nanoparticles could provide super-structures with many attractive properties. The design and construction of assemblies by controlling the size, shape and morphology is a challenging topic because conventional nanoparticles cannot completely fulfil all the requirements for certain applications.[182] The assemblies have properties that differ from the bulk as well as individual particles. Various studies have shown that the novel NP ensembles created, enhance the existing optical, electronic, magnetic and mechanical properties, while sometimes introducing dynamic new capabilities. These previously unknown properties usually emerge from the strong coupling between assembled nanoparticles.[182] This doctoral project is focussed on bio-medical applications of nanoparticles and their assemblies. Although some groups have worked in this direction, the focus has majorly been on gold nanoparticles. By aggregating Au nps or densely packing them into vesicles, the assembled structure show significant improvement in photothermal conversion and enhances the photoacoustic imaging capabilities.[223,224] It is well-established that assemblies can prove highly advantageous for nanomedicine and drug-delivery applications. The increase in size can ensure prolongation of circulation half-time and enhance permeability during delivery to the target site. Nanocapsules (180-500 nm) were fabricated by Zhao et al.[225], involving many polymers and up-down conversion nanoparticles for encapsulating doxorubicin. These capsules show four-fold accumulation within tumours and could undergo NIR-light triggered decomposition into 20 nm particles. These are smart and useful delivery vehicles but their synthesis involves long and multiple complicated steps in organic solvents, under harsh conditions including etching with concentrated NaOH.

A similar work involving Prussian Blue nanoparticles (40 nm) enclosed within a polymer shell was discussed in Chapter 1. Apart from the fact that there is no information available on the fate of the ~ 240 nm PB nanococktail particles, the drug loading percentage was also quite low at 7.2 %.[165] Prussian Blue nanoworm type structures were developed using block ionomers. It self-assembles in organic solvents into cylindrical micelles and were used as precursors to form metal oxide structures.[131] X.Roy et.al also developed hollow PBA nanocontainers using an emulsion-induced method. However, this innovative method to form nanorings (Figure 68), requires a mixture of chlorobenzene, THF and water, and it remains stable in solution only for a few days.[226]

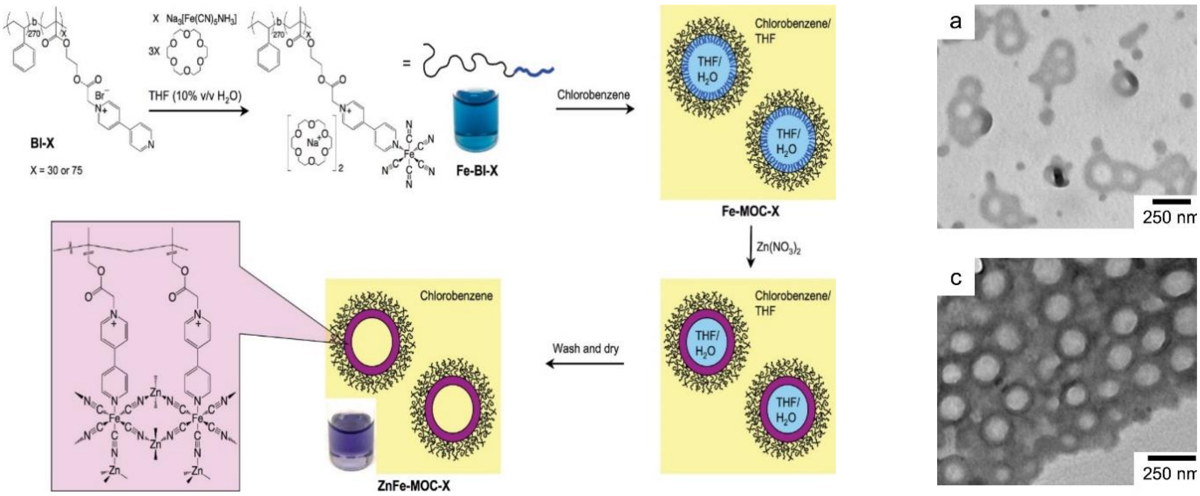

Figure 66. Synthetic approach to soluble block ionomer-PBA capsules through emulsion induced assembly. TEM micrograph of Zn-cross linked Fe-BI-75 and ZnFe-MOC-75 hollow aggregates.7

So far, there is a shortage in the field of nano-assemblies composed of Prussian Blue and their possible therapeutic applications. This chapter summarizes the work done on developing a controlled assembly of ultra-small PB nanoparticles using a green synthetic route. PB is chosen as the area of focus because of its versatile ability to act as photo thermal therapeutic agent, being a FDA approved drug, as well as a contrast agent for magnetic resonance imaging. Large (50-150 nm) aggregates could improve EPR effect, provide better MRI contrast property and increase the surface area available for drug encapsulation. The path followed in this project strictly uses water as the medium and only biocompatible additives that lend favourable properties to these theranostic nanoparticles. Coordination and polymer chemistry lays the foundation on which these novel nanostructures are constructed. Many synthetic routes, using multiple reagents were employed over the course of three years but only the most optimized path, capable of generating controlled assemblies would be discussed in detail. Complete characterization of PB assembly and the ability to diversify the formation route with new chelators and nanoparticles are explored.

3.2 PRUSSIAN BLUE NANO-ASSEMBLIES

3.2.1 Synthetic strategies

Ultra-small nanoparticles of Prussian Blue are synthesised in water using potassium ferrocyanide and ferric nitrate (0.5 mM each), while maintaining the reaction temperature at 2°C. The detailed procedure was discussed in chapter II. Once formed, the nanoparticles are extremely stable in solution. It maintains a hydrodynamic diameter of 5.3- 7.5 nm and has a negative zeta potential around – 25 mV. Since the surface of each individual nanoparticle is highly charged, they tend to remain separated and well-dispersed in solution over long periods of time. Hence, the strong electrostatic repulsions are the basis of their stability. In fact, this is one of the main factors hindering the formation of assemblies, as the particles need to be brought closer with short interparticle interactions, in order to link them together. Polymer assisted PB assembly formation using poly γ-cyclodextrin citrate was investigated.

3.2.1.1 Polymer Cyclodextrin Citrate

Cyclodextrins (CDs) are cyclic oligosaccharides made up of glucose molecules linked together by α-1,4 glycosidic bonds. Depending on the number of glucose subunits (6, 7 or 8) forming the macrocycle, three types: α-, β- and γ-CDs could be formed. They have a hollow cage-like structure with hydrophobic interior cavity and hydrophilic exterior. They are incorporated in many pharmaceutical formulations as the cavity could be used to host specific ions and drug molecules depending on the size. An increase in stability and penetration within the body has been observed while using these macrocyclic rings. The largest cavity diameter of 0.75-0.83 nm is obtained with γ-Cyclodextrin.[227] Citrate is a tricarboxylic acid anion with an alcohol functional group. It is a well-known chelator of metal ions and has a strong affinity for iron. Extensive studies have been conducted to understand the mechanics of ferric-citrate complex formation as they are found in various biological media.[228] Also, the first synthesis of Prussian Blue nanoparticles in aqueous media, involved usage of citrate as a chelator for the Fe^{III} precursor and it proved beneficial as a capping agent. Our collaborators at ISMO, R.Gref et.al had synthesized polymer chains composed of γ-CD linked together with citrate moieties and it was demonstrated that this polymer could enhance drug loading in nano-MOFS, as well as improve their colloidal stability.[229] The citric acid/ CD molar ratio in poly γ-CD-citrate were found to be 4:1 and the CD content in the oligomer is 64 wt.%. The molecular weight of the polymer was 13600 g/mol and the other details are provided in the annex 6.3.1.

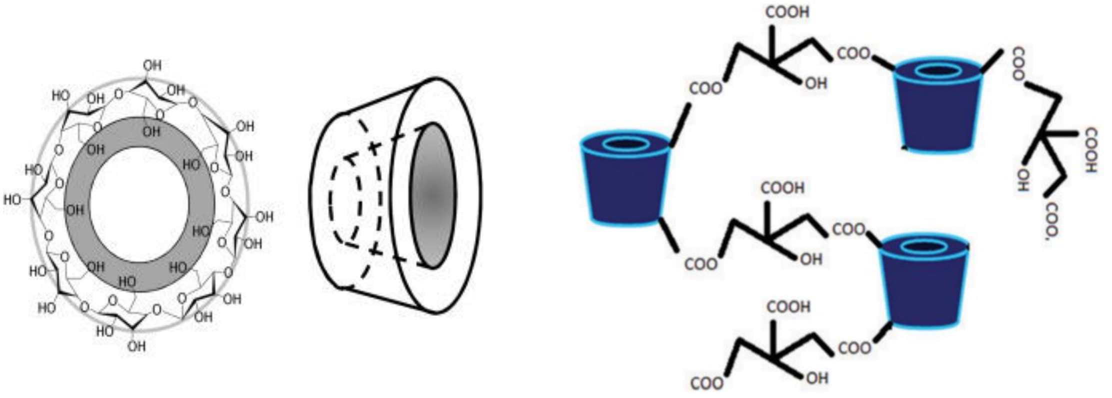

Figure 67. Structure of (a) γ-Cyclodextrin and (b) γ-CD citrate polymer[243]

Poly γ-CD-citrate fulfilled most of the criteria required for forming our targeted assemblies. Since Fe^{III} is present in abundance, it was expected that the citrate chelators could bind to the surface of PB nanoparticles and link them together. The CD cages were chosen to help drug encapsulation, as it has been well described for Dox[192]. The original idea was to interconnect the ultrasmall PB through citrate coordination to Fe^{3+} by playing on the ratios between them.

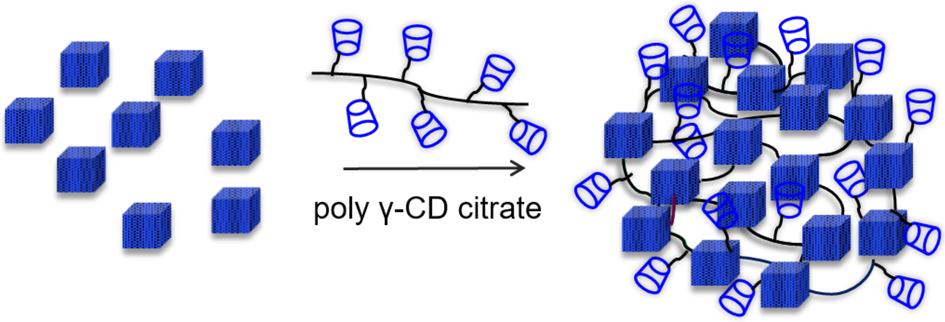

Figure 68. Scheme of PB assembly formation with poly CD-citrate.

Therefore, this water-soluble polymer was utilized and effect of different ratios between the starting precursors (1:0.05 to 1:2) were studied. Various sets of experiments were conducted and reproducibility was monitored. The optimization process revealed that the ratio of 1:1 between PB and γ-CD-citrate polymer was the most reliable for obtaining assemblies. Polymer solution (0.25 mM, M_w 13600 g/mol) was prepared in milli-Q water considering the whole chain would coordinate with the surface of PB nanoparticles. Earlier experiments revealed that the size of individual PB nanoparticles played a major role in determining assembly formation. Therefore, the freshly synthesized PB solution was first ultra-filtered (UF) using MWCO 300kDa tubes to remove any large particles, if present. Almost all of the solution passed through the pores and UV-Vis spectroscopy was used to determine the final concentration of Prussian Blue UF sample.

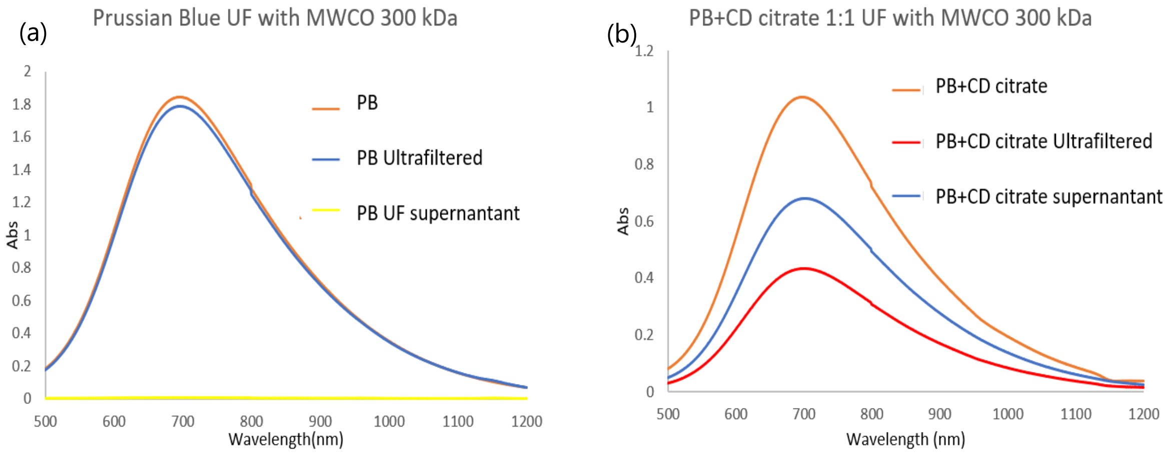

Figure 69. Effect of Ultra-filtration on (a) PB and (b) PB assembled with CD-citrate polymer

Then quick addition of the polymer to PB-UF (0.25 mM) solution was done, and the reaction was run at room temperature for 1 hr under constant stirring. DLS measurements were not helpful in this case, as the major peak lay around 4.7-6.7 nm and a only small percentage (~1%) was detected close to 45 nm. This could be due to the flexibility of the nanostructures. However, ultrafiltration of this polymer mixed sample lead to a separation based on size. From spectroscopic studies, it was clear that 58% of the nanoparticles remain in the supernatant giving an indication that (>10 nm) assemblies had indeed formed, while the rest passed down to the filtrate. Nanoparticle Tracking Analysis (NTA) was also performed on these samples. Since this method is not sensitive to sizes below 50 nm, it over-estimates the size of initial PB nanoparticles (annex 6.3.2). Therefore, it did not provide a true comparison for the samples.

TEM imaging with glow-discharge treated grids were necessary to get a proper idea and the results are displayed in Fig.72. PB with CD citrate (1:1) is composed of assemblies (mainly dimers and trimers of PB) but size distribution indicated that 30-35 % of the solution is made up of sub-10 nm particles. As mentioned above, UF was done to remove these nps. However, TEM micrographs of the supernatant (Fig. 72 b) show that the ultra-small nps are still present in the sample. They roughly take up 23 % of the nanoparticles detected.

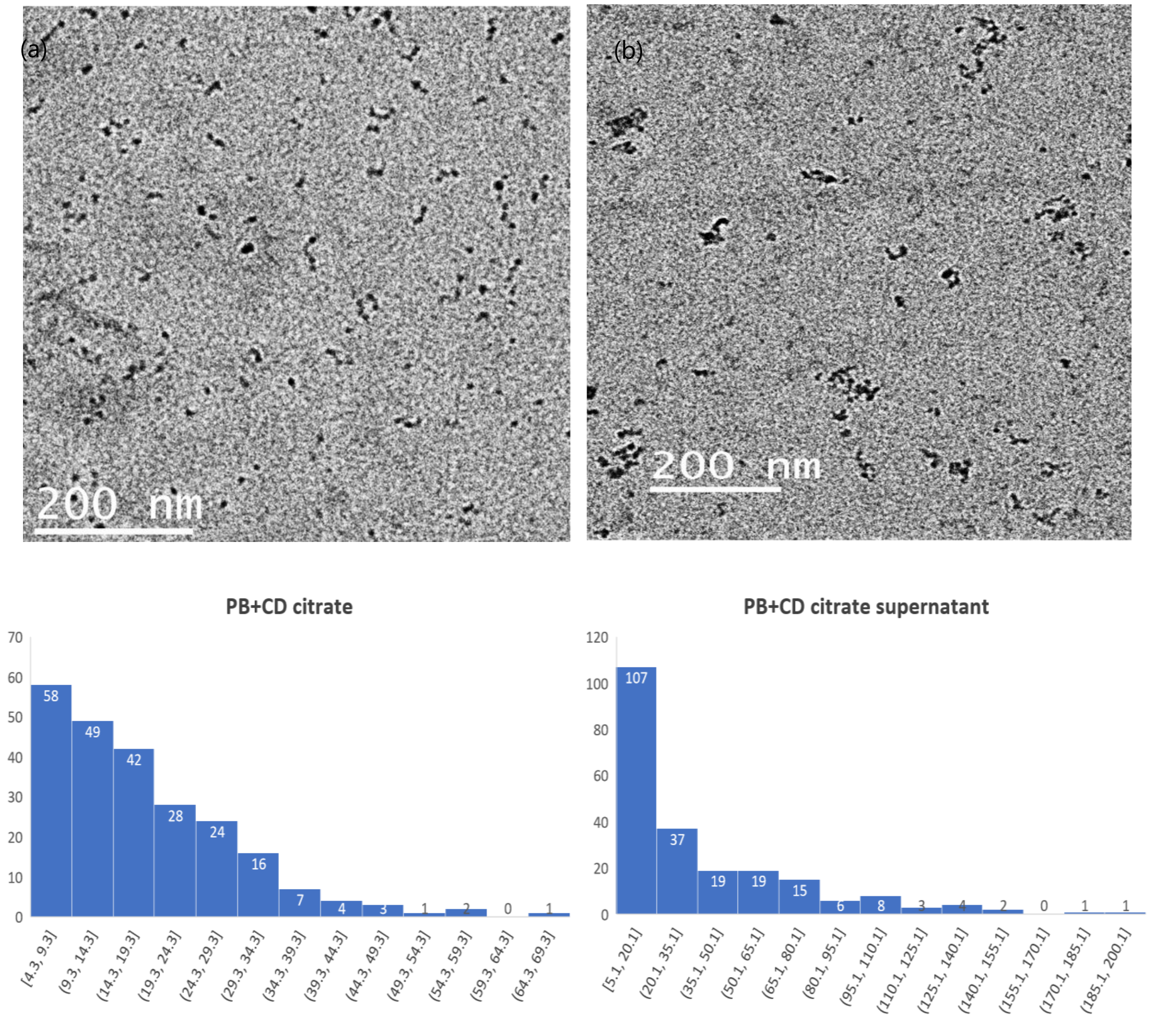

Figure 70.TEM micrograph and corresponding size distribution chart of (a) PB-CD citrate (1:1) and (b) PB-CD citrate (1:1) supernatant after ultrafiltration

As seen with the histogram, the sizes of aggregates formed are not very controlled. Majority lie below 40 nm in size and the aim was to create larger assemblies, with higher hydrodynamic diameter and controlled sizes, to help with tumour permeation and increase the circulation time. Many more experiments were conducted during the first year of my PhD, to further separate the un-bound individual particles, but the results were not conclusive. Analytical ultracentrifugation process was also employed but the move of the person responsible and enforcement of Covid-19 lockdown did not enable completion of the study. These experiments, however provided the first indication that the negatively charged, ultra-small PB could be assembled. It is possible that the steric hindrance of the poly-CD citrate precluded the formation of targeted spherical aggregates and assembles PB in a loose manner. We thus decided to explore alternative routes.

3.2.1.2 Guanidinium chloride attempts

Guanidinium chloride (GdnHCl) is the hydrochloride salt of guanidine. It is an orally administered drug for treatment of muscle weakness and fatigue. Recent work reported that GdnHCl could also be used for treating tumours and preventing the regeneration of cancerous tissues.[230] A dose of 10-35 mg/kg of the compound shows a significant destruction of hydrogen bond formed by polar molecules on cancer cell surface. This inhibits the uptake of DNA by cancer cells and therefore, the cell proliferation is inhibited. This could provide an added advantage to our Prussian Blue systems and hence attempts were made to use guanidinium cations to form assemblies with negatively charged PB.

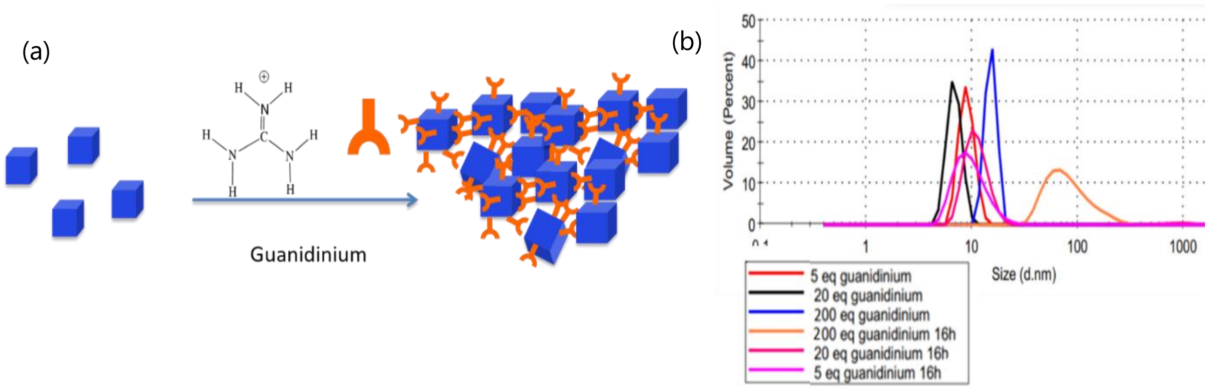

Figure 71. (a) Schematic illustration of PB aggregate formation with GdnHCl. (b) Size evolution of the samples containing varying amounts of Guanidinium.

A stock solution of GdnHCl (0.5 M) was prepared in water and various experiments were performed by changing the reaction conditions. Initial trials involved addition of varying quantities of GdnHCl to a solution of pre-formed Prussian Blue. The idea was to use a combination of H-bonding to the cyanide groups of the PB together with an electrostatic interaction of the cationic guanidinium with negatively charged PB. DLS measurements provided a quick way to probe the formation of assemblies. Starting from 0.2 and adding up to 100 equivalents of guanidinium (with respect to PB) did not cause a change in size of the nanoparticles, which remained around 6.2 nm. As expected, the zeta potential shifts to more positive values upon introduction of guanidine. Better results were obtained by adding GdnHCl solution (50 mM, 5 mL) into the same volume of PB (0.25 mM) under constant stirring for 30 minutes. It led to an increase in the hydrodynamic diameter and the peak appeared between 18-20 nm. Therefore, TEM imaging was done on this most optimized sample containing 200 equivalents of guanidinium, to understand the structure of assemblies formed.

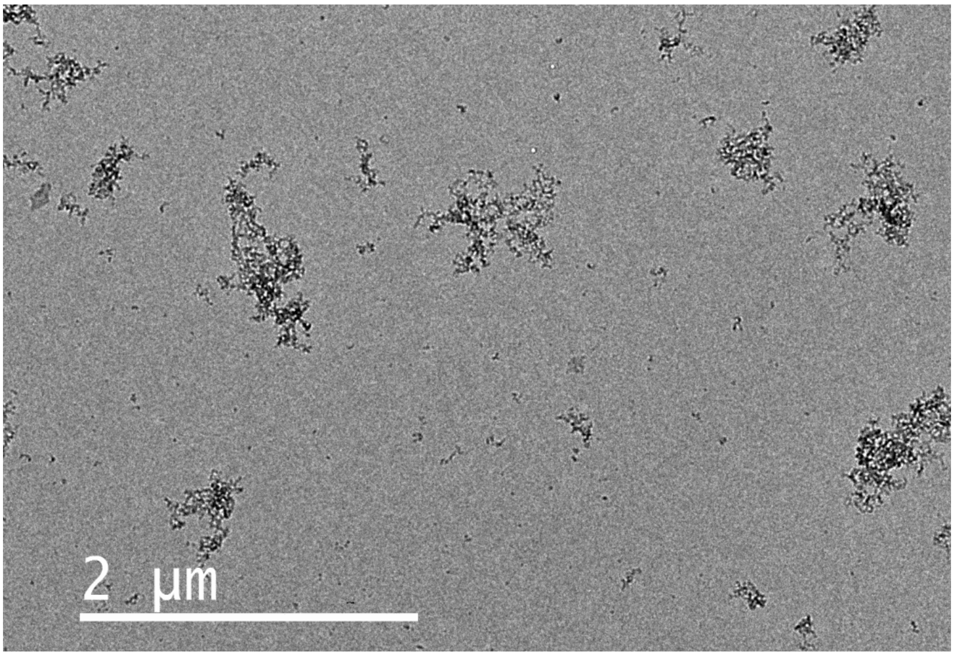

Figure 72. TEM micrograph of PB with 200 eq. guanidinium

The results indicated that aggregates of Prussian Blue had formed, however the size or shape are not controlled. Few single particles could be seen, along with some dimers and trimers of PB. Many huge >500 nm clusters could also be observed in the sample. Evaporation effects are limited as the grid was treated with glow discharge, prior to deposition. Moreover, as seen in Figure 73 (b), the hydrodynamic diameter detected with DLS increased significantly within 16 hrs after synthesis. This quick evolution with time is not ideal for our desired applications. It was realized that unlike spherical gold nanoparticles, manipulating the electrostatic repulsions to obtain controlled assemblies of PB was not so simple. Even if addition of a polymer to block the growth and use of microfluidics could help, other routes to form nano-structures that remain stable over time were necessary.

3.2.1.3 Gallic Acid

Gallic acid (3,4,5-trihydroxybenzoic acid) is a poly-phenol found in tea, gallnuts, fruits and vegetables. It is reported to have anti-oxidant and anti-inflammatory properties, and some *in-vitro* and animal model studies have shown inhibition of carcinogenesis in the presence of gallic acid (GA).[231,232] This organic molecule has an ability to form stable complexes with Fe^{III} via phenolate and carboxylate coordination bonds and many thorough studies have been done to identify the possible molecular structure of the network.[233,234] These properties have been used to synthesize renally-clearable Fe-GA nanoparticles with strong MRI contrast properties in the presence of PVP[101] and bovine serum albumin.[235]

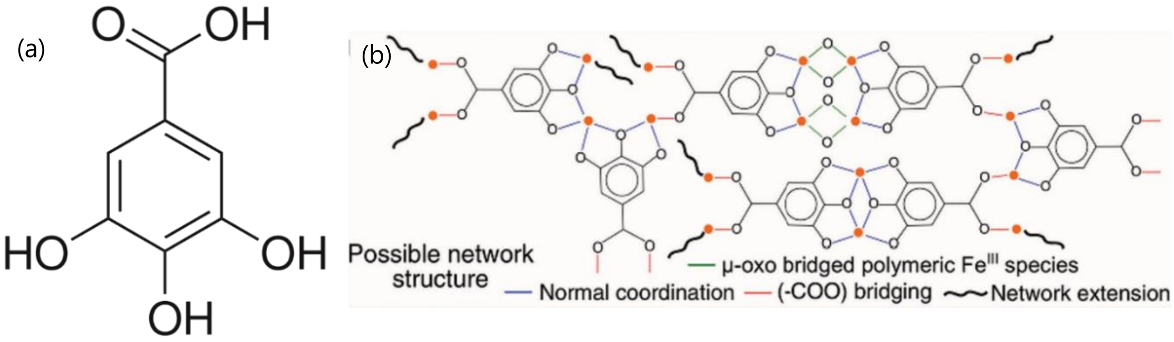

Figure 73. (a) Structure of gallic acid (b) Possible network structure of Fe^{III}*-gallic acid complex in solution*[234]

Caruso et.al demonstrated that surface functionalization of micro- and nanoparticles with polyphenols (tannic acid) could assemble them to form complex superstructures.[236] Polystyrene particles, metal oxides, $NaYF_4$:Yb/Er, Prussian Blue nanoparticles as well as AgCN and ZnO nanowires were organized into 3-D core-satellites, hollow supra-particles and macroscopic hybrid materials. Metal ion interactions with catechol/galloyl functional groups were the basis of formation of these assemblies (Figure 76). It was interesting to note that coordination of Fe^{3+} with tannic acid led to the formation of an iron-phenolic network that aided the modular assembling of these superstructures.

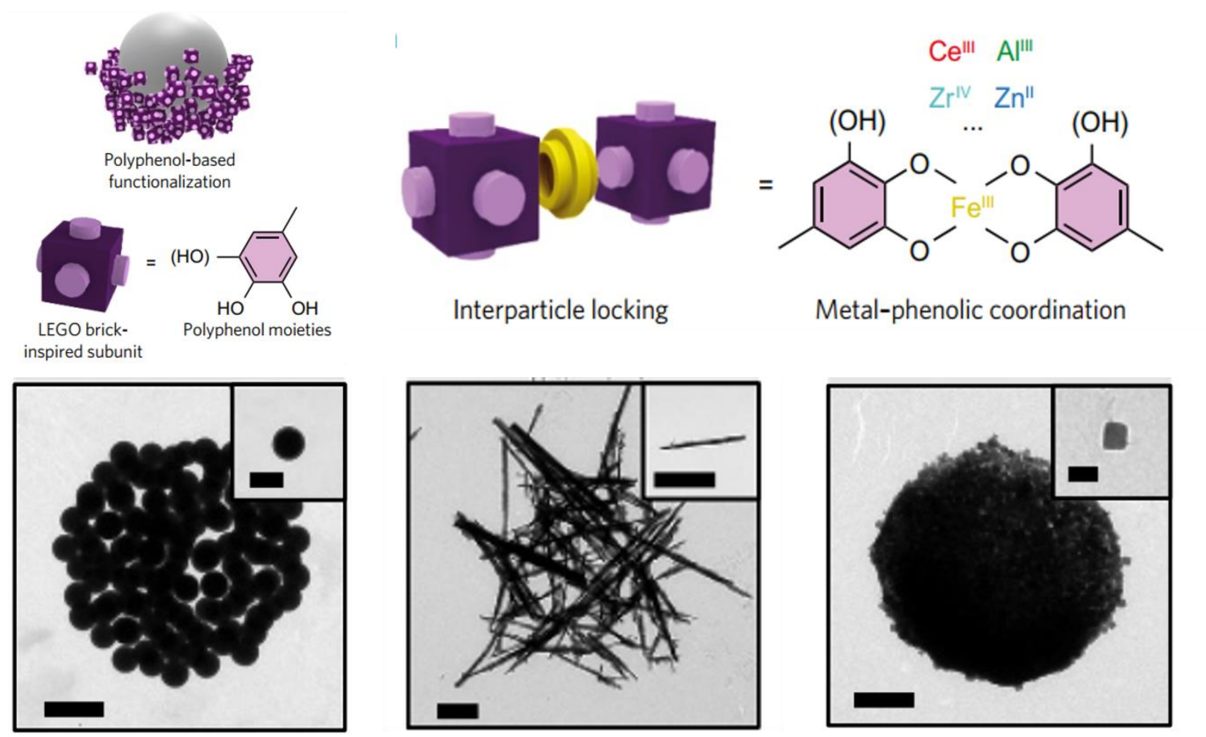

Figure 74. (a) LEGO brick-inspired modularization of building blocks using polyphenol based particle functionalization and linkage through metal ions. TEM images of assembled superstructures of (b)mesoporous SiO_2 nps (c) ZnO nanowires and (d) Prussian Blue nps (scale bars 1 μm)[236]

A recent work by Wang et.al had shown that iron-tannic acid nanoparticles could be synthesized using coordination interaction between phenolic group and Fe^{III} which could be disassembled by using Deferoxamine mesylate (DFO), a clinical drug used to treat iron-overload. [237] DFO is a chelating agent that specifically binds to Fe and forms ferrioxamine that can pass through the kidney. They showed that after injecting 75-80 nm FeTNPs and observing PTT, PA and MRI contrast effects, the renal clearance could be accelerated by injecting DFO. In this manner the potential damage of accumulation could be avoided. A recent review discusses a wide number of metal-phenolic network complexes created for theranostic purposes.[238]

Therefore, the effect of a similar polyphenol: Gallic acid, on Prussian Blue nanoparticles were investigated as possible interconnection through the rigid gallic linker could be beneficial in the formation of polymeric NP assemblies. So in order to try to incorporate this polyphenol within the PB nanoparticles, gallic acid solution was prepared in water and mixed with potassium ferrocyanide in different proportions (1, 2 and 10 equivalents with respect to Fe^{3+}in PB). Ferric nitrate solution was then added to the mixture, under the usual reaction conditions. DLS measurements showed that the size of nanoparticles formed, are sub-10 nm. Interestingly, the absorption of PB in the visible region rises with an increase in the amount of gallic acid added. A control experiment (without ferrocyanide) was also performed simultaneously and the purple complex of Fe-GA was formed. Since the complex absorbs in the 600-700 nm range, it contributes to the absorption of PB centered around 700 nm. This was an advantage since the photo thermal properties of the nanoparticle relies heavily on the amount of light that could be absorbed by the sample.

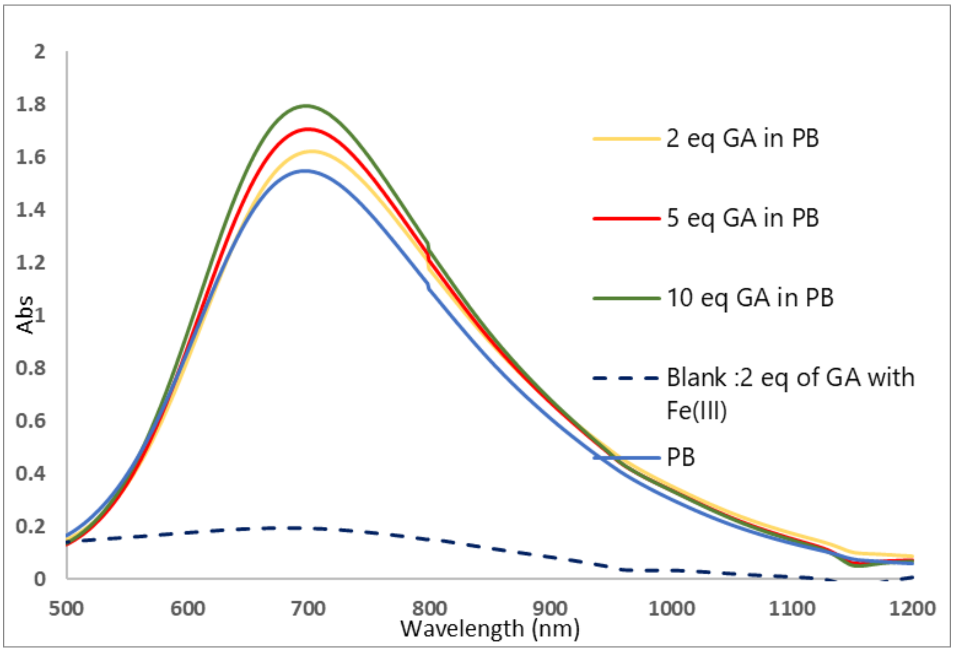

Figure 75. Effect of incorporating gallic acid in PB during synthesis. Absorption of FeGA complex for comparison

Then, the stability of the resulting suspension was monitored in Fetal Bovine Serum with a kinetic study using UV-Vis spectroscopy. As shown in Fig. 78 (a), usually absorption band of PB declines significantly within 2 hrs of exposure to FBS. This is a common phenomenon that occurs due to the complexation of phosphate present in the serum with Fe^{3+} on the surface of PB. Subsequently, a reduction in the number of Fe(II)-CN-Fe(III) pairs occur which leads to this decrease. When GA is included in the synthesis of PB, a different observation was recorded. There is still a quick decrease in the very first minutes of reacting with FBS, however as time passes a shift of the peak towards 600 nm is observed, coupled with an increase in absorption. It seemed that although the Fe^{II}-CN-Fe^{III} pairs were decreasing, the Fe^{III}-gallate complex was becoming more dominant in these experimental conditions. Therefore, the effect of pH was investigated. Results in Fig.78 (c) prove that indeed, the FeGA complex formation and its absorption is highly pH dependent.

An explanation for this could be found in the literature. The catechol-Fe^{3+} coordination system is pH sensitive. It has been conferred that iron-monocatecholate forms in acidic conditions, and upon increasing the pH from 5.5 to 10, bis- and tris-catechol complexes are formed.[239,240] It is interpreted that shift to an alkaline medium, leads to the deprotonation of hydroxy groups in catechol moieties, increasing the ligand denticity. This leads to a stronger chelation with metal (here Fe^{3+}) ions and each complex has a different colour. Figure 79 shows the complexes of Fe-Tannic acid that exists in different pH conditions.[241] Addition of FBS (pH 7.4) to gallic acid containing PB nanoparticles (pH~5), shifted the overall pH of the solution and therefore this evolution and shift in absorption maxima was observed. The effect of addition of FBS and neutralizing was clearly underlined by this study.

(a)

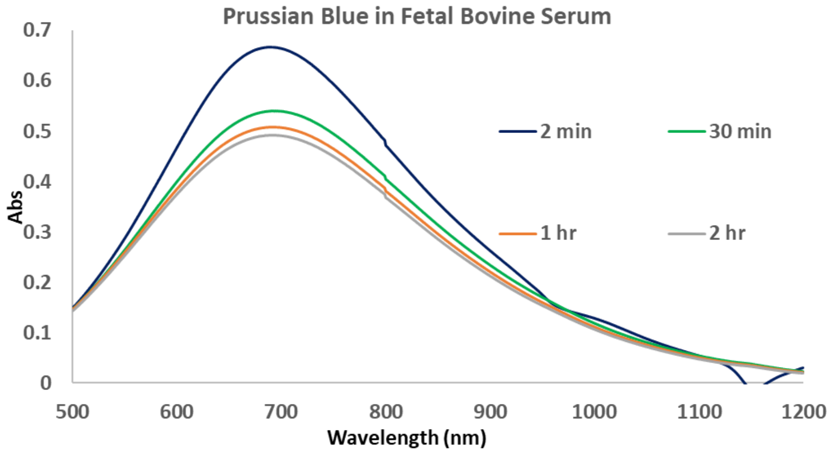

(b)

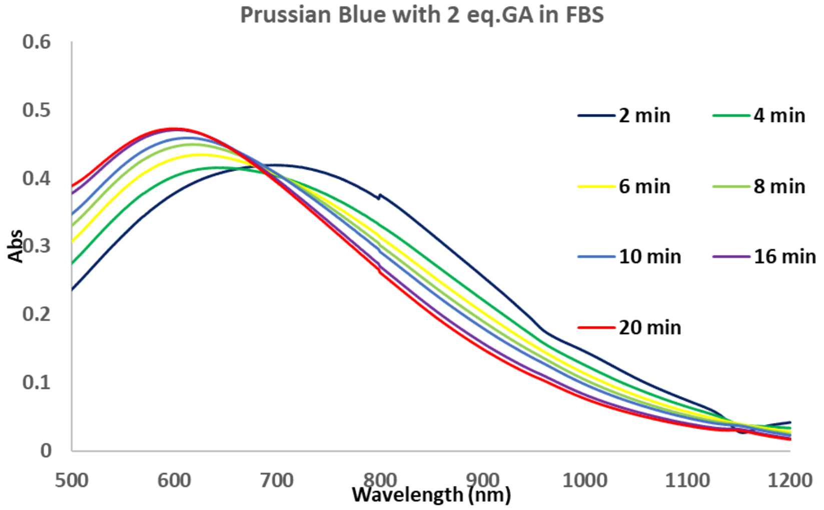

(c)

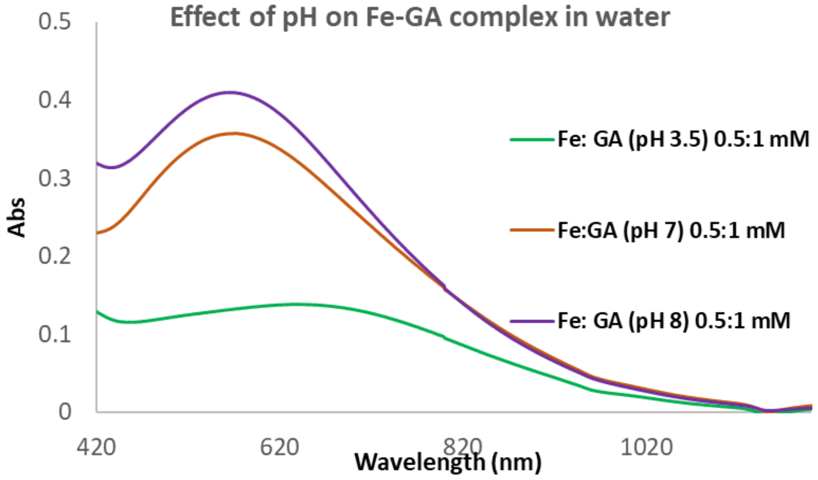

(d)

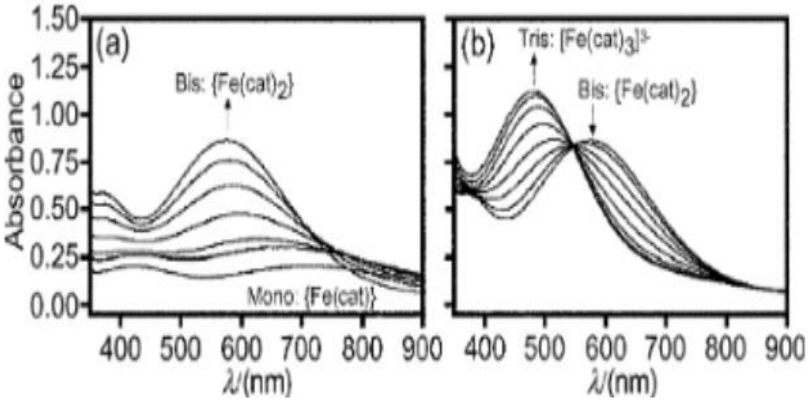

Figure 76. Comparison of evolution of PB nanoparticles (a) without and (b) with gallic acid in fetal bovine serum. (c) The shift and increase of absorption by studying Fe:GA complexes , in varying pH. (d) Results of similar study conducted on titration of Fe^{3+} catechol complex with NaOH.[239]

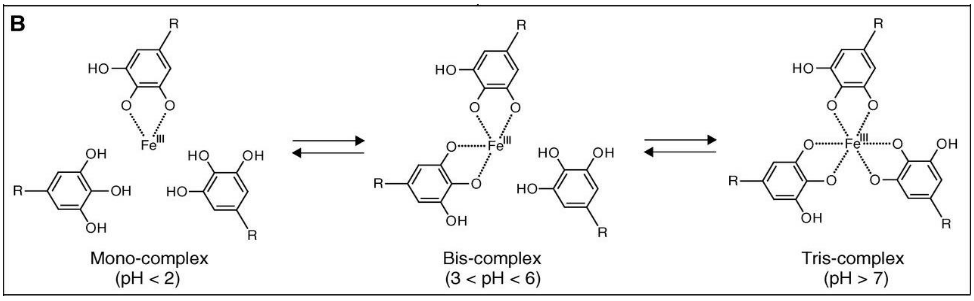

Figure 77. pH dependent transition of Fe^{III}-Tannic acid complexation state.[241]

However, after ultrafiltration, it became clear that the GA and ferrocyanide are competing for Fe(III) and the FeGA complex is formed besides the Prussian Blue nanoparticle solution. So the assembly formation does not occur and the particles remain sub-10 nm in size. Ultrasmall nanoparticles of FeGA (DLS: 4.6-5.5 nm) were then synthesized with PVP coating, at room temperature while maintaining a neutral pH. The kinetic studies conducted in phosphate buffer (PBS) and FBS, revealed that these FeGA particles are highly stable and resistant to phosphate attack. As shown in Fig.80 (b and c) the absorption of FeGA nanoparticles in visible region does not change upon exposure to these different media. This was a very interesting result which suggested that incorporating Fe-gallic acid complex with our PB nanoparticles could not only add to the absorption in Vis-NIR range but could in principle, improve its stability in physiological conditions. This double interest encouraged us to use GA as linker and vary our approach in building an assembly.

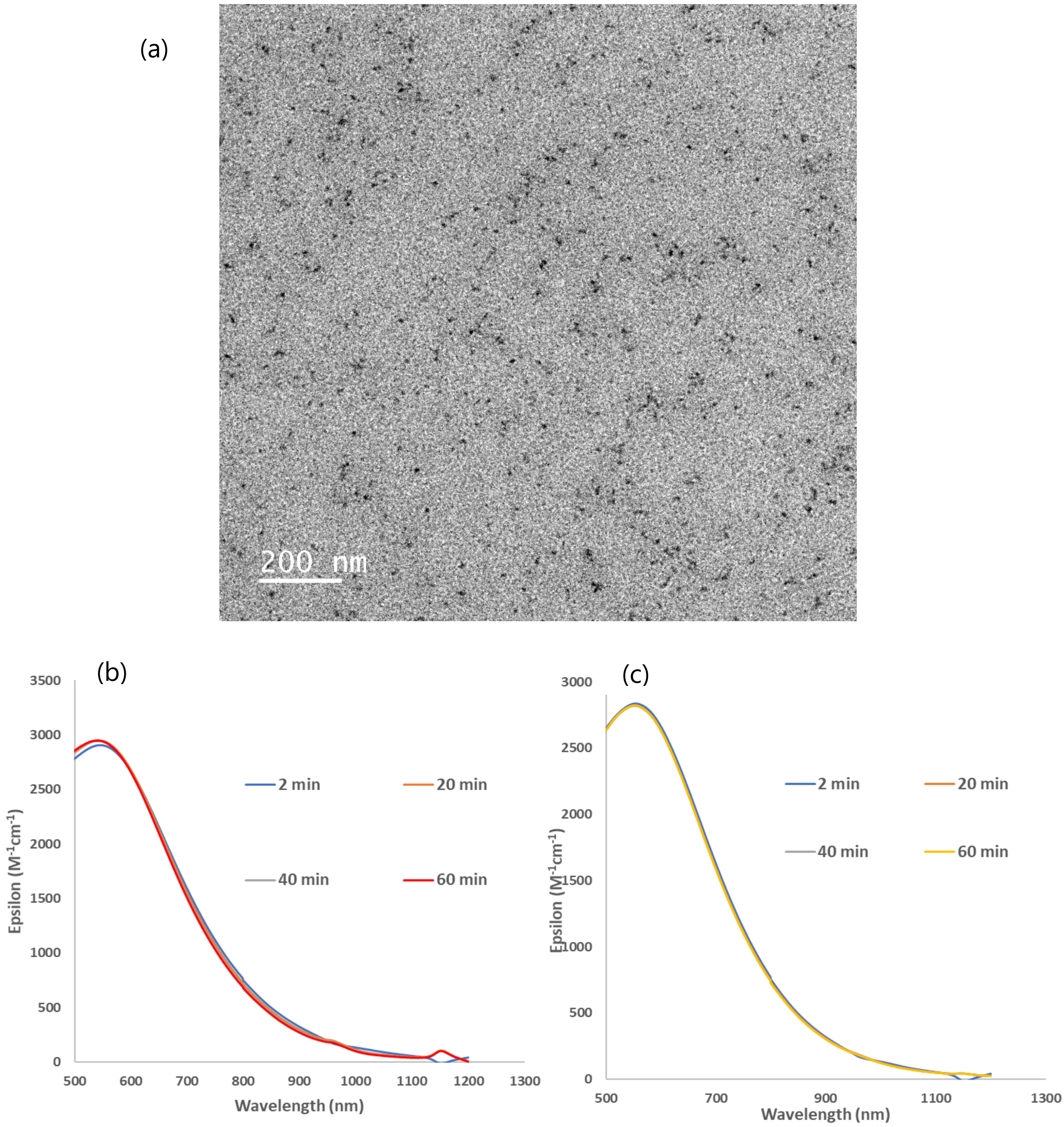

Figure 78. (a) TEM image of PVP coated iron gallic acid nanoparticles and their spectral evolution on exposure to (b) PBS and (c) FBS

3.2.1.4 Iron-gallate system

The original idea was to favour the encapsulation of PB in FeGA matrix, to protect PB in physiological medium and provide additional contribution for photothermal therapy. Versatile metal-phenolic coordination polymer networks could be easily formed using iron and gallic acid in aqueous solutions and therefore methodical studies were performed, carefully monitoring the effect of each parameter. First, pure Prussian Blue nanoparticles were synthesized in water using the method described in chapter II. Since it was determined that the pH is extremely important for complex formation, gallate solution(1 mM, 8 mL) was prepared by neutralizing gallic acid with dilute NaOH. Solution of $Fe(NO_3)_3$ (0.5 mM, 8 mL) was freshly prepared. Then, both the precursors were added to the pre-formed PB (0.25 mM, 8 mL) solution, in an alternative way to avoid nucleation of FeGA particles. This addition was performed dropwise, using a peristaltic pump, under constant stirring and the flow rate of 0.5 mL/ min was maintained. Once all the reagents were transferred, the reaction was run for 30 minutes at room temperature. Dark blue coloured solution was formed and complete characterization was done. The sample would hereafter be called PB-FeGA. Many other combinations and reagent proportions were experimented but the most optimized results would be described in the next section.

3.2.2 Characterization

3.2.2.1 DLS and Zeta potential

The first clear indication of assembly formation was obtained with dynamic light scattering studies. The 6-8 nm peak of PB underwent a significant shift to ~90 nm after slow, drop-wise addition of 2 equivalents of iron (0.5 mM) and gallate (1 mM) solutions. The solution was constantly monitored with time and the hydrodynamic diameter did not appear to evolve over several days. The solution had a negative zeta potential of -31 mV which signalled towards the inherent stability of the sample.

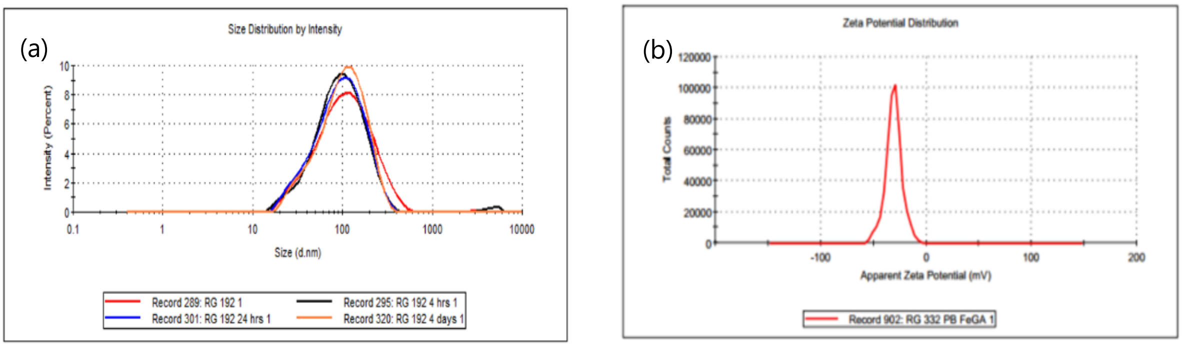

Figure 79. (a) Minimal evolution of hydrodynamic diameter of PB-FeGA assemblies, checked at multiple time points over 4 days after synthesis. (b) Zeta potential of PB-FeGA

Other experiments with varying parameters were performed, to get an idea of the best conditions. Firstly, the effect of added iron to PB was studied, while maintaining the ratio of Fe^{3+} to GA ratio constant at 1:2. Each experiment was performed in triplicate to ensure reproducibility. As shown in Fig.82 (a) adding just 1 equivalent of Fe GA leads to some assembly formation, however a significant proportion lies in the 20 nm range. Therefore, it could be said that this amount of reagents is not enough to assemble all the nanoparticles. On the other hand, with 3 equivalents of Fe (0.75 mM) and corresponding 1.5 mM of GA, lead to shift in the DLS peak to ~180 nm (Figure 82 (a) blue curve). It was understood that the size of the assemblies formed could be tuned by manipulating the amount of precursors added.

Once it was determined that 2 or 3 eq.s of added Fe is necessary, the importance of gallic acid was examined by performing blank experiments. Ferric nitrate solution was added to PB, together with water (pH 7) at 0.5 mL/min rate, while stirring. DLS indicated huge sizes in the range of 1000 nm and soon the solution started depositing. Therefore, the mixture of Fe^{3+} and GA was necessary for assembly formation.

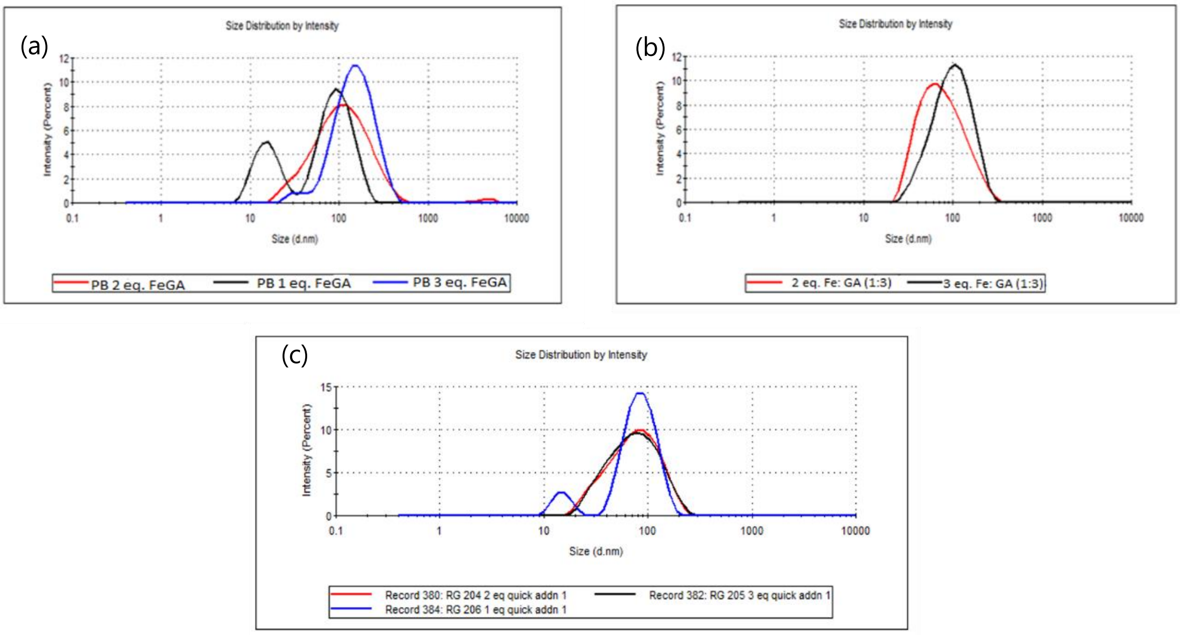

Figure 80. (a) Effect of addition of varying equivalents of precursors. (b) Effect of changing the Fe-GA ratio to 1:3. (c) DLS results of quick addition expt. with 1, 2 and 3 eq. precursors.

Changing the Fe:GA ratio to 1:3 was also explored and results are displayed in Fig. 82 (b). In this case, addition of 2 eq. gave rise to smaller assemblies with sizes around 65 nm, while 3 eq.s of Fe (0.75 mM) with 2.25 mM GA provided similar results with mean size of 100 nm. Hence, it was decided that there was no reason to add extra reagents when similar results could be obtained at lower ratios. Next, quick addition of Fe^{3+} and GA experiments were performed. The neutral GA was first added to pre-formed PB under stirring to avoid deposition. This was followed by addition of Fe^{3+} solution in one go, to the mixture and reacted for 30 minutes. The DLS analysis revealed that, similar to dropwise experiments, 1 eq. of precursor was not enough for complete conversion of nanoparticle to assembly (Fig.82 c). However, for the other equivalents the peak was around 80 nm, but the signal was broad indicating that maybe smaller assemblies are formed. TEM measurements were performed to visualize these formed structures.

3.2.2.2 Transmission Electron Microscopy

TEM imaging was performed by depositing the samples on formwar carbon coated copper grids after glow-discharge. The ultra-small PB nanoparticles formed pearl-necklace like assemblies that will be called nanochains. The results from different repeat experiments performed with 2 eq. addition of Fe^{3+} and Gallic acid are displayed in Figure 83. The average size of the assemblies were 94 ± 35 nm with very minimal single nps.

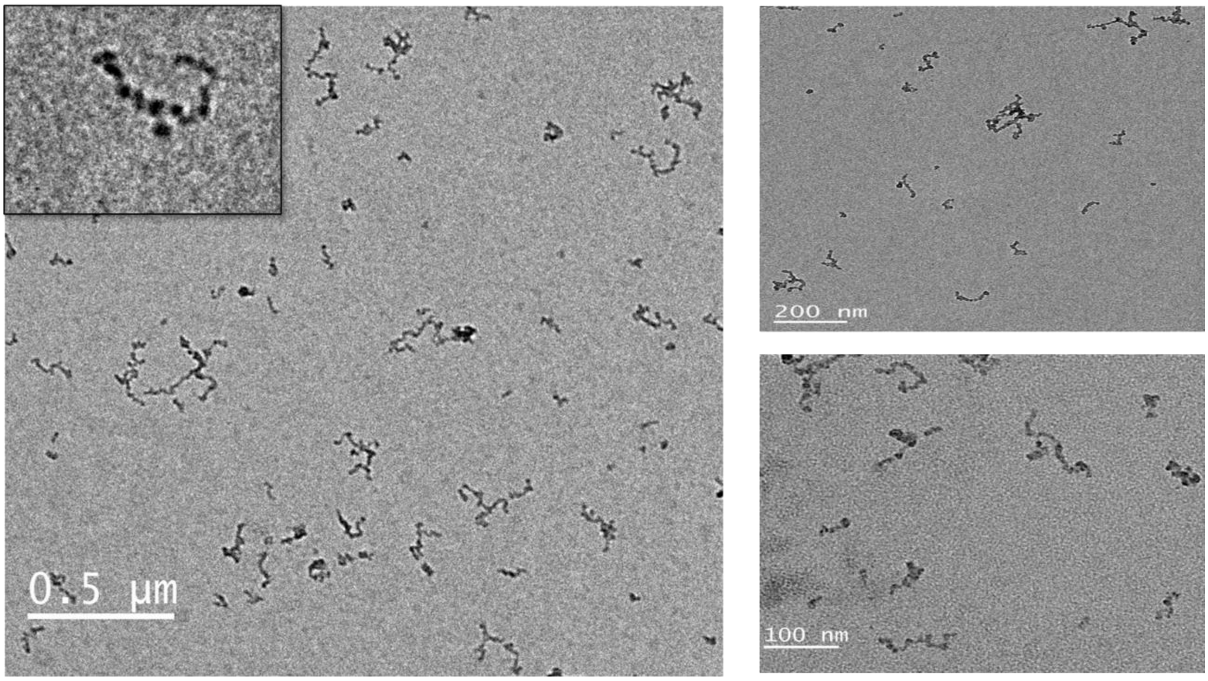

Figure 81. TEM micrographs of PB FeGA assemblies formed by dropwise addition of 2 equivalent of precursors into pre-formed PB nanoparticles

The results obtained with DLS could be verified with TEM. The addition of 1 eq. of reagents forms assemblies but the presence of more single and individual particles could be seen. In contrast, 3 eq. of FeGA with PB forms larger and less controlled aggregates (Figure 84 a, b). When the precursors are added quickly and in one go, smaller sized assemblies are formed. Therefore, considering all the results it was concluded that the best synthetic method involved slow dropwise addition of Fe^{3+}(0.50 mM) and GA (1 mM) into 0.25 mM Prussian Blue solution.

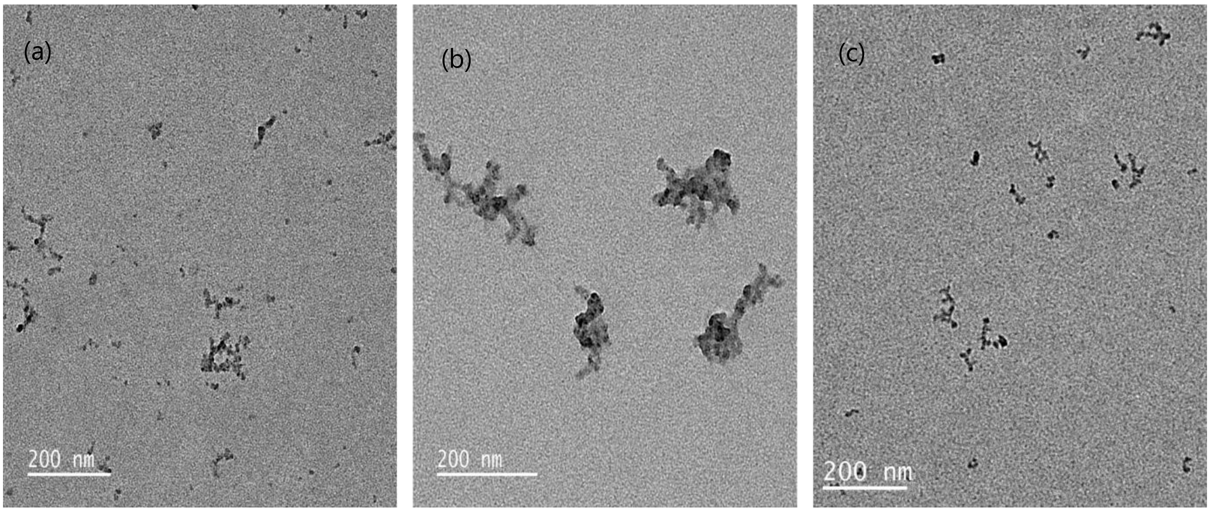

Figure 82. Assemblies obtained (a) 1 eq. (b) 3 eq. and (c) 2 eq. quick addition of Fe GA

3.2.2.3 Nanoparticle Tracking analysis

The optimised nanochains were visualized using NTA to determine its hydrodynamic diameter in solution. The sample was injected and studied with an ultramicroscope, under laser illumination at Université de Paris. The light scattered by the PB FeGA assemblies was captured over multiple frames and the size was detected and calculated by Nanosight software. The average size over 5 measurements was reported as 106.3 ± 2.8 nm, which is in close agreement with the previously conducted DLS and TEM studies.

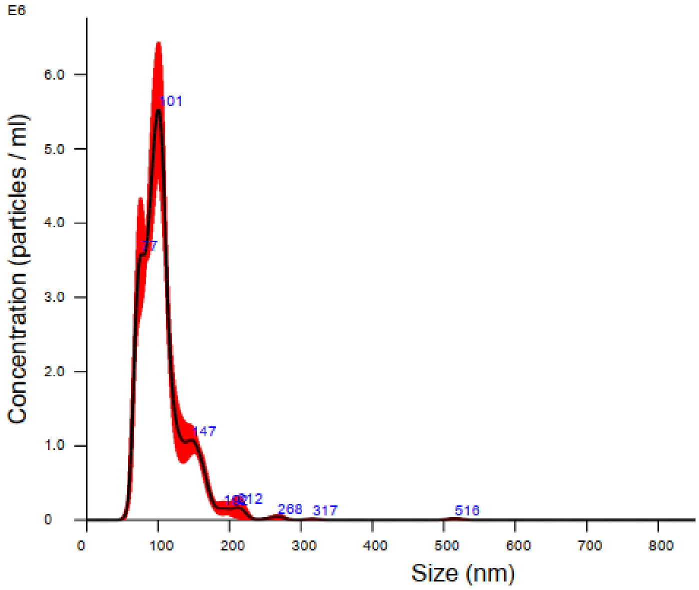

Figure 83. Nanoparticle tracking analysis (NTA) results of PB FeGA nanochains in water.

3.2.2.4 Infra-Red Spectroscopy

The PB-FeGA assembly solution was ultra-filtered and washed twice to remove all the unreacted precursors. The filtrate was light purple in colour, indicating that excess FeGA complexes are eliminated. Then the sample was concentrated and brought to a low volume, before drying it under vacuum. The powder obtained was used for IR spectral analysis. The signal from the assemblies were compared to that of FeGA and bare Prussian Blue nanoparticles.

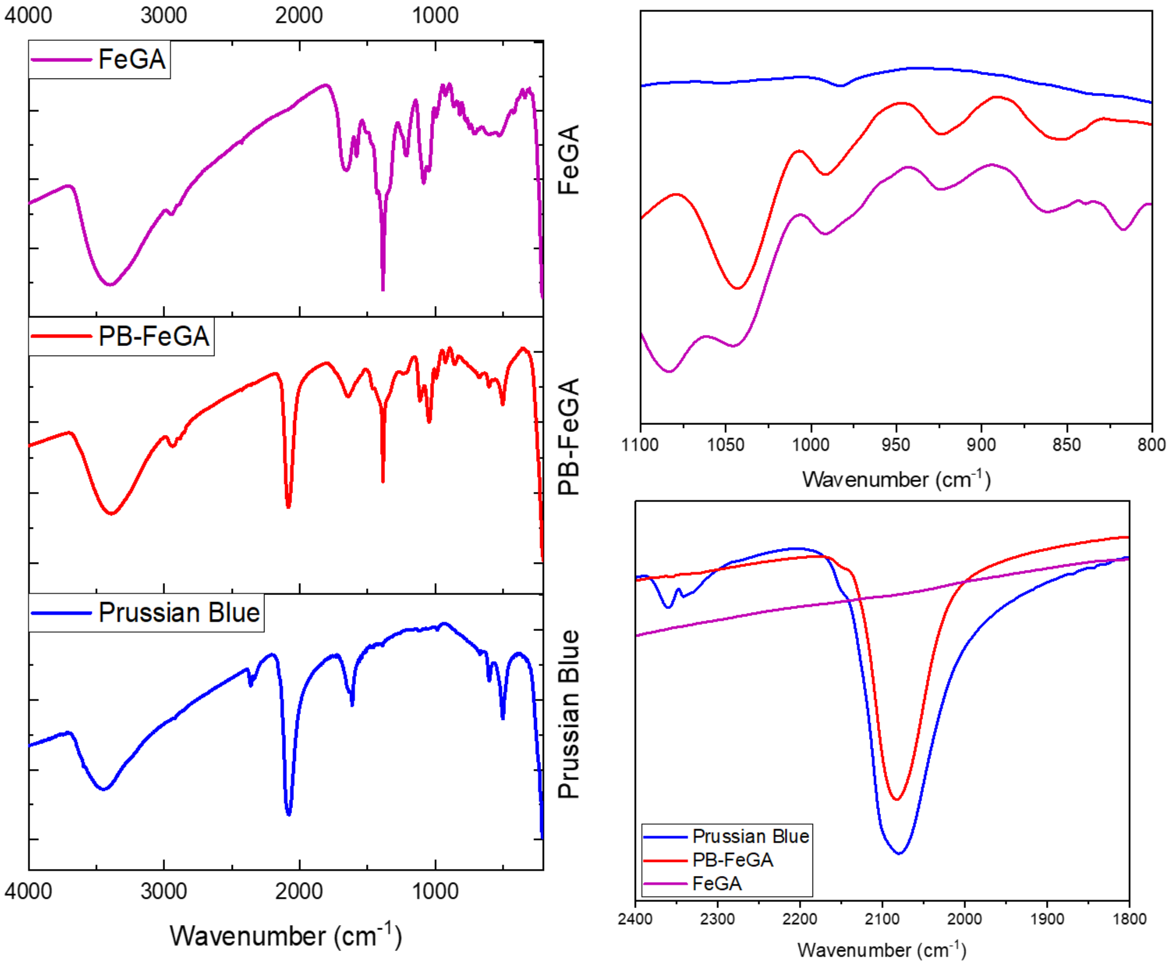

Figure 84. IR spectral comparison of PB-FeGA with its constituents.

A weak and broad signal at 2935 cm^{-1} corresponding to -OH stretching could be observed in the assemblies and FeGA (2942 cm^{-1}). The characteristic ν_{CN} of PB is seen both in the bare nanoparticle and assemblies at 2080 cm^{-1}. The intense peak at 1580 cm^{-1} is characteristic of antisymmetric Fe-O-C stretch of Fe(III)-gallate complex,[242] and it is shifted to 1578 cm^{-1} in PB FeGA (small peak). The vibrations of C-O bonds including ester links at 1213 cm^{-1} is merged within a broad band in the assemblies. The other peaks of C=C and C-H bending arising from polyphenol are still present in the assembly. The infra-red data provides a clear indication that the assemblies are indeed linked through FeGA polymeric network and they remain intact after the washing steps.

3.2.2.5 UV-Visible Spectroscopy

An evident colour change to darker blue was observed at the end of the assembly formation reaction. Addition of iron-gallate to Prussian Blue nanoparticles increases its absorbance in the visible region. There is a slight shift to lower wavelengths (700 to 685 nm) as the number of equivalents added increases. For the most optimized PB-FeGA sample, UV-Vis analysis showed a significant enhancement in the absorption around 700 nm (1.58 times), at the same PB concentration. The peak also appears slightly broader. This improvement is attributed to i) an increase in the number of Fe(II)-CN-Fe(III) pairs formed upon addition of extra Fe^{3+} and ii) the contribution of the FeGA complex.

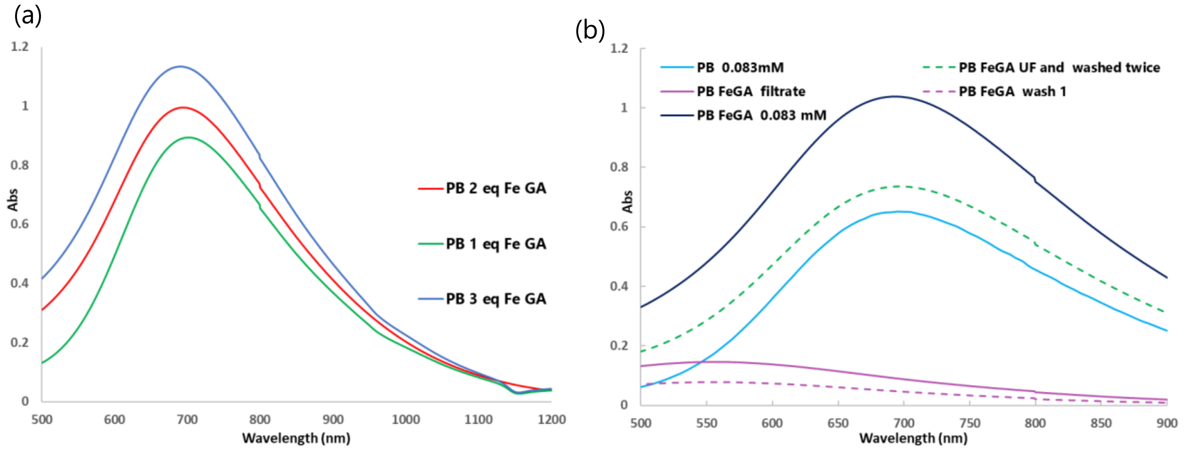

Figure 85. (a) UV-Vis absorption of PB assemblies with1,2 and 3 eq. of FeGA. (b) The absorption of optimized sample compared to PB nanoparticles and effect of UF

As discussed in the earlier section, pH plays an important role in the absorbance of such iron-catecholate complexes. Ultra-filtration (UF) and washing steps take away the excess and unbounded reagents and the signal from the separated filtrate (Fig. 87 b) provide clear indication of FeGA. A part of the sample is also lost during the vigorous UF process, as it gets stuck in the pores of the membrane. So the overall absorption of the sample is brought down, but it is still 13% higher than pure PB nanoparticles. The absorbance at 800 nm is most significant for our samples as the near infrared (NIR) laser used for photo-thermal therapy usually operates at this wavelength. It can be seen from the plot below that the assembly formation enhances the signal at 800 nm by 18.5 %, indicating that it may aid in better photothermal therapy.

3.2.2.6 Energy Dispersive Spectroscopy

It was important to understand the amount of added precursors are retained in the final nanochain structure after the UF and washing steps. However, since iron is added to an already iron-rich PB to form the assemblies, it would be difficult to deduce any information from EDS analysis. Therefore, the assembly formation process was tweaked to include gallium ions Ga(III) instead of added Fe(III). The idea was to check whether the nanochain would be formed with Ga(III) and then determining the amount of added gallium, retained after purification. The reaction conditions were maintained and 2 equivalents (with respect to PB) of Gallium nitrate solution ($Ga(NO_3)_3$) and solution of gallate at pH 7 was added dropwise to the nanoparticles. DLS analysis showed PB-GaGA assemblies were synthesized with an average size of 82 nm. TEM imaging also proved that nanochains are present in the solution, they appear slightly longer and less controlled than PB-FeGA. The experimental conditions might need some optimization but eitherway, it was the first indication that other metal ions could also be used to form nano-assemblies with Prussian Blue. Then, the solution was ultra-filtered and washed twice before addition of acetone to induce flocculation. The precipitate obtained after centrifugation at 2°C, was dried under vacuum. EDS of the powdered sample indicated that Ga/Fe ratio was 1.55. Therefore, if it is considered that iron and gallium cations behave similarly with gallic acid, around 74-82 % of the added metal ions is still incorporated within the assembly. Since EDS indicated that only 1.5 out of the 2 equivalents are necessary to bind the PB nps together, further experiments with 1.5 eq. FeGA addition was attempted. DLS and TEM results show that smaller assemblies were formed with this combination (results in annex 6.3.3). Therefore, 2 eq. was maintained as the standard for further experiments as the slight excess could be easily washed away, post-synthesis.

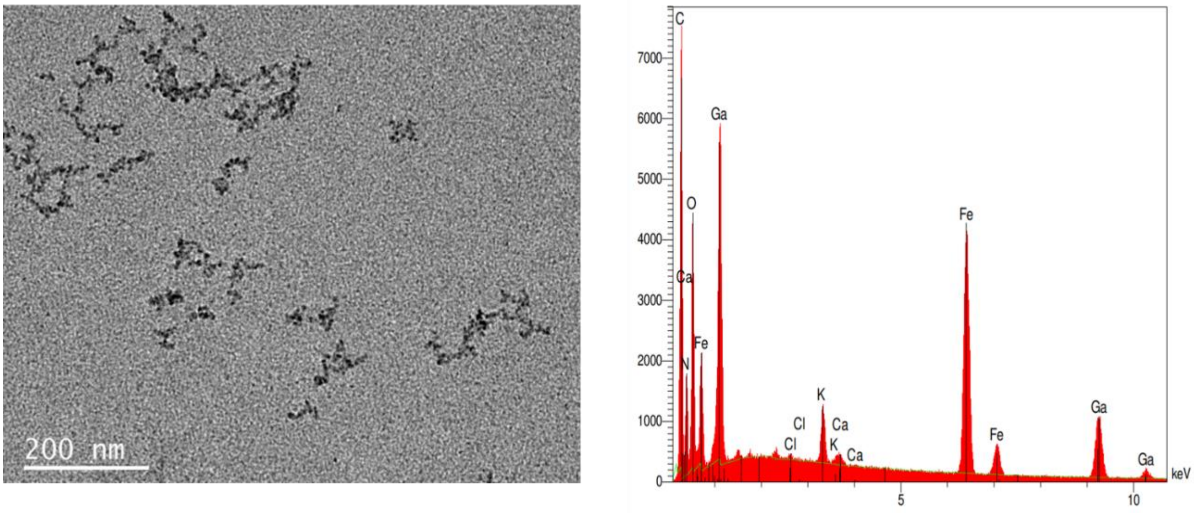

Figure 86. (a) TEM micrograph and (b) results of EDS analysis of PB-Gallium GA assembly

3.2.2.7 STEM-HAADF

High-angle annular dark-field scanning transmission electron microscopy was used to obtain a better understanding of the structure of nanochains formed. These studies were performed by Alexandre Gloter at Laboratoire de Physique des Solides. The results clearly showed that between two Prussian Blue nanoparticles (brighter contrast in Fig. 89 a) was a more transparent region, that can be attributed to a part with less metal content. Furthermore some texture appears around the PB particles. EELS spectra was recorded across the nanochains and regions of different compositions can be distinguished. The nanoparticle region, marked by the blue square and corresponding curve shows presence of iron and nitrogen originating from cyanides in Prussian Blue, but also the presence of oxygen. This oxygen may come from water molecules coordinated in the PB structure but other EELS spectra recorded on PBA particles reveal that this signal is almost undetectable. Hence, we attribute the O peak to the presence of gallic acid coming from Fe-GA moieties, corresponding to the additional texture seen all around the PB particles. The area between the nanoparticles, marked by the red rectangle and the corresponding red spectrum shows the presence of iron and oxygen and no nitrogen. This gives a direct indication of the presence of Fe-GA moieties that are located in between two PB particles. High resolution TEM could not provide additional information probably due to the beam damages.

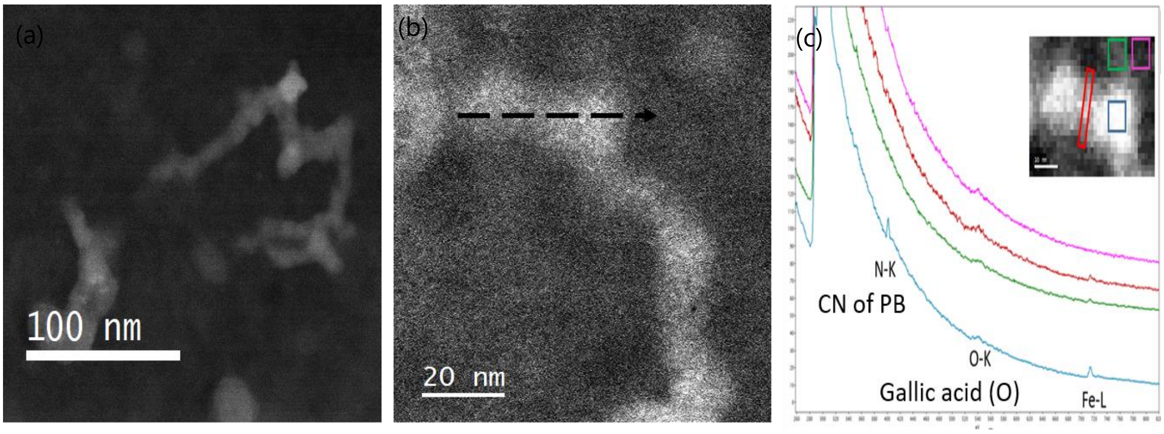

Figure 87. (a) HAADF STEM images. (b) STEM-EELS spectra recorded in the areas denoted as squares on the inset with the corresponding colour curves

3.2.3 Polymer coating

The important advantage of our approach is that the chains remain stable and that the coating can be varied and its effect studied. Coating of nanoparticles with polymer is considered essential for bio-medical applications. It has been shown that polymers can improve bioactivity and compatibility in physiological medium, while certain polymers can also impart special properties and increase functionalities. PVP (polyvinylpyrrolidone) is a water-soluble, inert and bio-compatible polymer. It is non-toxic, pH-stable and therefore used in many medical and cosmetic formulations. Dextran is a biodegradable branched polymer composed of glucose units linked through α-1,6 and 1,3 linkages. It has functional hydroxyl groups that can aid chemical conjugation and has been used as drug delivery agents.

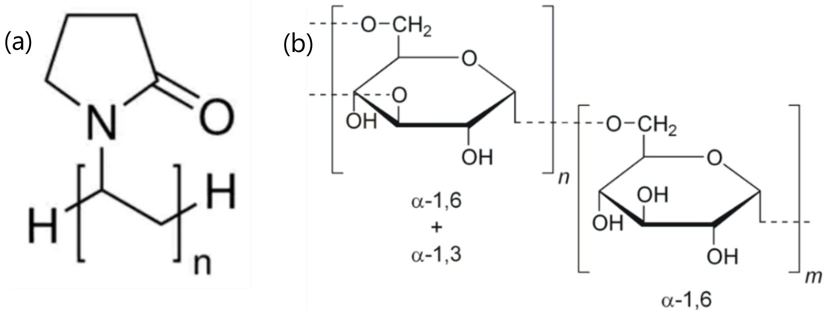

Figure 88. Structure of (a) PVP and (b) Dextran polymer

3.2.3.1 Coating assemblies with PVP and Dextran

Firstly, 30 equivalents (2.5 mM) (with respect to 0.083 mM PB in the assembly) of each polymer was dissolved in water to form a homogenous solution (10 mL). It was then added to 10 mL of PB-FeGA solution in one go, under continuous stirring and mixed for 30 minutes. This was followed by regular characterization with DLS, TEM and UV-Visible analysis. No changes in the hydrodynamic diameter of the assemblies were seen with PVP, however a small percentage of population appeared around 20 nm, when 30 eq.s of dextran is added to the solution. The zeta potential of the solution after adding PVP to Prussian Blue assemblies was around -27 mV and dextran addition shifted it to -36 mV. As shown in Figure 91, the addition of polymers do not change the basic structure of the nano-assemblies. They appear to be more well-dispersed in the presence of polymer and the average size was 97 ± 38 nm and 90 ± 37 nm with PVP and dextran respectively.

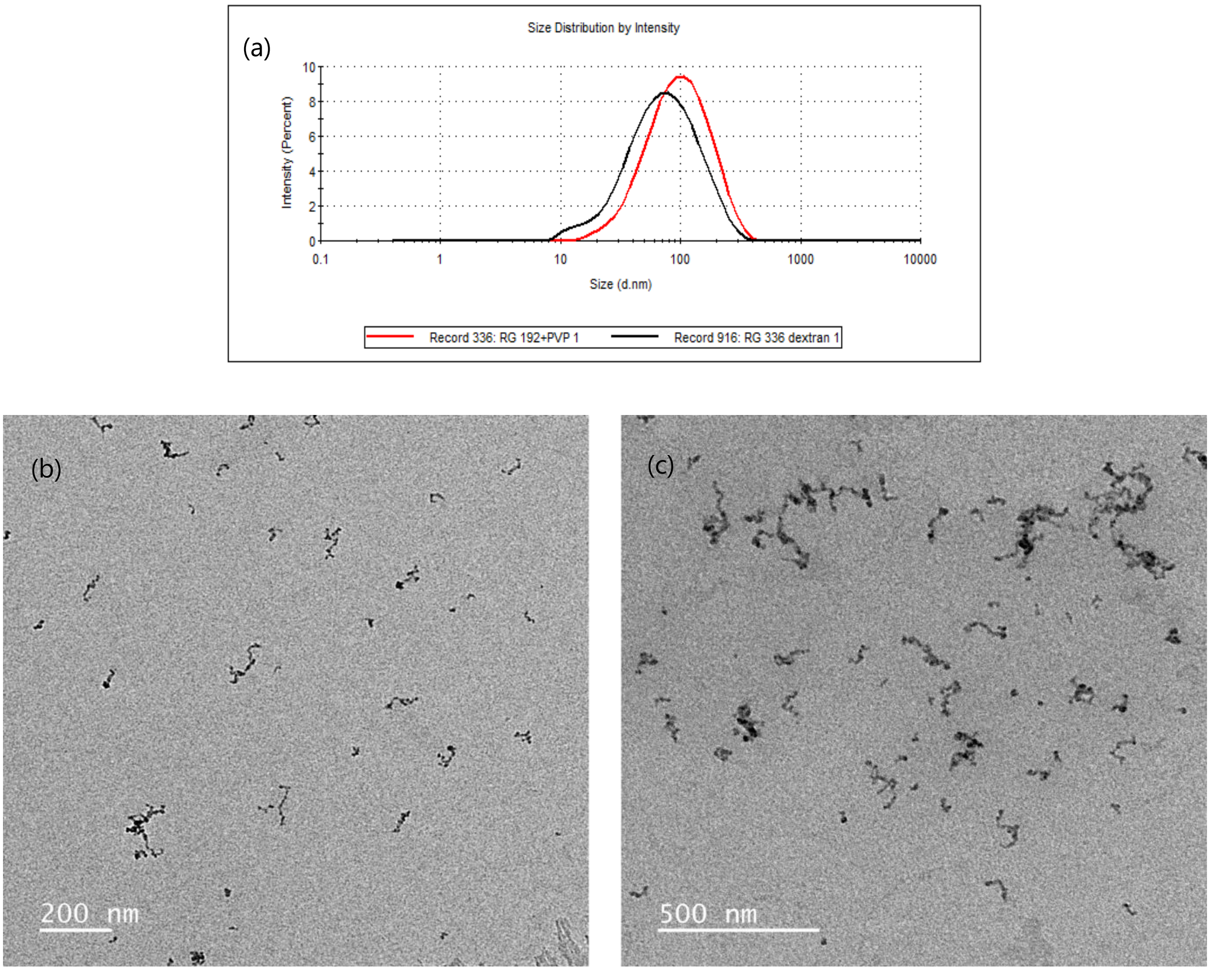

Figure 89. (a) Hydrodynamic diameter of PVP and dextran coated assemblies. TEM images of PB-FeGA assemblies with (b) PVP and (c) dextran polymers

A very big advantage on addition of such polymers was observed after the ultra-filtration process. UF is a necessary step of purification before *in-vitro* and *in-vivo* studies. It is done to remove the dissolved contaminants. The solution is forced through a semi-permeable membrane and depending on the pore size of the tubes used, the nanoparticles and their assemblies are retained at the top, while excess salts or complexes are removed in the filtrate at the bottom. As mentioned before, first filtration is done, the sample is brought back to its initial volume with distilled/milli-Q water and then 2 successive washing steps are performed. Since this is quite vigorous, the purified assembly sample obtained at the end of the process is more aggregated (Fig 92 (a)) and is not ideal. It was observed that the presence of PVP and dextran (Fig. 92 b, c) clearly minimizes this aggregation and helps maintain the structural integrity of the nano-chains after ultra-filtration and washing. This is extremely important for the targeted applications and hence the samples prepared were always coated with polymers before moving on to the next step.

The effect of addition of chitosan polymer was also studied briefly. Addition of 30 eq.s shifts the zeta potential to positive values of +34 mV, since it is a positively charged polymer (images appendix 6.3.4). Although the chain like structure is retained, as DLS indicated the sizes are much larger(~200 nm) and some aggregation could be seen. Lowering the proportion of this polymer might be beneficial in getting more controlled results.

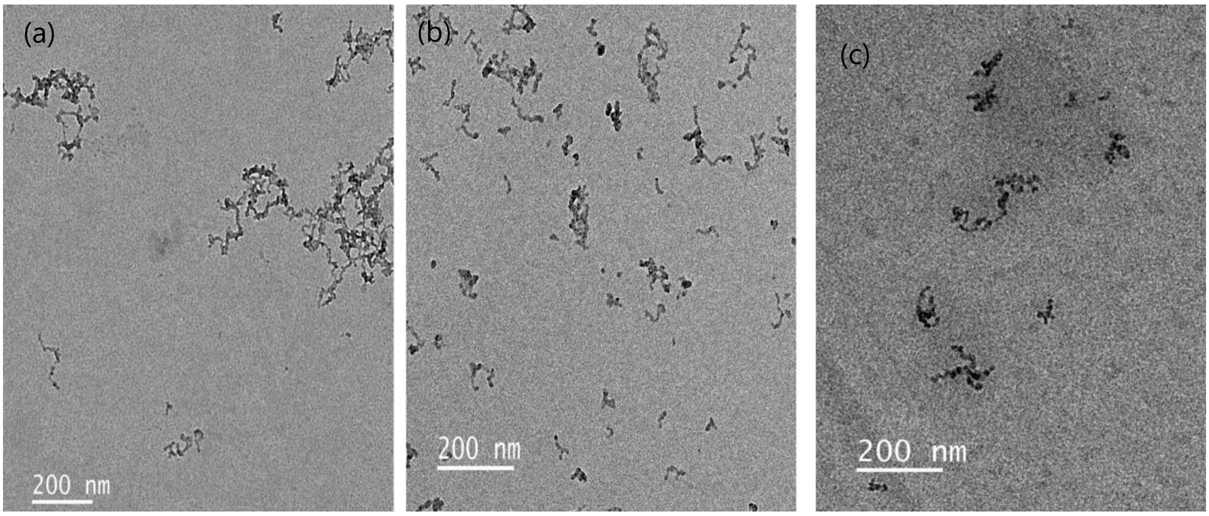

Figure 90. Effect of UF and washing on (a) bare PB-FeGA assemblies (b) with PVP (c) with dextran polymer coating

3.2.3.2 Poly γ-Cyclodextrin Citrate

Once it was determined that the formed assemblies could be easily post-coated with regular polymers, the focus was shifted to added functionalities. As described in section 3.1.1 gamma-cyclodextrin citrate polymer includes cage-like structures that can aid drug loading and citrate moieties that could bind to the surface of PB nanoparticles. This polymer was synthesized by Jingwen Qiu at ISMO, following the method developed by Ruxandra Gref et.al.[243] First set of experiments were performed with 10 equivalents of the polymer with respect to the nanoparticles. The addition of 0.83 mM CD-citrate solution into PB-FeGA solution led to a sharp colour change from dark blue to light prussian blue. This was due to the pH effect, as addition of large amounts of this citrate-rich polymer brought down the pH ~2.8, lowering the

FeGA complex signal. Multiple proportions (1,0.5 and 0.05 eq.s) were tried out in order to i) decrease the amount of free polymer ii) reduce the weight of the polymer to enhance payloads of drug in future experiments. It was determined that 0.05 eq. of the γ-CD citrate could fulfil these requirements.

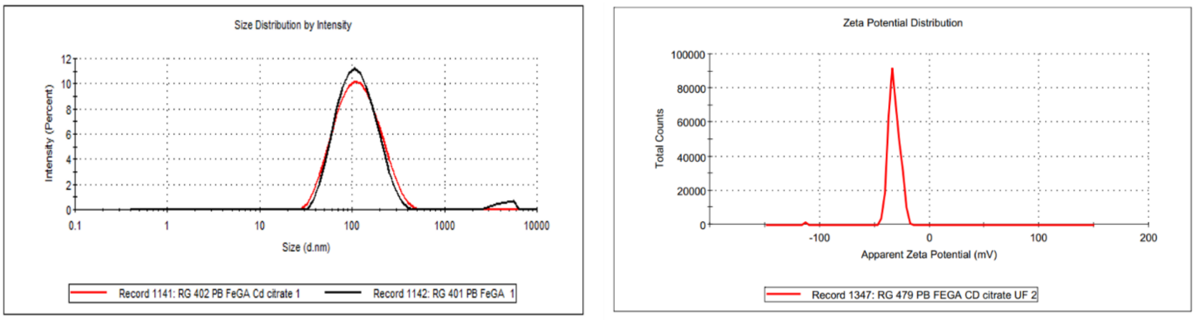

Figure 91. DLS and zeta potential results of PB FeGA with CD citrate polymer coating

DLS analysis showed no significant variation upon introduction of the polymer. The poly CD citrate coated sample could be ultra-filtered and washed without loss/deposition in the membrane pores, and the chain-like structure is well-maintained. The zeta potential lies around -30 mV. UV-analysis shows a certain loss in absorbance compared to starting assemblies, due to slight changes in pH effect and overall decrease in FeGA complexes.

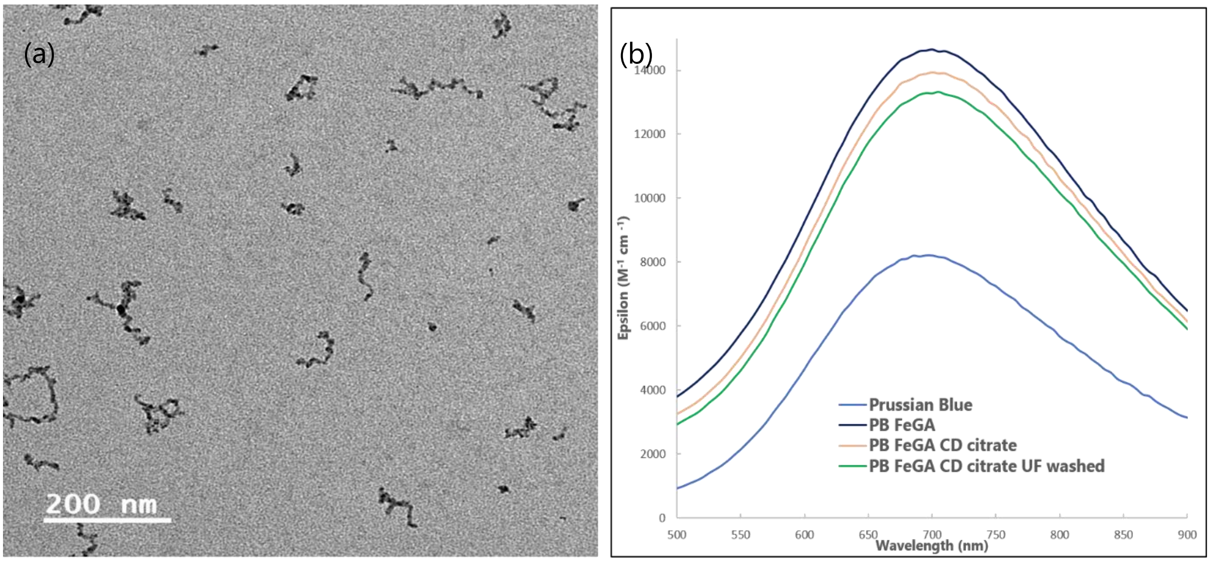

Figure 92. (a) TEM image of Prussian Blue assemblies coated with gamma-CD citrate polymer after UF and washing steps. (b) Effect of polymer addition on absorption of the assemblies and comparison to PB nanoparticle solution.

The signal is still significantly higher than pure PB nanoparticles at the same concentration indicating that the assembly formation and the polymer coating has advantages. Moreover, the coating with CD-citrate polymer allowed further concentration of the sample without aggregation.

3.2.4 Evolution in physiological media

It is important to understand changes occurring to a nanocomposite in biological pH. Therefore, kinetic evolution was monitored by absorption spectroscopy on poly CD-citrate coated PB-FeGA nanochains in 10% fetal bovine serum both at pH of 7.4 (using phosphate buffer, PBS) and at pH 5.5 (using acetate buffer). As described earlier PB is highly sensitive to phosphate attack and the absorption around 800 nm is crucial for photothermal therapy efficiency. Experiments performed with the bare PB Nps have shown that its $Abs_{800\ nm}$, reduces to 24% of its initial value within 2 hours in PBS (annex 6.3.5). But the FeGA nanoparticles (see Fig.80) is completely unaffected and retains its strong absorption over time in phosphate buffers.

Here, the PB-FeGA assemblies undergo only a 7% loss in $Abs_{800\ nm}$ after 30 minutes in the phosphate rich medium. The maxima shifts from 690 to 660 nm in 3 hours, but 86% of the initial absorbance of the nanochains is still retained, even after this long exposure (Figure 95(a)). It proves that this manner of assembly formation using iron-gallic acid complex not only improves the optical properties but also increases its stability in physiological media. Interestingly, it could be seen that the overall absorbance in 10% FBS with acetate buffer does not decrease, and even slightly increases over time. These results show that whatever the pH, the PTT efficiency of the nanochains should remain intact.

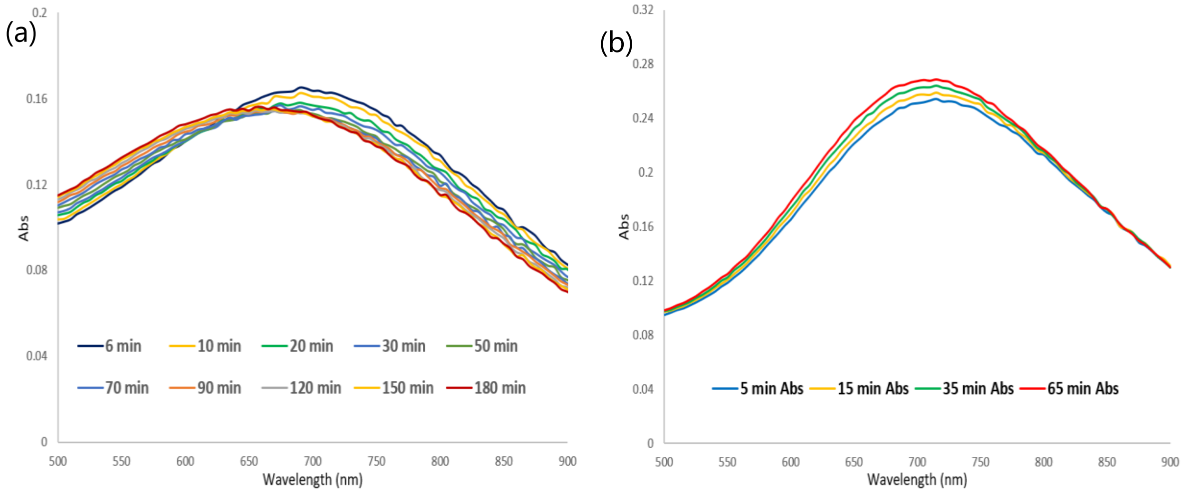

Figure 93. Results of UV-Visible spectroscopic studies on evolution of poly CD-citrate coated PB FeGA nanochains in 10% FBS with (a) phosphate buffer (pH 7.4) and (b) acetate buffer (pH 5.5)

3.2.5 Why 1D nanochains?

The work done during this thesis has led to self-assembly of negatively charged Prussian Blue nanoparticles into one-dimensional, sometimes branched nanochains. There have been some examples in the literature, that provide similar structures with other nanoparticles and using different approaches. One of first assembly formation ever reported was in 2002, when Tang et.al showed that 2.5-5.4 nm CdTe spontaneously organizes into 500 -1200 nm crystalline nanowires when the protective layer of the organic stabilizer was removed. [244] The intermediate step involved assembling the nps into a pearl-necklace formation which then gradually fused into highly luminescent long crystal wire. This occurred because electrostatic repulsion of nps were reduced and attractive dipole-dipole force in the solution was strengthened. There are many interesting examples of 1-D nanostructures based on magnetic nanoparticles.[181] Magnetostatic dipole-dipole interactions are responsible for the directional growth of nanochains which then produce necklace-type nanoring structures.[245] Many other examples have been reported with enhanced properties.[246]

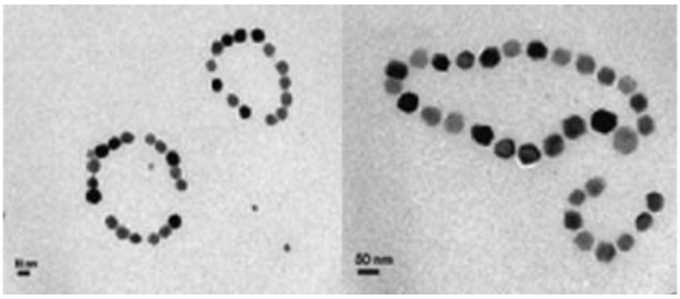

Figure 94. Necklace-like nanoarrays of magnetic nanoparticles.[245]

A bio-inspired polymeric template was developed for assembling quantum dots, gold and iron oxide nanoparticles into size-tuneable nanochains. It was outlined that the adhesive moiety in the template, surface charge and assembly method are critical factors for 1D assembly formation.[247] H. Zhang and D. Wang conducted a thorough study to shed light on mechanics behind chain formation using negatively charged 14 nm gold nanoparticles.[248] TGA capped-Au nps where chosen for their plasmon resonance properties and its sensitivity to electronic coupling. When assembled or aggregated, gold nps display a plasmon absorption band in the wavelength range of 600-800 nm. The colloidal stability of charged particles was estimated using Derjaguin-Landau-Verwey-Overbeek (DLVO) theory which states that total interaction potential (V_T) is the sum of electrostatic repulsion potential (V_{elec}), van der Waals attraction (V_{vdW}), dipole interaction (V_{dipole}) and charge-dipole interaction potentials ($V_{charge\text{-}dipole}$):

$$V_T = V_{elec} + V_{vdW} + V_{dipole} + V_{charge\text{-}dipole}$$

Usually, the nanoparticles have negligible dipole potentials and their stability in solution is maintained by opposing V_{elec} and V_{vdW}. Varying amounts of salts were added to weaken the electrostatic repulsions and assembly formation was observed. Similarly by creating a mixture of polar organic solvents, the dielectric constant of the medium could be tuned to decrease V_{elec} and increase the V_{dipole}. Their calculations for spherical nps revealed that V_{elec} and V_{vdW} are of the same order of magnitude and usually to maintain colloidal stability electrostatic repulsions value remain larger. If due to any change V_{elec} is brought down, the combination of van der Waals and anisotropic dipolar attraction becomes dominating and is able to overcome the repulsions between nps. So once a dimer is assembled, the electrostatic double layer re-arranges to form a uniform layer covering the chain. It then behaves as one elongated object, rather than two repelling nps. This modification to the model helps us understand the chain formation mechanism in one-direction.

$$V_{\text{elec}}^{\text{end}} = \sum_{n} \frac{Q}{D_i} = \int_{0}^{D_{\text{total}}} \frac{\rho A}{Di} \mathrm{d}D = \rho A \ln D_{\text{total}} = \rho A \ln 2 n a$$

$$V_{\text{elec}}^{\text{side}} = 2\rho A \ln n a$$

The electrostatic repulsion is split into two components : V_{elec}^{side} and V_{elec}^{end} where ρ is the charge density, A is the surface area, n is the number of particles (n>2) and D is the length of the chain. Once the dimer is formed V_{elec}^{side} amounts to a larger value as compared to V_{elec}^{end}. Therefore, the other nanoparticles preferentially attach to the ends making the chains longer in 1D (Figure 97 a). On the other hand, if the vdW becomes stronger than the V_{elec}^{side}, 2D and even 3D aggregates could be formed. So depending on the required end product, reaction conditions could be changed, to regulate the four parameters that contribute to the total interaction potential.

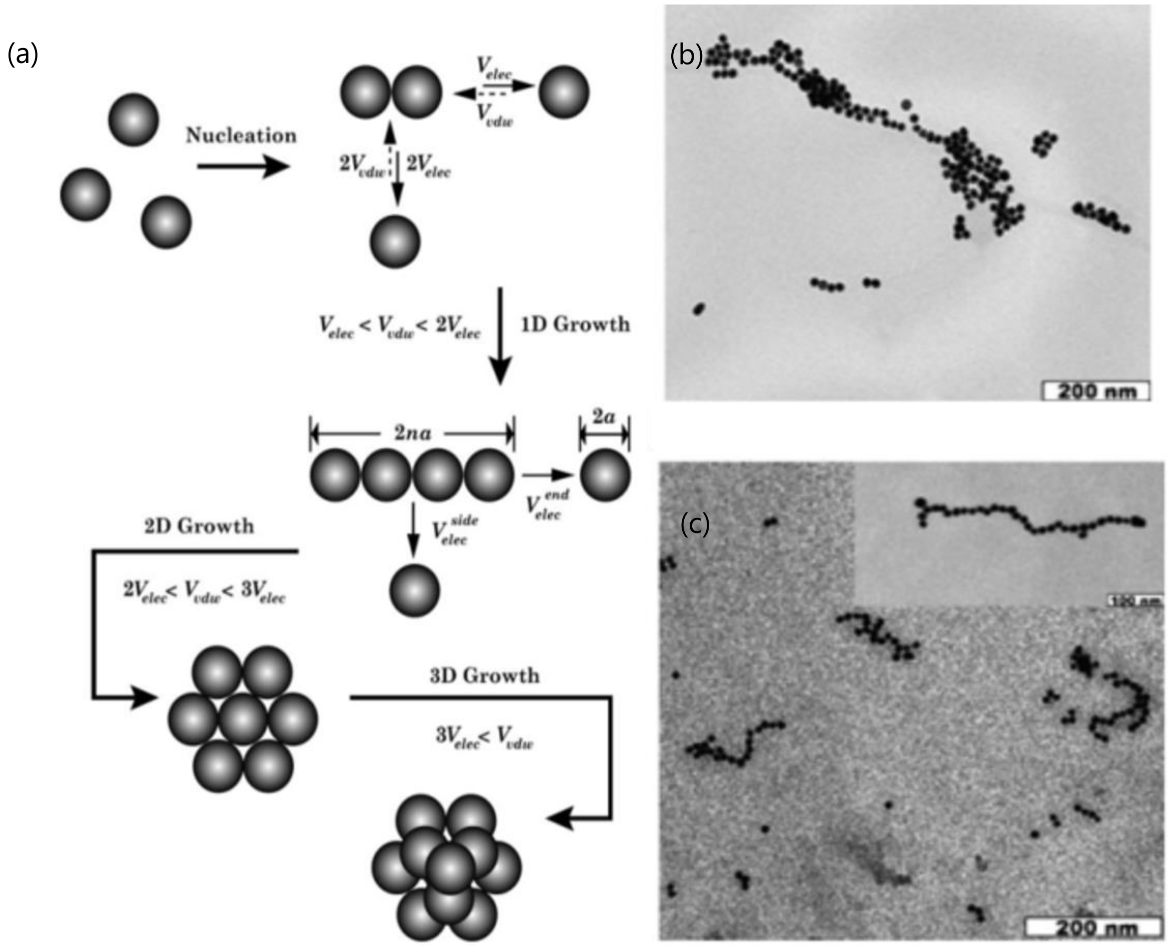

Figure 95. Mechanism of self-assembly of charged particles by a balance between isotropic long-range electrostatic repulsion and isotropic short-range van der Waals attraction in presence of short range anisotropic dipolar attractive forces.

(b) TEM image of TGA-capped gold np self-assembly formed in the presence of 22.5 mM NaCl. (c) Au np chains formed in 1:3 volume ratio of water-acetonitrile.[248]

It can be said that our negatively charged, ultra-small PB nanoparticles behave in a similar manner. But as discussed in section 3.2.1.2, simply manipulating the electrostatic repulsions by adding salts or introducing guanidinium cations were not sufficient in obtaining controlled assemblies of PB. Gallic acid coordination with iron is known to form a complex polymeric network but the addition of this polyphenol to Fe-rich PB nanoparticles did not yield the desired results. However, introducing extra Fe^{III} together with GA to pre-formed PB nanoparticles provide us with stable 1-D nanochains. The characterization studies reveal that the FeGA complex envelops the nanoparticle surface and forms this novel nanostructure.

It could be hypothesized that in the experimental conditions, the alternative addition of Fe^{III} and GA dropwise in diluted conditions will favour the reaction with the surface of PB particles. As a first step, the attraction between Fe^{III} and negative charge of PB nps will lead to immediate coordination of these to pendant CN of ferrocyanides. So all Fe^{III} is rapidly coordinated to form a new layer at the surface of the PB particle, decreasing the charge. The GA has a strong affinity towards Fe^{III}. So we expect the 2 equivalents of GA present in the drop to interact either by H bonds to the CN or encounter Fe^{III} and form a bis-GA complex. The saturation of the surface with new layer of Fe^{III} requires maximum 0.5 among the 2 equivalents to saturate all surface sites. The remaining 1.5 eq. of Fe^{III} and 3 eq. GA, will lead in a step- by-step manner, the growth of the FeGA network around the particles. We believe that only once a certain thickness of shell is obtained, the core-shell particles assemble by striking a balance between isotropic electrostatic repulsions and van der Waals attraction. The short-range anisotropic dipolar attraction also plays an important role in contributing to the final structure. Since electrostatic repulsions on the sides of this dimer would be higher than those at the end, the other core shell PB@FeGA nps in the vicinity preferentially attach to the end, further elongating the structure. This could be the mechanism behind formation of 1D nanochains of ultra-small PB nanoparticles. We see that after addition of 1 eq., some individual particles are still observed together with short chains.

The presence of Fe and gallic acid in between the particles with a thickness at least 1 nm (seen on STEM-EELS) supports the fact that the shell forms before PB associate into 1D-oligomers. We expect then that the addition of the second eq. of Fe^{III} (and 2 eq. GA) will further induce the oriented aggregation of these oligomers. We need complementary experiments to ascertain this explanation. For instance, we will monitor the in situ evolution during the addition by DLS on the new equipment at ISMO very soon. So far, the route followed to obtain the most optimized and controlled assemblies of ultra-small Prussian Blue nanoparticles has been described. The following section summarizes the attempts to diversify the nano-system with other nanoparticles that can incorporate more functionalities.

3.3 NANO-ASSEMBLY DIVERSIFICATION

3.3.1 Gadolinium-PB nanoassembly

Our group had worked on ultra-small gadolinium (Gd) doped Prussian Blue nanoparticles that display high relaxivities. The unprecedented value of 40 mM^{-1}s^{-1} and high T1-weighted contrast enhancement was attributed to the enrichment of surface with Gd^{III} ions, replacing 5% of Fe^{III} to form the PB structure.[177] The same synthesis route was followed to obtain the sub-10 nm particles in water. The GdFeFe[5] will hereafter be mentioned as Gd-PB. The nanoparticles were first UF and washed to remove any excess unbound Gd. Then the assembly formation with FeGA complex was induced. No significant difference was observed between the 2 assemblies and the approximate hydrodynamic diameter was 94 nm. It was further coated with poly CD-citrate polymer and completely characterized. After UF and washing the polymer coated samples, it was concentrated before proceeding to MRI contrast studies in University of Mons, Belgium. The results would be discussed in Chapter 4.

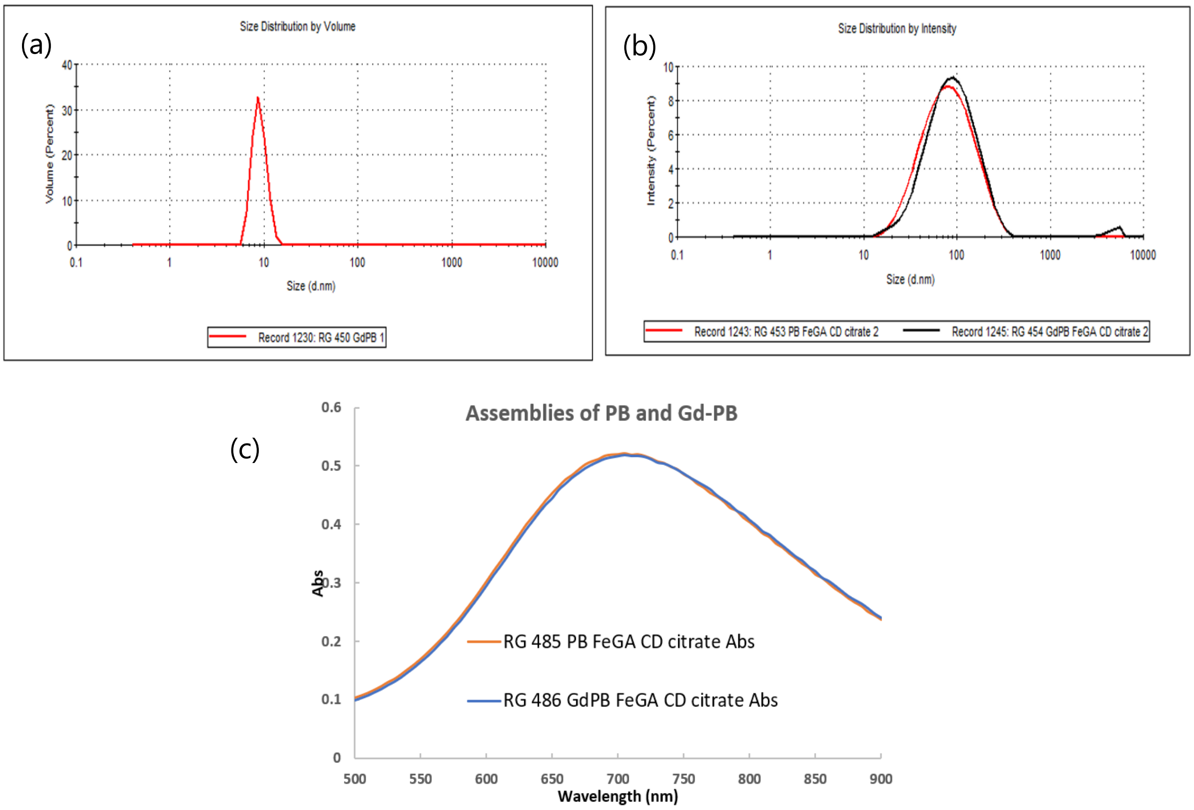

Figure 96. Hydrodynamic diameter of (a) Gd-PB and (b) polymer coated Gd-PB FeGA compared to PB FeGA and (c) UV-Vis analysis results

3.3.2 Cyanosol PBA nanoassembly

Platinum containing analogues of PB described in chapter II, had displayed promising radio-enhancement effect and were non-toxic for bio-medical applications. They were ultra-small particles lying in the size range of 1-5 nm. Assembly formation with these nanoparticles were also attempted. FePt and PtPt nanoparticles were first diluted from 5 mM to 0.5 mM concentration. The synthesis was changed accordingly and two equivalents of Fe^{III} (1 mM) and corresponding neutral gallic acid (2 mM) was added dropwise to both cyanosols. The colourless PtPt solution turned light purple, indicating formation of FeGA complex. DLS measurements revealed that majority of the population lay between 89-92 nm, while 3% has sizes around 9 nm. This was an indication of formation of aggregates of PtPt.

The green FePt solution turned blue at the end of the reaction due to the reaction of ferrocyanide at the surface of FePt with added Fe^{III}. DLS indicated that the sample was composed of 2 populations: 44% around 140 nm while the rest where small and below 15 nm. Transmission electron microscopy verified the results as FePt-FeGA had significant number of chain like assemblies together with single particles.

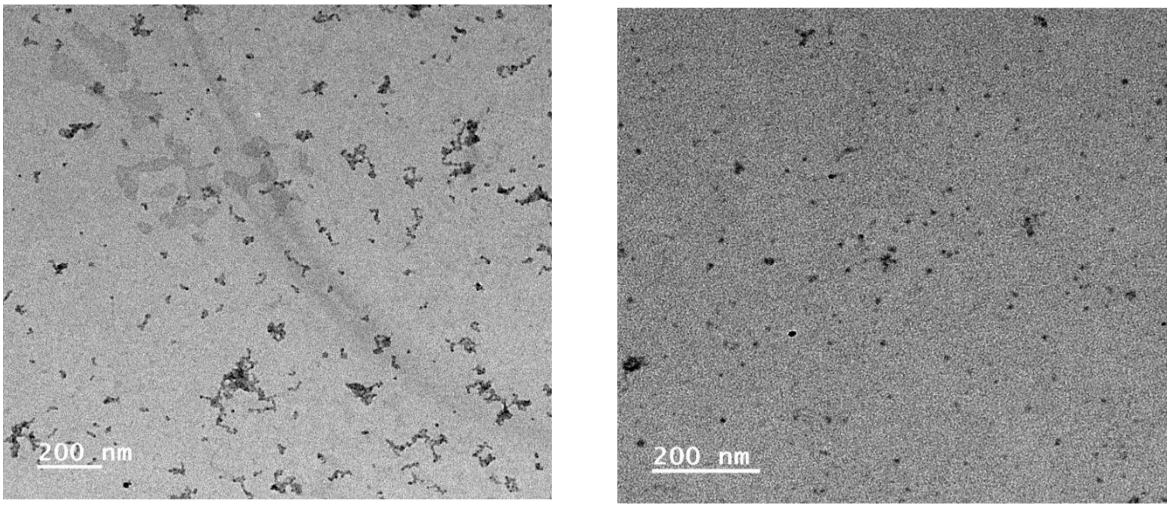

Figure 97. TEM micrographs of FePt-FeGA showing both assemblies and individual particles

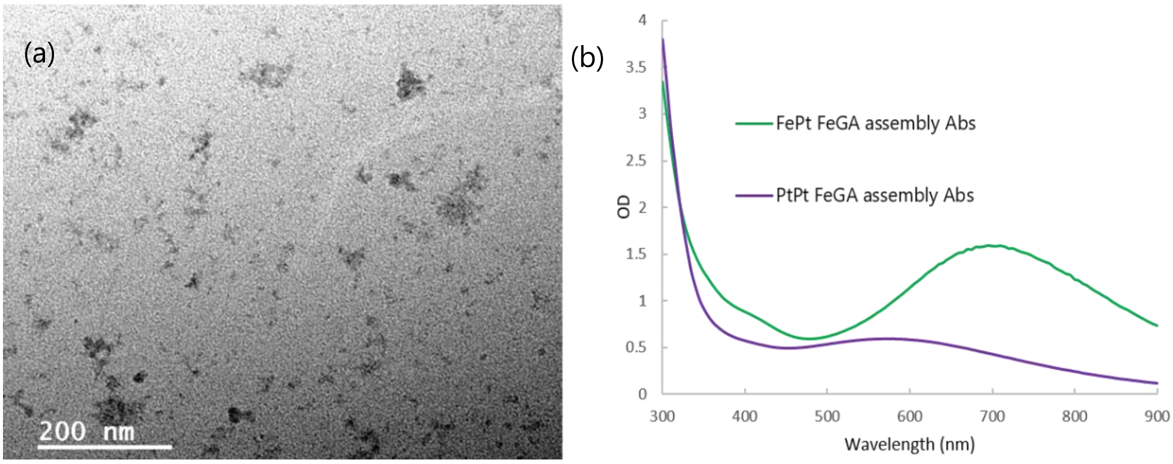

Figure 98. (a) Brightness enhanced-TEM image of PtPt-FeGA assemblies (b) Absorption spectra of assemblies formed with FePt and PtPt nanoparticles

Tuning the concentration and reaction conditions may lead to better, controlled chains of FePt nanoparticles. The pure PtPt nanoparticles are very small and appear with poor contrast in

TEM. The trial showed that the assemblies could be formed with it, but the images are not reliable. They indicate that there is less control over the shape of aggregates. These are preliminary results and the project would be continued in the future. Building assemblies of these nanoparticles can further improve radiation therapy as their tumour permeation and retention time within the body could be increased. This section proves that the strategy could be extended to GdPB and other modifications on PB will be described in Chapter 4.

3.4 LINKER VARIATIONS

3.4.1 Effect of cation

In an earlier section, PB-Gallium Gallate nano-assembly system was described. Introduction of Ga^{3+} yielded some assemblies even though it was less controlled than its Fe^{3+}counterpart. This led to the question, can Prussian Blue and its analogues be assembled in the presence of any cation? The effect of monovalent sodium and di-valent calcium ions were investigated. First, PB nanoparticles were synthesized in the usual manner. Gallic acid (1 mM, pH=7) and the salt solutions: NaCl (0.5 mM) or $CaCl_2$ (0.5 mM) were prepared in water. Then the salt solution and GA were introduced dropwise into PB, under constant stirring. The reaction proceeded for 30 minutes, as usual and DLS measurements were done. The hydrodynamic diameter of the particles changed to 13 nm in the presence of Na^+ and 11 nm with Ca^{2+}.

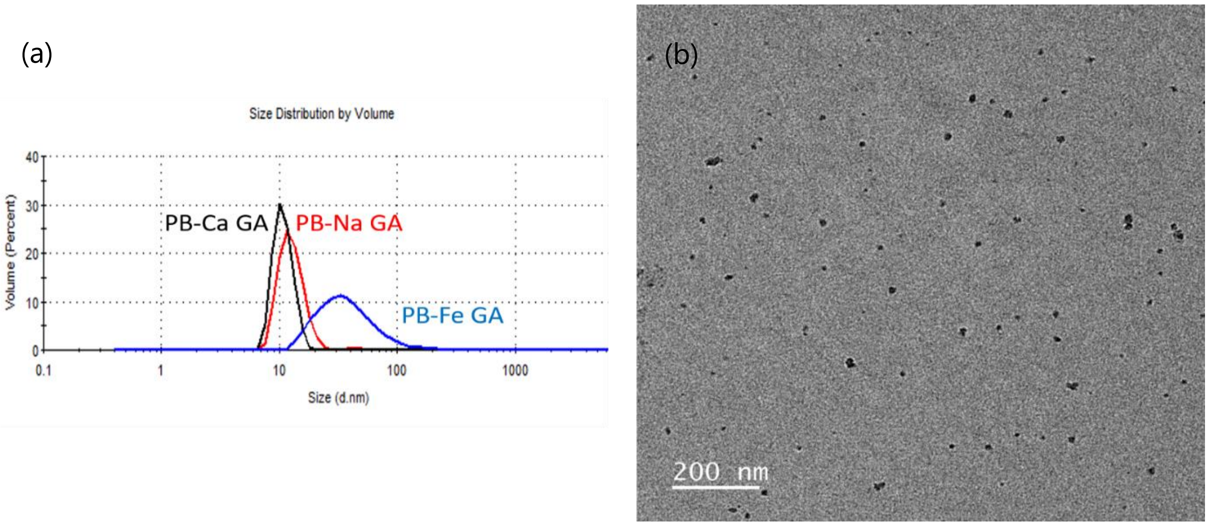

Figure 99. (a) Comparison of DLS results of PB assemblies in the presence of sodium, calcium and ferric ions (b) TEM micrograph of PB-Ca GA

TEM studies also showed only well-individualized single particles of PB in the presence of both salts. Addition of 1 mM salt also led to similar results. Therefore, it was concluded that the presence of ferric ions was necessary for gallic acid to behave as a linker for PB nanoparticles. The experiments were performed by Stella Bessiere and Aurelia Bertoux as a part of their Bachelors internship project.

3.4.2 Effect of polyphenol

It was established that the complex formed between Fe(III) and gallic acid was crucial for assembly generation. But it was important to know if this system could be further expanded with other linkers. Ellagic acid is another naturally occurring polyphenol, commonly found in fruits, berries and vegetables. It has a bulkier structure and is formed by dimerization of gallic acid by oxidative aromatic coupling with intramolecular lactonization. It is known to have antioxidant, antimutagenic and anticancer properties. Therefore, efforts were made to synthesize assemblies using Ellagic acid (EA). Unfortunately, a challenge with EA was its very low solubility in water. It is slightly soluble in ethanol, but a concentration of 1 mM cannot be achieved as it starts precipitating out. Therefore after multiple trials, EA clear solution was obtained in ethanol at a maximum concentration of 0.66 mM, after sonication for 30 minutes.

The assembly formation protocol also had to be changed to incorporate ellagic acid. Usually equal volumes of nanoparticle, Fe(III) and GA solution are used but in this case when the proportion of water is higher than alcohol content, the EA precipitates and destabilizes the whole system. The first set of experiments involved adding higher volume (10 V) of EA with respect to PB and iron nitrate. But the colloidal suspension turned turbid within 24 hours. Therefore, Fe^{3+} solution was also prepared in ethanol-water mixture and maintaining the ratio of 13:10 between the solvents, showed first set of positive results. This sample would hereafter be mentioned as PB- FeEA (10V). The hydrodynamic diameter was around 110 nm after the synthesis and TEM analysis displayed long strands of nanoparticles. The sample was regularly monitored with DLS and there was an indication of evolution with time. It deposited 3 days after the synthesis.

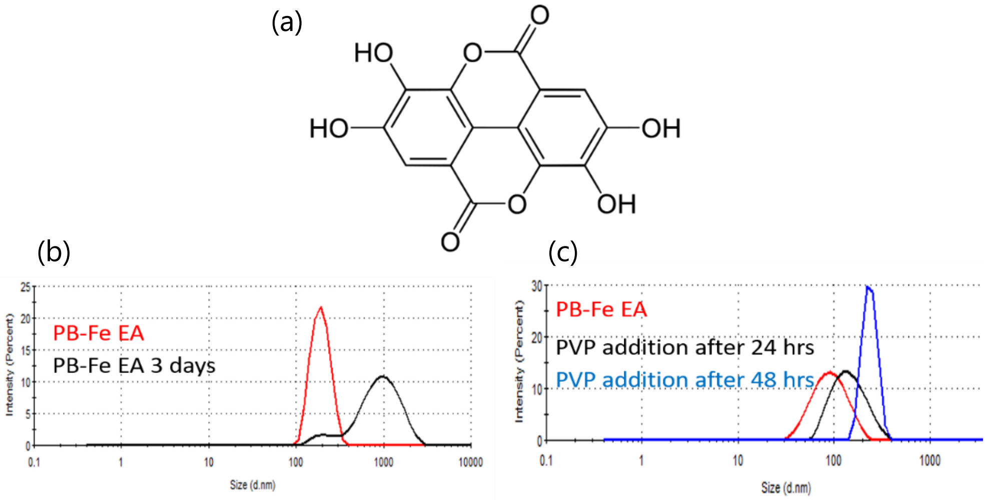

Figure 100. (a) Structure of Ellagic acid (b) Evolution of PB-FeEA assemblies with time (c) Effect of addition of PVP at different time points to arrest the aggregation process.

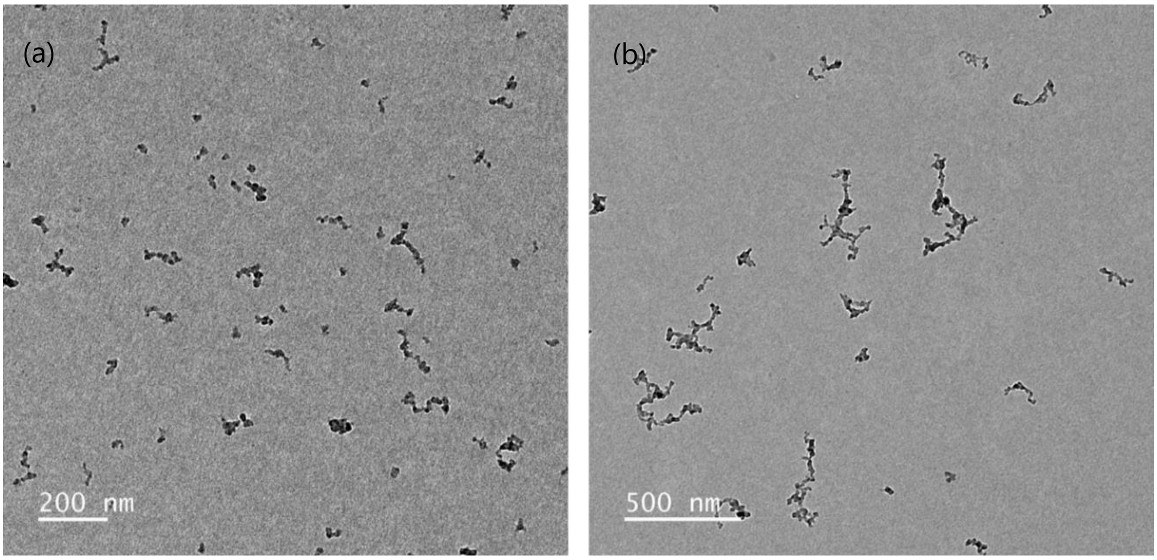

Figure 101. PB-FeEA assemblies with 30 equivalents PVP added (a) 30 mins and (b) 24 hrs after synthesis

Addition of 30 equivalents of PVP appeared to stop this aggregation and rendered some stability to the solution. Interestingly, it was also observed that depending on time of PVP addition, shorter or longer chains of PB-FeEA could be obtained. Surprisingly, in the presence of ellagic acid, assembly formation occurred with NaCl and $CaCl_2$ salts (0.33 mM solution in ethanol). The hydrodynamic diameter detected with DLS lay between 47- 50 nm. TEM imaging revealed that short assemblies are formed with sodium, while Ca^{2+} ions form ~120 nm long chains of PB nanoparticles. The mechanism of formation here, is certainly different from what was observed with gallic acid. It is hypothesized that the water- ethanol mixed solvent plays a major role in assembling the particles together. The synthesis optimization of EA assemblies was carried out by Haziq Naseer Khan as a part of his Masters internship project.

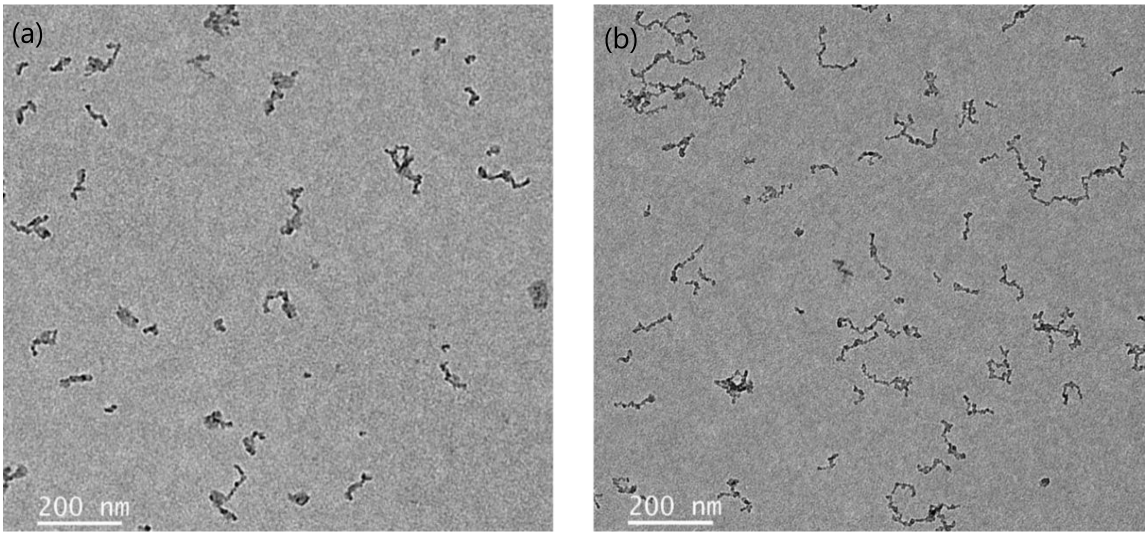

Figure 102. Assemblies of (a) PB-NaCl EA and (b) PB-$CaCl_2$ EA

3.5 CONCLUSIONS

This chapter reports the method development process behind forming assemblies of highly charged nanoparticles. At first, simple experiments were made to study the influence of varying electrostatic forces, using different polymers and organic linkers. But combining coordination and polymer chemistry and fine-tuning each parameter was required to assemble ultra-small Prussian Blue nanoparticles. Metal phenolic networks rising from iron- gallic acid interactions led to the organization of PB nanoparticles into chains. As far as we know, this is the first time such a system has been described. These 1-D nanochains are synthesized in water, at room temperature, without using any surfactants. The method developed is easily reproducible and the assemblies formed remain stable over long periods of time. They can be easily post-coated with desired polymers which further adds to the functionality of the nanochains. Moreover, when compared to individual nanoparticles some improvement in the optical properties was also observed in the assemblies. Complete characterization of these newly developed nano-systems have been described in the chapter.

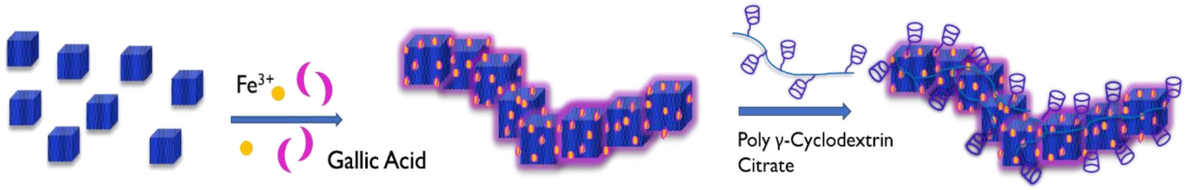

Figure 103. Schematic summary of PB nanochain formation, coating with CD-citrate polymer and its extrapolation to other nano-systems

Extension of the system with diverse building-blocks were also attempted. Prussian Blue nanoparticles doped with gadolinium could easily form similar assemblies. Platinum containing analogues of PB show promising results. Larger nanoparticles of PB (15-20 nm) were synthesized using a seed-mediated approach. These particles however, could not form assemblies. It is hypothesized that the electrostatic repulsions between these bigger particles are of a greater magnitude which in turn causes hindrance towards assembling. Applying the same synthetic path with CsNiCr and CsNiCo analogs of PB, did not lead to chain formation. It may be due to the interference of Cs^+ in the double layer. Therefore, for each new nanoparticle to form a stable and controlled system, rigorous and careful optimization of reaction conditions is required. PB nanoparticles could also be assembled with other polyphenol linkers like ellagic acid and its synthesis in water-ethanol mixture has been obtained.

In conclusion, it can be said that the aim with which we started this project was accomplished. Ultra-small PB nanoparticles could infact be assembled into larger nanostructures and this might lead to better EPR targeting, MRI contrast and increase the blood circulation time. So, the next step was to determine if forming such assemblies improve the drug-encapsulation capabilities of these sub-10 nm particles and if targeted release could be obtained. Moreover, it was recently found that when the delivery performance of nanocarriers of various shapes and sizes were compared, the short, tubular and non-rigid nanostructures was found to have better intra-tumoral invasion capacity. Also negatively charged nanoparticles evoke lower immune response from the body as compared to a positively charged system.[249,250] These factors make this new PB nano-system more desirable for bio-medical applications and its theranostic capabilities needed to be thoroughly investigated.

CHAPTER IV

4 NANOCHAINS FOR THERANOSTIC APPLICATIONS

4.1 INTRODUCTION

This chapter is devoted to the therapeutic and diagnostic applications of Prussian Blue nanochains developed during the doctoral thesis. It has been established that the tumour blood vessels are more leaky than healthy vessels and therefore nanomaterials can progressively accumulate in the pathological site.[15] Therefore, several types of drug carriers are synthesized in nano-size (>5 nm to avoid kidney clearance), to prolong blood circulation time and passively collect and be retained in the tumour. This phenomenon is called the EPR effect. The study of this passive drug targeting method is difficult as each cancer is starkly different and even within a single tumour, certain vessels are leakier than the others. Also, there could be a difference between the permeability of patient tumours and generally studied animal models. Many comprehensive studies have been performed over the last decade to clearly identify and characterize the EPR effect. Theek et.al employed a combination of fluorescence and contrast-enhanced ultra-sound imaging to follow drug targeting of 10 nm polymeric carrier to tumour site and it was found that a very low percentage of the injected dose accumulates at the target site with EPR.[18] Therefore, it is essential to maximize the amount of drugs encapsulated in any nanosystem, in order to enhance the therapeutic efficiency.

As discussed in chapter 1, a large variety of Prussian Blue nanomaterials have been developed for drug delivery purposes (see Table 1). The hollow or mesoporous etched nanoparticles lying in the size range of 100-300 nm, can carry anti-cancer molecules like doxorubicin, camptothecin etc. with high drug payload of 33-63 wt.%. The large size of these nanoparticles would be beneficial for EPR targeting, however their elimination would be problematic. Consequentially, attaining FDA approval for clinical application would be difficult. On the other hand PB particles, synthesized using green conditions in water, present low payloads in the range of 7 to 18.5 wt. %. This is because in the absence of etching with strong acid or base, the drugs could only be physisorbed on the PB nanoparticles. The aim behind building assemblies of ultra-small PB nanoparticles was to raise circulation time and improve EPR effect while also increasing the surface area available for drug loading. This chapter will describe the various experiments performed to maximize encapsulation of chemotherapeutic agents. Doxorubicin was used as a model drug to study the loading and release in different media. Then, the photothermal therapeutic properties of Prussian Blue and its assemblies were investigated under different experimental conditions. The enhancement of magnetic resonance imaging contrast and relaxivity measurements were performed to evaluate the diagnostic capabilities of these novel nanochains. The safety of these Prussian Blue structures were evaluated using toxicity studies. Loading fluorescent markers to follow the nanochains *in-vivo* and the diversification of the nanosystem to incorporate more therapeutic functionalities was attempted and the results have been briefly described in the last section.

4.2 DRUG ENCAPSULATION IN PRUSSIAN BLUE NANOCHAINS

The most commonly used anti-cancer drug is doxorubicin (Dox). It is isolated from bacteria Streptomyces peucetius var.caesius and has a chemical formula of $C_{27}H_{29}NO_{11}$. It is an anthracycline antibiotic, capable of killing cancer cells at every stage of their life cycle and is effective against various forms of cancers. Since Dox has a free amino group, it is positively charged at physiological pH. Recent studies have shown that this drug molecule undergoes dimerization in neutral buffers and precipitates out of solution. This covalent dimer formation is a result of keto-enol tautomerization, imine formation and oxidation and could occur in physiological conditions. It is also established that precipitation of doxorubicin occurs in the presence of other anti-cancer drugs, specifically 5-fluorouracil.[251] Therefore, it is necessary to use a cargo that can effectively mediate delivery of Dox in its intact form to the target site. Different types of carriers including liposomes, polymeric nanoparticles, micelles as well as exosomes have been developed over the past decade for this purpose.[252] Cyclodextrin cages have been well documented as being able to form inclusion complexes with doxorubicin and facilitate their delivery for cancer therapy. [253,254] Similarly, various types of PB nanoparticles (hollow/mesoporous/gelatin conjugated etc. Table 1, Section 1.3.3) have been used as Dox encapsulating agents.

The stability of Prussian blue nanoparticles in solution comes from its inherent negative charge. Electrostatic interaction between PB and Dox is favoured because of the opposite charges. But introducing high amounts of the drug to the nanoparticle solution may disturb the balance and lead to precipitation. The choice of the poly γ-CD citrate was guided to potentially enhance the loading capacities, in addition to the electrostatic interactions with the chains, and prevent the deposition. A wide range of drug concentrations were studied and careful optimization of experimental parameters was done to encapsulate Dox within PB nanochains; both bare and coated with poly γ-CD citrate. The experiments were conducted at Institute of Molecular Sciences (ISMO), Université Paris Saclay in the laboratory of Prof. Ruxandra Gref.

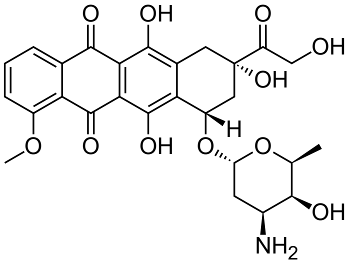

Figure 104. Structure of anti-cancer drug : Doxorubicin

4.2.1 Stability of sample with doxorubicin

As the first step, the stability of nanochains in the presence of doxorubicin was evaluated. The synthesis procedure described in chapter 3 was followed to form PB FeGA and the size and zeta potential was recorded. A part of the sample was separated and coated with γ-CD citrate polymer (0.5 equivalents). The final PB concentration in both samples were brought to 41.5 μM before starting the experiment. Doxorubicin stock solutions of three concentrations (0.1, 1 and 10 mM) were prepared and a constant volume of each was added to 2 mL of NP assembly solution to ensure same dilution. The samples contained 2, 20 and 200 μM of Dox respectively and were incubated for 18 hours at room temperature under gentle stirring. The changes were monitored using DLS, TEM and zeta-potential measurements and results are indicated in Fig.107.

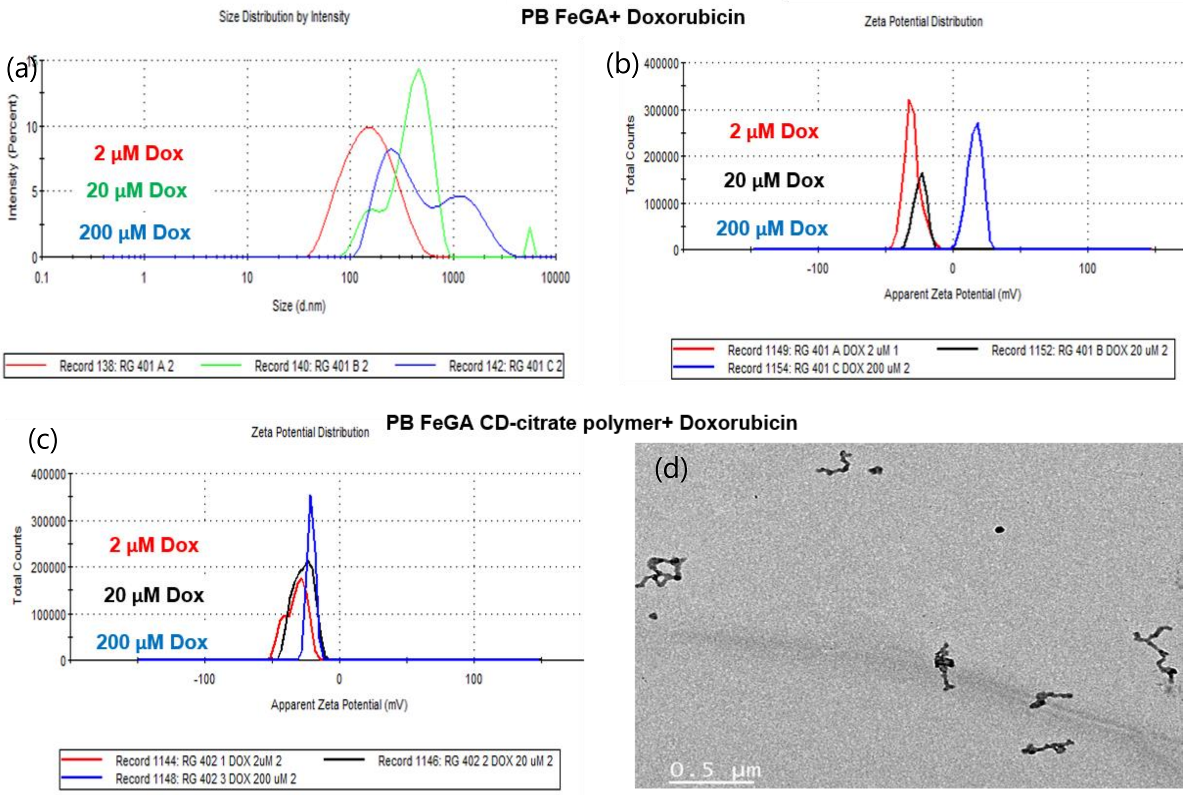

Figure 105. Effect of doxorubicin addition on (a) size and (b)zeta potential of PB FeGA assemblies (c) zeta potential of PB FeGA- 0.5 eq. CD citrate polymer and (d) TEM image of polymer coated PB FeGA with 200 μM Dox

After the incubation time, the solutions containing 2 μM of Dox appeared unchanged and had a clear blue colour. The bare PB FeGA assemblies (without poly γ-CD citrate) aggregate and completely precipitate out of the solution in the presence of 200 μM of Dox. DLS indicates large sizes (>1000 nm) and the zeta potential shifts drastically to the positive side with a value of +16 mV. Some deposition in the sample was also observed at 20 μM. Therefore, drug concentrations need to be lowered to ensure stability. Contrastingly, the polymer coated PB

FeGA remained much more stable in the presence of doxorubicin. At 20 µM, the sample appeared unchanged with DLS and TEM indicating no aggregation or deposition. The zeta potential of the solution remained negative with a value of -21.3 mV even upon addition of 200 µM Dox, but the size of chains significantly increased (< 500 nm). Therefore, further optimization was necessary but this was the first indication of increase in stability in the presence of polymer coating.

4.2.2 Drug loading and Sample optimization

The drug loading experiments involved multiple steps. The encapsulation of doxorubicin was evaluated in four types of samples:

a) Prussian Blue (PB) nanoparticle solution
b) Prussian Blue assembly (PB FeGA) solution
c) PB FeGA assembly + 0.5 equivalents γ-CD citrate polymer
d) PB FeGA assembly + 0.05 equivalents γ-CD citrate polymer

It was important to understand if building assemblies of ultra-small PB nanoparticles effect its drug loading capabilities. So the same concentration ([PB]=41.5 uM) of bare nanoparticles and assembly was compared with different amounts of Dox. It was earlier established that presence of CD-citrate polymer renders a certain stability to the assembly solution. But, it was necessary to modulate the exact amount of this high molecular weight polymer required to optimize the loading and ensure no free poly γ-CD citrate remains in solution. Therefore, different amounts (41.5 and 4.15 µM, 10 mL) of polymer was added to synthesised assemblies (83 µM,10 mL) before the ultra-filtration and washing steps. Depending on the required concentration of doxorubicin (9, 18, 47, 93 and 192 µM) in the final sample, stock solution of the drug was diluted and added to these samples. Every combination was studied twice to avoid experimental errors and obtain reliable results. The drug-nanoparticle mixture was incubated for 16 hours at room temperature, under gentle stirring.

Complete characterization using DLS, TEM and zeta potential was performed for each sample. Pure PB solution is very unstable in the presence of doxorubicin. The 3-4 nm PB nanoparticles evolved to ~85 nm aggregates in presence of 9 µM Dox and higher concentrations led to complete precipitation of the solution. The assembly formation helps stabilize the system and bare PB FeGA nanochains can tolerate up to 18 µM of doxorubicin. The percentage of large aggregates appear with 47 µM concentration and was indicated with dynamic light scattering experiments (Figure 109 c). Majority of the assemblies had evolved to sizes above 1400 nm, while only 11 % remained below 250 nm and this could be verified with TEM analysis using glow discharge treatment to prevent aggregation on the grids.

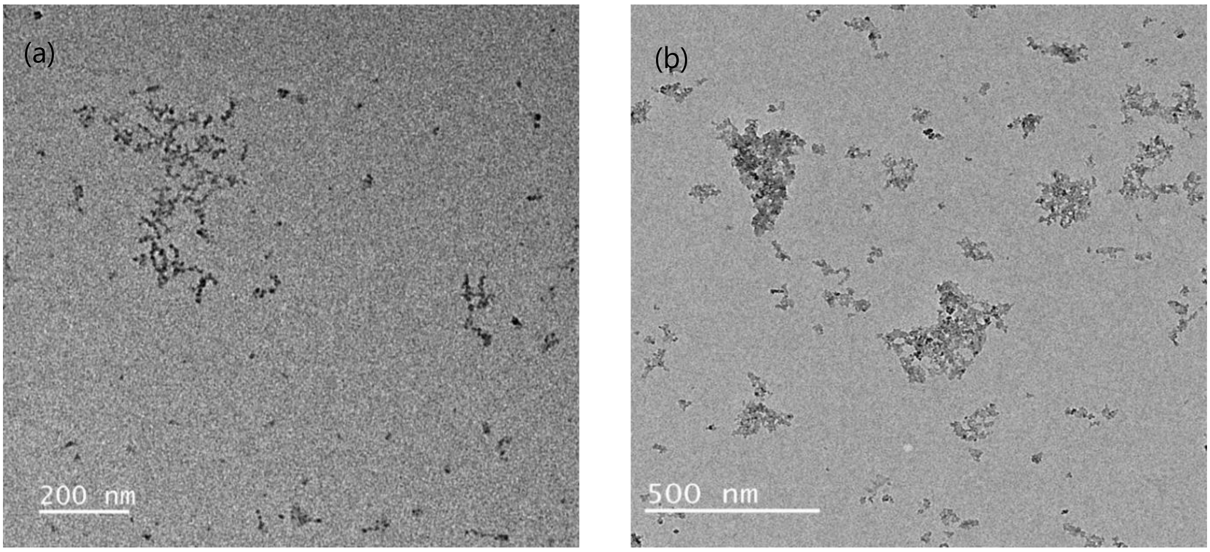

Figure 106. TEM images of Prussian Blue nanoparticles with (a) 9 µM and (b) aggregates observed on introduction of 18 µM doxorubicin.

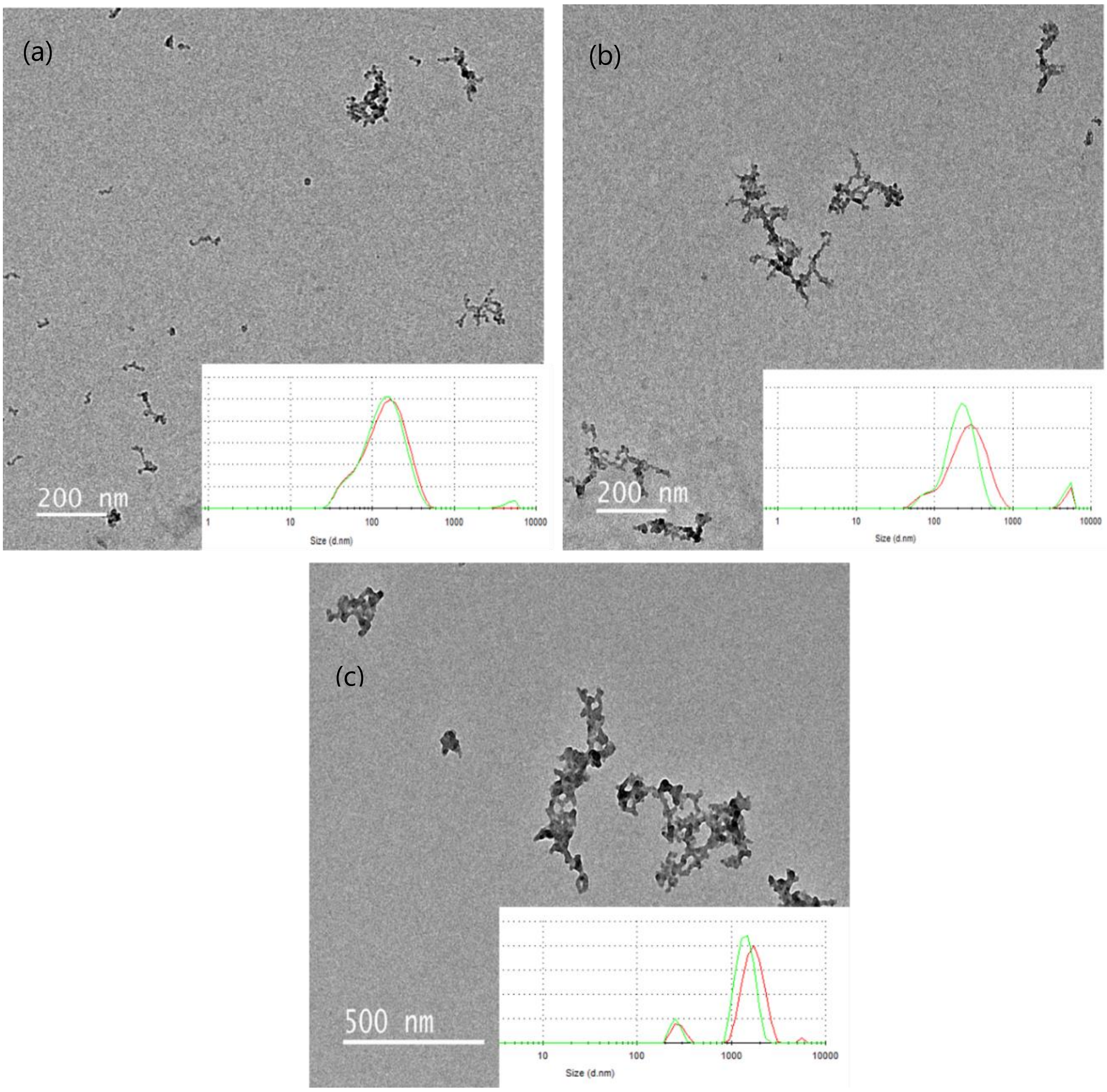

Figure 107. Results of TEM and DLS analysis of PB FeGA with (a) 9 µM (b) 18 µM (c) 47 µM of doxorubicin.

As mentioned in the earlier section, assemblies coated with poly γ-CD citrate remain more stable in the presence of higher drug concentration and the exact amount of polymer required, needed to be determined. PB FeGA with 0.05 eq. polymer is capable of encapsulating 47 µM of Dox (Fig.111 a) and starts precipitating only at 93 µM (DLS > 2000 nm) concentration. Presence of 10 more equivalents of polymer increases the tolerance of the sample. Although aggregation of the assemblies begin with the introduction of 93 µM doxorubicin as seen with TEM analysis (Fig. 111 b), the solution remains stable. Only when the amount of drug is 4.6 times the nanoparticle concentration (192 µM Dox), a small percentage of the sample forms 1000 nm aggregates and starts precipitating.

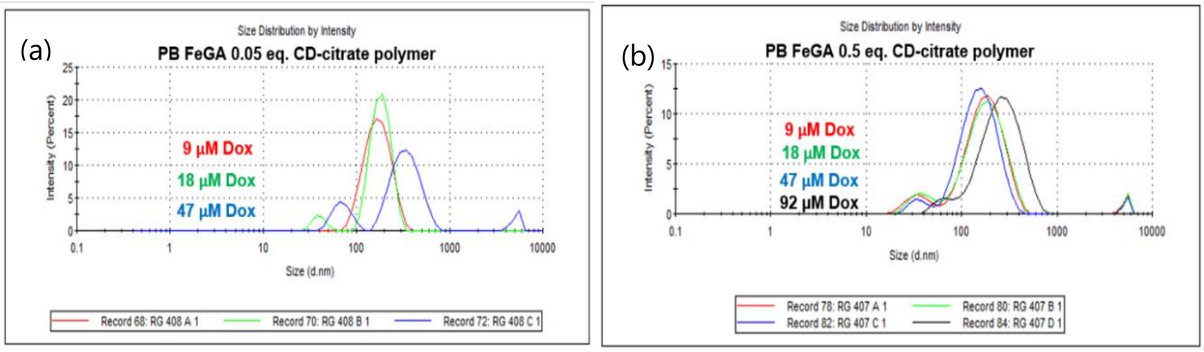

Figure 108. Effect of doxorubicin addition on hydrodynamic diameter of PB assembly coated with (a) 0.05 eq. (b) 0.5 eq. CD citrate polymer

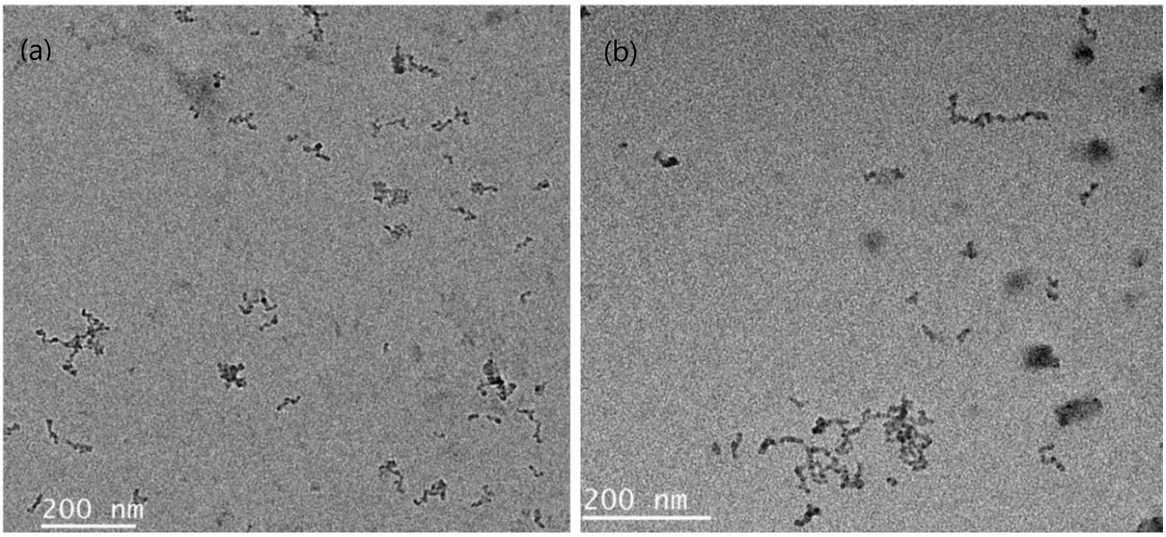

Figure 109. TEM micrographs of (a) PB FeGA 0.05 eq. polymer with 47 µM Dox and (b) PB FeGA 0.5 eq. polymer with 93 µM Dox.

Once the incubation period elapsed, an ultracentrifuge (114000 g, 60 minutes) was used to deposit the drug loaded nanoparticles/assembly into a pellet. The supernatant was carefully separated. As seen from UV-Visible spectra in Fig.112 (a), the characteristic absorption of Dox, centered around 490 nm is present together with the PB band at 700 nm in the starting sample. As expected the signal rises with an increase in the amount of doxorubicin added. The nanoparticles are completely removed after the ultra-centrifugation step, as the 700 nm signal vanishes in the supernatant. Only the free, un-encapsulated drug is present in the recovered supernatant which contributes to the absorption, evidenced in Fig.112 (b).

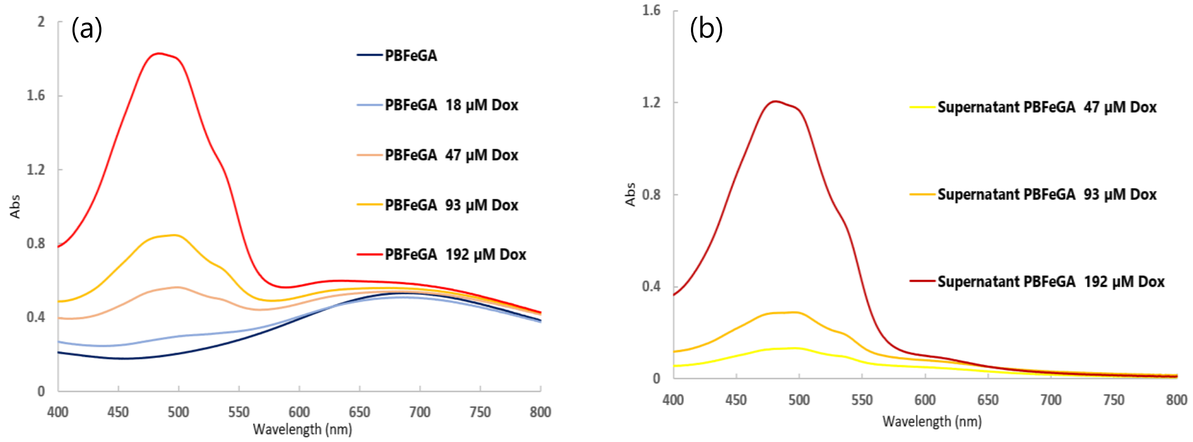

Figure 110. UV-Visible spectroscopy results of (a) PB assembly with varying amounts of doxorubicin and (b) Supernatants of PB assembly + Dox recovered after ultra-centrifugation.

The supernatant solutions were diluted with DMSO keeping the volume ratio constant at 1:1, to dissociate the complexes CD:Dox.[229] Doxorubicin has an intrinsic fluorescence with a characteristic emission around 590 nm (Fig. 113 a). This property was used to determine the concentration of free Dox in supernatant. The fluorescence spectra of each diluted supernatant mixture was recorded. Solutions with known concentrations of doxorubicin were prepared in DMSO-water mixture and a calibration curve was obtained. The exact amount of un-bounded drug in the supernatant could be quantified by comparing the fluorescence intensity with the calibration plot and incorporating the dilution factor. Percentage encapsulation efficiency of each of the four samples investigated, with their respective drug concentrations were then be calculated using the following formula:

Encapsulation Efficiency (EE %) =[(Total Dox Input – Dox in supernatant)/ Total Dox Input] × 100

Drug payload is the weight percentage of encapsulated drug molecule with respect to the weight of the nanocarrier. Since the CD-citrate chain has a high-molecular weight, bulky structure, a small increment in the amount of polymer drastically increases the overall weight of the nanoparticle assembly, thereby reducing the payload percentage.

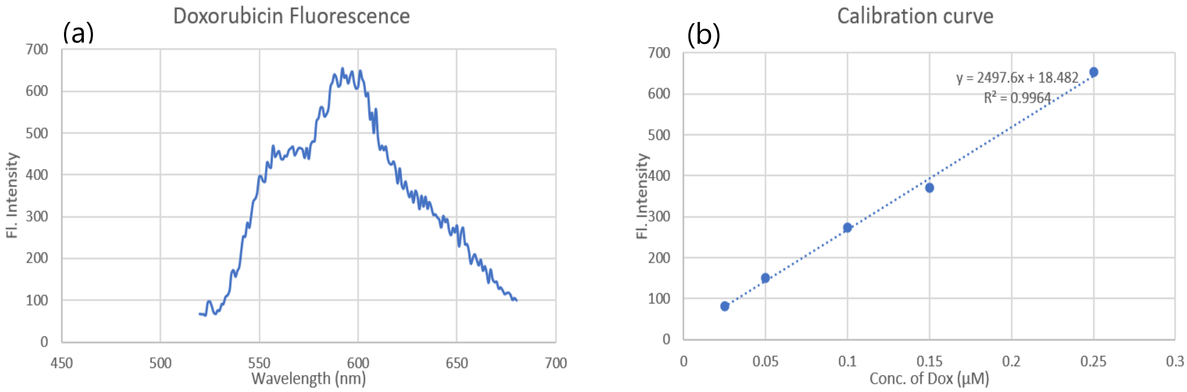

Figure 111. (a) Fluorescence signal of doxorubicin solution and (b) Calibration curve prepared using known concentrations for determining the un-encapsulated Dox in supernatant.

Table 5. Encapsulation Efficiency (EE %) obtained for the samples studied, at respective doxorubicin concentrations.

Dox conc.	**9 μM**	**18 μM**	**47 μM**	**93 μM**	**192 μM**
Prussian Blue EE	91.9 ±0.03 %	80.4 ±0.01 %	63.5 ± 0.8 %	60.3 ± 0.1%	54.2 ± 0.2%
PB FeGA assembly EE	95.2 ± 0.3 %	95.6 ± 0.1 %	90.7 ± 0.5 %	72.8 ± 0.6 %	51.7 ± 1.2%
PB FeGA @ 0.5 eq CD citrate EE	62.5 ± 0.7 %	49.2 ± 0.1 %	62.9 ± 0.05%	68.3 ± 0.5%	72.9 ± 0.01%
PB FeGA @ 0.05 eq CD citrate EE	91.8 ± 0.4 %	93.7 ± 0.1 %	96.2 ± 0.2%	78.2 ± 0.03 %	51.4 ± 0.1%

Ultra-small Prussian blue nanoparticles (~5 nm) were the building blocks used to create assemblies. These bare single nps are capable of interacting with doxorubicin, purely by electrostatic forces due to a difference of charge. Maximum encapsulation efficiency of ~92 % could be attained at the lowest concentration (9 μM). But as the amount of drug introduced is increased, the EE reduces and the sample deposits out of the solution. The formation of PB nanochains with iron and Gallic acid, imparts a certain stability to the solution and it can tolerate up to 18 μM of Dox. Maximum loading efficiency of 95.6 ±0.1 % can be obtained from

PB-FeGA assemblies at this concentration. This could be attributed to a higher surface area available in the nanochain for interaction with the drug. Higher quantities cause aggregation and form huge interconnected assemblies (seen in Fig. 109 c). The "nano" property is lost and once deposition begins, the drug loading capabilities are significantly lowered. This has to be avoided in order to form an effective and efficient theranostic system.

Coating the PB FeGA assemblies with poly γ-CD citrate is a crucial step. It improves the stability of the solution to a large extent. In the presence of 0.5 eq. of the polymer (20.75 µM γ-CD citrate on 41.5 µM PB FeGA) the sample can handle up to 10 times more doxorubicin without completely precipitating out. The gamma-cyclodextrin citrate polymer is capable of trapping Dox molecules in their cages but it was observed that the encapsulation percentage decreases to ~73 %. This might be due to the fact that the polymer chains are present in excess and the unlinked polymer present in solution also traps the drug introduced to the sample. In this manner the amount of drug available for encapsulation in polymer coated Prussian Blue was reduced, leading to a low EE %. This hypothesis was further verified. When the amount of polymer used was reduced to 0.05 equivalents (2.075 µM) with respect to the PB in assemblies (41.5 µM); the encapsulation efficiency increases from approximately 62 to 92% at the lowest drug concentration. It keeps rising until 96.2 ±0.2 % loading is achieved with 47 µM Dox, indicating almost complete encapsulation of the drug. This indicates that all the polymer added is coated on the nanochain surface, maximizing the drug payload, while also providing a stabilizing effect. High concentrations cause deposition and consequentially the EE % decreases. The experiments were reproduced and intermediate Dox concentrations (between 47 and 92 µM) were also attempted. Sample optimization was done in this manner. It could be concluded that PB FeGA assemblies coated with 0.05 equivalents of γ-CD citrate polymer provided the best balance between stability and encapsulation efficiency, and therefore would be used for further experiments.

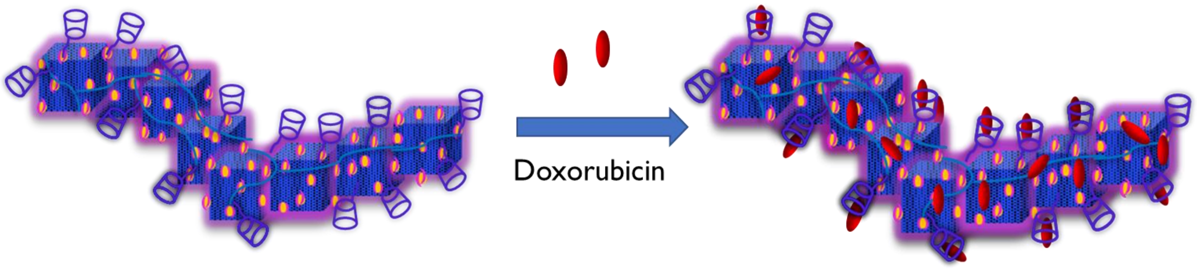

Figure 112. Schematic representation of doxorubicin loading on PB FeGA -CD citrate assemblies

4.2.3 Optimization of Incubation time

Once the sample type with best drug interaction and encapsulation efficiency was determined, effect of other experimental parameters were investigated. Usually nanocarriers need to be incubated for 24 or 48 hours with respective drug molecules to successfully load them.[167,255]

It would be experimentally beneficial to reduce this time duration. Therefore, it was important to determine the appropriate amount of incubation period needed for optimal drug loading. Fresh PB FeGA-0.05 eq. CD citrate was synthesised. After ultra-filtration and washing steps, the sample was divided into multiple aliquots and 47 μM of Dox was added to each. The vials were protected from light and incubated at room temperature under gentle stirring for 1, 4 and 16 hour periods. Each time point was studied in triplicate to incorporate error between measurements. At the end of the designated incubation time, the samples were treated with ultracentrifugation, supernatant separation, UV-Vis and fluorescence spectroscopic studies.

Drug Payload (wt. %) =[(Weight of encapsulated Dox/ Weight of PBFeGA-0.05 eq. CD citrate] × 100

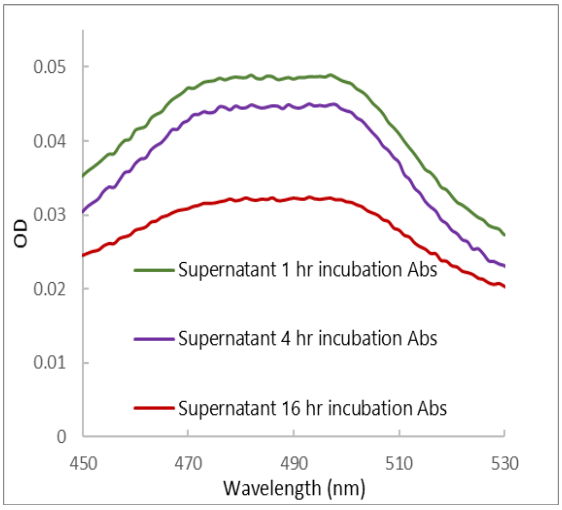

Incubation time	Encapsulation Efficiency (EE)	Drug Payload
16 hr	93.5 ± 1.7 %	35.6 ± 0.6 %
4 hr	89.8 ± 0.7 %	34.2 ± 0.3 %
1 hr	84.6 ± 2.3 %	32.2 ± 0.9 %

Figure 113. (a) UV-Visible spectral plot (doxorubicin region) of recovered supernatant solutions and (b) Average encapsulation efficiency and drug payload percentages calculated for the same sample under different incubation time periods.

The spectroscopy results provide a clear indication that more drug could be encapsulated with longer incubation times. The supernatant separated after 1 and 4 hours have a higher Dox signal compared to the sample incubated for 16 hours. However, the difference is not huge and exact amount of un-bounded doxorubicin in all three cases were determined using fluorimetry. The calculation revealed that almost 94 % of input drug is encapsulated in the PB nanochains within 16 hrs and a high drug payload of ~36 wt.% could be achieved. Furthermore, only a 4 hr period provided a loading efficiency of 90 %. Surprisingly, even just 1 hour incubation of doxorubicin with our nanosystem led to a 84.6 ± 2.3 % encapsulation. The low error bars prove that the experiments are reproducible and the results are reliable. As far as we know, such high EE % at low incubation times has never been reported before for PB containing systems. Moreover, obtaining a drug payload of 32-36 % with ultra-small, non-etched PB nanoparticles is unprecedented.

It could be hypothesized that a combination of electrostatic attractions between Prussian Blue nanoparticles and Dox, together with the host-guest interactions and formation of inclusion complexes within cyclodextrin cages are responsible for such high encapsulation. Furthermore, the citrate moieties covering the nano-assembly structure attract the positively charged doxorubicin and contributes to the enhanced loading of drug molecules within a short time duration. These results suggest that the nanochains would be very efficient drug carriers.

4.3 DRUG RELEASE FROM PB NANOCHAINS

The previous experiments provided encouraging results regarding doxorubicin loading in the nano-assembly. It was important to determine if the encapsulated drug could be released at the target site and whether external stimuli would aid in the process. For the targeted therapeutic applications, a drug carrier would have to be introduced into the body, travel via blood and reach the tumour site. Blood contains different components including proteins, metals and enzymes that can interact with the injected nanosystem. It is known that the normal physiological pH is 7.4. Due to cancerous growth the metabolic systems undergo changes and many complex cellular mechanisms take place. The differences in vasculature and the rapid, disorganized growth, renders the tumour environment hypoxic in nature. This lack of oxygen, glycolytic mechanism, combined with poor lymphatic drainage leads to a build-up of lactate in the area. Therefore, the diseased region has an acidic pH which lies between 5.5-6.8.[13,14]

Doxorubicin as well as other chemotherapeutic drugs have some adverse side-effects. As discussed in Chapter 1, they can damage the normal dividing cells present in the body, cause painful sores, nausea and hair loss. These molecules are capable of producing ROS that can interact with proteins, lipids and carbohydrates, causing serious damages and mutations. Cardiomyopathy and hepatotoxicity has also been reported for doxorubicin. [256,257] Therefore, it is necessary to limit its interaction with healthy tissues and target it specifically to the cancer cells. Utilizing the pH difference between the two types of cells is a well explored path in targeted drug delivery research. Different sets of experiments were performed to simulate the physiological environment and verify if the encapsulated drug could be released.

4.3.1 Effect of pH

The healthy cellular environment was replicated with the help of fetal bovine serum (FBS) and a phosphate buffer (PBS) at pH of 7.4. The tumour micro-environment was mimicked using 10 % FBS with acetate buffer to obtain a pH of 5.5. It was observed with fluorescence studies that the characteristic emission of doxorubicin at 590 nm is gradually quenched as the incubation time with PB assembly is increased (Fig.116 (a)). This occurs as a result of nano-surface energy transfer and is an indication of interaction between doxorubicinyl groups and our nanoparticles. The quenched fluorescence of the drug is recovered upon introduction of acidic buffer with 10% FBS. This was an indication that the drug could be released from the nanosystem but the exact quantity had to be determined precisely.

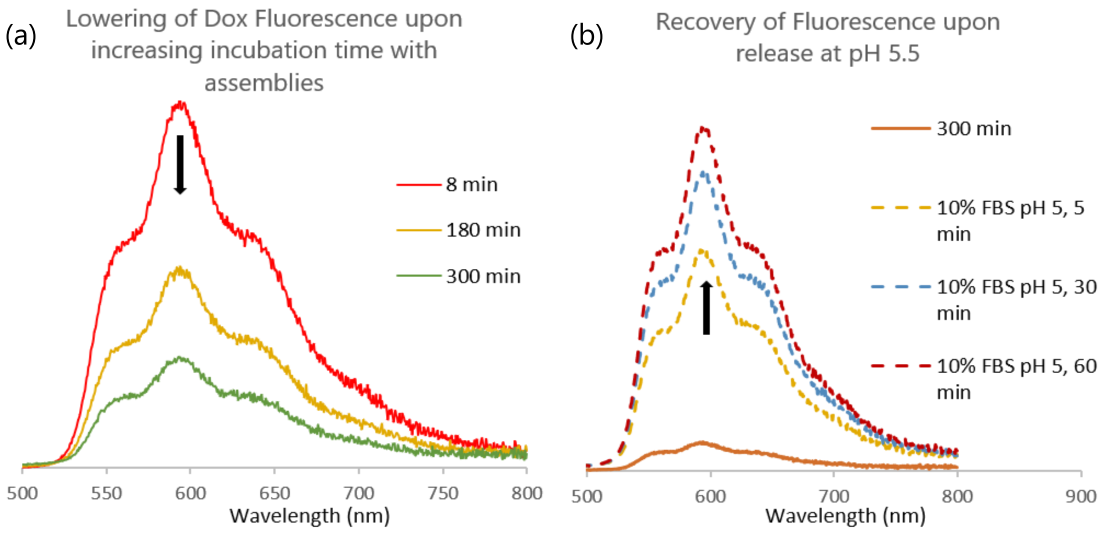

Figure 114. (a) Quenching of doxorubicin fluorescence upon interaction with PB nanoassembly over time and (b) The recovery of quenched signal in simulated tumoral environment.

The release of doxorubicin from CD-citrate coated PB FeGA assemblies needed to be monitored over time and each time point was triplicated to ensure reproducibility. Therefore, each set of the sample was divided into 15 aliquots and 47 µM of drug was introduced. For experimental ease, the lowest incubation time of one hour was employed. The steps used to determine encapsulation efficiency were repeated by separating the supernatant. Table 14 (annex 6.4.1) summarizes the results obtained. The results were comparable to the previous sets of experiment conducted with 1 hr incubation time and average encapsulation efficiency of 85.6 ±1.0% was obtained.

The pellet formed after ultracentrifugation contained the nanoparticle assembly with the bound doxorubicin. To study the release in healthy cells, each pellet was redispersed in 10 % FBS, PBS buffer and water was added to bring back the initial volume. These mixtures was placed in an oven with gentle stirring at 37°C, to mimic the human body temperature. At different time points, 3 aliquots each were removed from the set and ultracentrifuged for 30 minutes. Once again, the nanoparticles deposited at the bottom of the tube with the drug that was still encapsulated. The doxorubicin that was released under these healthy cell conditions separated out in the supernatant and fluorescence studies were employed to determine the percentage of doxorubicin release at respective time points. Similar experiment was repeated at simulated acidic tumour environment. After drug loading, the sample pellets were redispersed in 10 % FBS with acetate buffer to maintain the pH at 5.5 and incubated at 37°C. At certain intervals, the samples were taken out of the oven, analysed using ultracentrifugation and fluorimetry to calculate the percentage of drug released. The results are tabulated below.

Table 6. Doxorubicin release percentages from Prussian Blue-CD citrate coated nano-assembly at 37°C under pHs of 7.4 and 5.5

Incubation time at 37°C	Percentage release pH 7.4	Percentage release pH 5.5
5 min	12.0 ± 0.5	38.1 ± 1.14
1 hr	14.1 ± 0.5	49.9 ± 1.0
3 hr	15.3 ± 0.6	52.0 ±1.9
5 hr	-	54.1 ± 2.9
17 hr	-	55.6 ± 3.1
20.5 hr	23.0 ± 0.1	-

The results clearly indicate that the amount of drug released increases progressively with time. However, pH plays an extremely important role in determining the quantity of Dox that can be freed from the Prussian Blue nanosystem. At neutral pH, only 12-15 % of the encapsulated drug is expelled out and a maximum release of only 23 % could be seen after overnight incubation at 37°C. On the other hand at pH 5.5, a burst release of 38 % is seen within the first 5 minutes of incubation. This is very interesting as it suggests that a significant proportion of drug could be delivered as soon as the tumoral pH is encountered. Within one hour in the acidic environment, half of the encapsulated doxorubicin is released from the assemblies. The experiment was followed only until 17 hours and the results suggest that the release is slower, and a maximum of ~56 % could be reached. It could be hypothesized that at acidic pH, the nanosystem undergoes various changes. The carboxylate (COO^-) groups undergo neutralization changing the overall surface charge of the polymer coated assembly to less negative values. Therefore, the electrostatic interactions with the drug molecules is lowered, leading to significant increase in the release. It has also been demonstrated that the amino group of Dox is protonated at low pH values and its solubility in solution is increased.[158]

4.3.2 Effect of temperature

It is well-established that PB is an efficient photo-thermal agent capable of reaching high local temperatures, comparable to that of gold nanorods or carbon nanotubes used for the same purposes.[177] Therefore, the effect of elevated temperature on drug release was investigated. As described earlier, the pellet containing encapsulated doxorubicin within PB FeGA-CD citrate was dispersed in simulated physiological medium containing fetal bovine serum and pH 7.4 and 5.5 buffers. As a first approach to mimic the PTT conditions, 15 samples prepared under each condition was incubated in an oven maintained at 50°C. At certain time intervals, the solutions were separated and ultra-centrifuged to separate the supernatant. The fluorometric studies revealed the amount of Dox released at each time point. The experiments were performed in triplicate to ensure reproducibility and results are tabulated below.

Table 6. Release percentages of doxorubicin from PB assembly at 50°C

Incubation time at 50°C	Percentage release pH 7.4	Percentage release pH 5.5
5 min	18.4 ± 0.9	35.7 ± 0.5
1 hr	25.6 ± 0.4	55.5 ± 0.9
3 hr	28.1 ± 1.1	58.3 ±1.8
5 hr	28.7 ± 1.3	63.1 ± 1.1

The observed release percentages at 50°C prove that temperature also contributes to the release of doxorubicin at the target site. At neutral pH and high temperature, there is 10-13 % increase in the amount of drug expelled in the first 3 hours, as compared to the activity at 37°C. The highest release of encapsulated drug was 63 % which could be observed after 5 hours of incubation at pH 5.5 and 50°C environment. In acidic pH, the amount of Dox released after 17 h in 37°C could be ejected within one hour at 50°C. The temperature factor is related to irradiation with near infrared (NIR) laser. So, the ~56 % release in the first hour is extremely significant as the NIR radiation is generally performed as multiple cycles lasting 5-10 minutes. It is highly interesting that a majority of drug could be unloaded within a short duration in tumoral environment. The results of doxorubicin release under different conditions are summarised in Fig. 118.

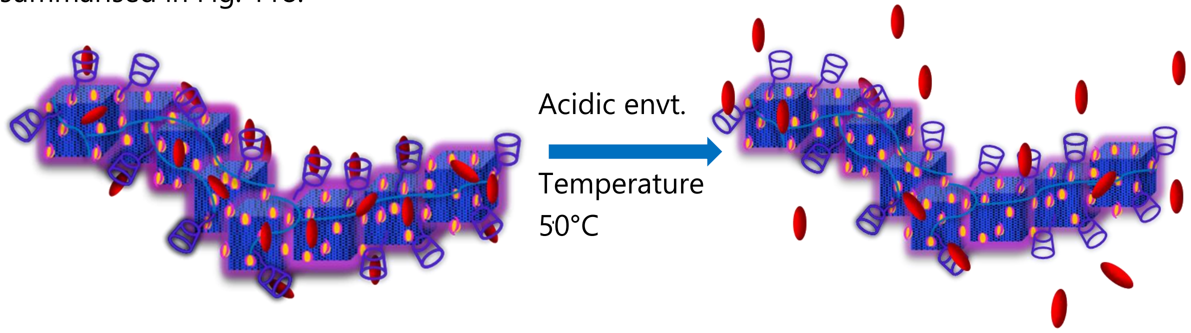

Figure 115. Schematic representation of doxorubicin release from PB nanochains in tumoral microenvironment.

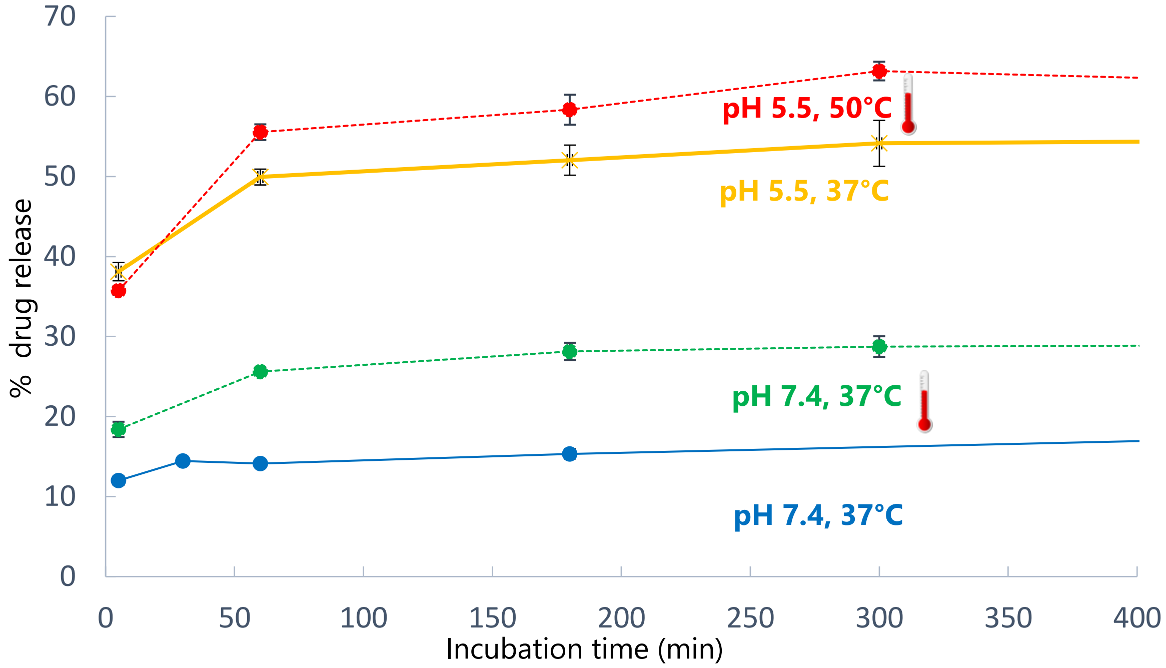

Figure 116. Plot displaying doxorubicin release from PB nano-assembly in healthy and acidic tumoral environments and the effect of increasing temperature (dotted lines).

In conclusion, it can be said that the self-standing, PB FeGA poly γ-CD citrate system synthesized using green conditions in water, is infact a smart drug vehicle for anti-cancer agent doxorubicin. The ~100 nm long chains of sub-10 nm Prussian Blue nanoparticles are capable of achieving high encapsulation values for doxorubicin. A triggered release (38 % within 5 mins) at acidic pH could be easily obtained with this novel nano-assembly. A high percentage of the loaded drug could be carried and delivered specifically to the tumour site within a few hours. This drug release could be further enhanced by incorporating an additional external stimulus of temperature, which could be easily attained using PB nanoparticles. It has to be noted that an even higher release may be achieved when performing irradiation with NIR laser due to more localized heating in the vicinity of the nanochains during PTT experiments. Only a small fraction of Dox is expelled in the healthy cell environment at normal body temperature. This proves advantageous as it would minimize the adverse side-effects usually associated with chemotherapeutic drug molecules.

4.4 IN-VITRO STUDIES

Since it was established that doxorubicin could be released from PB nano-assemblies, the next important step for moving towards medical applications was the understanding whether they could be internalized within cells and evaluate its toxicity. The *in-vitro* studies were conducted in the laboratory of Prof. Lucie Sancey at IAB, Université Grenoble Alpes, France. The experiments were performed on U87-MG (human glioblastoma astrocytoma) cells. Fresh solutions of PB FeGA-poly CD citrate and the assemblies incubated with doxorubicin were prepared for the analysis. Confocal microscopy was used to monitor the internalization of the fluorescent drug molecule within the cancer cells.

4.4.1 Confocal Microscopy

U-87 MG cells were seeded in LabTek Chamber-I, 24 hours before experiment. Cells were labelled with Lysotracker Green (#L7526, ThermoFischer Scientific) to identify the lysosomes, and with Hoechst 33342 at 1 µM. In parallel, cells were incubated with Doxorubicin (0.1 µM) and PB-FeGA nanochain incubated with Dox (0.1 µM) and observed under a confocal microscope using a LSM 7 MP (Zeiss, Germany) equipped with a 40 × water-immersion objective (NA 1.2; Zeiss) and ZEN 2010 software for detection of the different channels. Laser excitations/emissions were 760 nm biphotonic/400-450 nm for Hoechst, 488 nm/500-550 nm for Lysotracker Green, 543 nm/550-650 nm for Doxorubicin, respectively.

The parameters and contrast adjustments were kept constant to have an accurate comparison between the nanochain-Dox conjugate and free Dox activity *in-vitro* and the images taken at regular intervals are shown below. The cell nucleus is coloured blue, lysosomes appear green and doxorubicin appears red in colour. Endosomes are organelles responsible for transporting materials from the extra-cellular matrix to the inside of the cells. The yellow spots originate from the overlap of green and red signals, indicating colocalization of doxorubicin within the lysosomes of the cells.

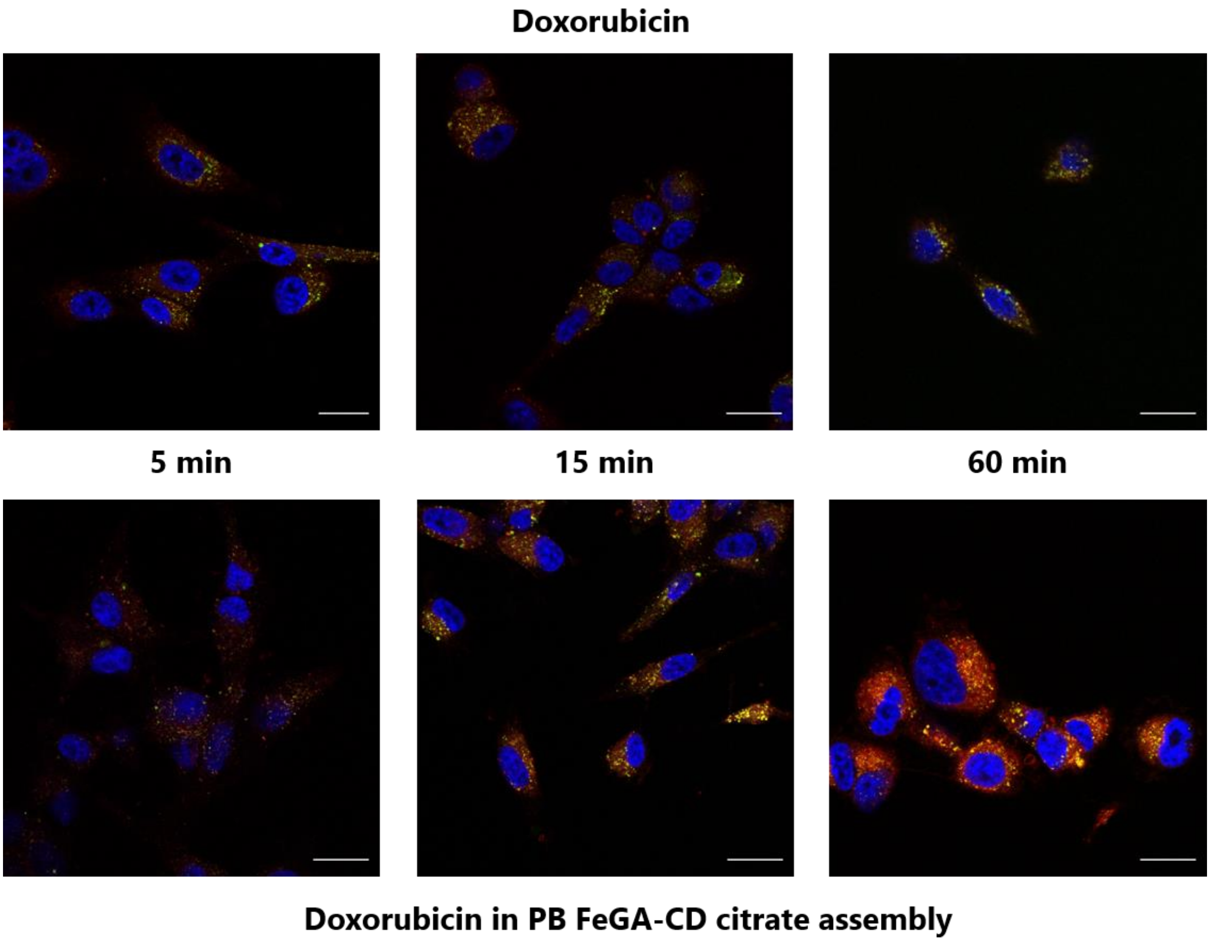

Figure 117. Confocal microscopy images at different time points with U87-MG glioblastoma cells in the presence of free doxorubicin (top) and doxorubicin loaded in PB nanoassembly (bottom).

The results indicate that the free-Dox quickly enter the cell compartments within 10 minutes. On the other hand, when doxorubicin in encapsulated in the PB nano-assembly, the signal coming from Dox is quite minimal in the first 5 minutes. But gradually, it could be observed that the internalization of the drug is much higher in this case, as the intensity of the red signal continuously grows despite similar monitoring parameters. Colocalization with the lysosomes (yellow) is also evident at the 15 minutes time point but the Dox signal keeps increasing. This time evolution gives an indication that the drug release seems to occur only within the target environment. When the acidic lysosomal environment is encountered, the percentage of drug expelled from the nanosystem is amplified, leading to a higher red fluorescence in 60 minutes as compared to when the drug solution is simply introduced to the cells. This is due to the restored fluorescence of Dox once it is dissociated from the chains. It is an additional proof that PB FeGA assemblies are effective anticancer drug nanocarriers that can help penetrate the cells and internalize more drug molecules within a short period of time. This would prove beneficial for medical applications, as a lower quantity of drug would be enough to generate the same effect if loaded into such delivery vehicles. The presence of PB nanochain by itself, inside the cells could not be directly seen using this experiment. It requires decoration of the nanostructure with another fluorescent probe and these studies will be conducted in the coming months.

4.4.2 Cytotoxicity experiments

In order to act as a therapeutic agent, it is necessary that the Prussian Blue nanosystem is safe and non-toxic for the cells in the body. Therefore, cell viability experiments were conducted using PB FeGA-CD citrate nanochains loaded with and without doxorubicin. Concentrated solutions containing 110 µM of nanoparticles were prepared using ultra-filtration. The U87 cell-line was used to obtain comparable results in the clonogenic assay. The number of colonies formed after incubation with nano-agents determine their survival fraction and provided information on its toxicity. The effect of different concentrations (0.01-0.5 µM) for each sample was evaluated and compared to the effect of free Dox. The cells incubated with the samples were cultured for 8 days. The cells that survive the exposure to NPs/drug would divide several times and form colonies. At the end of incubation time, the plates were rinsed, fixed with ethanol, colored, and counted for colony assay. The control condition was used to determine the plating efficiency (PE) as indicated in Equation 1.

$$PE = \frac{no.of\ colonies\ formed}{no.of\ cells\ seeded} \times 100 \text{ (Eq. 1)}$$

The surviving fraction (SF) was calculated using equation 2.

$$SF = \frac{no.of\ colonies\ formed\ after\ treatment}{no.of\ cells\ seeded \times PE} \text{ (Eq. 2)}$$

The fraction of cells alive in presence of nanoassembly with and without the drug, provided an estimate of toxicity of our samples. Each measurement was triplicated to obtain an average value within a margin of error and the results are represented below.

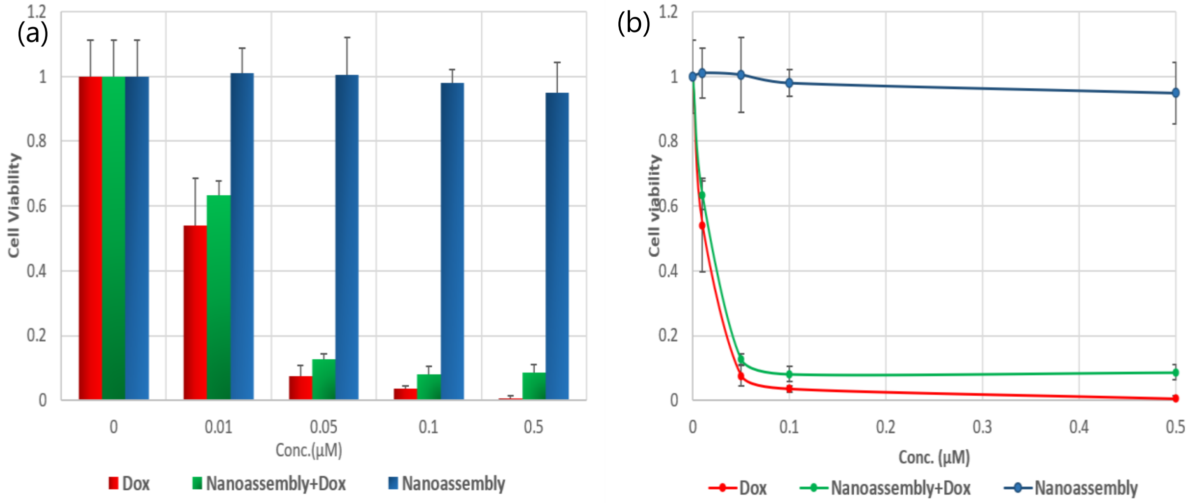

Figure 118. Cell survival plots of U87 cells in the presence of PB FeGA-CD citrate assemblies (blue), assemblies loaded with doxorubicin (green) and effect of pure doxorubicin solution (red).

It is evident that PB nanoassembly created using iron and gallic acid linkers are safe and non-toxic. More than 95 % of the cells remain alive even after exposure to the highest concentration of these nanoparticles. Therefore, they could be used for further studies and is a promising candidate for bio-medical applications. As expected, doxorubicin was highly cytotoxic for the cells. It kills almost half of the cells at the lowest concentration and only 1% survives in the presence of 0.5 µM Dox. Very interestingly, the non-toxic PB FeGA nanochains when loaded with the drug behaves in an almost similar manner. It is capable of eliminating a maximum of the cancerous cells, and only 8% remain alive at 0.5 µM concentration. This shows that a maximum of the encapsulated drug is released inside the cells, and the small difference when compared to free doxorubicin is due to the fact that the release is not complete. This effect can be easily enhanced by combining photothermal therapy. NIR laser is expected to act as an additional trigger for generating a high cytotoxic effect within tumours. The PTT properties have not been evaluated *in cellulo* but are reported *in vitro* in the following section.

4.5 PHOTOTHERMAL THERAPY WITH PB NANOCHAINS

Photothermal therapy (PTT) is a form of non-invasive treatment involving the use of near-infrared light. The biological window lies in the wavelength range between 650-1024 nm because skin, haemoglobin and other tissues of the body have a minimal absorbance here.[61] Therefore the NIR radiation can penetrate deeper compared to other wavelengths. In PTT, the death of cancerous cells is induced by increasing the temperature of the local environment. Photothermal agents that absorb light and convert the energy to heat are used in this therapeutic method. Such agents need to have a large absorption cross-section in the biological window and have a high light to heat conversion efficiency. Most of the commonly used nanomaterials used for PTT were discussed in chapter 1. Since Prussian Blue has an intense absorption around 700 nm, lot of research had been focussed on its PTT capabilities. It was established in 2012 that PB is an efficient and stable photothermal ablation agent due to its high molar extinction coefficient.[138] More recently, our group had shown that ultra-small Gd-doped PB nanoparticles display a high photo-thermal conversion rate, which was at par with the gold nanorods and carbon nanotubes used for the same purpose.[177] It was necessary to understand if the assemblies constructed would behave in a similar manner and if physiological conditions affect the conversion rate and the temperature that can be achieved.

4.5.1 Photo-thermal conversion nanoparticle vs nanoassembly

The experiments were conducted in the lab of Prof. Florence Gazeau, with PhD student Theotim Lucas at Université de Paris. Fresh samples of Prussian Blue nanoparticles, PB-FeGA assembly, optimized PB FeGA-0.05 eq. CD citrate were prepared. The nanoparticle and polymer coated assembly solutions were ultra-filtered, washed and concentrated to reach the [PB]= 0.125 mM. The setup involved an infra-red laser at wavelength of 808 nm. The power of the laser was adjusted to 1W/cm^2 and arranged to be 1.6 cm above the sample (200 µL) solution.

As a blank experiment, water was first irradiated in the setup for 15 minutes and heat rise was monitored using thermal camera. The recorded video was analysed to determine the exact temperature at different time points and data extracted was plotted to give final results. The same experiment was repeated with the UF and washed PB FeGA CD citrate sample. Continuous irradiation for 15 minutes provided information on the maximum possible temperature that could be reached and the plots are presented in Figure 121 (b).

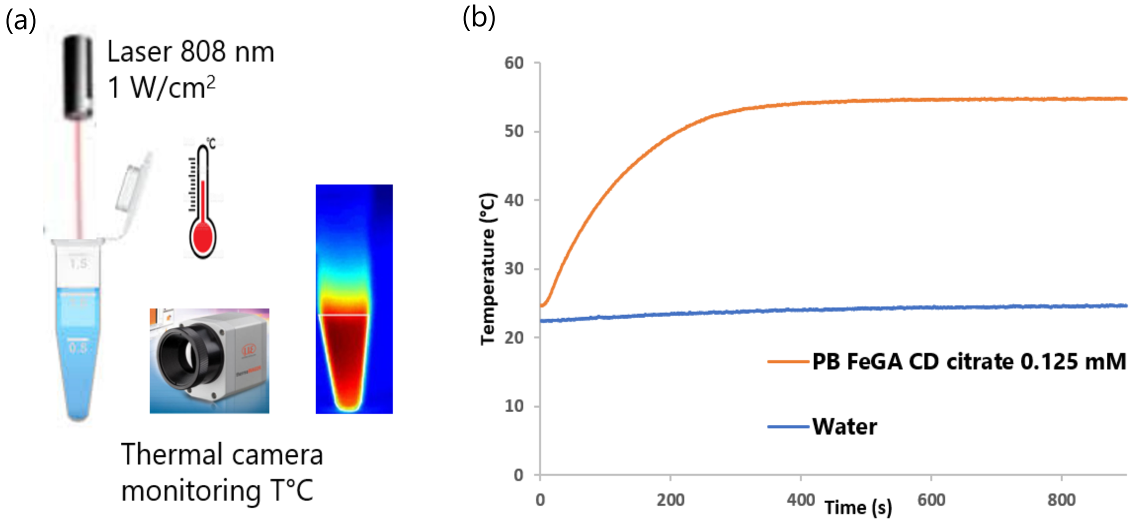

Figure 119. (a) Schematic illustration of experimental setup for photothermal experiments (b) Plot of temperature evolution in PB assembly upon 15 min NIR irradiation in comparison to blank experiment performed with water.

It could be observed that irradiation of water with NIR laser for 15 minutes led to a temperature rise of only 2.3°C, while the change in PB FeGA CD citrate nanoassembly solution was of 30.1°C (Δ T). The final temperature reached in the sample was 54.8°C which is more than sufficient for cell killing. Moreover, the usual radiation procedure for photothermal therapy involves multiple cycles of 5 or 10 minutes. From the curve plotted in Fig.121 (b), it could be seen that 98 % of maximum temperature could be reached with just 5 minutes of exposure to the laser. Therefore, further experiments were performed with this time setup. Pure PB nanoparticles (0.125 mM) and PB FeGA CD citrate (0.125 mM) solutions were irradiated with the laser for 300 seconds and then allowed to cool down. Interestingly, it could be seen that the maximum temperature reached was 6.5°C higher for the assemblies compared to the bare nanoparticles (47.7°C) at the same concentration. This could be directly attributed to increased absorption of the PB FeGA CD Citrate in the visible-NIR region (Fig. 122 b). This additional contribution arises from the coloured and highly stable Fe-Gallic acid complexes and the new Fe(II)-CN-Fe(III) pairs formed due to bonding of iron gallate to the surface of PB during formation of the nano-chains.

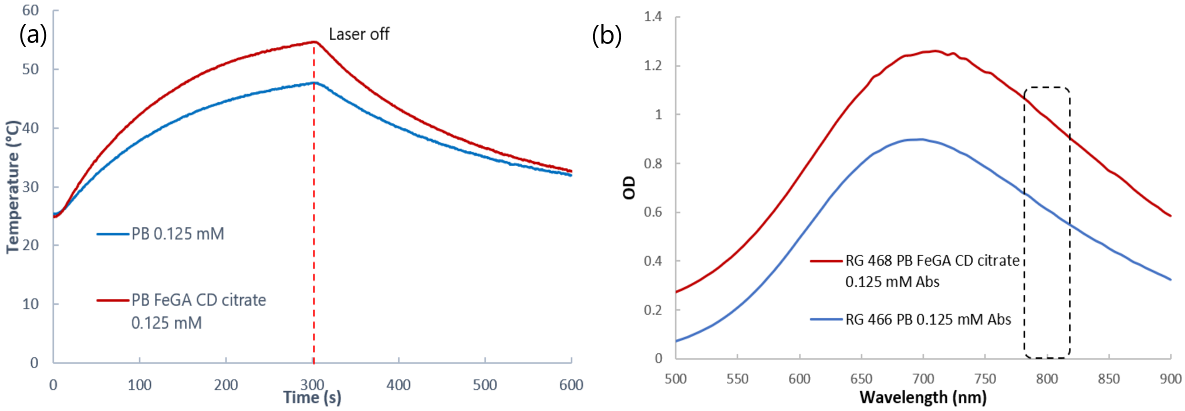

Figure 120. (a) Increase of local temperature upon 5 min NIR laser irradiation on PB nanoparticle and PB nanoassembly solution (b) Corresponding UV-Visible spectral plot of the solutions with PTT region of interest

The experiment proved that the synthesized PB nanochains have a high photo thermal conversion rate and would in fact, have better therapeutic activity as compared to the individual nanoparticles. However, it was important to verify the stability of these nanostructures over multiple cycles of heating for translation to medical applications. The PB FeGA CD citrate solution was subjected to 5 cycles of irradiation, each lasting 5 minutes, followed by a cool down (laser off) period of 5 minutes.

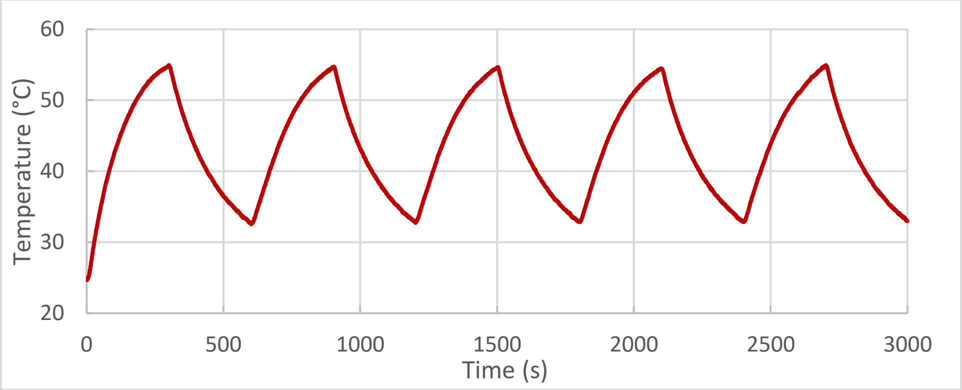

Figure 121. Plot of temperature fluctuation in PB FeGA CD citrate (0.125 mM) solution subjected to 5 cycles of NIR radiation (808 nm, 1 W/cm^2)

The results shown in Fig.123, reveal that the efficiency is maintained and that a ΔT of 30°C (temperature above 54°C) could be obtained even with multiple cycles of laser irradiation on the Prussian Blue nanochain solution. The sample is highly photo-stable and capable of absorbing light energy and dissipating it in the form of heat. Literature survey had indicated that a temperature of 43°C is enough to ensure death of cancerous cells. Therefore, a lower concentration of these nano-assemblies is sufficient for the targeted applications. The above mentioned trials were conducted in water and it was important to understand if the same behaviour could be maintained under physiological conditions.

4.5.2 Effect of physiological medium

Two concentrations of PB FeGA-CD citrate (0.1 and 0.14 mM) samples were prepared for the next set of experiments. Each sample was divided into two aliquots of 0.5 mL and fetal bovine serum (10 % vol.) was introduced. The total volume was made up to 1 mL using buffer solutions: PBS for pH 7.4 and acetate buffer for pH 5.5. Therefore, the final concentration of PB in samples were 0.05 and 0.07 mM respectively. All 4 assembly mixtures were subjected to 5 cycles of NIR radiation under the same conditions and the results obtained are plotted below.

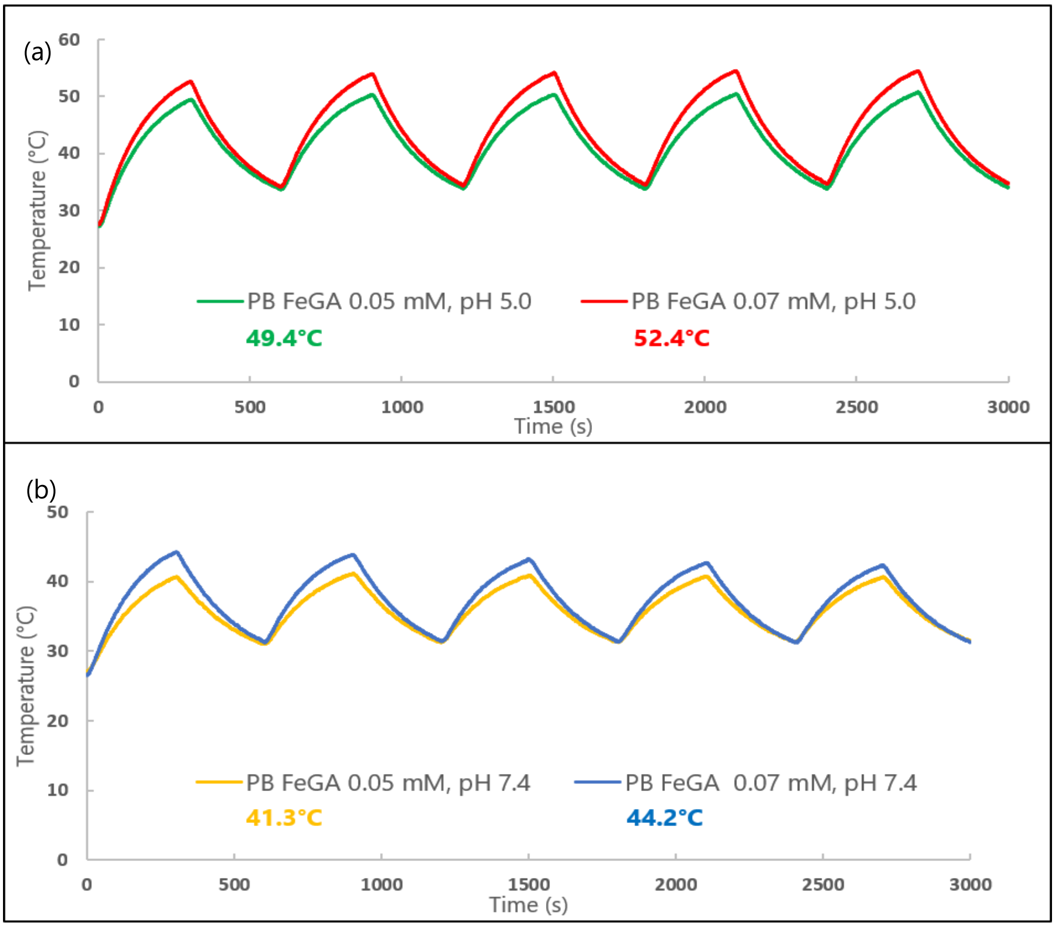

Figure 122. (a) Study of photo-thermal effect in polymer coated PB FeGA nanoassembly with 10% FBS at (a) acidic tumoral pH and (b) neutral physiological pH

It is evident that the concentration of PB nanoparticles has a direct effect on local heat produced by the sample and tuning the concentration can help attain any desired temperature. The results suggest that the nano-assemblies have a good photo-thermal efficiency and stability even in physiological media, and would therefore be effective therapeutic agents. It was interesting to notice that in acidic environment (Fig.124 a), 0.07 mM sample could display a ΔT = 24.8°C reaching a temperature of 52.4°C, whereas the same concentration only leads to a maximum temperature of 44.2°C (ΔT=16.6°C) in neutral pH of 7.4 (Fig. 124 b). The same effect is seen at the concentration of 0.05 mM in both environments.

This can be attributed to the behaviour of Prussian Blue in different buffers. The high amount of phosphate ions present in PBS is known to complex Fe^{3+} located at the surface of PB and reducing the number of Fe-CN-Fe pairs present in the solution. So the absorption band in 600-900 nm region, arising from PB Nps slightly decrease over increased exposure to PBS buffer. This effect was described with spectroscopic studies section 3.2.4. This is also the reason for a small decline in the maximum temperature reached after every cycle, at pH 7.4.

It can be concluded that the assemblies of ultra-small PB nanoparticles synthesized during this doctoral project are efficient photo-thermal therapeutic agents. It remains stable in water and physiological environment containing different ions and proteins. The PB FeGA-CD citrate chains can endure multiple cycles of irradiation without a loss in light to heat conversion rate and relatively low concentrations are capable of generating high temperatures with $\Delta T=30°C$. As described in earlier sections, these nano-assemblies are capable of encapsulating chemotherapeutic drug molecules and performing stimuli-responsive delivery. A majority of the loaded doxorubicin could be delivered within short amount of time upon interaction with acidic environment at elevated temperatures. The photothermal effect produced by the PB nanochains will ensure local temperature rise only on the NIR laser focussed region. This would be associated with enhanced drug release at the specific site leading to eradication of cancerous tissues. This two-pronged approach of synergistically combining chemo and photo-thermal treatments make PB FeGA nano-assemblies efficient therapeutic agents.

4.6 NITRIC OXIDE LOADING AND RELEASE

Nitric Oxide (NO) is a water-soluble gas that is usually used for relaxing muscles, as vasodilators and in the treatment of respiratory failure. In 2008 it was established that at concentrations above 200 nM, NO has anticancer properties.[258] Tumour progression is inhibited, multi-drug resistance could be overcome and it has been shown that NO also sensitizes tumours towards radiotherapy.[259,260] In the body, NO is generated by oxidation of l-arginine amino acid, in the presence of certain enzymes and co-factors. However, this can rapidly react with other compounds and has a short half-life. So this NO generated from intrinsic sources have unpredictable response to cancerous tissues. Therefore, development and inclusion of NO into the body through external donors have been widely studied over the past decade.[261] One of the most commonly used agents for this purpose is sodium nitroprusside (SNP).

Interestingly, SNP has a structure similar to ferrocyanide that is used in Prussian Blue synthesis. This property has been exploited and T.Feng et.al showed that PB has an ability to act as a carrier for NO. Mesoporous PB-SNP (~100 nm) particles were synthesized by mixing the precursors in HCl at 80°C (12 hrs). They proved that SNP is included in the framework of the porous nanoparticle and the gas release could be triggered by NIR laser irradiation to the target site.[262] This adds a new perspective to an already versatile theranostic nanoparticle. The aim of our project was to determine if this property could be incorporated within our sub-10 nm PB nanoparticles and nanochains while maintaining a green method of synthesis.

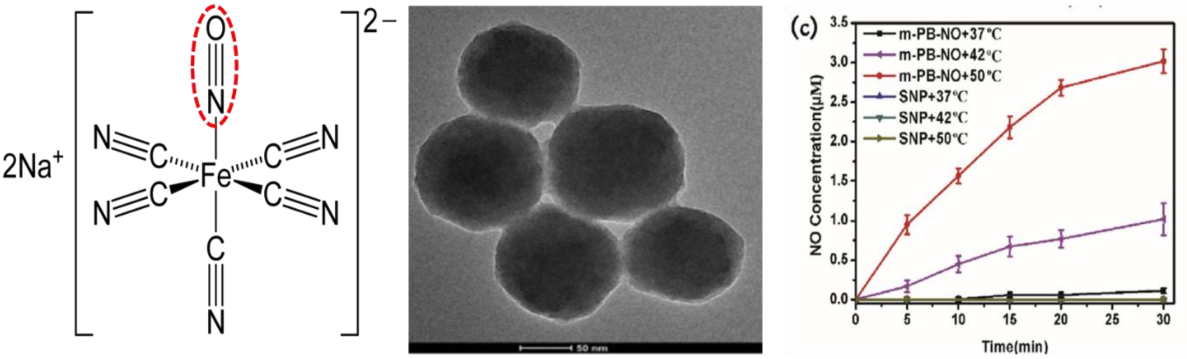

Figure 123. (a) Structure of Sodium Nitroprusside (SNP) (b) TEM micrograph of mesoporous PB-NO and (c) NO release profile of m PB-NO at different temperatures[262]

4.6.1 Synthesis of PB-SNP nanoparticles and characterization

Two strategies were employed to synthesize PB-SNP nanoparticles. The first involved direct synthesis from the constituents where the Fe^{II} complexes: ferrocyanide and nitroprusside were mixed in different proportions (0.9:0.1 to 1:12) to make a homogenous solution in water before adding 1 equivalent of ferric nitrate precursor. The reaction conditions were maintained at 2°C but the suspensions formed were unstable and deposited with time. This was because the formation of our nanoparticles relies heavily on the controlled nucleation step which is strongly dependent on the precise balance between the reagents and charge of the surface.

The second strategy included exchange of ligands, and grafting NO onto the surface of pre-formed PB nanoparticles. Concentrated stock solution of SNP (180 mM) was prepared and different volumes depending on the required concentration was added onto 0.25 mM PB solution at room temperature. This was done to minimize dilution of Prussian Blue solution and was determinant to obtained SNP grafting. Ratios ranging from 1:1 to 1:14 between PB and SNP were studied. The reaction was run for 90 minutes to maximize the surface exchange. This method was successful and addition of upto 12 equivalents of nitroprusside resulted in a stable colloidal solution. The size of the functionalized nanoparticles remained below 10 nm. This was verified by DLS and TEM analysis.

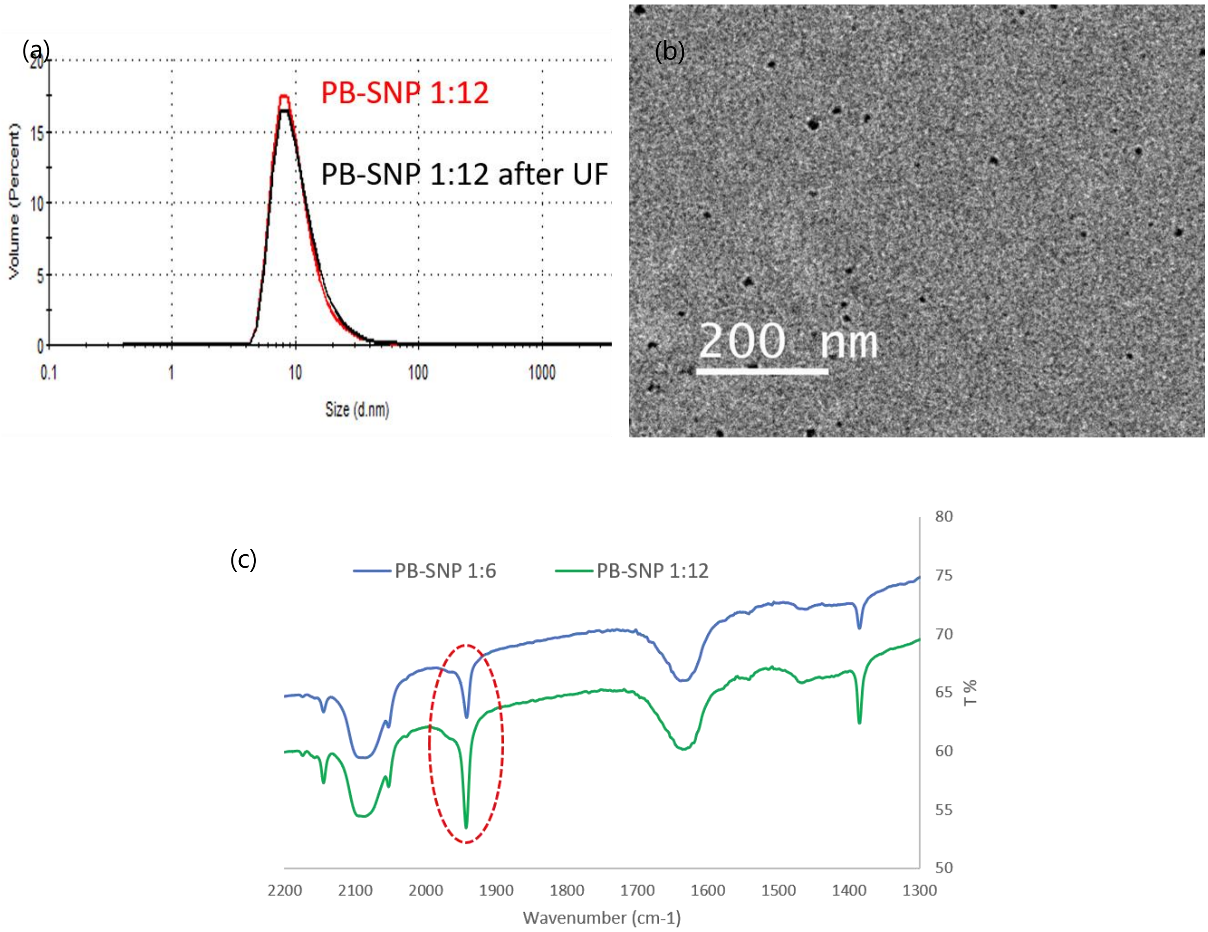

Figure 124. (a) Hydrodynamic diameter of nitroprusside grafted PB nanoparticles before and after ultra-filtration (b) TEM image of PB:SNP 1:12 sample (c) IR spectral comparison of 1:6 and 1:12 sample after purification

UV-Vis spectroscopic studies showed that the PB absorption band is not effected by the surface functionalization. The only clear method of verifying the presence of NO in the particles was through infra-red spectroscopy. But prior to this, each solution was UF and washed twice to remove the un-bonded SNP. Saturated salt solution was added to precipitate the sample and powder was recovered after drying under vacuum. The 1:6 sample provided the first indication that the doping with SNP was successful. The N=O vibration could be clearly seen at 1944 cm^{-1} and the characteristic peak of ν_{CN} from Prussian Blue is observed at 2086 cm^{-1}. An increase in intensity of the nitroso band could be seen with the 1:12 sample. Therefore, this sample with maximum NO substitution was considered for further experiments and is hereafter mentioned as PB-SNP. The optimization of these nanoparticles were performed by Andrea Merlo during his Master thesis internship.

4.6.2 Assembly formation with functionalized nanoparticles

The sub-10 nm PB-SNP nanoparticles were used to prepare assemblies following the method described in chapter 3. Physico-chemical characterization of PB-SNP FeGA revealed similar results to the normal assemblies. However, the intensity of nitroso band in IR was significantly diminished. It was assumed that the dilution involved in assembly formation steps displaces some of the NO. The dilution factor is 3 as one volume each of Fe^{3+} and gallic acid is added to the preformed PB-SNP nanoparticle solution. And attempt was made to reduce the dilution factor and doubly concentrated precursor solutions (1 and 2 mM) were used. The chains formed in this manner are longer with the hydrodynamic diameter ~200 nm. A more pronounced NO peak is visible in the IR spectra, with this change in the synthetic process.

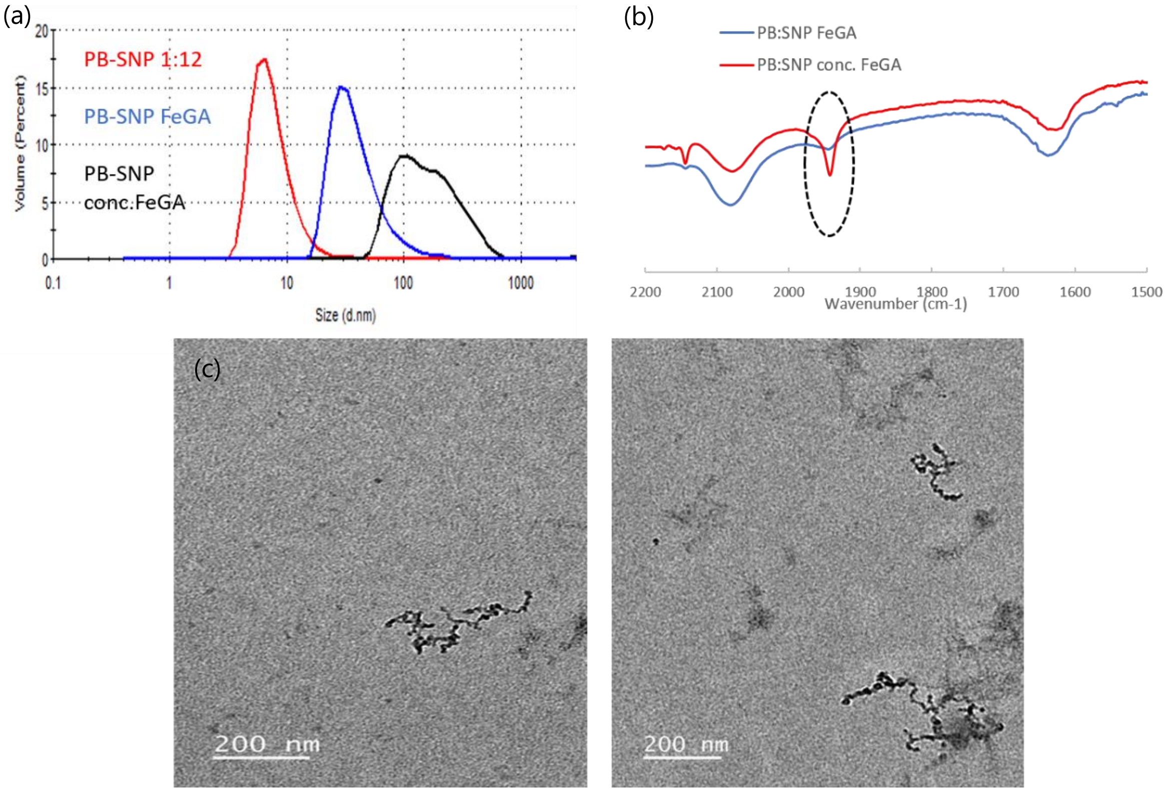

Figure 125. (a) Hydrodynamic diameter of PB-SNP nanoparticles and their assemblies. Higher sizes observed on using concentrated precursor solutions to minimize dilution (b) IR results of PB-SNP FeGA assemblies synthesized with different precursor concentration. (c) PB-SNP FeGA assemblies visualized by TEM.

Further optimization of this nano-system is required, and results will be reproduced in the following weeks, but the initial results are encouraging. It is clear that nitric oxide could effectively be grafted on to the ultra-small PB nanoparticles and this process could be done easily at room temperature, in water, without use of harsh conditions. Assemblies of these versatile nanoparticles could also be formed. The next step was to determine if NO could be released from these newly designed systems.

4.6.3 NO release from nanoparticles and assemblies

Similar to doxorubicin drug delivery, it was important to know if NO gas release from the nanoparticles could be triggered using external stimuli. Infra-red spectroscopic analysis only provided a qualitative proof of NO presence and it required multiple steps: precipitation, centrifugation and drying, for each sample. Moreover, detection of a change in intensity requires rather high release percentage.

In order to simplify the procedure an indirect method of NO detection was employed using a Griess assay kit (Sigma Aldrich). This assay included 2 reagents (GR 1 and 2). NO is easily oxidised to nitrite in air and the sulphanilamide reagent reacts with the NO_2^- to form a diazonium salt in solution.[263] The second reagent: naphthyl ethylenediamine dihydrochloride is then added to the mixture and a magenta coloured azo dye formation takes place. The reaction mechanism is demonstrated in Figure 128 (a). This dye absorbs at 540 nm. A calibration curve ($OD_{540\ nm}$ vs conc.) was prepared using solutions with known nitrite concentrations. The absorbance coming from the specifically treated PB-SNP nanoparticles were compared to the curve and amount of NO released was determined.

As described in section 4.5.1, stable ultra-small Prussian Blue nanoparticles with high NO content could be synthesized by maintaining 1:12 ratio between PB and SNP precursor solutions. The synthesis was followed by UF and washing steps to ensure that only the nitric oxide bound to the surface of nanoparticle is detected. The effect of temperature and pH on the release of NO was studied and the results were compared to a sample of PB-SNP maintained at room temperature. To simulate the NIR laser triggered heating effect rising within the nanoparticles, the PB-SNP solution was subjected to a temperature of 70°C using a water bath, maintained under reflux for one hour. This is of course an approximation since larger local temperature rise can happen in the vicinity of the PB during PTT, leading to larger release.

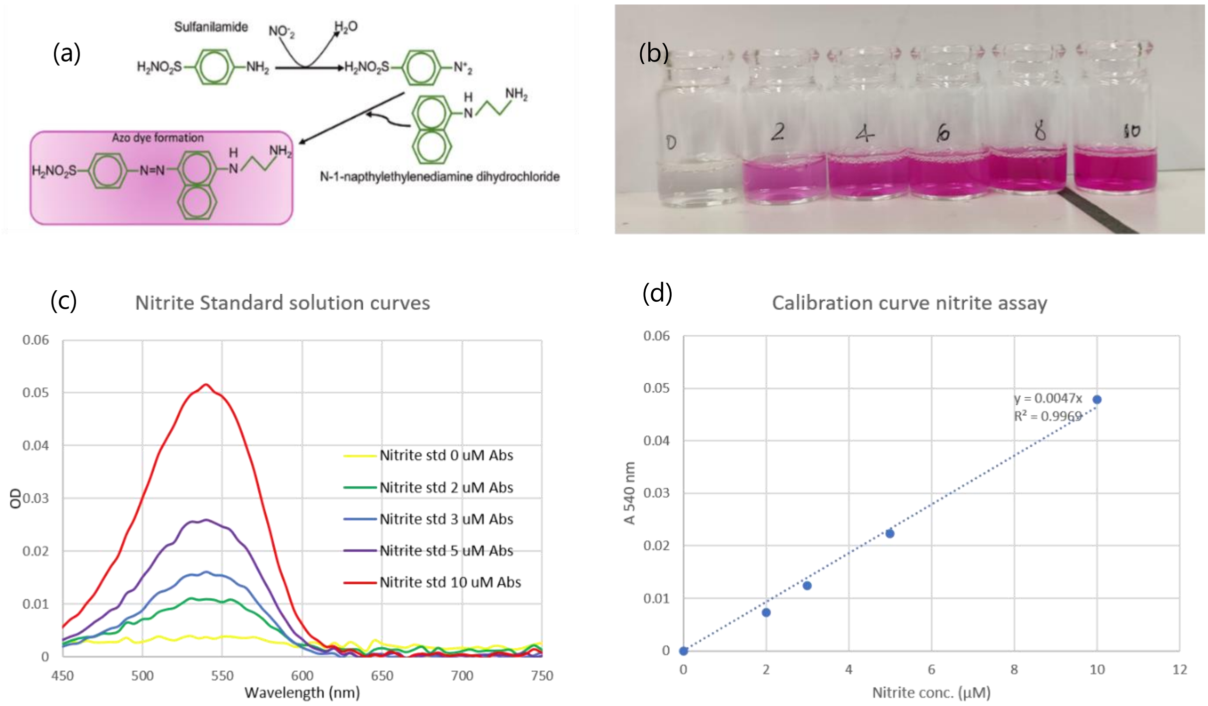

Figure 126. (a) Reaction mechanism of conversion of nitrite into a coloured azo compound that can be detected spectroscopically.[264] *(b) Solutions prepared using nitrite standard and Griess reagents in the lab. (c) The absorption plots of the prepared standard solution and (d) corresponding calibration curve.*

PB-SNP solution was mixed with acetate buffer (pH 5.5) and divided into two aliquots. Fraction 1 was stirred for an hour at room temperature to understand the effect of pH, while the second part was heated to 70°C, under reflux to see the combined effect of pH and temperature. The solutions appeared stable and unchanged with no deposition, similar to bare PB-SNP solution maintained at room temperature. Each sample was then dispersed in nitrite assay buffer (NAB), before adding Griess reagents 1 and 2. The mixtures turned light pink in colour and were incubated at room temperature for 10 minutes before beginning the spectroscopic analysis. As seen in Figure 129 (a), the spectra of the solutions provided a clear signal that NO could indeed be released from the sample. The band of the azo-dye centered around 540 nm is highly enhanced in the heated sample compared to the nps maintained at room temperature. This indicated that temperature rise would aid in the release of NO from our nanoparticles.

The absorption at 540 nm of all 4 mixtures were recorded to detect the amount of NO released. The spectra of bare nanoparticles diluted to the same extent, in absence of Griess reagents was also measured. This value was subtracted from the recorded $A_{540\ nm}$, in order to correct the measurements and isolate the contribution arising purely from azo-dye. The corrected OD values were used to quantify the NO content in the mixture, using the calibration curve. Considering the dilution factor, the exact amount of NO released due to temperature and pH effect was calculated and the results are tabulated below.

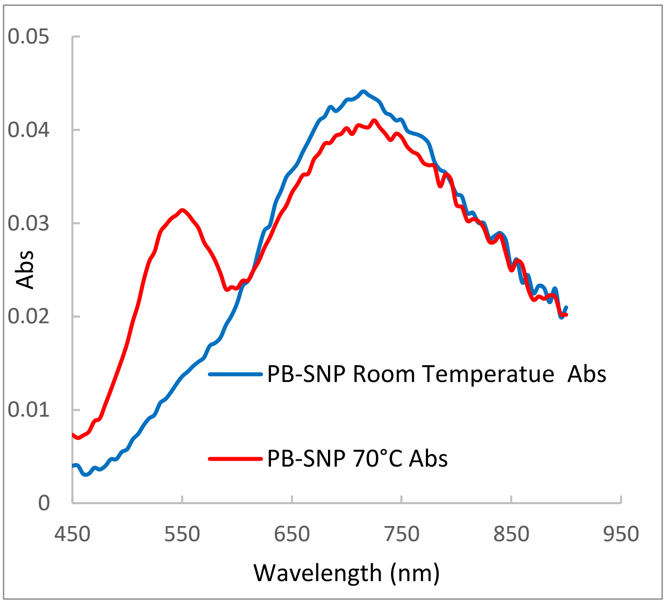

Sample with NAB and GR 1+2	**NO released (μM)**
PB-SNP RT, 1 hr	2.72
PB-SNP 70°C, 1 hr	18.51
PB-SNP, pH 5, 1 hr	7.14
PB-SNP, pH 5, 70°C, 1 hr	22.57

Figure 127. (a) UV-Visible spectra of PB-SNP nanoparticles heated to 70°C, compared to a RT sample, treated with Griess assay. (b) Amount of NO released from PB-SNP under different temperature and pH conditions.

The starting concentration of NO, grafted on the nanoparticle surface after UF could not be accurately determined with IR. Quantification of NO could not be done by elemental analysis a N content from cyanide in PB is often unreliable and hence the exact release percentages cannot be calculated. However, the results make it clear that the nitroprusside doped ultra-small Prussian Blue nanoparticles can act as good carriers of nitric oxide. The release at room temperature is very minimal but encountering the acidic environment of tumours produces a 2.6x (7.1 μM) increase in the rate. It has to be noted that here, the temperature is a much bigger factor that determines the amount of NO expelled from the nanoparticles.

When heated, the release of this radio-sensitizing gas is improved by a factor of ~7. It is hypothesized that the added thermal energy helps dissociation of NO from the Fe-NO coordination bond in the nanoparticle, leading to such high values of release. Since PB is capable of converting absorbed light energy into heat, this enhanced NO release could work synergistically with NIR laser controlled photothermal therapy. The combined effect of temperature + pH led to the maximum release of 22.5 µM. It was 8.3 times more than the amount that could be released in normal conditions. The same set of experiments were repeated with nanochains built using PB-SNP particles. The assembly formation included some dilution steps therefore the amount of total NO in the starting sample is lower than the ones discussed above. The effect of temperature and heat were studied and the amount of NO released was detected using the Griess assay kit (results in annex 6.4.2). No nitrite was formed when the assemblies were set at room temperature, and heating to 70°C led to the detection of 1.46 µM nitric oxide. Incubation of sample in acidic buffer, at room temperature indicated only a small release of 0.76 µM. But surprisingly, the combined effect of pH 5 and heating led to an 11-fold increase in the amount of NO expelled from the nanochains. These set of experiments need to be repeated in the following weeks, under optimal conditions to make a definitive statement.

As far as we know, this is the first time self-standing, NO-conjugated sub-10 nm PB nanoparticles have been prepared. The synthesis method followed was green and did not involve the use of surfactants or harsh chemicals. These newly developed particles have versatile applications and stimuli responsive NO delivery could be achieved. It can work as an effective anticancer agent, by overcoming multi-drug resistances and combining radio-sensitization with photothermal therapy. Assemblies of these PB-SNP nanoparticles could also be synthesized to ensure longer blood circulation time and possibly encapsulate drugs for chemotherapy. Preliminary investigations reveal that these nanochains could also release NO upon exposure to acidic pH and high temperature. Further experiments are required to evaluate the effect of NIR laser and quantify the exact release percentages of nitric oxide from these nano-assemblies.

4.7 DIAGNOSTIC APPLICATIONS

Diagnosis is a pre-requisite for determining the course of action or treatment strategy for any ailment or disease. Magnetic resonance imaging is one of the most commonly used test to diagnose medical conditions. It is a safe, painless and non-invasive method to generate high resolution images of certain regions in the body. In case of cancer patients, apart from detecting the presence of tumours, MRI helps monitor its growth and provides information on the performance of a therapeutic strategy applied. Therefore, it is a useful routine tool in monitoring treatments. Contrast agents (CA) are used to improve the sensitivity of this diagnostic method and the working principle was described in chapter 1. Prussian Blue has a unique porous structure, containing water molecules bound to the paramagnetic Fe^{3+} ions. The inner and outer sphere relaxation pathways help PB generate a positive T_1 contrast. However, the relaxivities of pure PB nanoparticles are lower than the commercially used CAs that are made of highly paramagnetic Gd^{3+} ion complexes. Most of the commonly used methods to improve the r_1 and r_2 of PB systems have been discussed in section 1.3.4. Most of them involve doping with high spin manganese(II), zinc(II) or gadolinium(III) ions. The effect of constructing assemblies of PB with an iron-gallic acid polymeric network was explored in this project. The experiments were conducted during a stay at Université de Mons, Belgium in collaboration with Prof. Sophie Laurent and PhD student Thomas Gevart.

4.7.1 Prussian Blue system for MRI

Evaluation of the efficiency of Prussian Blue nanoparticles and their assemblies as MRI contrast agents were conducted using Minispec Bruker instruments operating at 20 MHz and 60 MHz. Both the solutions were prepared using the synthesis method outlined earlier. The total amount of accessible paramagnetic ions in the sample is the deciding factor for MRI contrast. PB nanoparticle dispersions were concentrated using ultra-filtration and the exact concentration was verified by comparing the absorbance to a calibration curve. Prussian Blue solution containing [Fe]=1 mM was prepared. In the case of PB FeGA-CD citrate assemblies, the process is slightly more complicated. The PB content could be determined, but 2 more equivalents of ferric ion solution is added together with the gallic acid to create the assemblies. We also know that a part of this excess FeGA complex is removed during the ultra-filtration and washing steps. By preparing an PB- gallium GA analogue of the assemblies and conducting EDS studies it was determined that only 1.5 equivalents of the complex is retained in the final washed sample (chapter 3, section 3.2.2.6). Applying the same principle here, the polymer coated assembly solution was also concentrated to reach a total [Fe]= 1.16 mM (*exact to be determined by ICP studies*). It has to be noted that only 40% of this total iron content can be attributed to the PB nanoparticle and the remaining comes from the FeGA complex network linking the particles together.

Each solution was then diluted to obtain a range of concentrations. The samples were transferred to a glass tube and placed in thermo dri-block to bring the temperature to 37°C. Once the samples were optimized, the longitudinal (T_1) and transverse (T_2) relaxation times at 20 MHz and T_1 at 60 MHz were recorded using the table-top TD-NMR system. Each measurement was recorded thrice to ensure minimal error. The average values were used for the inverse of relaxation time vs concentration plots after removing the contribution rising from water ($1/T_{1,water} = 0.2826\ ms^{-1}$) . The relaxivity values at each frequency, for Prussian Blue nanoparticles and its FeGA containing assemblies were obtained from the slope of linearly fit curve. The plots are presented in Figure 130 and results are discussed below.

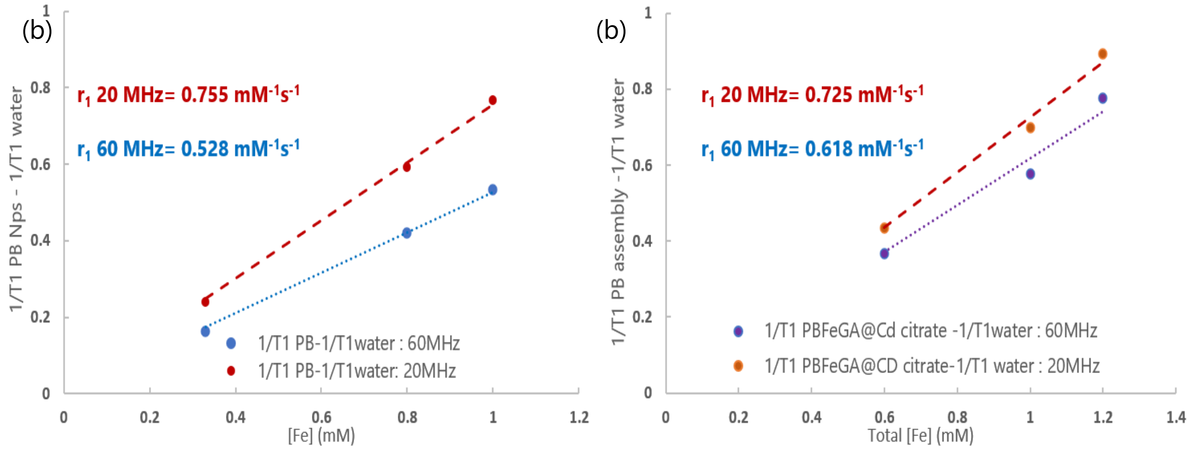

Figure 128. Variation of the inverse of longitudinal relaxation times as a function of [Fe] concentration at 20 MHz (dashed line) and 60 MHz (dotted line) for (a) PB nanoparticles and (b) PB FeGA-CD citrate assemblies

Table 7. Longitudinal (r_1) and transverse relaxivities (r_2) in $mM^{-1}s^{-1}$ of PB nanoparticles and assembly at 20 MHz, 37°C and longitudinal relaxivity at 60 MHz, 37°C.

Sample	**20 MHz**			**60 MHz**
	r_1	r_2	**r_2/r_1**	r_1
PB nanoparticles	0.755	0.862	**1.142**	0.528
PB FeGA-CD citrate assembly	0.725	0.922	**1.271**	0.618

The calculated relaxivities do not show a significant difference between the activity of PB nanoparticles and their assemblies, as they are both around 0.7 $mM^{-1}s^{-1}$ at 20 MHz (0.47 T). However, it is to be noted that the total paramagnetic ions (Fe^{3+}) concentration in the sample had been considered for the calculations. The PB nanoparticles only make up 40% of the Fe in the assembly. Therefore, theoretically the r_1 value should have been significantly lower than that observed for the nanoparticles. Moreover, it can be assumed that building elongated chains of these nanoparticles would decrease the number of ferric ions available at the surface. As compared to the bare nanoparticles, some of the surface Fe(III) ions are linked to gallate complexes, thereby leading to lesser exchangeable water molecules at the surface. However, despite these factors the longitudinal relaxation times observed with the assembly was similar to those of single particles. This indicates that the iron-gallate complex used to create the assemblies positively contributes to its activity. The polymeric network formed using the carboxylate and hydroxyl groups of gallic acid with Fe^{3+}, also contain water molecules that are active and exchangeable. This additional interaction with protons from water helps in providing a quicker relaxation pathway. The r_2/r_1 value is lower than 2, proving that the PB assemblies could behave as good T_1 agents and provide a positive contrast enhancement to the T_1-weighted MRI. It was also observed that the assemblies perform even better than the individual nanoparticles at higher frequencies as the r_1 value was 0.6 $mM^{-1}s^{-1}$ at 60 MHz (1.5 T) as opposed to 0.5 $mM^{-1}s^{-1}$ obtained for PB Nps. It means that FeGA complex covering the nanoparticle surface generates a stronger effect at high fields.

T_1 weighted-contrast was measured on all samples. The phantom images were recorded using solutions containing different concentrations of Prussian Blue nanoparticles and was compared to the PB-FeGA assemblies. The T_1-weighted phantoms were recorded at 1T with a recovery time (TR) of 100 ms. TR corresponds to the time between two consecutive radiofrequency pulses. Water was studied simultaneously as a blank to understand the degree of contrast obtained with the samples.

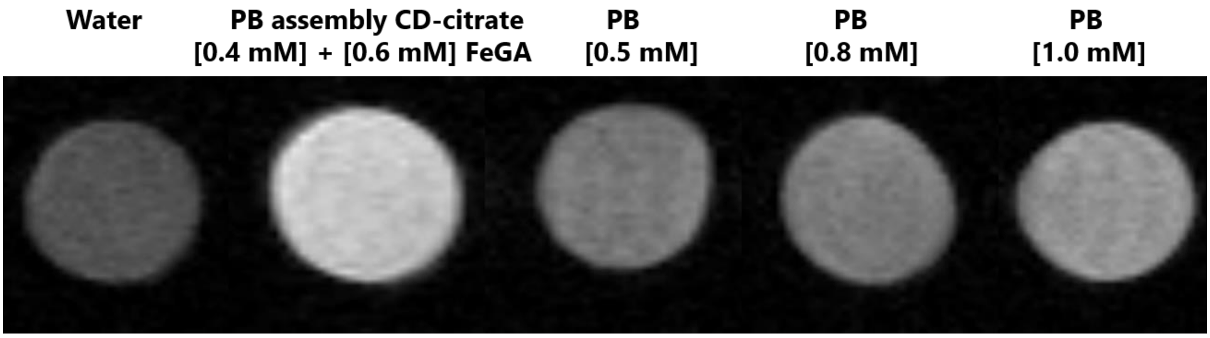

Figure 129. T_1 weighted MRI contrast phantom images of PB assemblies and nanoparticles with corresponding Fe^{3+}concentrations, obtained at 1T.

The images reveal that the PB-FeGA nanoassembly built using iron-gallate polymeric network could act as an efficient diagnostic agent as it enhances the T_1 contrast to a large extent when compared to pure water. On comparing to a similar concentration of PB nanoparticles (~0.5 mM), the assemblies displays a much higher contrast. Furthermore, considering the total Fe content of the newly synthesized chains (1 mM Fe), the contrast obtained is much brighter than 1mM suspension of PB nanoparticle suspension. The improvement is evident in the phantom images (Fig.131). It proves that the iron-gallate network, instead of hindering the relaxation rates of the ultra-small Prussian Blue nanoparticles, adds on to it and positively enhances it.

4.7.2 Gd-Prussian Blue system

Most commercial contrast agents used for clinical MRI contain gadolinium (Gd^{3+}). These paramagnetic ions have 7 unpaired electrons and are therefore able to generate the highest contrast for medical applications. Gd^{3+} is usually strongly chelated to different types of linear or macrocyclic ligands to limit its leaching or interaction with other ions present in the human body, and reduce adverse effects. These complexes are marketed under brand names of

Magnevist, Dotarem, MultiHance, ProHance, Omniscan etc. The use of some of these CAs are restricted or suspended in the EU due to high risk of potentially fatal nephrogenic systemic fibrosis.[265] Therefore, there is a need for renally-clearable and high performance MRI contrast agents and Gd-Prussian Blue nanoparticles provide a safe alternative with added therapeutic benefits.

The 5% Gd-doped PB showing remarkable relaxivity values were developed by Dr. L.Fetiveau during her PhD thesis in our group.[177] Controlled assemblies of these ultra-small nanoparticles were synthesized using the method described in Chapter 3. Similar to the PB system discussed above, the nanoparticle solution was concentrated to reach a concentration of [Fe]=1 mM. Considering 1% of the gadolinium is lost during UF and washing steps, the concentration of [Gd] in the concentrated sample is 0.04 mM (*ICP is under progress to check this hypothesis*). The GdPB FeGA-CD citrate nanoassembly was also concentrated using ultra-filtration to lead to a total [Fe] of 1 mM (*exact to be determined by ICP*), out of which only 40 % is composed of Gd-PB nanoparticles. Therefore, Gd content in the most concentrated assembly solution was only 0.016 mM. The relaxation time measurements with various degrees of dilutions were repeated for all Gd containing samples at 20 and 60 MHz in 37°C temperature. The plots and results are tabulated below.

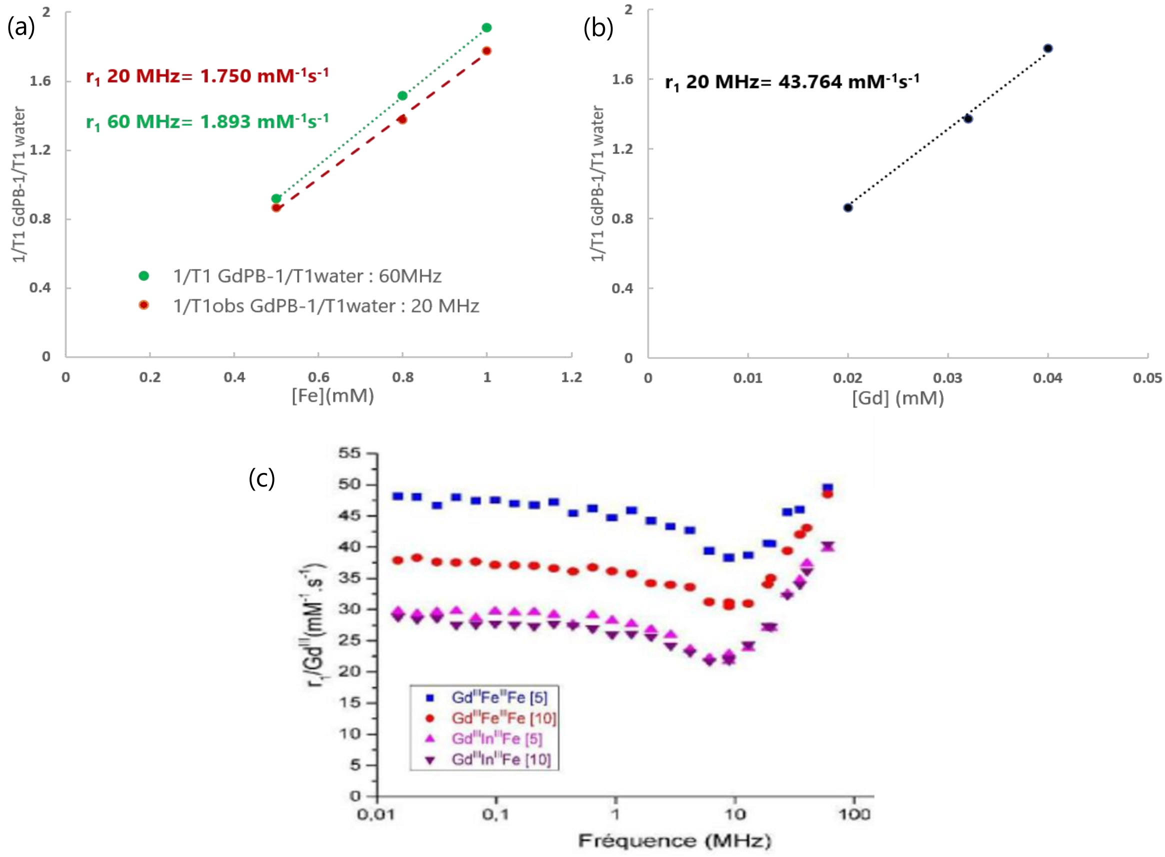

Figure 130. Variation of inverse of longitudinal relaxation time as a function of (a) iron and (b)

gadolinium concentration in Gd-PB nanoparticle solutions, recorded at 37°C. (c) NMRD profiles showing evolution of relaxivity with respect to frequencies for 5 and 10 % Gd doped PB (Fe^{II}Fe) and PB analogue (In^{II}Fe) from the doctoral thesis of L.Fetiveau.[177]

Experimentally, it was clearly observed that the relaxation time with Gd doped PB (1 mM at 485 ms) nanoparticles were much shorter than its pure PB (953 ms) counterpart. The plots shown in Figure 132, prove that introducing a small percentage of paramagnetic ions into the structure significantly increases the relaxivity values to 43.7 mM^{-1}s^{-1} per Gd ion. Considering only the iron content in the nanoparticle, r$_1$ of 1.89 mM^{-1}s^{-1} could be obtained at 60 MHz and it is slightly lower at 20 MHz frequency. This trend is characteristic of the influence of gadolinium ions. NMRD profiles recorded with comparable samples show a similar trait of increase in r$_1$ per Gd in the 10-100 MHz region due to the effect of long rotational correlation time. Therefore, increasing the field strength should improve the relaxivity, and consequentially the MRI contrast for these gadolinium containing CAs. Assemblies synthesized using Gd-doped PB were treated similarly. However, as explained above adding 2 volume equivalents of other reagents into the pre-formed Gd-PB nanoparticles, reduces the overall effect of gadolinium ions in the chains. Instead of 5 % of the total sample, Gd content is effectively reduced to just 1.6 % which is once again diluted by the polymer addition step. Therefore, the concentration of Gd is quite low in the final assembly sample studied. However, the influence of its slight presence could be observed as the relaxivity plots in Figure 133 show significant improvement compared to PB-FeGA assemblies.

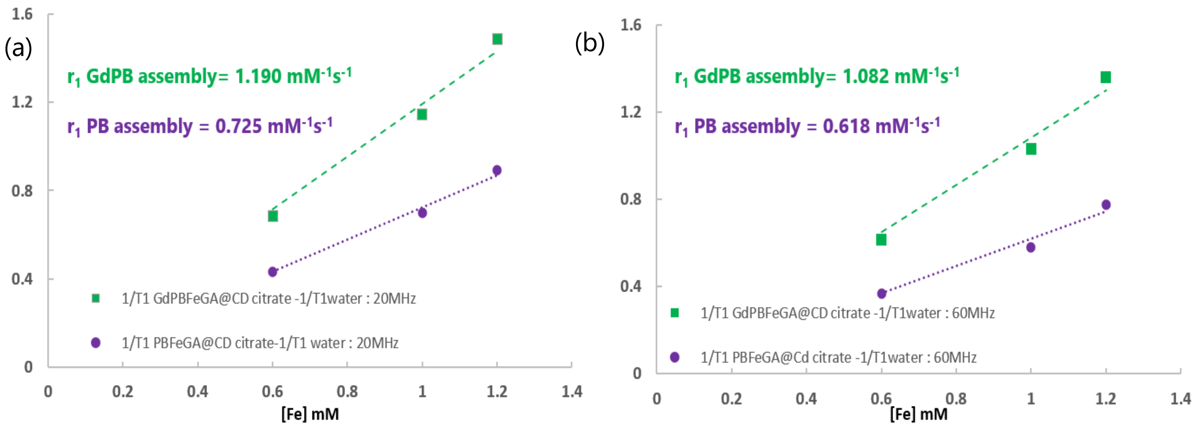

Figure 131. Effect of presence of Gd ions on the longitudinal relaxivities in PB FeGA-CD citrate assemblies at (a) 20 MHz and (b) 60 MHz.

The apparent longitudinal and transverse relaxivities of the Gd containing nanoparticles and assemblies created using iron-gallate are summarized in Table 8. The average r$_2$/r$_1$ of the assembly is 1.225 and that of the Gd-PB individual nanoparticles is 1.133. The values are lower than 2, indicating that both these nanostructures could act as T$_1$ contrast agents and provide a bright contrast in magnetic resonance imaging. The longitudinal relaxivity per Gd^{3+} ion in the assemblies reaches unprecedentedly high value of 74 mM^{-1}s^{-1}. However, this has been calculated by ignoring the contribution coming from Fe^{3+} ions and is therefore over-estimated. The exact ion concentrations will be determined using ICP studies.

Table 8. Summary of longitudinal (r_1) and transverse (r_2) relaxivities in $mM^{-1}s^{-1}$, per Fe ion measured for Gd-PB nanoparticles and assemblies, at 20 and 60 MHz in 37°C

Sample	**20 MHz**				**60 MHz**
	r_1	r_2	**r_2/r_1**	r1 per Gd	r_1
GdPB nanoparticles	1.750	1.982	**1.133**	43.76*	1.893
GdPB FeGA-CD citrate assembly	1.190	1.457	**1.225**	74.43*	1.082

The phantom images of Gd-PB nanoparticles at different concentrations and the synthesized assemblies were recorded at 1T. The samples were studied alongside the most commonly used commercial contrast agent, Gd-DOTA (Dotarem) at 0.05 mM concentration. The images prove that the ultra-small gadolinium doped PB nanoparticles are very efficient T_1 contrast agent. The performance of the Gd-PB is distinctly better than Gd-DOTA having the same amount of Gd^{3+} ions. Therefore, these particles can work effectively at low concentrations, minimizing the adverse effects. As expected, the PB FeGA assembly has the lowest contrast, since its Gd content is zero. Interestingly, Gd containing Prussian Blue assembly provides a brighter and improved contrast even when compared to single particles containing higher [Gd] (0.025 mM).

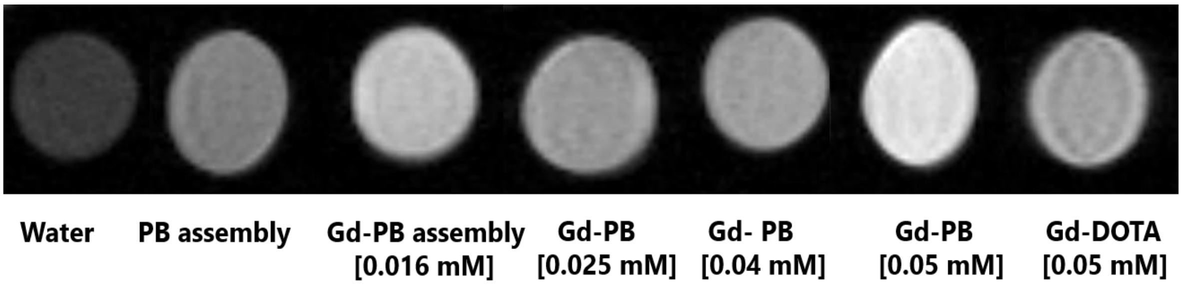

Figure 132. T1 weighted MRI contrast phantom images of Gd-PB assemblies and nanoparticles with corresponding [Gd^{3+}] concentrations, obtained at 1T compared to Gd-DOTA

This once again proves that building assemblies of these ultra-small nanoparticles is advantageous and the type of linker used plays a very important role. Since the polymeric network that supports the chain formation of PB/Gd-PB nanoparticles, was created using active, paramagnetic Fe^{3+} ions coordinated with gallic acid, the resultant structure benefits from improved relaxivities, which in turn brightens the contrast in MRI. By considering that the relaxivities observed with the assembly samples is an additive result of its individual components, the contribution of FeGA network could be roughly quantified using the following equation:

$$r_{1,FeGA} = (r_{1,PB\ FeGA}\,[T.Fe] - r_{1,PB}\,[PB])/\,[FeGA]$$

Here, [PB] refers to the Fe^{3+} concentration in Prussian Blue nanoparticle solution, [FeGA] is the added iron content, remaining in the assemblies after UF and washing steps and [T.Fe] is the total sum of iron present in the sample. The values calculated at different frequencies are reported below and was verified using the experimental values obtained with Gd-PB system.

Table 9. Summary of experimentally determined longitudinal relaxivities of nanoparticles and assemblies and the calculated values for FeGA complex at different frequencies.

Sample	**r1 20 MHz**	**r1 60 MHz**	**Sample**	**r1 20 MHz**	**r1 60 MHz**
PB (exp.)	0.755	0.528	Gd-PB (exp.)	1.750	1.893
PB FeGA (exp.)	0.725	0.618	Gd-PB FeGA (exp.)	1.190	1.082
FeGA complex (calc.)*	**0.705**	**0.678**	Gd-PB FeGA (calc.)*	1.12	1.16

Calculations revealed that the FeGA polymeric network constructing the PB nanochains have longitudinal relaxivity values of 0.678 $mM^{-1}s^{-1}$ at 60 MHz and 0.705 $mM^{-1}s^{-1}$ at 20 MHz at 37°C. The substitution of these values into the equation for Gd-PB FeGA using known r_1 values of Gd-PB at both frequencies generated values that were close to the experimentally determined ones. In this way, the contribution coming from each of the components in our nanosystem was accounted for.

4.8 CONCLUSIONS

This chapter highlighted the various possible bio-medical applications of the novel nanostructures created using Prussian Blue nanoparticles. The poly-CD-citrate coated assemblies are capable of carrying a high payload of positively charged doxorubicin and delivering it efficiently to acidic tumoral sites. The release of Dox in physiological pH was minimal, pointing to low non-specific release in neutral healthy environment. The electrostatic interactions and inclusion-complex formations between the chain and the drug molecules were responsible for high encapsulation (94%) values. In order to understand the effect of each of these factors separately and extend the applications further, loading of a neutral anti-cancer drug was also attempted. 5-Fluorouracil used to treat pancreatic cancers was chosen as the model drug. However, its characteristic band in the UV region was overlaid by the signals coming from various components of our assembly. HPLC separation was necessary for accurate determination of its loading within PB-FeGA. Since it was not available, other routes were applied to make the nanoparticle assemblies more functional.

Loading of other neutral molecules, like 7-hydroxy coumarin was attempted. Since it is a fluorescent molecule like doxorubicin, its encapsulation could be followed using fluorimetry. Various sets of experiments revealed that this substituted coumarin could also be effectively loaded onto the PB nanochains with a 45 % encapsulation efficiency. This is an indirect indication that other neutral molecules could also be effectively loaded onto the PB nanochains. Unfortunately, a burst release of ~29% of the loaded dye occurs within a short time in neutral pH. Therefore, this fluorescent system could not be used for *in vivo* tracking and understanding the bio-distribution of our nano-assemblies. Other routes have to be explored. A pre-loading of 10% of coumarin prior to the addition of the polymer could favour the formation of H-bonds with the CN groups and increase the stability. Conjugation using cyanin dyes (ICG) are planned for the future to detect the nano-assemblies *in vivo* and evaluate their biodistribution.

Confocal microscopy studies proved that doxorubicin loaded in the assemblies were internalized more inside cells as compared to free doxorubicin in solution. Cell-colony assays were conducted which demonstrated that the PB FeGA assemblies by itself are very safe and non-toxic, even at significantly high concentrations. However, doxorubicin loaded nanoparticle chains can efficiently kill cancerous cells. Photo-thermal conversion of the nanoparticles in response to near infra-red light radiation was also studied. The therapeutic activity of PB is improved upon creating assemblies as the same concentrations lead to higher temperatures. The performance remains constant over multiple cycles, even in simulated physiological environments. In addition to killing cancerous tissues with the heat generated, the amount of drug released from the system could be amplified using this laser triggered rise in temperature. Therefore, the PB FeGA nanochains can achieve synergistic photothermal and chemotherapy which can lead to complete elimination of tumours. Novel sub-10 nm PB particles containing nitric oxide were also synthesized during this doctoral thesis, in a green synthetic procedure. These nanoparticles release NO gas upon heating, which was verified using a Griess assay. NO release can lead to tumour growth inhibition and sensitization of cancerous tissues towards radiation therapy. This adds another therapeutic perspective to these versatile nanoparticles. Chains of these PB-NO particles could also be created, further diversifying our nanosystem.

Lastly, the diagnostic applications of the PB FeGA-CD citrate assemblies were investigated using relaxivity measurements. Instead of reducing the overall activity due to change in nanoparticle alignment and concentration, the building of assemblies provide a positive enhancement to the observed T_1 contrast. The results showed that the PB and Gd-PB nanochains provide a brighter contrast in phantom images as compared to the respective concentrations in individual self-standing particles. Clinical MRI machines usually operate at 1.5 or 3T and as seen with the relaxivity values, the PB FeGA assemblies perform better than bare PB nanoparticles at high fields. This is because FeGA complex network was used to form the assemblies. The water molecules coordinated to the paramagnetic Fe^{3+} are responsible for this effect and its contribution was calculated. Liu et. al had reported that renally-clearable, PVP supported iron-gallic acid nanodots could behave as efficient MRI contrast agents.[101] Their nanoparticles exhibited higher relaxivities and better contrast at acidic pH as compared to neutral environment. It was attributed to the dissociation of Fe^{3+}-GA complex from tris-coordination to bis-coordination under mildly acidic conditions. It was suggested that this reduction in the coordination number enhances the quantity and mobility of the water coordinated to the paramagnetic Fe center, thereby improving the relaxivity.[101] This property is beneficial for tumour detection and occurrence of such a phenomenon is also possible using our PB-FeGA nanosystem. Therefore, in principle the contrast obtained in phantom images could be further improved.

Additionally, preliminary studies show that the enhanced absorption of PB FeGA assemblies in the visible-NIR region could be translated to photoacoustic signal and which can contribute to PAI (annex 6.4.3). In conclusion, it can be said that a stimuli-responsive, activatable assembly of ultra-small nanoparticles was created in this doctoral project. It is an effective theranostic agent that combines disease diagnosis using magnetic resonance imaging, NIR activated photothermal therapy and NO gas release, together with chemotherapeutic drug delivery to target sites. Tracking of these PB nanochains *in-vivo* using ICG, a fluorescent molecule, has been planned. Bio-distribution studies in mice need to be conducted. Dis-assembling of the iron-gallate network and renal clearance of the ultra-small PB nanoparticles need to be investigated.

5 CONCLUSIONS AND PERSPECTIVES

The work done in this thesis project has been focussed on adding new therapeutic and theranostic modalities to ultra-small PB-like nanoparticles while maintaining a green synthetic pathway. It can be broadly divided into three main sections. The first part was dedicated to creating new analogues of Prussian Blue by substituting one or both of the ions with a heavy metal ion. This was done to incorporate a never before explored radiation therapy perspective into PB. It is known that when high energy radiation interact with high-Z elements a cascade of Auger electrons are generated. These are responsible for radiolysis of water and help form reactive oxygen species (ROS) that can kill cancer cells in their vicinity. Three individualized and self-standing PBA nanoparticles containing gold, iron and platinum in different combinations were produced in water. The synthesis and complete characterization of these novel compounds are reported in Chapter II. These solutions called cyanosols were synthesized in an easily scalable, green manner, in the absence of surfactants and reducing agents, in a cost-effective method. The nanoparticles obtained were homogenous and remained stable in water without any aggregation or deposition, over long periods of time.

By optimizing the experimental conditions, ~30 nm long, rice-grain shaped gold nanorods with tapered ends were obtained. This unique nanostructure is made up of AuCN nanocrystal while the surface was decorated with 1 nm, spherical Pt^{II}-containing cyanosol nanoparticles. Such bi-metallic gold-platinum alloy nanoparticles with Au^{I} and Pt^{II} has never been described before in the literature. The regular periodic decoration of the AuCN nanostructure with Pt(II) has to be understood. Unfortunately, no photoluminescence was observed. Spherical 5 nm platinum hexacyanoferrate (FePt) and 1-2 nm platinum tetracyanoplatinate (PtPt) nanoparticles were also developed during this thesis. These porous nanoparticles containing Fe^{II} and Pt^{II} ions are extremely stable in water as well as physiological media. Importantly, they could be post-coated with different polymers depending on the requirements. Here, the polymer polyvinyl pyrrolidone was used to cover the surface of these nanoparticles to avoid any quenching of radicals formed under irradiation, which was previously observed with dextran. Fetal bovine serum and artificial lysosomal fluid were used to mimic biological conditions and even with the introduction to such media and exposure to 37°C for 6-15 hours, the UV-Vis signatures of FePt and PtPt remain intact. When subjected to a γ-radiation dose of 4000 Gy, there was an appearance of a SPR band at 540 nm, in case of AuPt cyanosol which is characteristic to pure gold nanoparticles. Therefore, a small proportion of Au^{I} in the nanoparticles underwent reduction under this large dose. However, no significant changes appeared in case of FePt and PtPt nanoparticles providing further indication that they could be used for radio-therapy purposes.

Effect of their presence on biomolecules were studied using plasmids as a nanoprobe. Its double-stranded structure is considered similar to DNA and is generally used to understand its behaviour on exposure to high-energy beams. A significant enhancement in the instigation of lethal, irreparable DSBs were observed upon combining these porous Pt^{II}-containing nanoparticles with plasmids before γ-irradiation. The experiments help provide an understanding of the molecular mechanisms behind radiation induced damages. Then, *in cellulo* experiments were conducted. FePt and PtPt cyanometallate nanoparticles appear non-toxic to biologically relevant, healthy, primary fibroblast cells. They are also safe towards cervical cancer cells (HeLa) upto a total metal concentration of 2.5×10^{-4} $mol.L^{-1}$. These cells incubated with nanoparticles were irradiated using a Cs-137 source, in order to verify if the radiation response obtained with plasmids could be translated to cells. The survival fractions obtained as a function of dose supplied, demonstrated that both the nanoparticles significantly amplify the death of cancer cells when compared to the control experiment. Interestingly, it could be seen that sub-lethal lesions are predominant and add up to generate an overall lethal consequence. This is an uncommon phenomenon and maybe the result of the porosity of our nanoparticles. The water coordinated to the surface as well as the ones in the cyano-bridged metallic network are available for conversion to ROS. It is hypothesized that they could disperse and diffuse farther through the porous system as compared to a dense metallic particles. Therefore, the damages are more spread out and the additive lesions cause cell death, improving the therapeutic index. The uptake of nanoparticles within cells is currently being analysed using ICP measurements. The chemical design of these Prussian Blue analogues allow for easy modification of the structure through coordination networks. MRI contrast studies with FePt nanoparticles are being planned. Gadolinium or manganese ions could also be doped on the surface of these nanoparticles to improve the diagnostic perspective. Additionally, PtPt nanoparticles are made of 2 D sheets with close Pt-Pt intersheet distances that explain the blue photo-luminescence observed. It is very rare to obtain luminescence in PB analogues and this result appears very promising. It could aid in tracking the ultra-small nanoparticles *in vivo* and help follow their biodistribution.

In continuation to this work, fluorescence imaging studies will be conducted *in cellulo* at ISMO to study the localisation and degradation of the PtPt particles. A deeper study of the photoluminescence properties (quantum yield, lifetime) as well as the investigation of the polymer coating nature to tune the emission are planned. Any core-shell strategy favouring shorter PtPt distances between the 2D planes could shift the emission towards NIR. Also X-Ray computed tomography could also be envisaged with these nanoagents. Synergistic effect of chemotherapy and radiation treatment for cancer could be combined by the interaction of the nanoparticles with doxorubicin as observed on some MOFs@dox systems.[266] Regarding the FePt particles, an interesting strategy would be to grow a PB shell of 1 nm that would be strongly influenced by the presence of FePt. This would lead to : i) some T1 contrast for MRI due to the presence of Fe(III) ions at the surface ii) the shift towards 800 nm that would provide enhanced PTT efficiency or PAI imaging.

The second area of focus of this thesis project was building assemblies of ultra-small theranostic nanoparticles in order to overcome a major obstacle in their use in medicine. Large nanoparticles (>10 nm) cannot be renally cleared out, so accumulation and possible side-effects are common concerns, while sub-10 nm particles are prematurely eliminated from the body lowering its therapeutic activity. In order to obtain a safe, multifunctional and efficient theranostic agent formation of activatable assemblies of ~5 nm PB particles was attempted. It was challenging to obtain homogenous assemblies while trying to maintain a green synthetic pathway. We have shown here for the first time that a metal phenolic network (MPN) built using iron and gallic acid can self-assemble charged ultra-small, PB nanoparticles into controlled 1-dimensional nanochains. This could be done in water, without the use of surfactants, at room temperature. The formed assemblies were stable and improved the optical properties compared to single, individual nanoparticles. The nanochains could be post-coated with different polymers like PVP, dextran, and poly γ-Cyclodextrin citrate and its complete characterization is reported in chapter 3.

The mechanism of formation of these assemblies was investigated. Since changing the ion introduced during synthesis to sodium/ calcium (Na^+/Ca^{2+}) does not lead to formation of similar assemblies, it can be said that the μ-oxo bridged polymeric Fe^{3+}-gallic acid network species is necessary for linking the individual Fe-rich PB nanoparticles. It was observed that substitution with similar gallium ions (Ga^{3+}) could lead to nanochain formation, although it was less controlled. This work sheds light on the possibility of interesting features that could be developed with focus on Ga^{3+}-gallic acid complexes and their formation of metal phenolic networks. It is hypothesized that similarly to charged gold NPs, once a dimer of two PB NPs (linked through FeGA) are formed, the electrostatic double layer rearranges to form a uniform layer covering the surface. Then the other NPs in the vicinity preferentially attach to the ends of the dimer, in order to minimize the electrostatic repulsions between the negatively charged particles and this might be the reason of formation of elongated PB FeGA nanochains. In situ experiments by DLS and UV-visible spectroscopy during the formation are needed to ascertain the formation mechanism. Other polyphenols could also act as PB linkers and help form similar nanostructures. The variation with ellagic acid in water-ethanol mixture with Fe^{3+}, Na^+ and Ca $^{2+}$ions leading to size-tuneable assemblies have been described in this thesis. 1D nanochains could also be formed using other ultra-small nanoparticles. 5% Gd-doped PB, sodium nitroprusside linked PB and FePt cyanosol, display interesting results that open a wide array of possibilities for future studies.

The last section of this thesis was devoted to evaluation of the theranostic efficiency of PB-based nanochains. Drug loading experiments revealed that there was a marked increase in the overall stability of the nano-system on assembling the nanoparticles. Additionally, the coating with poly-Cyclodextrin (CD) citrate polymer enhances the encapsulation efficiency (~85% within 1 hour incubation) and stabilizes the PB FeGA system to withstand a higher amount of oppositely charged anti-cancer drug molecules. This is the first time such high encapsulation of doxorubicin has been reported in ultra-small PB systems.

Experiments in physiological media made it clear that almost 50% of the encapsulated drug could be released within one hour in simulated acidic environment of the tumour, while only a small amount escapes from the system even on prolonged exposure to neutral, healthy cellular pH. It could also be seen that a rise in local temperature would increase the amount of drug released in the area of focus. Since PB nanoparticles have photo-thermal conversion capability this temperature rise could easily be attained. Near infrared laser radiation tests revealed that the PB FeGA assemblies behave as better PTT agents when compared to the starting PB ultra-small particles. Therefore, synergistic photo-thermal and chemotherapy could lead to effective cancer cell killing using these novel, drug-loaded PB nanochains. In-vitro experiments conducted showcased the safety and non-toxicity of the nanochains towards cells, while the doxorubicin-loaded PB FeGA were efficient in killing the cancer cells. The internalisation of the drug was visualized through confocal microscopy studies, and confirmed the drug delivery ability under acidic pH once in lysosomes.

Diversification of the nanochains with nitric oxide (NO) containing ultra-small nanoparticles led to interesting results and added functionalities. NO, a tumour growth inhibitor and radio-sensitizing gas could be released from the nanoparticles on heating. So apart from being a drug delivery vehicle, this nanostructure is also a carrier for NO, which can be released with NIR radiation and work together with photo-thermal therapy. The results of these positive preliminary experiments would be reproduced in the coming months before moving to *in-vitro* tests.

In order to have an idea of the diagnostic capabilities of the nanochains, relaxivity studies were performed in Mons, Belgium. Pure PB and Gd-PB single nanoparticles and their respective assemblies were evaluated. Since FeGA complexes were used to create the PB assembly, they positively enhance the T1 weighted MRI contrast of both assemblies. Therefore, not only has the overall therapeutic index of ultra-small PB NPs improved, but the assembly formation proves beneficial for diagnosis as well. We need to verify if the MRI contrast could be further increased in acidic pH, possibly making it more sensitive for tumour detection. This is suggested because theoretically a lower pH, could disassemble the Fe^{3+}-GA complex, increasing the water mobility and thereby the total relaxivity. Breaking the nanostructure into its composite single particles and renal clearance studies need to be performed. Tracking the PB nanochains using indocyanine green and *in-vivo* biodistribution studies have been planned for the coming months. Depending on these results, post-coating with designed polymers to avoid liver capture or specifically targeting tumours could be done in collaboration with expert groups in the field. A better control over the length of the nanochain is still needed and microfluidics may be helpful in this direction.

In a nutshell, this new family of self-assembled nanochains of ultrasmall particles appear promising for several types of theranostic applications.

6 ANNEX

6.1 CHARACTERIZATION TECHNIQUES

6.1.1 Dynamic light scattering and zeta potential measurements

The solution was illuminated with laser beam and the light scattered back from the sample was used to determine the average hydrodynamic diameter of the nanoparticles. The size distribution data provided information on the homogeneity and regular analysis of the sample provided a clear idea on its evolution with time. Malvern Zetasizer with 173° backscattering mode instrument was used for DLS measurements. Zeta potential is a consequence of existence of charge on the surface of particles and this could also be measured using Zetasizer instrument. The surface charge of nanoparticles is an important parameter that determines the interactions between them and is a measure of stability of the suspension. A combination of electrophoresis and laser doppler velocimetry using scattered light, is used to determine the zeta potential spectrum of nanoparticles.[267] This type of measurement requires approximately 1 mL of sample.

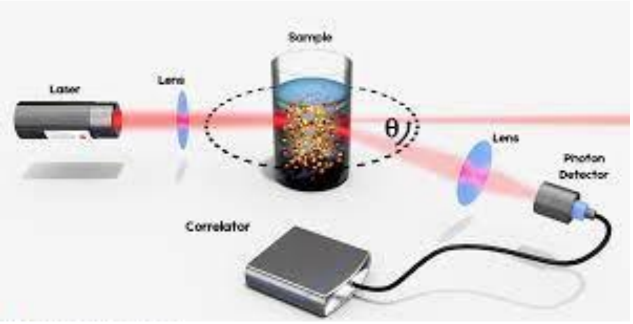

Figure 133. Working principle of dynamic light scattering

6.1.2 Nanoparticle Tracking Analysis

NTA uses principles of light scattering and Brownian motion to estimate the size of nanoparticles in liquid suspension. The solution is injected into the sample chamber and illuminated by a laser beam. The scattered light is collected by a microscope and viewed using a digital camera in real-time. The size-distribution and concentration of particles in solution could be obtained using NTA.[268] Malvern Nanosight was used to perform these studies in ISMO, Université Paris Saclay and Université de Paris.

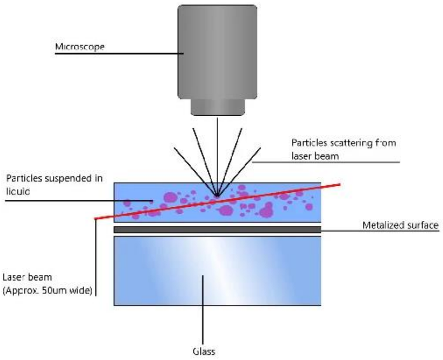

Figure 134. Working principle of nanoparticle tracking analysis.

6.1.3 Transmission electron microscopy

Transmission electron microscopy uses a beam of electrons emitted from a tungsten source and accelerates it through an electromagnetic field. This electron beam passes through the sample on the grid and depending on density, atomic number and other properties of the analysed material, a contrasted image is generated using a charge-coupled device (CCD).[269]TEM images reported in the thesis were using JEOL microscopes (80 and 120 kV) at the institute for integrative biology of the cell (I2BC) laboratory in CNRS, Gif-sur-Yvette, France. Formvar-coated copper grids from Agar Scientific were used. The grids were made hydrophilic using glow discharge technique (PELCO easyGLow), prior to deposition of 100 µL of diluted sample.

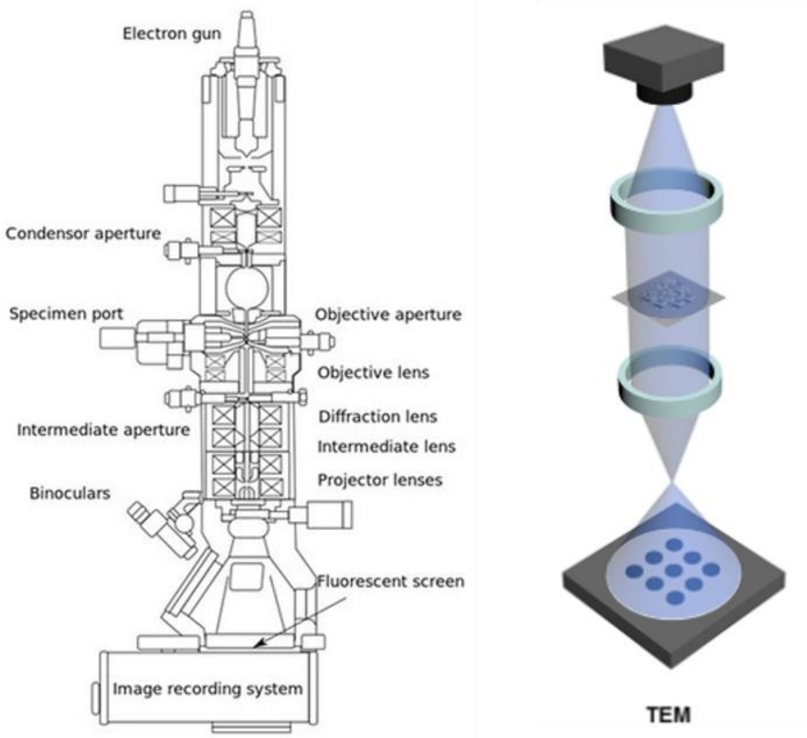

Figure 135. Setup of transmission electron microscope and scheme of image formation[269]

6.1.4 STEM-EELS

In scanning transmission electron microscopy, the electron beam is focussed on a specific spot of the sample and then pixel by pixel scan is performed. The detector collects the transmitted electrons and sample could be visualized. STEM coupled with electron energy loss spectroscopy (EELS) is performed by characterizing the transmitted electrons using a magnetic prism. Chemical properties of thin samples deposited on a grid can be analysed using STEM-EELS. The experiments were conducted by Alexander Gloter in LPS, Université Paris Saclay.

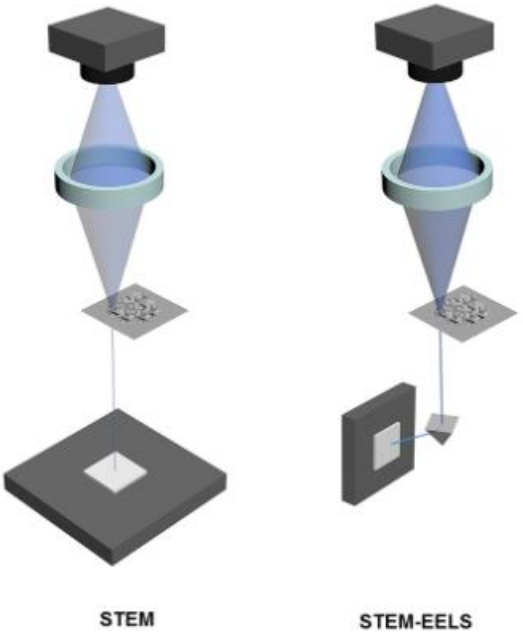

Figure 136. Scheme of STEM and STEM-EELS experiments.[269]

6.1.5 Infrared spectroscopy

IR spectroscopy helped identify the bonds present in the compound. The nanoparticle samples were prepared in powder form after centrifugation and vacuum drying. 1 mg of sample is ground into a fine powder with 99 mg of KBr (transparent in the IR) and made into a pellet. Perkin Elmer Fourier-Transform infrared spectrometer was used and each sample spectra was recorded between 200 cm^{-1} and 4000 cm^{-1}.

6.1.6 Energy Dispersive Spectroscopy

EDS spectra was recorded to detect the amount of each element (K, Cl, Pt, Fe, Au) present in the samples. A X-ray beam is passed through the sample. This causes an ejection of core electrons from the material and the hole created is filled by an electron from higher energy layer. Energy released during this relaxation process is characteristic to elements of the periodic table. The composite material as well as the proportion they are present in can be identified in this manner.[270] These studied were conducted by Francois Brisset at ICMMO, Université Paris-Saclay.

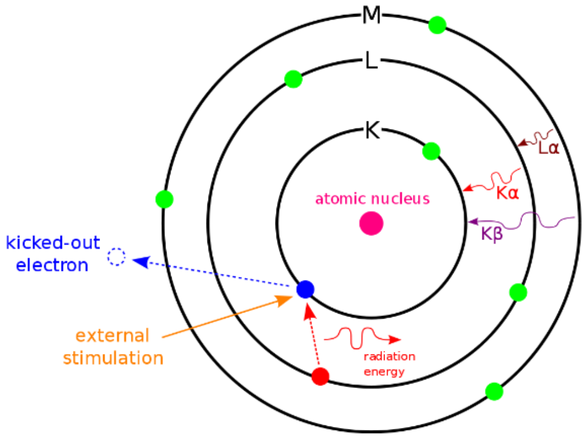

Figure 137. Schematic representation of core electron ejection and subsequent relaxation processes [270]

6.1.7 X-ray Photoelectron Spectroscopy

In this method, x-rays (photons) are focussed on the sample. The energy is absorbed and electrons from the sample are ejected with a certain kinetic energy (KE). Depending on the energy, electrons follow different paths and this is analyzed by the detector. The binding energy of elements present in the sample is determined using incident photon energy and KE of ejected electrons.[271] This provides information about the composition of the sample and the oxidation state of metals present. The measurements were performed by Diana Dragoe at ICMMO, Université Paris Saclay.

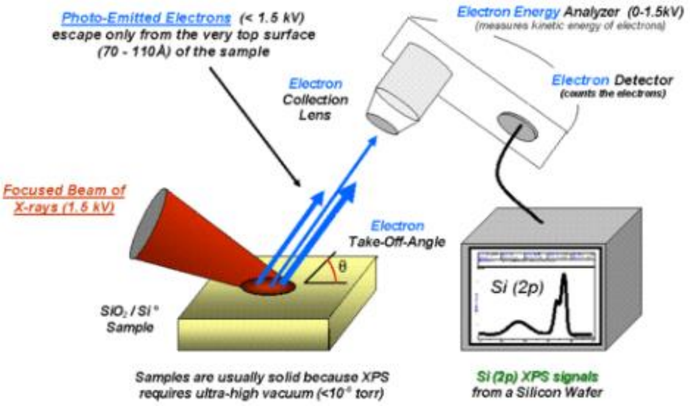

Figure 138. Diagram depicting instrumentation of X-ray photoelectron spectrometer.[271]

6.2 CHAPTER 2

6.2.1 HR-TEM AuPt

Results of high-resolution TEM studies conducted on AuPt cyanosol by Alexander Gloter, LPS. The AuCN nanorods with ordered striations and 1 nm particle decorated surface is seen. The rods could be indexed with a and b distances of P6mm.

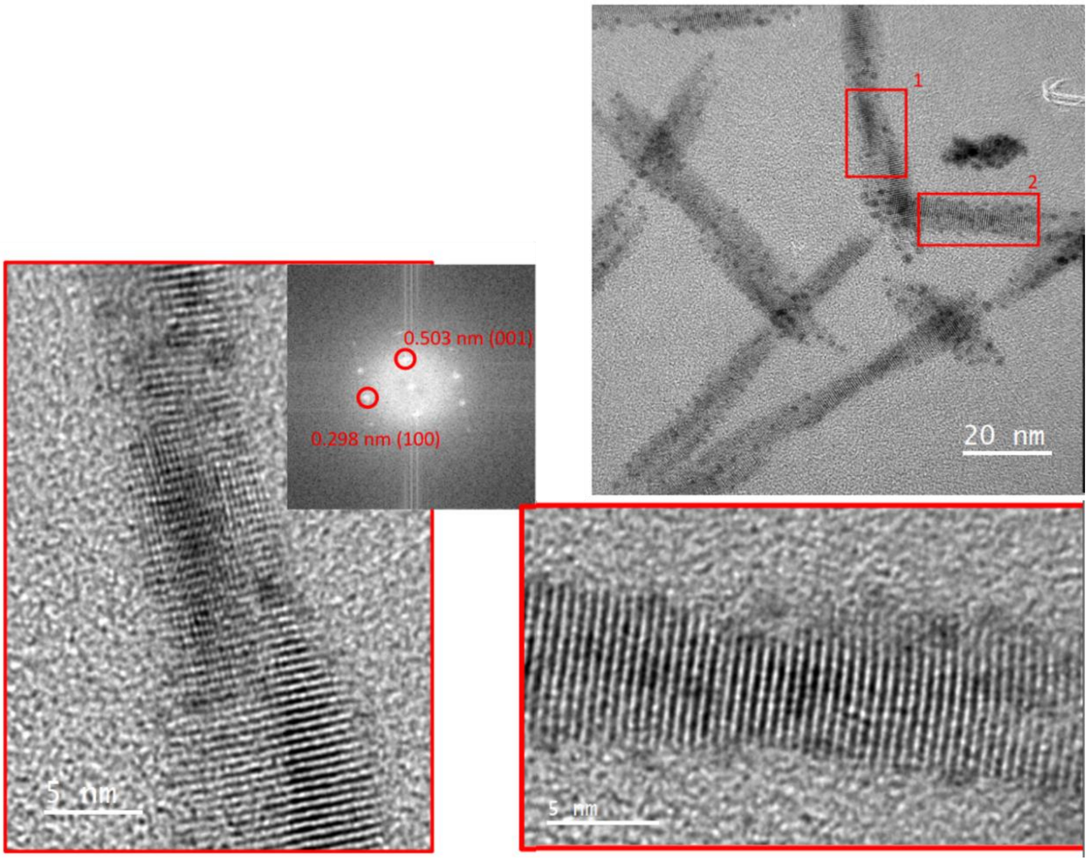

Figure 139. HR TEM images of AuPt nanorods.

6.2.2 UV-Visible spectroscopic studies

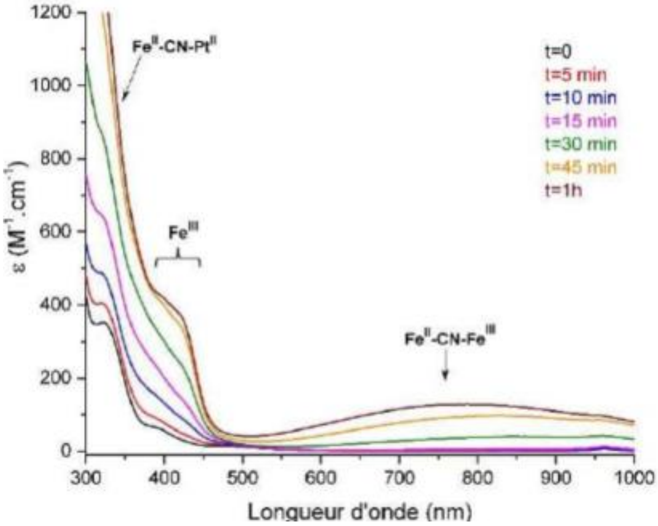

Figure 140. UV-Visible spectra during the formation of $Fe^{II}Pt^{II}$ nanoparticles at 55°C using 10 mM of precursors[201]

Ultrafiltration of the FePt cyanosol was done after polymer addition. So, most of the free Fe^{III}-CN pairs are removed from the solution leading to UV-Visible plot shown in chapter 2, Fig.49. However some of the ferricyanide pairs formed during the synthesis could be trapped with the PVP polymer, causing the re-appearance of the band on exposure to fetal bovine serum (Fig. 56 (a).

6.2.3 Infra-red spectroscopy

The IR spectra of precursors: potassium ferrocyanide and potassium tetracyanoplatinate is reported in Figure 3, for reference.

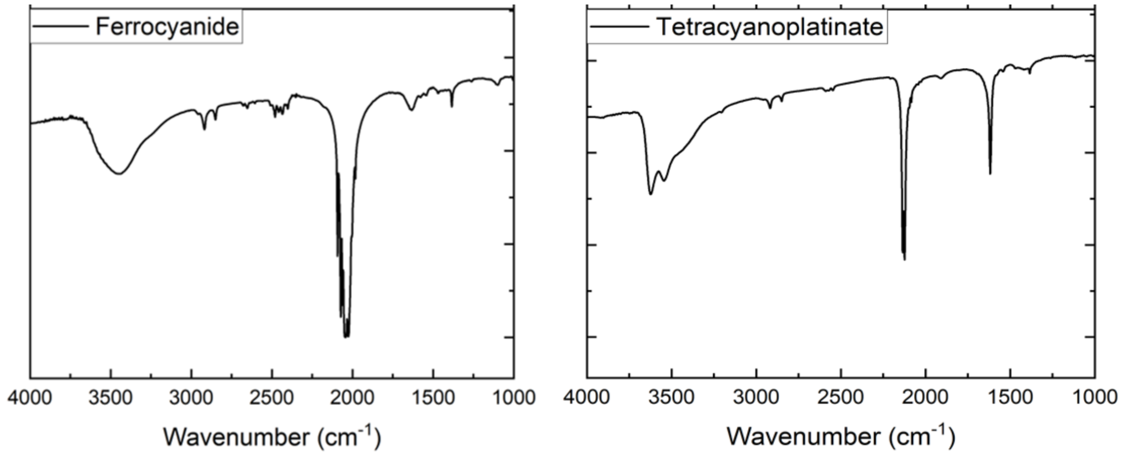

Figure 141. Infrared spectra of FePt and PtPt cyanosol nanoparticles and their respective precursors

6.2.4 X-ray Photoelectron spectroscopy

Comparison to available literature and recording spectra of reference compounds were used to assign the oxidation state of metals in the final cyanosol sample.

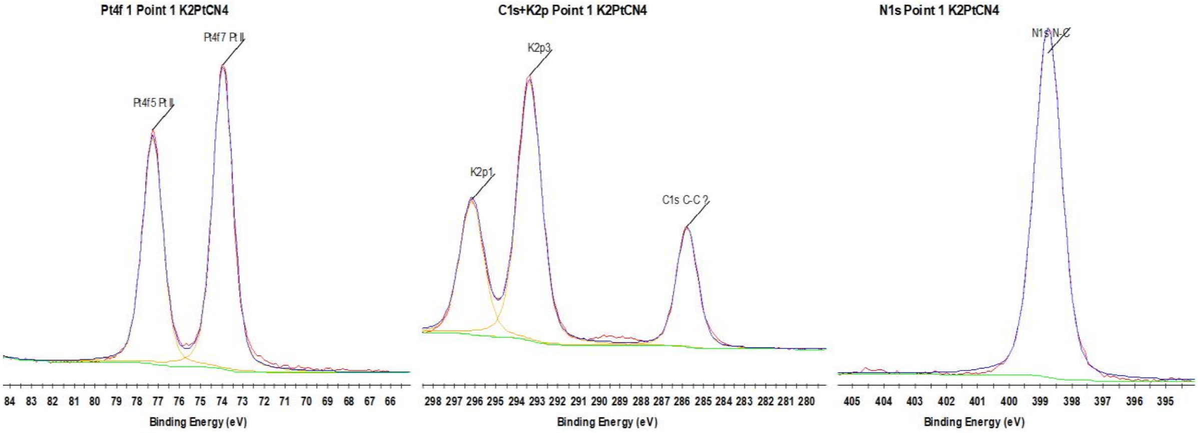

Figure 142. XPS spectra of potassium tetracyanoplatinate (II) precursor

Table 10. Results of XPS analysis on powdered cyanosol nanoparticles

Sample name	Pt 4f region	Metal (Fe and Au)	C 1s region	N 1s region
$K_2[Pt(CN)_4]$	73.9, 77.2		285.7	398.7
PtPt cyanosol	73.8, 77.1		284.7, 285.9,287.6	397.8,399.3, 402.4
AuPt cyanosol	73.8, 77.0	85.1, 88.8	284.9,285.9, 287.6	399.7, 401.3
FePt cyanosol	73.5, 76.8 eV	708.3	284.7,285.7, 287.6	397.6,398.3, 399.7

The Pt^{II} peaks are slightly shifted to lower binding energies in the nanoparticle, as compared to the precursor due to binding through N end to the second metal (Au^{I}, Fe^{II} and Pt^{II}). The C 1s spectral region indicated the peak of C bound to N from cyanides in $K_2[Pt(CN)_4]$, while the nanoparticle spectra have multiple contributions in the region. Deconvolution of this broad peak with a shoulder indicate that those peaks arise from C-O, C-C, C-N in the PVP polymer. Similar effect of N 1s N-C from polymer is visible in the nitrogen edge of the spectra of cyanosol nanoparticles.

6.2.5 Stability in physiological media

The AuPt and PtPt cyanosols showed no evolution over 6 hour duration in artificial lysosomal fluid (ALF). The characteristic peaks (302 and 414 nm of AuPt and 316 nm of PtPt) undergo no deterioration in this acidic medium.

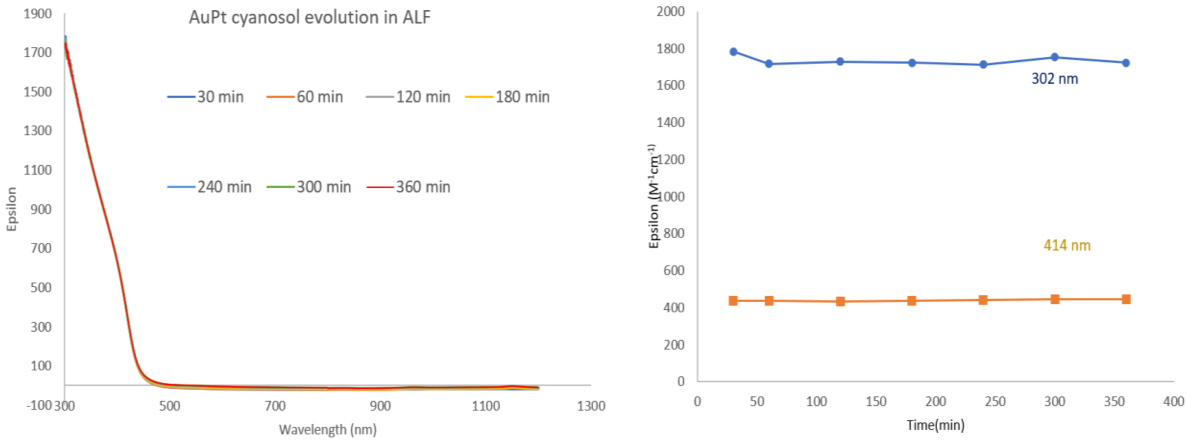

Figure 143. UV-Visible spectral evolution of AuPt cyanosol in ALF medium over a course of 6 hours.

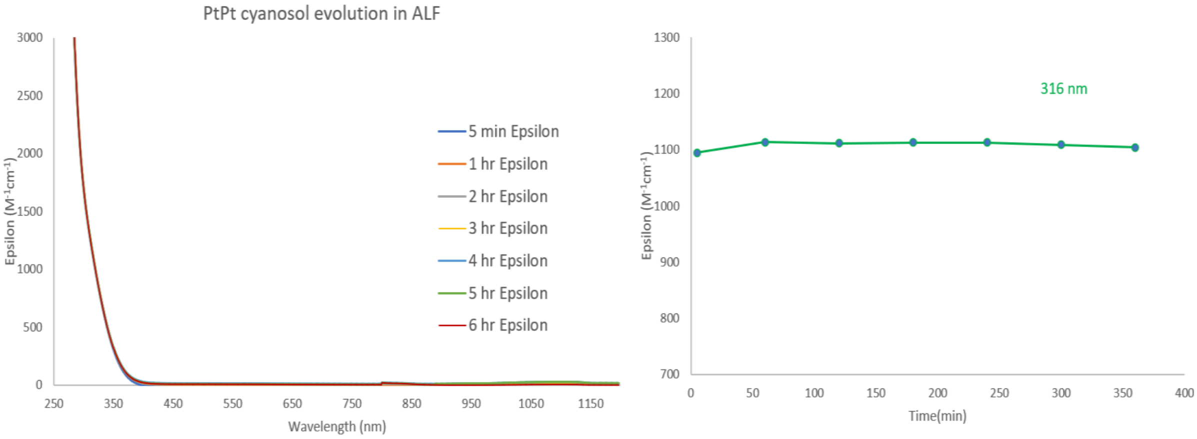

Figure 144. UV-Visible spectral evolution of PtPt cyanosol in ALF over a course of 6 hours.

6.2.6 Radio-enhancing effect of cyanosols on plasmid

The polymer coated solutions were ultra-filtered, washed twice and diluted to reach a total metal concentration of 4 $\times 10^{-5}$ mol.L^{-1}. The amount of each additive in sample preparation prior to irradiation of plasmids is recorded in Table 2(a). The final concentration of nanoparticles combined with the plasmid is 5.3 $\times 10^{-6}$ mol.L^{-1}. The Co-60 gamma source was used for radiation, which had a dose rate of 3.96 Gy/min. Depending on the time of radiation, the dose supplied to each aliquot is recorded in Table 2(b).

Table 11. (a) Preparation of cyanosol solutions with plasmid prior to irradiation and (b) dose

applied to each aliquot

Sample formulation	Control	Cyanosols
TE buffer 1x (µL)	123	123
DNA pBR322(µL)	10	10
NP solution (µL)	-	24
H_2O(µL)	47	23
Total Volume(µL)	180	180

Aliquot	Irradiation time (min)	Dose applied (Gy)
A1	0	0
A2	8	31.6
A3	16	63.3
A4	24	95.0
A5	32	126.7
A6	40	158.4

The amount of lethal, irreparable double strand breaks obtained in the presence of FePt and PtPt cyanosol from the fitted-curve is recorded in table 3 and these values were used to calculate the sensitizing enhancement ratio (SER) reported in chapter 2.

Table 12. Yields of nanosized breaks/plasmid/Gy× 10-3 in the presence of FePt and PtPt cyanosol compared to the control.

Dose (Gy)	Control DSB	FePt DSB	PtPt DSB
30	12.4 ± 2.3	16.6 ± 2.8	18.6 ± 8.9
65	31.1 ± 4.6	44.7 ± 5.7	46.1 ± 17.8
95	55.9 ± 7.0	84.2 ± 8.5	82.5 ± 26.7
125	86.9 ± 9.3	135.2 ± 11.4	127.7 ± 35.6
160	124.2 ± 13.8	197.5 ± 16.8	181.8 ± 52.8

6.2.7 MTT assay

Nanoparticle solutions were lyophilised to powder form and dissolved in 0.5 mL sterile water to obtain a final metal concentration of 25 mM. The cyanosol solutions were then diluted using a complete medium to desired concentration (0.1 mM to 1 mM). Depending on the cell line used, the complete medium varied : RPMI + 10% FBS + 1% P/S for PC3 cells and DMEM + 10% FBS + 1% S/S + 1% L-glu for fibroblast cell line. MTT solution was prepared by dissolving 75 mg of tetrazolium reagent in 15 mL phosphate buffer (PBS). The solution is filtered and stored between 2-8°C. Lysis buffer is prepared by diluting acidified isopropanol solution with pure isopropanol. Menadione solution in DMSO is used as a negative control for MTT assays.

Three flasks of (PC3/ Fibroblast) cells were trypsinated and collected in a tube. They were centrifuged and resuspended in the medium. The cells were counted using LUNA and diluted to obtain a concentration of 8×10^5 cells/mL. 100 µL of cell solution was introduced in columns 2-12 of the 96-well plate, and left overnight. The cells were incubated with different concentrations of nanoparticle solutions (columns 3-11) in the medium for a total of 6 hrs, at 37°C. Menadione is added to the last column and incubated for 3.5 hrs. Once the incubation time lapsed, the medium from each well was removed and replaced with 100µL of MTT solution, except the control wells. The plate was once again incubated for 4 hrs at 37°C. Then 100 µL of lysis buffer was added to each well and the absorbance at 560 nm, was recorded at 1 hour time intervals.

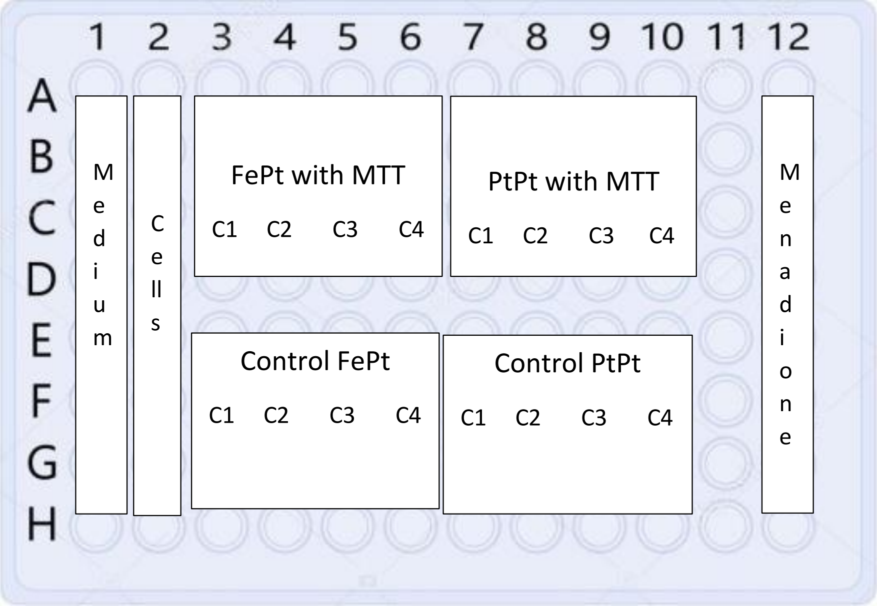

Figure 145. Optimized MTT assay formulation for FePt and PtPt cyanosol in 96-well plate

Table 13. Cell survival percentages calculated for 2 cell lines in the presence of cyanosols from optimized MTT assay

Sample	**Cell line**	**Concentration**	**Survival Fraction**
PtPt cyanosol	Fibroblast	0.10 mM 0.25 mM 0.50 mM 1.0 mM	99.3 % 115 % 96.4 % 97.5 %
PtPt cyanosol	PC3	0.10 mM 0.25 mM 1.0 mM	85.8 % 81.1 % 78.6 %
FePt cyanosol	PC3	0.10 mM 0.25 mM 0.50 mM 1.0 mM	77.8% 77.4 % 74.6 % 85.9 % *(high abs)

6.3 CHAPTER 3

6.3.1 Poly γ-Cyclodextrin citrate

Synthesis of polymer γ-Cyclodextrin citrate was done by Dr.Jingwen Qiu at ISMO, Université Paris Saclay, using a method described earlier.[243] The yield of the reaction was 30% and the synthesized polymer has a molecular weight of 13600 g/moL. It was 4 times larger than the molecular weight of the parent CD-PEG and was characterized using nuclear magnetic resonance (NMR) and FTIR spectroscopy.

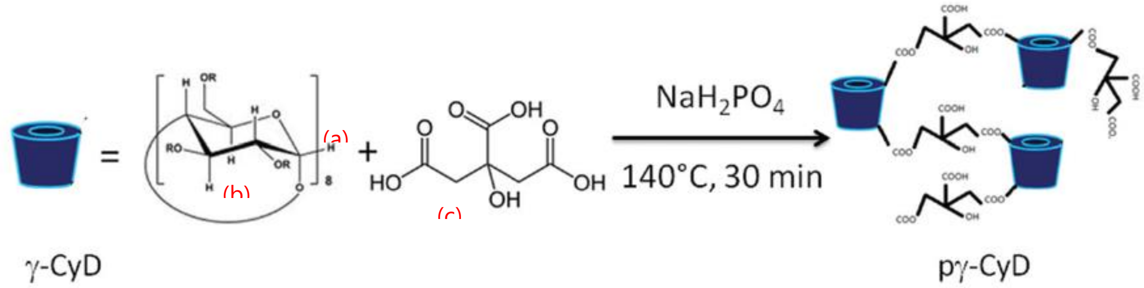

Figure 146. Scheme of synthesis of poly CD citrate

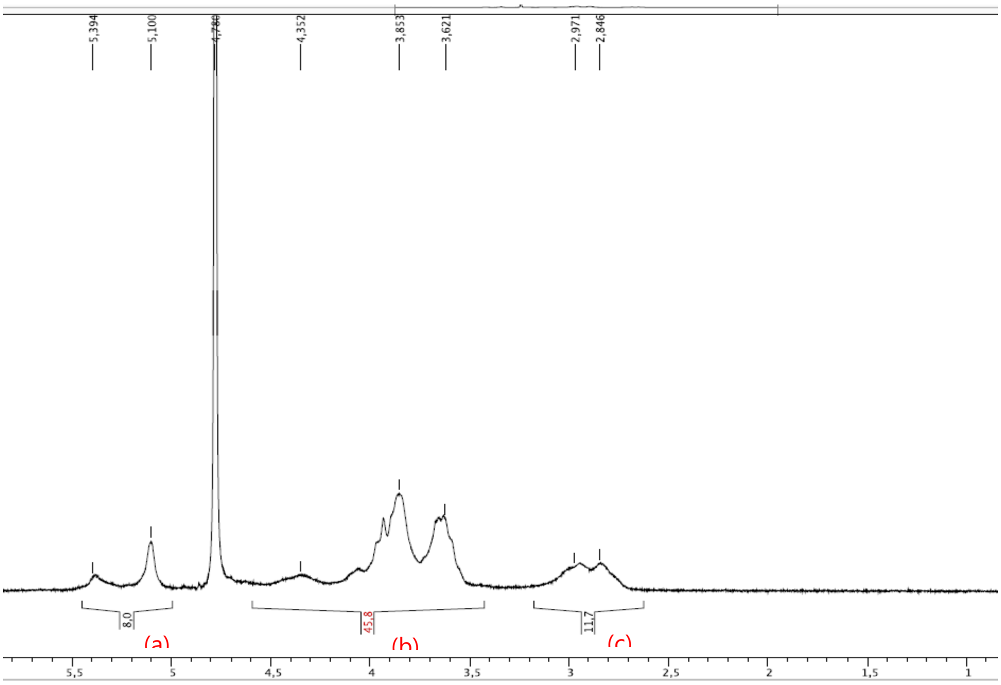

Figure 147. NMR spectra of polymer CD-citrate with protons from CD assigned (a, b) and citrate moieties marked (c)

The citric acid/CD molar ratio in the product was estimated by integrating the peaks assigned to 4 protons of the citric acid methylene group divided by 8 anomeric protons of CD units, showing citric acid/CD molar ratio= (11,7/4) : (8/8) =3,7:1. The final composition was considered $(CD)_2$-$(citrate)_8$. Infra-red spectra revealed that carbonyl groups of the carboxylic acids (1750 and 1700 cm^{-1}) were converted to ester functional group (1730 cm^{-1}) in the polymer. The presence of cyclodextrin in the polymers was verified by the COH vibration (2900 cm^{-1}) and CO of the ether groups (1000 cm^{-1}).

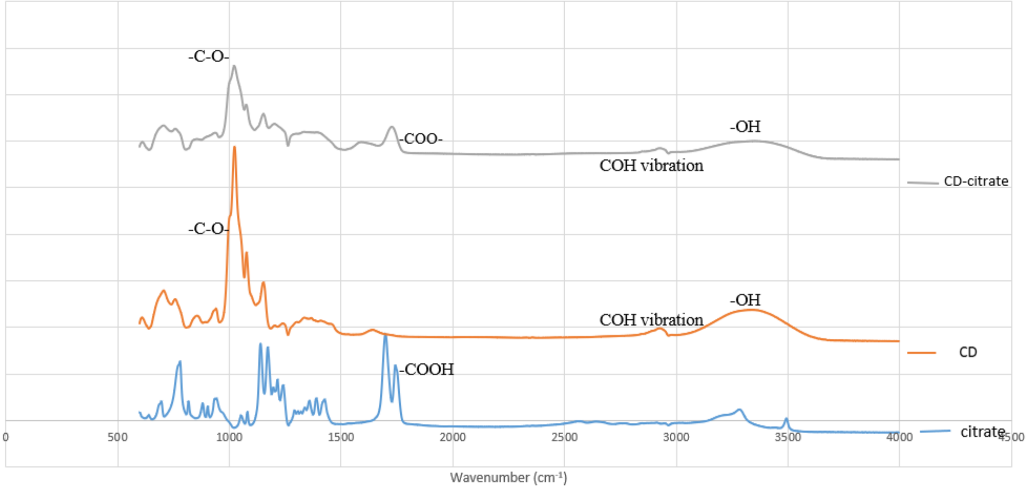

Figure 148. IR spectral comparison of precursors with poly CD-citrate

6.3.2 Prussian Blue with polymer Cyclodextrin-citrate

NTA analysis showed that PB + γ-CD citrate formed assemblies in the size range of 120.6 ±2.8 nm. But the reliability of this technique is questionable as the starting solution of single PB nanoparticles were also detected to have sizes around 100 nm, although the analysis videos acquired show stark difference. The results are summarized below:

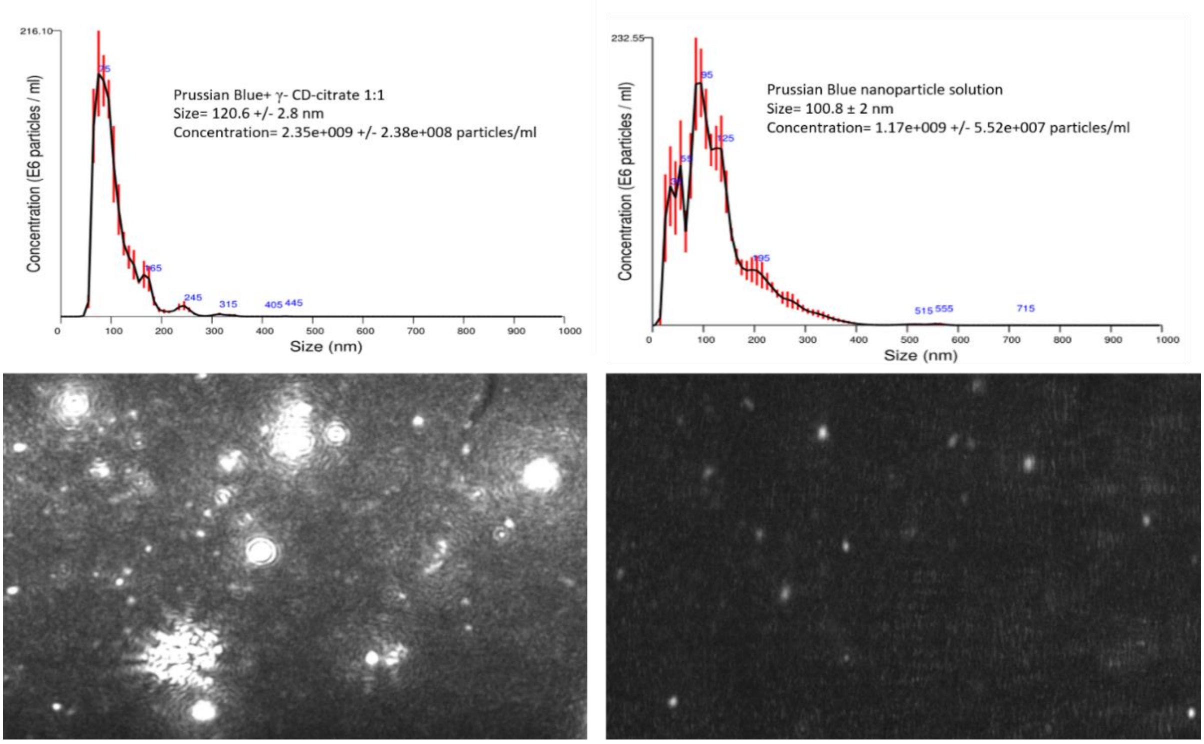

Figure 149. Results from NTA analysis on PB-CD citrate assemblies (left) and PB nanoparticle solutions (right)

NTA is not sensitive to particle sizes below 50 nm. Therefore the sizes detected here, are an over-estimation and not a true comparison between samples.

6.3.3 Prussian Blue 1.5 equivalent iron-gallate

It was determined through EDS, that only 1.5 out of the 2 equivalents of FeGA added was retained in the UF and washed PB-FeGA sample. Therefore, attempts to form PB assemblies using 1.5 equivalents (fast and drop-wise addition)of FeGA were made. Fe^{3+}(0.375 mM) solution and neutralized gallic acid (0.75 mM) solutions were added to PB (0.25 mM). Results are reported in Figure 9. DLS showed a small population around 20 nm, apart from the peak ~90 nm. TEM analysis revealed that smaller assemblies were formed as compared to PB-2FeGA. Moreover, a large proportion of single, individual PB nanoparticles could be observed.

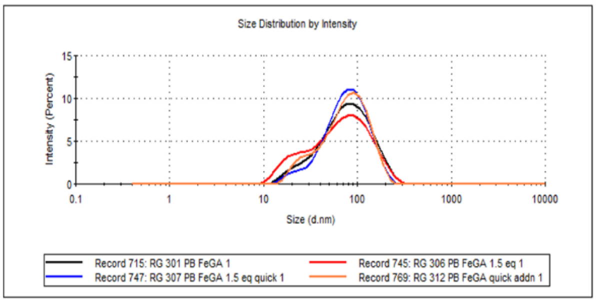

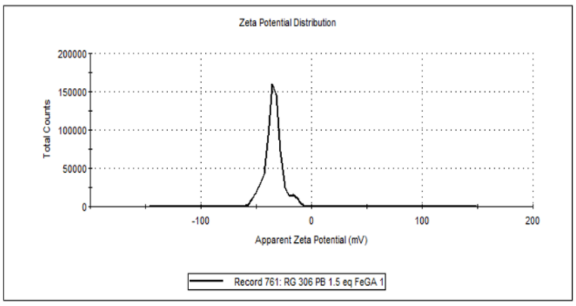

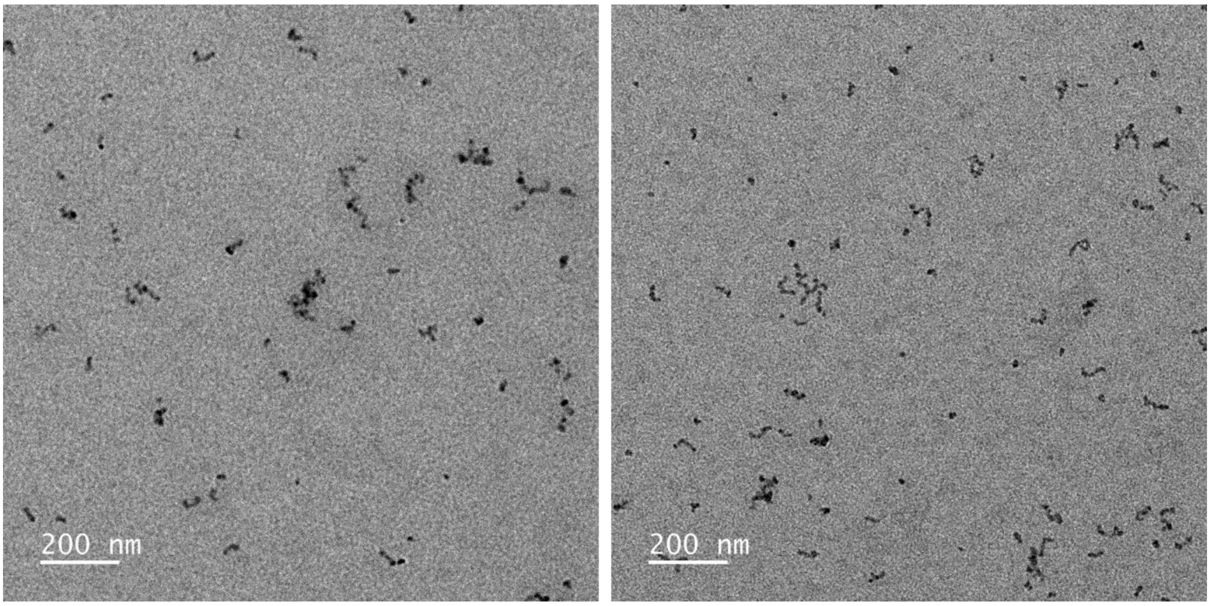

Figure 150. PB-FeGA synthesized using 1.5 equivalents of FeGA precursors : (a) DLS comparison (b) zeta potential and TEM images obtained with (c) slow drop-wise addition and (d) quick addition

6.3.4 PB-FeGA with chitosan

Addition of 30 equivalents of a positively charged chitosan polymer led to a shift in the hydrodynamic diameter of the assemblies to ~200 nm and zeta potential to + 16 mV. TEM images indicate slight aggregation.

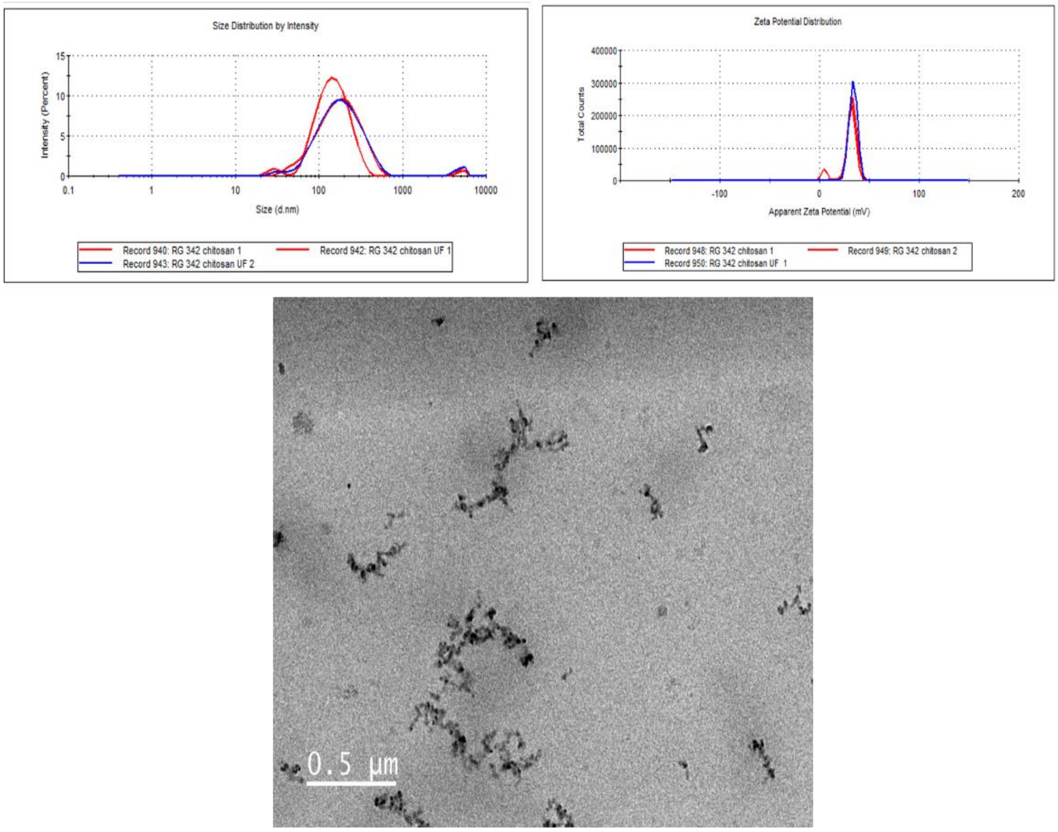

Figure 151. (a) Hydrodynamic diameter (b) zeta-potential and (c) TEM image of PB-FeGA assemblies coated with 30 equivalents of chitosan polymer.

6.3.5 Effect of phosphate on Prussian Blue

The principle of phosphate attack on Fe^{III} present on the surface of Prussian Blue nanoparticles has been described in chapter 3. Figure 11, presents the effect of phosphate buffer and foetal bovine serum (contains $PO_4{}^{3-}$) on bare, uncoated PB nanoparticles.

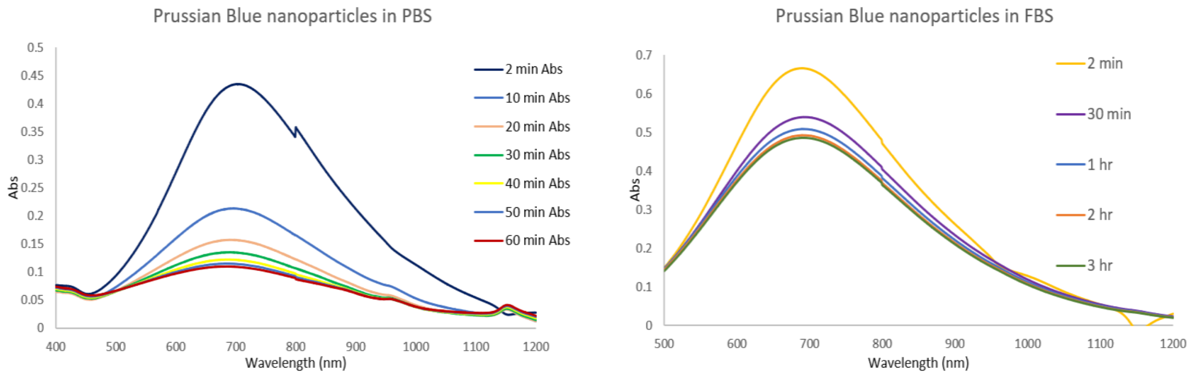

Figure 152. UV-Visible spectra evolution of PB in (a) Phosphate Buffer and (b) Fetal Bovine serum

The absorption at 800 nm is important for PTT. It is seen that within 10 minutes in PBS, PB undergoes a drastic change and loses 54% of its $Abs_{800\ nm}$. After 1 hour of exposure only 24%

of the absorbance is retained. The effect of foetal bovine serum is less intense as 80% of the PB absorbance is still maintained at 1 hr. Only a 3% loss occurs in the next 3 hours. Therefore, it can be hypothesized that the protein corona formed around the nanoparticles due to the serum has a protecting effect. FeGA complex and assembly formation further protects the PB nanoparticles from phosphate attack in the PBS.

6.4 CHAPTER 4

6.4.1 Doxorubicin loading and release

Table 14. Encapsulation efficiency and weight percentages of doxorubicin in poly CD citrate coated PB FeGA self-assembled nanochains.

Sample	**EE %**	**Payload %**	**Sample**	**EE %**	**Payload %**
1	84.21	32.08	**9**	87.22	33.23
2	85.86	32.71	**10**	85.91	32.72
3	85.28	32.49	**11**	87.37	33.28
4	85.57	32.59	**12**	87.27	33.25
5	83.96	31.98	**13**	87.19	33.21
6	85.15	32.44	**14**	84.19	32.07
7	83.32	31.74	**15**	85.62	32.61
8	86.55	32.97	**Average**	**85.64 ±1.04**	**32.62±0.39**

6.4.2 NO release from nanoparticle assembly

The Griess assay kit was used to determine the amount of NO released from sodium nitroprusside conjugated PB-FeGA assembly (PB-SNP FeGA) as described in chapter 4. The effect of raising solution temperature to 70°C and acidic pH environment was investigated and the plots are shown below. The absorption of azo-dye around 540 nm is used to determine the NO amount. The experiments need to be repeated to confirm the results.

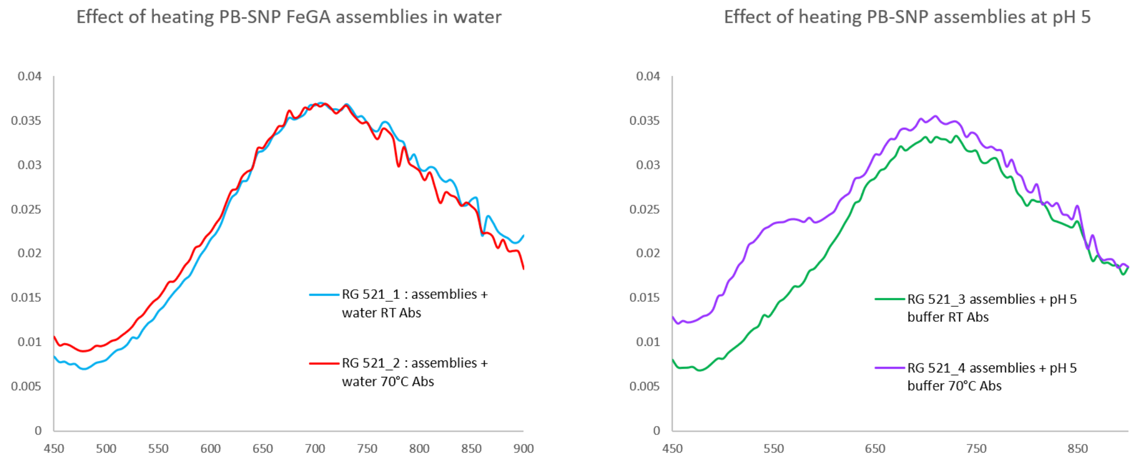

Figure 153.(a) UV-Vis spectral plot of heated PB-SNP FeGA assembly, after treatment with Griess reagents and (b) corresponding plots at pH 5 (acetate buffer)

Table 15. Amount of NO release detected from PB-SNP FeGA assemblies in different conditions

Sample	NO released (μM)
PB-SNP FeGA room temp.	0
PB-SNP FeGA 70°C, 1 hr	1.46
PB-SNP FeGA pH 5, 1 hr	0.76
PB-SNP FeGA pH 5, 70°C, 1 hr	8.83

6.4.3 Photoacoustic imaging

Preliminary photoacoustic imaging experiments were performed in Université de Paris. Comparative analysis of different samples show that increased absorption of the assemblies in the visible range could be translated into enhanced PA signal when compared to the single nanoparticles.

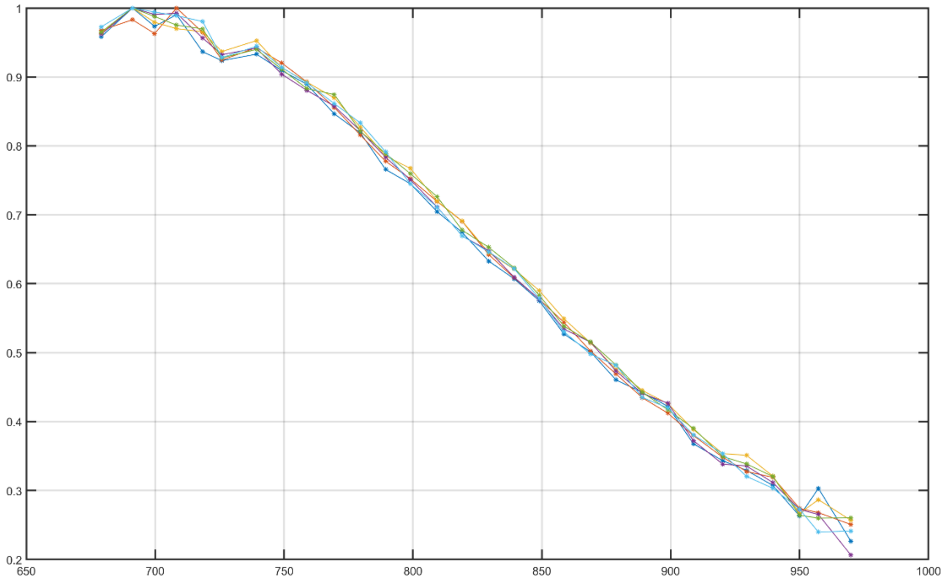

Figure 154. Normalized photoacoustic signal obtained using poly CD-citrate coated PB-FeGA (0.125 mM) assemblies

6.5 LIST OF PUBLICATIONS AND CONFERENCES

1) L. Fétiveau, G. Paul, A. Nicolas-Boluda, J. Volatron, R.George, S. Laurent, R. Muller, L. Sancey, P.Mejanelle, A. Gloter, F. Gazeau and L. Catala : Tailored ultra-small Prussian Blue based nanoparticles for MRI imaging and combined photothermal/photoacoustic theranostics, **Chem. Comm., 2019**,55, 14844-14847
2) R.George, L.Fetiveau, E.Porcel, F.Savina, C.Bosson, D.Dragoe, H.Remita, S.Lacombe and L.Catala : Ultrasmall Prussian blue-like nanoparticles as radioenhancers for therapy (draft to be submitted before December)
3) 7th International Conference on Multifunctional, Hybrid and Nanomaterials (October 2022, Genoa, Italy) -oral presentation
4) 44th International Conference on Coordination Chemistry (August 2022, Rimini, Italy)- oral communication and poster presentation
5) French Society of Nanomedicine conference (SF Nano 2021, Angers, France)- Young Scientists Session presentation
6) European Summer School for Nanoscience and Nanotechnology (ESONN, Grenoble, France)- Poster presentation
7) Association of Molecular Magnetism (AM2 2021, Dourdan)- oral presentation

7 REFERENCES

1. Vert M, Doi Y, Hellwich KH, et al. Terminology for biorelated polymers and applications (IUPAC recommendations 2012). *Pure and Applied Chemistry*. 2012;84(2):377-410. doi:10.1351/PAC-REC-10-12-04/MACHINEREADABLECITATION/RIS

2. Sun X, Zhang Y, Chen G, Gai Z. Application of Nanoparticles in Enhanced Oil Recovery: A Critical Review of Recent Progress. *Energies 2017, Vol 10, Page 345*. 2017;10(3):345. doi:10.3390/EN10030345

3. Khan I, Saeed K, Khan I. Nanoparticles: Properties, applications and toxicities. *Arabian Journal of Chemistry*. 2019;12(7):908-931. doi:10.1016/J.ARABJC.2017.05.011

4. Size-comparison-Bio-nanoparticles nanometer scale comparison nanoparticle size comparison nanotechnology chart ruler – Wich Research Lab. Accessed June 3, 2022. https://www.wichlab.com/nanometer-scale-comparison-nanoparticle-size-comparison-nanotechnology-chart-ruler-2/

5. Irving B, Victoria N. Nanoparticle Drug Delivery Systems.

6. Jain PK, ElSayed IH, El-Sayed MA. Au nanoparticles target cancer. *Nano Today*. 2007;2(1):18-29. doi:10.1016/S1748-0132(07)70016-6

7. AshaRani P v., Mun GLK, Hande MP, Valiyaveettil S. Cytotoxicity and genotoxicity of silver nanoparticles in human cells. *ACS Nano*. 2009;3(2):279-290.

8. Laurent S, Forge D, Port M, et al. Magnetic Iron Oxide Nanoparticles: Synthesis, Stabilization, Vectorization, Physicochemical Characterizations, and Biological Applications. *Chem Rev*. 2008;108(6):2064-2110. doi:10.1021/CR068445E

9. Han X, Xu K, Taratula O, Farsad K. Applications of Nanoparticles in Biomedical Imaging. *Nanoscale*. 2019;11(3):799. doi:10.1039/C8NR07769J

10. Alexis F, Pridgen E, Molnar LK, Farokhzad OC. Factors Affecting the Clearance and Biodistribution of Polymeric Nanoparticles. *Mol Pharm*. 2008;5(4):505-515. doi:10.1021/MP800051M

11. di Lonardo A, Nasi S, Pulciani S. Cancer: We should not forget the past. *J Cancer*. 2015;6(1):29-39. doi:10.7150/JCA.10336

12. Sung H, Ferlay J, Siegel RL, et al. Global Cancer Statistics 2020: GLOBOCAN Estimates of Incidence and Mortality Worldwide for 36 Cancers in 185 Countries. *CA Cancer J Clin*. 2021;71(3):209-249. doi:10.3322/CAAC.21660

13. Fukumura D, Jain RK. Tumor microenvironment abnormalities: Causes, consequences, and strategies to normalize. *J Cell Biochem*. 2007;101(4):937-949. doi:10.1002/JCB.21187

14. Justus CR, Dong L, Yang L v. Acidic tumor microenvironment and pH-sensing G protein-coupled receptors. *Front Physiol*. 2013;4 DEC:354. doi:10.3389/FPHYS.2013.00354/BIBTEX

15. Matsumura Y, Maeda H. A New Concept for Macromolecular Therapeutics in Cancer Chemotherapy: Mechanism of Tumoritropic Accumulation of Proteins and the Antitumor Agent Smancs. *Cancer Res*. 1986;46(12 Part 1).

16. Aryasomayajula B, Torchilin VP. Nanoformulations: A lucrative tool for protein delivery in cancer therapy. *Nanobiomaterials in Cancer Therapy: Applications of Nanobiomaterials*. 2016:307-330. doi:10.1016/B978-0-323-42863-7.00010-4

17. Siemann DW. The Unique Characteristics of Tumor Vasculature and Preclinical Evidence for its Selective Disruption by Tumor-Vascular Disrupting Agents. *Cancer Treat Rev*. 2011;37(1):63. doi:10.1016/J.CTRV.2010.05.001

18. Theek B, Gremse F, Kunjachan S, et al. Characterizing EPR-Mediated Passive Drug Targeting using Contrast-Enhanced Functional Ultrasound Imaging. *J Control Release*. 2014;182(1):83. doi:10.1016/J.JCONREL.2014.03.007

19. Salahpour Anarjan F. Active targeting drug delivery nanocarriers: Ligands. *Nano-Structures & Nano-Objects*. 2019;19:100370. doi:10.1016/J.NANOSO.2019.100370

20. Patil Y, Amitay Y, Ohana P, Shmeeda H, Gabizon A. Targeting of pegylated liposomal mitomycin-C prodrug to the folate receptor of cancer cells: Intracellular activation and enhanced cytotoxicity. *Journal of Controlled Release*. 2016;225:87-95. doi:10.1016/J.JCONREL.2016.01.039

21. Paranjpe P v., Chen Y, Kholodovych V, Welsh W, Stein S, Sinko PJ. Tumor-targeted bioconjugate based delivery of camptothecin: design, synthesis and in vitro evaluation. *Journal of Controlled Release*. 2004;100(2):275-292. doi:10.1016/J.JCONREL.2004.08.030

22. Bidram E, Esmaeili Y, Ranji-Burachaloo H, et al. A concise review on cancer treatment methods and delivery systems. *J Drug Deliv Sci Technol*. 2019;54:101350. doi:10.1016/J.JDDST.2019.101350

23. Li X, Lovell JF, Yoon J, Chen X. Clinical development and potential of photothermal and photodynamic therapies for cancer. doi:10.1038/s41571-020-0410-2

24. Bienia A, Wiecheć-Cudak O, Murzyn AA, Krzykawska-Serda M. Photodynamic Therapy and Hyperthermia in Combination Treatment—Neglected Forces in the Fight against Cancer. *Pharmaceutics*. 2021;13(8). doi:10.3390/PHARMACEUTICS13081147

25. Dejene Tolossa Debela, Seke GY, Kidist Digamo H, et.al. New approaches and procedures for cancer treatment: Current perspectives. doi:10.1177/20503121211034366

26. Chemotherapy Side Effects | American Cancer Society. https://www.cancer.org/treatment/treatments-and-side-effects/treatment-types/chemotherapy/chemotherapy-side-effects.html

27. Senapati S, Mahanta AK, Kumar S, Maiti P. Controlled drug delivery vehicles for cancer treatment and their performance. *Signal Transduction and Targeted Therapy 2018 3:1*. 2018;3(1):1-19. doi:10.1038/S41392-017-0004-3

28. Rives V, del Arco M, Martín C. Intercalation of drugs in layered double hydroxides and their controlled release: A review. *Appl Clay Sci*. 2014;88-89:239-269. doi:10.1016/J.CLAY.2013.12.002

29. Bianco A, Kostarelos K, Prato M. Applications of carbon nanotubes in drug delivery. *Curr Opin Chem Biol*. 2005;9(6):674-679. doi:10.1016/J.CBPA.2005.10.005

30. Kumar S, Jain S, Nehra M, Dilbaghi N, Marrazza G, Kim KH. Green synthesis of metal–organic frameworks: A state-of-the-art review of potential environmental and medical applications. *Coord Chem Rev*. 2020;420:213407. doi:10.1016/J.CCR.2020.213407

31. Kim TY, Kim DW, Chung JY, et al. Phase I and Pharmacokinetic Study of Genexol-PM, a Cremophor-Free, Polymeric Micelle-Formulated Paclitaxel, in Patients with Advanced Malignancies. *Clinical Cancer Research*. 2004;10(11):3708-3716. doi:10.1158/1078-0432.CCR-03-0655

32. Jin X, Zhang P, Luo L, et al. Efficient intravesical therapy of bladder cancer with cationic doxorubicin nanoassemblies. *Int J Nanomedicine*. 2016;11:4535-4544. doi:10.2147/IJN.S103994

33. Abraxane approved for metastatic pancreatic cancer. *Cancer Discov*. 2013;3(11). doi:10.1158/2159-8290.cd-nb2013-137/334721/p/abraxane-approved-for-metastatic-pancreatic

34. Xue B, Kozlovskaya V, Liu F, et al. Intracellular Degradable Hydrogel Cubes and Spheres for Anti-Cancer Drug Delivery. doi:10.1021/acsami.5b03360

35. Jaffray DA, Gospodarowicz MK. Radiation Therapy for Cancer. *Taehan Uihak Hyophoe Chi*. 2015;6:142-146. doi:10.1596/978-1-4648-0349-9_CH14

36. Holley AK, Miao L, st. Clair DK, st. Clair WH. Redox-Modulated Phenomena and Radiation Therapy: The Central Role of Superoxide Dismutases. *Antioxid Redox Signal*. 2013;20(10):1567-1589. doi:10.1089/ars.2012.5000

37. Dracham CB, Shankar A, Madan R. Radiation induced secondary malignancies: a review article. *Radiat Oncol J*. 2018;36(2):85. doi:10.3857/ROJ.2018.00290

38. Adams GE. Chemical radiosensitization of hypoxic cells. *Br Med Bull*. 1973;29(1):48-53. doi:10.1093/oxfordjournals.bmb.A070956/2/29-1-48.

39. Fowler JF, Adams GE, Denekamp J. Radiosensitizers of hypoxic cells in solid tumours. *Cancer Treat Rev*. 1976;3(4):227-256. doi:10.1016/S0305-7372(76)80012-6

40. Matsudaira H, Ueno AM, Furuno I. Iodine Contrast Medium Sensitizes Cultured Mammalian Cells to X Rays but Not to γ Rays. *Source: Radiation Research*. 1980;84(1):144-148.

41. Boeckman HJ, Trego KS, Turchi JJ. Cisplatin sensitizes cancer cells to ionizing radiation via inhibition of nonhomologous end joining. *Mol Cancer Res*. 2005;3(5):277-285. doi:10.1158/1541-7786.MCR-04-0032

42. Carter R, Westhorpe A, Romero MJ, et al. Radiosensitisation of human colorectal cancer cells by ruthenium(II) arene anticancer complexes. *Sci Rep*. 2016;6. doi:10.1038/SREP20596

43. Teicher BA, Jacobs JL, Cathcart KNS, Abrams MJ, Vollano JF, Picker DH. Some complexes of cobalt(III) and iron(III) are radiosensitizers of hypoxic EMT6 cells. *Radiat Res*. 1987;109(1):36-46. doi:10.2307/3576865

44. Chibber R, Stratford IJ, Ahmed I, Robbins AB, Goodgame D, Lee B. Radiosensitization of mammalian cells by transition metal complexes containing nitroimidazole ligands. *Int J Radiat Oncol Biol Phys*. 1984;10(8):1213-1215. doi:10.1016/0360-3016(84)90320-1

45. Young SW, Qing F, Harriman A, et al. Gadolinium(III) texaphyrin: a tumor selective radiation sensitizer that is detectable by MRI. *Proc Natl. Acad. Sci U S A*. 1996;93(13):6610-6615. doi:10.1073/PNAS.93.13.6610

46. Kobayashi K, Usami N, Porcel E, Lacombe S, le Sech C. Enhancement of radiation effect by heavy elements. *Mutation Research/Reviews in Mutation Research*. 2010;704(1-3):123-131. doi:10.1016/J.MRREV.2010.01.002

47. Gill MR, Vallis KA. Transition metal compounds as cancer radiosensitizers. *Chem Soc Rev*. 2019;48(2):540-557. doi:10.1039/C8CS00641E

48. Hainfeld JF, Slatkin DN, Smilowitz HM. The use of gold nanoparticles to enhance radiotherapy in mice. *PHYSICS IN MEDICINE AND BIOLOGY Phys Med Biol*. 2004;49:309-315. doi:10.1088/0031-9155/49/18/N03

49. Kwatra D, Venugopal A, Anant S. Nanoparticles in radiation therapy: A summary of various approaches to enhance radiosensitization in cancer. *Transl Cancer Res*. 2013;2(4):330-342. doi:10.3978/j.issn.2218-676X.2013.08.06

50. Libutti SK, Paciotti GF, Byrnes AA, et al. Cancer Therapy: Clinical Phase I and Pharmacokinetic Studies of CYT-6091, a Novel PEGylated Colloidal Gold-rhTNF Nanomedicine. doi:10.1158/1078-0432.CCR-10-0978

51. Verry C, Dufort S, Villa J, et al. Theranostic AGuIX nanoparticles as radiosensitizer: A phase I, dose-escalation study in patients with multiple brain metastases (NANO-RAD trial).*Radiotherapy and Oncology*. 2021;160:159-165. doi:10.1016/J.RADONC.2021.04.021

52. Bonvalot S, Rutkowski PL, Thariat J, et al. NBTXR3, a first-in-class radioenhancer hafnium oxide nanoparticle, plus radiotherapy versus radiotherapy alone in patients with locally advanced soft-tissue sarcoma (Act.In.Sarc): a multicentre, phase 2–3, randomised, controlled trial. *Lancet Oncol*. 2019;20(8):1148-1159. doi:10.1016/S1470-2045(19)30326-2

53. Crapanzano R, Secchi V, Villa I. Co-Adjuvant Nanoparticles for Radiotherapy Treatments of Oncological Diseases. *Applied Sciences 2021, Vol 11, Page 7073*. 2021;11(15):7073. doi:10.3390/APP11157073

54. Li Y, Yun KH, Lee H, Goh SH, Suh YG, Choi Y. Porous platinum nanoparticles as a high-Z and oxygen generating nanozyme for enhanced radiotherapy in vivo. *Biomaterials*. 2019;197:12-19. doi:10.1016/J.BIOMATERIALS.2019.01.004

55. Mignot A, Truillet C, Lux F, et al. A top-down synthesis route to ultrasmall multifunctional Gd-based Silica nanoparticles for theranostic applications. *Chemistry - A European Journal*. 2013;19(19):6122-6136. doi:10.1002/CHEM.201203003

56. Gharibshahi E, Saion E, Ashraf A, Gharibshahi L. Size-Controlled and Optical Properties of Platinum Nanoparticles by Gamma Radiolytic Synthesis. *Applied Radiation and Isotopes*. 2017;130:211-217. doi:10.1016/J.APRADISO.2017.09.012

57. Bao Z, He M, Quan H, et al. FePt nanoparticles: a novel nanoprobe for enhanced HeLa cells sensitivity to chemoradiotherapy.2016. doi:10.1039/c6ra03990a

58. Pérez-Hernández M, del Pino P, Mitchell SG, et al. Dissecting the molecular mechanism of apoptosis during photothermal therapy using gold nanoprisms. *ACS Nano*. 2015;9(1):52-61. doi:10.1021/NN505468V

59. Bastiancich C, da Silva A, Esteve MA, Esteve Photothermal MA, da Silva A, Estève MA. Photothermal Therapy for the Treatment of Glioblastoma: Potential and Preclinical Challenges. doi:10.3389/fonc.2020.610356ï

60. Weissleder R. A clearer vision for in vivo imaging. *Nature Biotechnology 2001 19:4*. 2001;19(4):316-317. doi:10.1038/86684

61. Smith AM, Mancini MC, Nie S. Bioimaging: second window for in vivo imaging. *Nat Nanotechnol*. 2009;4(11):710-711. doi:10.1038/NNANO.2009.326

62. Jaque D, Martínez Maestro L, del Rosal B, et al. Nanoparticles for photothermal therapies. *Nanoscale*. 2014;6(16):9494-9530. doi:10.1039/C4NR00708E

63. Liu Y, Bhattarai P, Dai Z, Chen X. Photothermal therapy and photoacoustic imaging via nanotheranostics in fighting cancer †. *Chem Soc Rev*. 2019;48:2053. doi:10.1039/c8cs00618k

64. Chen F, Cai W. Nanomedicine for targeted photothermal cancer therapy: where are we now? 2015;10(1):1-3. doi:10.2217/NNM.14.186

65. Han HS, Choi KY. Advances in Nanomaterial-Mediated Photothermal Cancer Therapies: Toward Clinical Applications. *Biomedicines 2021, Vol 9, Page 305*. 2021;9(3):305. doi:10.3390/BIOMEDICINES9030305

66. Deng X, Shao Z, Zhao Y. Solutions to the Drawbacks of Photothermal and Photodynamic Cancer Therapy. *Advanced Science*. 2021;8(3):2002504. doi:10.1002/ADVS.202002504

67. Deng X, Shao Z, Zhao Y. Solutions to the Drawbacks of Photothermal and Photodynamic Cancer Therapy. *Advanced Science*. 2021;8(3):2002504. doi:10.1002/ADVS.202002504

68. Shi J, Wang L, Zhang J, et al. A tumor-targeting near-infrared laser-triggered drug delivery system based on GO@Ag nanoparticles for chemo-photothermal therapy and X-ray imaging. *Biomaterials*.2014;35(22):5847-5861. doi:10.1016/J.BIOMATERIALS.2014.03.042

69. Fass L. Imaging and cancer: A review. *Mol Oncol*. 2008;2(2):115. doi:10.1016/J.MOLONC.2008.04.001

70. Mejia-Ariza R, Graña-Suárez L, Verboom W, Huskens J. Cyclodextrin-based supramolecular nanoparticles for biomedical applications. *J Mater Chem B*. 2017;5(1):36-52. doi:10.1039/c6tb02776h

71. Griffeth LK. Use of PET/CT scanning in cancer patients: technical and practical considerations. *Proc (Bayl. Univ. Med Cent)*. 2005;18(4):321. doi:10.1080/08998280.2005.11928089

72. Al-Sharify ZT, Al-Sharify TA, Al-Sharify NT, Naser HY. A critical review on medical imaging techniques (CT and PET scans) in the medical field. *IOP Conf Ser Mater Sci Eng*. 2020;870(1). doi:10.1088/1757-899X/870/1/012043

73. Idrees Muhammad. An overview on MRI physics and its clinical applications. *International Journal of Current Pharmaceutical & Clinical Research* . 2014;4(4):185-193.

74. Grover VPB, Tognarelli JM, Crossey MME, Cox IJ, Taylor-Robinson SD, McPhail MJW. Magnetic Resonance Imaging: Principles and Techniques: Lessons for Clinicians. *J Clin Exp Hepatol*. 2015;5(3):246. doi:10.1016/J.JCEH.2015.08.001

75. Haouimi A, Drew Z. T1 values (1.5 T). *Radiopaedia.org*. 2018. doi:10.53347/RID-60740

76. Young IR, Clarke GJ, Baffles DR, Pennock JM, Doyle FH, Bydder GM. Enhancement of relaxation rate with paramagnetic contrast agents in NMR imaging. *Journal of Computed Tomography*. 1981;5(6):543-547. doi:10.1016/0149-936X(81)90089-8

77. Carr DH, Brown J, Bydder GM, et al. Intravenous chelated gadolinium as a contrast agent in NMR imaging of cerebral tumours. *The Lancet*. 1984;323(8375):484-486. doi:10.1016/S0140-6736(84)92852-6

78. EMA's final opinion confirms restrictions on use of linear gadolinium agents in body scans | European Medicines Agency. https://www.ema.europa.eu/en/news/emas-final-opinion-confirms-restrictions-use-linear-gadolinium-agents-body-scans

79. Strijkers GJ, M. Mulder WJ, F. van Tilborg GA, Nicolay K. MRI Contrast Agents: Current Status and Future Perspectives. *Anticancer Agents Med Chem*. 2008;7(3):291-305. doi:10.2174/187152007780618135

80. Bousquet JC, Saini S, Stark DD, et al. Gd-DOTA: characterization of a new paramagnetic complex;166(3):693-698. doi:10.1148/RADIOLOGY.166.3.3340763

81. Parizel PM, Degryse HR, Gheuens J, et al. Gadolinium-DOTA enhanced MR imaging of intracranial lesions. *J Comput Assist Tomogr*. 1989;13(3):378-385. doi:10.1097/00004728-198905000-00002

82. Idée JM, Port M, Raynal I, Schaefer M, le Greneur S, Corot C. Clinical and biological consequences of transmetallation induced by contrast agents for magnetic resonance imaging: a review. *Fundam Clin Pharmacol*. 2006;20(6):563-576. doi:10.1111/J.1472-8206.2006.00447.X

83. Kurtkoti J, Snow T, Hiremagalur B. Gadolinium and nephrogenic systemic fibrosis: Association or causation. *Nephrology*. 2008;13(3):235-241. doi:10.1111/J.1440-1797.2007.00912.X

84. Perry HL, Botnar RM, Wilton-Ely JDET. Gold nanomaterials functionalised with gadolinium chelates and their application in multimodal imaging and therapy. *Chemical Communications*. 2020;56(29):4037-4046. doi:10.1039/D0CC00196A

85. Mi P, Kokuryo D, Cabral H, et al. A pH-activatable nanoparticle with signal-amplification capabilities for non-invasive imaging of tumour malignancy. doi:10.1038/NNANO.2016.72

86. Thorek DLJ, Chen AK, Czupryna J, Tsourkas A. Superparamagnetic Iron Oxide Nanoparticle Probes for Molecular Imaging. *Annals of Biomedical Engineering* 2006;34(1):23-38. doi:10.1007/S10439-005-9002-7

87. Na H bin, Lee JH, An K, et al. Development of a T1 Contrast Agent for Magnetic Resonance Imaging Using MnO Nanoparticles. *Angewandte Chemie International Edition*. 2007;46(28):5397-5401. doi:10.1002/ANIE.200604775

88. Choi HS, Frangioni J v. Nanoparticles for Biomedical Imaging: Fundamentals of Clinical Translation. *Mol Imaging*. 2010;9(6):291. doi:10.2310/7290.2010.00031

89. Cheng L, Jiang D, Kamkaew A, et al. Renal-Clearable PEGylated Porphyrin Nanoparticles for Image-Guided Photodynamic Cancer Therapy. *Adv Funct Mater*. 2017;27(34). doi:10.1002/adfm.201702928

90. Adhipandito CF, Cheung SH, Lin YH, Wu SH. Atypical Renal Clearance of Nanoparticles Larger Than the Kidney Filtration Threshold. *International Journal of Molecular Sciences 2021, Vol 22, Page 11182*. 2021;22(20):11182. doi:10.3390/IJMS222011182

91. McLeod SM, Robison L, Parigi G, et al. Maximizing Magnetic Resonance Contrast in Gd(III) Nanoconjugates: Investigation of Proton Relaxation in Zirconium Metal-Organic Frameworks. *ACS Appl Mater Interfaces*. 2020;12(37):41157-41166. doi:10.1021/ACSAMI.0C13571

92. Luo D, Johnson A, Wang X, et al. Targeted Radiosensitizers for MR-Guided Radiation Therapy of Prostate Cancer. *Nano Lett*. 2020;20(10):7159-7167. doi:10.1021/ACS.NANOLETT.0C02487

93. Gao A, Kang YF, Yin XB. Red fluorescence-magnetic resonance dual modality imaging applications of gadolinium containing carbon quantum dots with excitation independent emission. *New Journal of Chemistry*. 2017;41(9):3422-3431. doi:10.1039/C7NJ00597K

94. Li X, Sun Y, Ma L, Liu G, Wang Z. The Renal Clearable Magnetic Resonance Imaging Contrast Agents: State of the Art and Recent Advances. *Molecules*. 2020;25(21). doi:10.3390/MOLECULES25215072

95. Sancey L, Lux F, Kotb S, et al. The use of theranostic gadolinium-based nanoprobes to improve radiotherapy efficacy. *British Journal of Radiology*. 2014;87(1041). doi:10.1259/BJR.20140134

96. Fries AP, Morr D, Müller A, et al. Evaluation of a Gadolinium-Based Nanoparticle (AGuIX) for Contrast-Enhanced MRI of the Liver in a Rat Model of Hepatic Colorectal Cancer Metastases at 9.4 Tesla. 2015;187:1108-1115. doi:10.1055/s-0035-1553500

97. Sancey L, Kotb S, Truillet C, et al. Long-term in Vivo clearance of gadolinium-based AGuIX nanoparticles and their biocompatibility after systemic injection. *ACS Nano*. 2015;9(3):2477-2488. doi:10.1021/ACSNANO.5B00552

98. Verry C, Sancey L, Dufort S, et al. Treatment of multiple brain metastases using gadolinium nanoparticles and radiotherapy: NANO-RAD, a phase I study protocol. *BMJ Open*. 2019;9(2). doi:10.1136/BMJOPEN-2018-023591

99. Lux F, Long Tran V, Thomas E, et al. AGuIX® from bench to bedside-Transfer of an ultrasmall theranostic gadolinium-based nanoparticle to clinical medicine. *British Journal of Radiology*. 2019;92:20180365. doi:10.1259/bjr.20180365ï

100. Stereotactic Brain-directed Radiation With or Without Aguix Gadolinium-Based Nanoparticles in Brain Metastases - Full Text View - ClinicalTrials.gov. https://clinicaltrials.gov/ct2/show/NCT04899908

101. Liu F, He X, Chen H, Zhang J, Zhang H, Wang Z. Gram-scale synthesis of coordination polymer nanodots with renal clearance properties for cancer theranostic applications. *Nature Communications 2015 6:1*. 2015;6(1):1-9. doi:10.1038/NCOMMS9003

102. Chen L, Chen J, Qiu S, et al. Biodegradable Nanoagents with Short Biological Half-Life for SPECT/PAI/MRI Multimodality Imaging and PTT Therapy of Tumors. *Small*. 2018;14(4):1702700. doi:10.1002/SMLL.201702700

103. Ma D, Shi M, Li X, et al. Redox-Sensitive Clustered Ultrasmall Iron Oxide Nanoparticles for Switchable T2/T1-Weighted Magnetic Resonance Imaging Applications. *Bioconjug Chem*.2020;31(2):352-359.

104. Manwar R, Zafar M, Xu Q. Signal and Image Processing in Biomedical Photoacoustic Imaging: A Review. *Optics 2021, Vol 2, Pages 1-24*. 2020;2(1):1-24. doi:10.3390/OPT2010001

105. Yao J, Wang L v. Sensitivity of photoacoustic microscopy. *Photoacoustics*. 2014;2(2):87-101. doi:10.1016/J.PACS.2014.04.002

106. Wang X, Xu X. Thermoelastic wave induced by pulsed laser heating. *American Society of Mechanical Engineers, Heat Transfer Division HTD*. 2000;366:201-210. doi:10.1007/978-94-007-2739-7_19

107. Luke GP, Yeager D, Emelianov SY. Biomedical Applications of Photoacoustic Imaging with Exogenous Contrast Agents. *Annals of Biomedical Engineering* 2011;40(2):422-437. doi:10.1007/S10439-011-0449-4

108. Jeon M, Song W, Huynh E, et al. Methylene blue microbubbles as a model dual-modality contrast agent for ultrasound and activatable photoacoustic imaging 2014. doi:10.1117/1.JBO.19.1.016005

109. Thawani JP, Amirshaghaghi A, Yan L, Stein JM, Liu J, Tsourkas A. Photoacoustic-Guided Surgery with Indocyanine Green-Coated Superparamagnetic Iron Oxide Nanoparticle Clusters HHS Public Access. *Small*. 2017;13(37). doi:10.1002/smll.201701300

110. Lemaster JE, Jokerst J v. What is new in nanoparticle-based photoacoustic imaging? doi:10.1002/wnan.1404

111. Yang X, Skrabalak SE, Li ZY, Xia Y, Wang L v. Photoacoustic tomography of a rat cerebral cortex in vivo with Au nanocages as an optical contrast agent. *Nano Lett*. 2007;7(12):3798-3802. doi:10.1021/NL072349R

112. Wang Y, Xie X, Wang X, et al. Photoacoustic tomography of a nanoshell contrast agent in the in vivo rat brain. *Nano Lett*. 2004;4(9):1689-1692. doi:10.1021/NL049126A

113. Pramanik M, Swierczewska M, Green D, Sitharaman B, Wang L v. Single-walled carbon nanotubes as a multimodal-thermoacoustic and photoacoustic-contrast agent. doi:10.1117/1.3147407

114. de La Zerda A, Zavaleta C, Keren S, et al. Carbon nanotubes as photoacoustic molecular imaging agents in living mice. *Nature Nanotechnology 2008 3:9*. 2008;3(9):557-562. doi:10.1038/NNANO.2008.231

115. Phan TTV, Bui NQ, Cho SW, et al. Photoacoustic Imaging-Guided Photothermal Therapy with Tumor-Targeting HA-FeOOH@PPy Nanorods. *Scientific Reports 2018 8:1*. 2018;8(1):1-13. doi:10.1038/S41598-018-27204-8

116. Kraft A. On the discovery and history of Prussian Blue. *Bull Hist Chem*. 2008;33(2).

117. J. F. Keggin and F. D. Miles. *Structures and Formulae of the Prussian Blues and Related Compounds*. Vol 18.; 1936.Nature, 137:577–578, 1936. doi: 10.1038/137577a0

118. Cheyne RM, W Jones CH, Wilson RM, et al. *International Tables for X-Ray Crystallography*. Vol 16. Kynoch Press; 1977.

119. Avila Y, Acevedo-Peña P, Reguera L, Reguera E. Recent progress in transition metal hexacyanometallates: From structure to properties and functionality. *Coord Chem Rev*. 2022;453:214274. doi:10.1016/J.CCR.2021.214274

120. Buser HJ, Ludi A, Schwarzenbach D, Petter W. The Crystal Structure of Prussian Blue: Fe4[Fe(CN)6]3·xH2O. *Inorg Chem*.1977. doi:10.1021/ic50177a008

121. WHO Model List of Essential Medicines 17th List.

122. Valverde NJ, Oliveira AR. *The early medical response to the Goiania accident*.

123. Qin Z, Li Y, Gu N. Progress in Applications of Prussian Blue Nanoparticles in Biomedicine. *Adv Healthc. Mater*. 2018;7(20). doi:10.1002/adhm.201800347

125. Busquets MA, Estelrich J. Prussian blue nanoparticles: synthesis, surface modification, and biomedical applications. *Drug Discov Today*. 2020;25(8):1431-1443. doi:10.1016/j.drudis.2020.05.014

127. Shokouhimehr M, Soehnlen ES, Hao J, et al. Dual purpose Prussian blue nanoparticles for cellular imaging and drug delivery: a new generation of T1-weighted MRI contrast and small molecule delivery agents. *J Mater Chem*. 2010;20(25):5251-5259. doi:10.1039/B923184F

128. Hu M, Furukawa S, Ohtani R, et al. Synthesis of Prussian Blue Nanoparticles with a Hollow Interior by Controlled Chemical Etching. *Angewandte Chemie International Edition*. 2012;51(4):984-988. doi:10.1002/ANIE.201105190

129. Kjeldgaard S, Dugulan I, Mamakhel A, Wagemaker M, Iversen BB, Bentien A. Strategies for synthesis of Prussian blue analogues. *R Soc Open Sci*. 2021;8(1). doi:10.1098/RSOS.201779

130. Sébastien Vaucher Dr., Mei Li, Stephen Mann; Synthesis of Prussian blue nanoparticles and nanocrystal superlattices in reverse microemulsions. *Angew. Chem. Int. Ed.* 2000, 39,10

131. Roy X, Hui JKH, Rabnawaz M, Liu G, MacLachlan MJ. Soluble Prussian blue nanoworms from the assembly of metal-organic block ionomers. *Angewandte Chemie - International Edition*. 2011;50(7):1597-1602. doi:10.1002/anie.201005537

132. Shen Q, Jiang J, Fan M, et al. Prussian blue hollow nanostructures: Sacrificial template synthesis and application in hydrogen peroxide sensing. *Journal of Electroanalytical Chemistry*. 2014;712:132-138. doi:10.1016/J.JELECHEM.2013.11.008

133. Wu Y, Yang H, Shin HJ. Encapsulation and crystallization of Prussian blue nanoparticles by cowpea chlorotic mottle virus capsids. *Biotechnol Lett*. 2014;36(3):515-521. doi:10.1007/S10529-013-1399-8

134. Fornasieri G, Aouadi M, Delahaye E, et al. Elaboration of Prussian Blue Analogue/Silica Nanocomposites: Towards Tailor-Made Nano-Scale Electronic Devices. *Materials 2012, Vol 5, Pages 385-403*. 2012;5(3):385-403. doi:10.3390/MA5030385

135. Catala L, Mallah T. Nanoparticles of Prussian blue analogs and related coordination polymers: From information storage to biomedical applications. *Coord Chem Rev*. 2017;346:32-61. doi:10.1016/j.ccr.2017.04.005

136. Wang X, Cheng L. Multifunctional Prussian blue-based nanomaterials: Preparation, modification, and theranostic applications. *Coord Chem Rev*. 2020;419. doi:10.1016/j.ccr.2020.213393

137. Lavaud C, Marilyn Kajdan ab, Compte E, et al. In situ synthesis of Prussian blue nanoparticles within a biocompatible reverse micellar system for in vivo Cs + uptake †. *New J Chem*. 2017;41:2887-2890. doi:10.1039/c6nj03770d

138. Fu G, Liu W, Feng S, Yue X. Prussian blue nanoparticles operate as a new generation of photothermal ablation agents for cancer therapy. *Chemical Communications*. 2012;48(94):11567-11569. doi:10.1039/C2CC36456E

139. Hoffman HA, Chakrabarti L, Dumont MF, Sandler Abcd AD, Fernandes R. Prussian blue nanoparticles for laser-induced photothermal therapy of tumors. doi:10.1039/c4ra05209a

140. de Melo-Diogo D, Pais-Silva C, Dias DR, Moreira AF, Correia IJ. Strategies to Improve Cancer Photothermal Therapy Mediated by Nanomaterials. *Adv Healthc Mater*. 2017;6(10). doi:10.1002/ADHM.201700073

141. Cai X, Gao W, Zhang L, et al. Enabling Prussian Blue with Tunable Localized Surface Plasmon Resonances: Simultaneously Enhanced Dual-Mode Imaging and Tumor Photothermal Therapy. 2016. doi:10.1021/acsnano.6b05990

142. Yang ZL, Tian W, Wang Q, et al. Oxygen-Evolving Mesoporous Organosilica Coated Prussian Blue Nanoplatform for Highly Efficient Photodynamic Therapy of Tumors. *Advanced Science*. 2018;5(5):1700847. doi:10.1002/ADVS.201700847

143. Hu JJ, Chen Y, Li ZH, Peng SY, Sun Y, Zhang XZ. Augment of Oxidative Damage with Enhanced Photodynamic Process and MTH1 Inhibition for Tumor Therapy. *Nano Lett*. 2019;19(8):5568-5576. doi:10.1021/ACS.NANOLETT.9B02112

144. Zhang H, Chen J, Zhu X, et al. Ultrasound induced phase-transition and invisible nanobomb for imaging-guided tumor sonodynamic therapy. *J Mater Chem B*. 2018;6(38):6108-6121. doi:10.1039/C8TB01788C

145. Tada M, Nakai Y, Sasaki T, et al. Recent progress and limitations of chemotherapy for pancreatic and biliary tract cancers. *World J Clin Oncol*. 2011;2(3):158. doi:10.5306/WJCO.V2.I3.158

146. Webster RM. Combination therapies in oncology. *Nat Rev Drug Discov*. 2016;15(2):81-82. doi:10.1038/NRD.2016.3

147. Gong L, Yan L, Zhou R, Xie J, Wu W, Gu Z. Two-dimensional transition metal dichalcogenide nanomaterials for combination cancer therapy. *J Mater Chem B*. 2017;5(10):1873-1895. doi:10.1039/C7TB00195A

148. Wang X, Cheng L. Multifunctional two-dimensional nanocomposites for photothermal-based combined cancer therapy. *Nanoscale*. 2019;11(34):15685-15708. doi:10.1039/C9NR04044G

149. Huang P, Lin J, Li W, et al. Biodegradable gold nanovesicles with an ultrastrong plasmonic coupling effect for photoacoustic imaging and photothermal therapy. *Angew Chem Int Ed Engl*. 2013;52(52):13958-13964. doi:10.1002/ANIE.201308986

150. Shen S, Wang S, Zheng R, et al. Magnetic nanoparticle clusters for photothermal therapy with near-infrared irradiation. *Biomaterials*. 2015;39:67-74. doi:10.1016/J.BIOMATERIALS.2014.10.064

151. Horcajada P, Serre C, Vallet-Regí M, Sebban M, Taulelle F, Férey G. Metal–Organic Frameworks as Efficient Materials for Drug Delivery. *Angewandte Chemie International Edition*. 2006;45(36):5974-5978. doi:10.1002/ANIE.200601878

152. Horcajada P, Chalati T, Serre C, et al. Porous metal-organic-framework nanoscale carriers as a potential platform for drug delivery and imaging. *Nat Mater*. 2010;9(2):172-178. doi:10.1038/NMAT2608

153. Hu M, Furukawa S, Ohtani R, et al. Synthesis of Prussian Blue Nanoparticles with a Hollow Interior by Controlled Chemical Etching. *Angewandte Chemie International Edition*. 2012;51(4):984-988. doi:10.1002/anie.201105190

154. Lian HY, Hu M, Liu CH, Yamauchi Y, C-W Wu K. Highly biocompatible, hollow coordination polymer nanoparticles as cisplatin carriers for efficient intracellular drug delivery. *Chem Commun*. 2012;48:5151-5153. doi:10.1039/c2cc31708g

155. You J, Zhang G, Li C. Exceptionally high payload of doxorubicin in hollow gold nanospheres for near-infrared light-triggered drug release. *ACS Nano*. 2010;4(2):1033-1041. doi:10.1021/NN901181C

156. Dong K, Liu Z, Li Z, Ren J, Qu X. Hydrophobic Anticancer Drug Delivery by a 980 nm Laser-Driven Photothermal Vehicle for Efficient Synergistic Therapy of Cancer Cells In Vivo. *Advanced Materials*. 2013;25(32):4452-4458. doi:10.1002/ADMA.201301232

157. Xue P, Cheong KKY, Wu Y, Kang Y. An in-vitro study of enzyme-responsive Prussian blue nanoparticles for combined tumor chemotherapy and photothermal therapy. *Colloids Surf. B Biointerfaces*. 2015;125:277-283. doi:10.1016/J.COLSURFB.2014.10.059

158. Wu M, Wang Q, Liu X, Liu J. Highly efficient loading of doxorubicin in Prussian Blue nanocages for combined photothermal/chemotherapy against hepatocellular carcinoma. *RSC Adv*. 2015;5(39):30970-30980. doi:10.1039/c4ra16138f

159. Chen H, Ma Y, Wang X, Wu X, Zha Z. Facile synthesis of Prussian blue nanoparticles as pH-responsive drug carriers for combined photothermal-chemo treatment of cancer. *RSC Adv*. 2016;7(1):248-255. doi:10.1039/C6RA24979E

160. Jing L, Shao S, Wang Y, Yang Y, Yue X, Dai Z. Hyaluronic acid modified hollow Prussian blue nanoparticles loading 10-hydroxycamptothecin for targeting thermo-chemotherapy of cancer. *Theranostics*. 2016;6(1):40-53. doi:10.7150/THNO.13250

161. Cai X, Gao W, Ma M, et al. A Prussian Blue-Based Core-Shell Hollow-Structured Mesoporous Nanoparticle as a Smart Theranostic Agent with Ultrahigh pH-Responsive Longitudinal Relaxivity. 2015. doi:10.1002/adma.201503381

162. Feng Xiao, Jialong Fan, Chunyi Tong, et al. An erythrocyte membrane coated mimetic nano-platform for chemo-phototherapy and multimodal imaging. doi: 10.1039/C9RA05867B

163. Li Y, Dang J, Liang Q, Yin L. Thermal-Responsive Carbon Monoxide (CO) Delivery Expedites Metabolic Exhaustion of Cancer Cells toward Reversal of Chemotherapy Resistance. *ACS Cent Sci*. 2019;5(6):1044-1058. doi:10.1021/ACSCENTSCI.9B00216

164. Chen H, Ma Y, Wang X, Zha Z. Multifunctional phase-change hollow mesoporous Prussian blue nanoparticles as a NIR light responsive drug co-delivery system to overcome cancer therapeutic resistance. *J Mater Chem B*. 2017;5(34):7051-7058. doi:10.1039/C7TB01712J

165. Shang T, Liu J, Chen Y, et al. In Vivo Targeted Cancer Theranostics by Core/Shell-Structured Multifunctional Prussian Blue/PLGA "Nanococktails." *Particle and Particle Systems Characterization*. 2018;35(2). doi:10.1002/PPSC.201700306

166. Yu B, Wang C. Tunable Synthesis of Mesoporous Prussian Blue@Calcium Phosphate Nanoparticles for Synergic Chemo-Photothermal Cancer Therapy. *ChemistrySelect*. 2020;5(35):10841-10847. doi:10.1002/slct.202001234

167. Ali LMA, Mathlouthi E, Cahu M, et al. Synergic effect of doxorubicin release and two-photon irradiation of Mn2+-doped Prussian blue nanoparticles on cancer therapy. *RSC Adv*. 2020;10(5):2646-2649. doi:10.1039/c9ra09133e

168. Mei X, Han Y, Xi J, et al. Preparation of hollow mesoporous prussian blue coated with mesoporous silica shell nanocubes for photothermal therapy and drug carrier. *Mater Lett*. 2022;312:131697. doi:10.1016/J.MATLET.2022.131697

169. Liang X, Deng Z, Jing L, et al. Prussian blue nanoparticles operate as a contrast agent for enhanced photoacoustic imaging. *Chemical Communications*. 2013;49(94):11029-11031. doi:10.1039/C3CC42510J

170. Cheng L, Gong H, Zhu W, et al. PEGylated Prussian blue nanocubes as a theranostic agent for simultaneous cancer imaging and photothermal therapy. *Biomaterials*. 2014;35(37):9844-9852. doi:10.1016/J.BIOMATERIALS.2014.09.004

171. Dumont MF, Hoffman HA, Yoon PRS, et al. Biofunctionalized gadolinium-containing Prussian blue nanoparticles as multimodal molecular imaging agents. *Bioconjug Chem*. 2014;25(1):129-137. doi:10.1021/BC4004266

172. Cai X, Gao W, Zhang L, et al. Enabling Prussian Blue with Tunable Localized Surface Plasmon Resonances: Simultaneously Enhanced Dual-Mode Imaging and Tumor Photothermal Therapy. *ACS Nano*. 2016;10(12):11115-11126. doi:10.1021/ACSNANO.6B05990

173. Shou P, Yu Z, Wu Y, et al. Zn2+ Doped Ultrasmall Prussian Blue Nanotheranostic Agent for Breast Cancer Photothermal Therapy under MR Imaging Guidance. *Adv Healthc. Mater*. 2020;9(1). doi:10.1002/adhm.201900948

174. Perrier M, Busson M, Massasso G, et al. 201Tl+-labelled Prussian blue nanoparticles as contrast agents for SPECT scintigraphy. *Nanoscale*. 2014;6(22):13425-13429. doi:10.1039/C4NR03044C

175. Szigeti K, Hegedus N, Rácz K, et al. Thallium Labeled Citrate-Coated Prussian Blue Nanoparticles as Potential Imaging Agent. *Contrast Media Mol Imaging*, 2018. doi:10.1155/2018/2023604

176. Jia X, Cai X, Chen Y, et al. Perfluoropentane-encapsulated hollow mesoporous prussian blue nanocubes for activated ultrasound imaging and photothermal therapy of cancer. *ACS Appl Mater Interfaces*. 2015;7(8):4579-4588. doi:10.1021/AM507443P

177. Fétiveau L, Paul G, Nicolas-Boluda A, et al. Tailored ultra-small Prussian blue-based nanoparticles for MRI imaging and combined photothermal/photoacoustic theranostics. *Chemical Communications*. 2019;55(98):14844-14847. doi:10.1039/c9cc07116d

178. Soo Choi H, Liu W, Misra P, et al. Renal clearance of quantum dots. *Nat. Biotechnol.* 2007;25(10):1165-1170. doi:10.1038/NBT1340

179. Wang L, Xu L, Kuang H, Xu C, Kotov NA. Dynamic nanoparticle assemblies. *Acc Chem Res*. 2012;45(11):1916-1926. doi:10.1021/AR200305F

180. Mirkin CA, Letsinger RL, Mucic RC, Storhoff JJ. A DNA-based method for rationally assembling nanoparticles into macroscopic materials. *Nature 1996 382:6592*. 1996; 607-609. doi:10.1038/382607A0

181. Singamaneni S, Bliznyuk VN, Binek C, Tsymbal EY. Magnetic nanoparticles: recent advances in synthesis, self-assembly and applications. doi:10.1039/c1jm11845e

182. Huang C, Chen X, Xue Z, Wang T. Effect of structure: A new insight into nanoparticle assemblies from inanimate to animate. *Sci Adv*. 2020;6(20). doi:10.1126/SCIADV.ABA1321

183. Eslami P, Rossi F, Fedeli S. Hybrid nanogels: Stealth and biocompatible structures for drug delivery applications. *Pharmaceutics*. 2019;11(2). doi:10.3390/pharmaceutics11020071

184. Oishi M, Hayashi H, Uno T, Ishii T, Iijima M, Nagasaki Y. One-Pot Synthesis of pH-Responsive PEGylated Nanogels Containing Gold Nanoparticles by Autoreduction of Chloroaurate Ions within Nanoreactors. *Macromol Chem Phys*. 2007;208(11):1176-1182. doi:10.1002/MACP.200700094

185. Hossain MA, Ikeda Y, Hara T, Nagasaki Y. Novel biocompatible nanoreactor for silica/gold hybrid nanoparticles preparation. *Colloids Surf B Biointerfaces*. 2013;102:778-782. doi:10.1016/J.COLSURFB.2012.09.034

186. Yahia-Ammar A, Sierra D, Mérola F, Hildebrandt N, le Guével X. Self-Assembled Gold Nanoclusters for Bright Fluorescence Imaging and Enhanced Drug Delivery. *ACS Nano*. 2016;10(2):2591-2599. doi:10.1021/ACSNANO.5B07596

187. Mejia-Ariza R, Huskens J. Formation of hybrid gold nanoparticle network aggregates by specific host-guest interactions in a turbulent flow reactor. *J Mater Chem B*. 2014;2(2):210-216. doi:10.1039/C3TB21228A

188. Engel S, Möller N, Stricker L, et al. A Modular System for the Design of Stimuli-Responsive Multifunctional Nanoparticle Aggregates by Use of Host–Guest Chemistry. *Small*. 2018;14(16):1704287. doi:10.1002/SMLL.201704287

189. Zan M, Li J, Huang M, et al. Near-infrared light-triggered drug release nanogels for combined photothermal-chemotherapy of cancer. *Biomater Sci*. 2015;3(7):1147-1156. doi:10.1039/c5bm00048c

190. Zhang L, Xue H, Cao Z, Keefe A, Wang J, Jiang S. Multifunctional and degradable zwitterionic nanogels for targeted delivery, enhanced MR imaging, reduction-sensitive drug release, and renal clearance. *Biomaterials*. 2011;32(20):4604-4608. doi:10.1016/J.BIOMATERIALS.2011.02.064

191. Zhang L, Cao Z, Li Y, Ella-Menye JR, Bai T, Jiang S. Softer zwitterionic nanogels for longer circulation and lower splenic accumulation. *ACS Nano*. 2012;6(8):6681-6686. doi:10.1021/NN301159A

192. Li X, Porcino M, Qiu J, Constantin D, Martineau-Corcos C, Gref R. Doxorubicin-loaded metal-organic frameworks nanoparticles with engineered cyclodextrin coatings: Insights on drug location by solid state NMR spectroscopy. *Nanomaterials*. 2021;11(4). doi:10.3390/nano11040945

193. Pfennig BW, Bocarsly AB, Prud RK. Synthesis of a Novel Hydrogel Based on a Coordinate Covalent Polymer Network. *J Am Chem Soc*. 1993;115:2661-2665.

194. Vondrova M, Burgess CM, Bocarsly AB. Cyanogel coordination polymers as precursors to transition metal alloys and intermetallics - From traditional heating to microwave processing. *Chemistry of Materials*. 2007;19(9):2203-2212. doi:10.1021/CM0630284

195. Xu J, Liu X, Chen Y, Zhou Y, Lu T, Tang Y. Platinum–Cobalt alloy networks for methanol oxidation electrocatalysis. *J Mater Chem*. 2012;22(44):23659-23667. doi:10.1039/C2JM35649J

196. Liu ZY, Fu GT, Zhang L, et al. PdCo/Pd-Hexacyanocobaltate Hybrid Nanoflowers: Cyanogel-Bridged One-Pot Synthesis and Their Enhanced Catalytic Performance. *Scientific Reports 2016 6:1*:1-10. doi:10.1038/SREP32402

197. Lin SY, Yao YQ, Zhang L, Feng JJ, Wang AJ. Cyanogel and its derived-materials: properties, preparation methods, and electrochemical applications. *Mater Today Energy*. 2021;20:100701. doi:10.1016/J.MTENER.2021.100701

198. Burgess CM, Yao N, Bocarsly AB. Stabilizing cyanosols: Amorphous cyanide bridged transition metal polymer nanoparticles. *J Mater Chem*. 2009;19(46):8846-8855. doi:10.1039/b911682f

199. Mukherjee S, Rao BR, Sreedhar B, Paik P, Patra CR. Copper Prussian blue analogue: investigation into multifunctional activities for biomedical applications. *Chemical Communications*. 2015;51(34):7325-7328. doi:10.1039/C5CC00362H

200. Mukherjee S, Kotcherlakota R, Haque S, et al. Silver Prussian Blue Analogue Nanoparticles: Rationally Designed Advanced Nanomedicine for Multifunctional Biomedical Applications. *ACS Biomater Sci Eng*. 2020;6(1):690-704. doi:10.1021/ACSBIOMATERIALS.9B01693

201. Fetiveau L, UPS. Nanoparticles de reseaux de coordination à visée théranostique. 2018.

202. Bowmaker GA, Kennedy BJ, Reid JC. Crystal Structures of AuCN and AgCN and Vibrational Spectroscopic Studies of AuCN, AgCN, and CuCN † . *Inorg Chem*. 2002;37(16):3968-3974. doi:10.1021/ic9714697

203. Leznoff DB, Lefebvre J. Coordination polymers with cyanoaurate building blocks: Potential new industrial applications for gold. *Gold Bull*. 2005;38(2):47-54. doi:10.1007/BF03215233

204. Huang H, Alvarez K, Lui Q, Barnhart TM, Snyder JP, Penner-Hahn JE. *Infrared Spectroscopic Characterization of Cyanocuprates*. Vol 104. John Wiley & Sons, Inc; 1996.

205. Bowmaker GA, Kennedy BJ, Reid JC. *Crystal Structures of AuCN and AgCN and Vibrational Spectroscopic Studies of AuCN, AgCN, and CuCN †*; 1998.

206. Mikuriya M, Ono K, Kawauchi S, Yoshioka D, Mitsuhashi R, Handa M. Mixed-Metal Pentanuclear Complexes of Ruthenium(II,III) Carboxylate and Tetracyanidoplatinate(II). *Chemistry Journal of Moldova*. 2017;10(2):48-53. doi:10.19261/cjm.2015.10(2).05

207. Falvello LR, Tomás M. *[{Cu(Bipy)(H 2 O)Pt(CN) 4 } 2]·2H 2 O: The First Synthesis and Crystal Structure of a Discrete Heterometallic Square Cyano-Bridged Compound with Terminal Cyano Ligands.*; RSC 1999, 273.

208. Safo IA, Werheid M, Dosche C, Oezaslan M. The role of polyvinylpyrrolidone (PVP) as a capping and structure-directing agent in the formation of Pt nanocubes. *Nanoscale Adv*. 2019;1(8):3095-3106. doi:10.1039/C9NA00186G

209. Li R, Kobayashi H, Tong J, et al. Radical-involved photosynthesis of AuCN oligomers from Au nanoparticles and acetonitrile. *J Am Chem Soc*. 2012;134(44):18286-18294. doi:10.1021/ja305198p

210. Braunstein P, Herberich GE, Neuschütz M, Schmidt MU. Cyano-bridged Fe–CN–Pt–NC–Fe chain complexes: structural and spectroscopic characterization of four isomers of [{η5-(1-phenylborole)Fe(CO)2(μ-CN)}2Pt(PEt3)2]. *J Organomet Chem*. 1999;580(1):66-71. doi:10.1016/S0022-328X(98)01089-4

211. Saito D, Omohiro Ogawa T, Yoshida M, et al. Intense Red-Blue Luminescence Based on Superfine Control of Metal-Metal Interactions for Self-Assembled Platinum(II) Complexes. doi:10.1002/anie.202008383

213. Gliemann G, Yersin H. Spectroscopic Properties of the Quasi One-Dimensional Tetracyanoplatinate(II) Compounds.

215. Zhao Z, Wang Z, Tavakoli J, et al. Revisiting an ancient inorganic aggregation-induced emission system: An enlightenment to clusteroluminescence. 2021. doi:10.1002/agt2.36

216. Spotheim-Maurizott M, Charliert M, Sabattier R. *DNA Radiolysis by Fast Neutrons*. Vol 57.; 1990.

217. Zhang XD, Wu D, Shen X, et al. Size-dependent radiosensitization of PEG-coated gold nanoparticles for cancer radiation therapy. *Biomaterials*. 2012;33(27):6408-6419. doi:10.1016/J.BIOMATERIALS.2012.05.047

218. Ma N, Wu FG, Zhang X, et al. Shape-Dependent Radiosensitization Effect of Gold Nanostructures in Cancer Radiotherapy: Comparison of Gold Nanoparticles, Nanospikes, and Nanorods. *ACS Appl Mater Interfaces*. 2017;9(15):13037-13048. doi:10.1021/ACSAMI.7B01112

219. Ghasemi M, Turnbull T, Sebastian S, Kempson I. The MTT assay: Utility, limitations, pitfalls, and interpretation in bulk and single-cell analysis. *Int J Mol Sci*. 2021;22(23). doi:10.3390/IJMS222312827/S1

220. Biological evaluation of medical devices-16:45:28 MDT 2009.

221. McMahon SJ. The linear quadratic model: Usage, interpretation and challenges. *Phys Med Biol*. 2019;64(1). doi:10.1088/1361-6560/AAF26A

222. Salado-Leza D, Traore A, Porcel E, et al. Radio-Enhancing Properties of Bimetallic Au:Pt Nanoparticles: Experimental and Theoretical Evidence. doi:10.3390/ijms20225648

223. Cheng X, Sun R, Yin L, et al. Light-Triggered Assembly of Gold Nanoparticles for Photothermal Therapy and Photoacoustic Imaging of Tumors In Vivo. *Advanced Materials*. 2017;29(6):1604894. doi:10.1002/ADMA.201604894

224. Huang P, Lin J, Li W, et al. Biodegradable Gold Nanovesicles with an Ultrastrong Plasmonic Coupling Effect for Photoacoustic Imaging and Photothermal Therapy. *Angewandte Chemie International Edition*. 2013;52(52):13958-13964. doi:10.1002/ANIE.201308986

225. Zhao T, Wang P, Li Q, et al. Near-Infrared Triggered Decomposition of Nanocapsules with High Tumor Accumulation and Stimuli Responsive Fast Elimination. *Angewandte Chemie International Edition*. 2018;57(10):2611-2615. doi:10.1002/ANIE.201711354

226. Roy X, Hui JKH, Rabnawaz M, Liu G, MacLachlan MJ. Prussian blue nanocontainers: Selectively permeable hollow metal-organic capsules from block ionomer emulsion-induced assembly. *J Am Chem Soc*. 2011;133(22):8420-8423. doi:10.1021/JA2016075

227. Baykal A, Bozkurt A, Jeremy R, et al. Multistimuli-responsive magnetic assemblies. *Stimuli Responsive Polymeric Nanocarriers for Drug Delivery Applications: Volume 2: Advanced Nanocarriers for Therapeutics*. 2019:155-193. doi:10.1016/B978-0-08-101995-5.00006-4

228. Silva AMN, Kong X, Parkin MC, Cammack R, Hider RC. Iron(III) citrate speciation in aqueous solution. *Dalton Transactions*. 2009;(40):8616-8625. doi:10.1039/B910970F

229. Qiu J, Li X, Steenkeste K, et al. Self-assembled multifunctional core–shell highly porous metal–organic framework nanoparticles. *Int J Pharm*. 2020;581. doi:10.1016/j.ijpharm.2020.119281

230. US Patent Application for USES OF GUANIDINE HYDROCHLORIDE AS A DRUG FOR TREATING CANCERS/TUMORS Patent Application (Application #20210154159 issued May 27, 2021)

231. Bin-Chuan JI, Hsu WH, Yang JS, et al. Gallic Acid Induces Apoptosis via Caspase-3 and Mitochondrion-Dependent Pathways in Vitro and Suppresses Lung Xenograft Tumor Growth in Vivo *J Agric Food Chem*. 2009;57(16):7596-7604. doi:10.1021/jf901308p

232. Priyadharshni Subramanian A, Kumar Jaganathan S, Mandal M, Supriyanto E, Idayu Muhamad Aruna Priyadharshni Subramanian I, Idayu Muhamad I. *World J Gastroenterol*. 2016;22(15):3952-3961. doi:10.3748/wjg.v22.i15.3952

233. Ponce A, Brostoff LB, Gibbons SK, et al. Elucidation of the Fe(III) Gallate Structure in Historical Iron Gall Ink. *Anal Chem*. 2016;88(10):5152-5158. doi:10.1021/acs.analchem.6b00088

234. Arifur Rahim M, Björnmalm M, Bertleff-Zieschang N, et al. Rust-Mediated Continuous Assembly of Metal-Phenolic Networks. *Adv Mater*. 2017;29:1606717. doi:10.1002/adma.201606717

235. Mu X, Yan C, Tian Q, Lin J, Yang S. BSA-assisted synthesis of ultrasmall gallic acid-Fe(III) coordination polymer nanoparticles for cancer theranostics. *Int J Nanomedicine*. 2017;12:7207-7223. doi:10.2147/IJN.S146064

236. Guo J, Tardy BL, Christofferson AJ, et al. Modular assembly of superstructures from polyphenol-functionalized building blocks. *Nature Nanotechnology 2016 11:12*:1105-1111. doi:10.1038/NNANO.2016.172

237. Wang Y, Wang Z, Xu C, Tian H, Chen X. A disassembling strategy overcomes the EPR effect and renal clearance dilemma of the multifunctional theranostic nanoparticles for cancer therapy. *Biomaterials*. 2019;197:284-293. doi:10.1016/J.BIOMATERIALS.2019.01.025

238. Xie W, Guo Z, Zhao L, Wei Y. Metal-phenolic networks: facile assembled complexes for cancer theranostics. *Theranostics*. 2021;11(13):6407-6426. doi:10.7150/thno.58711

239. Sever MJ, Wilker JJ. Visible absorption spectra of metal-catecholate and metal-tironate complexes. *Dalton Transactions*. 2004:1061-1072. doi:10.1039/b315811j

240. Xu H, Nishida J, Ma W, et al. Competition between Oxidation and Coordination in Cross-Linking of Polystyrene Copolymer Containing Catechol Groups. *ACS Macro Lett*. 2012;1:457-460. doi:10.1021/mz200217d

241. Ejima H, Richardson JJ, Liang K, et al. One-step assembly of coordination complexes for versatile film and particle engineering. *Science (1979)*. 2013;341(6142):154-157. doi:10.1126/SCIENCE.1237265

242. Boyatzis S, Velivasaki G, Malea E. A study of the deterioration of aged parchment marked with laboratory iron gall inks using FTIR-ATR spectroscopy and micro hot table. 2016. doi:10.1186/s40494-016-0083-4

243. Anand R, Malanga M, Manet I, et al. Citric acid-γ-cyclodextrin crosslinked oligomers as carriers for doxorubicin delivery. *Photochemical and Photobiological Sciences*. 2013;12(10):1841-1854. doi:10.1039/c3pp50169h

244. Tang Z, Kotov NA, Giersig M. Spontaneous organization of single CdTe nanoparticles into luminescent nanowires. *Science*. 2002;297(5579):237-240. doi:10.1126/SCIENCE.1072086

245. Wang H, Chen QW, Sun YB, Wang MS, Sun LX, Yan WS. Synthesis of necklace-like magnetic nanorings. *Langmuir*. 2010;26(8):5957-5962. doi:10.1021/LA9041343

246. Toulemon D, Rastei M v., Schmool D, et al. Enhanced Collective Magnetic Properties Induced by the Controlled Assembly of Iron Oxide Nanoparticles in Chains. *Adv Funct. Mater*. 2016;26(15):2454-2462. doi:10.1002/ADFM.201505086

247. Lee Y, Lee H, Messersmith PB, Park TG. A Bioinspired Polymeric Template for 1D Assembly of Metallic Nanoparticles, Semiconductor Quantum Dots, and Magnetic Nanoparticles. *Macromol. Rapid Commun*. 2010;31(24):2109-2114. doi:10.1002/MARC.201000423

248. Zhang H, Wang D. Controlling the growth of charged-nanoparticle chains through interparticle electrostatic repulsion. *Angewandte Chemie - International Edition*. 2008;47(21):3984-3987. doi:10.1002/ANIE.200705537

249. Bao W, Tian F, Lyu C, et al. Experimental and theoretical explorations of nanocarriers' multistep delivery performance for rational design and anticancer prediction. *Sci Adv*. 2021;7(6). doi:10.1126/SCIADV.ABA2458

250. Mundekkad D, Cho WC. Nanoparticles in Clinical Translation for Cancer Therapy. *International Journal of Molecular Sciences 2022*.23(3):1685. doi:10.3390/IJMS23031685

251. Yamada Y. Dimerization of Doxorubicin Causes Its Precipitation. *ACS Omega*. 2020;5(51):33235-33241. doi:10.1021/acsomega.0c04925

252. Zhao N, Woodle MC, Mixson AJ. Advances in delivery systems for doxorubicin. *J Nanomed Nanotechnol*. 2018;9(5). doi:10.4172/2157-7439.1000519

253. Hyun H, Lee S, Lim W, et al. Engineered beta-cyclodextrin-based carrier for targeted doxorubicin delivery in breast cancer therapy in vivo. *Journal of Industrial and Engineering Chemistry*. 2019;70:145-151. doi:10.1016/J.JIEC.2018.09.052

254. Anand R, Ottani S, Manoli F, Manet I, Monti S. A close-up on doxorubicin binding to c-cyclodextrin: an elucidating spectroscopic, photophysical and conformational study{. doi:10.1039/c2ra01221a

255. Mahdavi B, Shokrani P, Hejazi SH, Talebi A, Taheri A. Doxorubicin-loaded PVP coated Gd2O3 NPs for effective chemoradiotherapy in melanoma. *J Drug Deliv Sci Technol*. 2019;53. doi:10.1016/j.jddst.2019.101189

256. Ajaykumar C, Ajaykumar C. Overview on the Side Effects of Doxorubicin. *Advances in Precision Medicine Oncology*. 2020. doi:10.5772/INTECHOPEN.94896

257. Cappetta D, de Angelis A, Sapio L, et al. Oxidative Stress and Cellular Response to Doxorubicin: A Common Factor in the Complex Milieu of Anthracycline Cardiotoxicity. *Oxid Med Cell Longev*. 2017; doi:10.1155/2017/1521020

258. Ridnour LA, Thomas DD, Switzer C, et al. Molecular mechanisms for discrete nitric oxide levels in cancer. *Nitric Oxide*. 2008;19(2):73-76. doi:10.1016/j.niox.2008.04.006

259. Huerta S. Nitric oxide for cancer therapy. *Future Sci OA*. 2015;1(1). doi:10.4155/fso.15.44

260. Scicinski J, Oronsky B, Ning S, et al. NO to cancer: The complex and multifaceted role of nitric oxide and the epigenetic nitric oxide donor, RRx-001. *Redox Biol*. 2015;6:1-8. doi:10.1016/j.redox.2015.07.002

261. Huerta S. Nitric oxide for cancer therapy. *Future Sci OA*. 2015;1(1). doi:10.4155/FSO.15.44

262. Feng T, Wan J, Li P, et al. A novel NIR-controlled NO release of sodium nitroprusside-doped Prussian blue nanoparticle for synergistic tumor treatment. *Biomaterials*. 2019;214. doi:10.1016/j.biomaterials.2019.05.024

263. Bryan NS, Grisham MB. *Methods to Detect Nitric Oxide and Its Metabolites in Biological Samples*.

264. Vishwakarma A, Wany A, Pandey S, et al. Current approaches to measure nitric oxide in plants. *J Exp Bot*. 2019;70(17):4333-4343. doi:10.1093/jxb/erz242

265. Gadolinium-containing contrast agents: removal of Omniscan and iv Magnevist, restrictions to the use of other linear agents - GOV.UK.

266. Li X, Porcel E, Menendez-Miranda M, et al. Highly Porous Hybrid Metal–Organic Nanoparticles Loaded with Gemcitabine Monophosphate: a Multimodal Approach to Improve Chemo- and Radiotherapy. *ChemMedChem*. 2020;15(3):274-283. doi:10.1002/cmdc.201900596

267. Using Malvern Zetasizer To Measure Zeta Potential. https://www.silver-colloids.com/tutorials/intro/zetaintro/

268. Nanoparticle Tracking Analysis NTA | Malvern Panalytical. https://www.malvernpanalytical.com/en/products/technology/light-scattering/nanoparticle-tracking-analysis

269. Scanning Transmission Electron Microscope - Electron Energy Loss Spectroscopy (STEM-EELS) - Physical Methods in Chemistry and Nano Science - OpenStax CNX. https://cnx.org/contents/uieDnVBC@25.2:U1BUJroV@3/Scanning-Transmission-Electron-Microscope-Electron-Energy-Loss-Spectroscopy-STEM-EELS

270. Energy-Dispersive X-ray Spectroscopy (EDS) - Chemistry LibreTexts. https://chem.libretexts.org/Courses/Franklin_and_Marshall_College/Introduction_to_Materials_Characterization__CHM_412_Collaborative_Text/Spectroscopy/Energy-Dispersive_X-ray_Spectroscopy_(EDS)

271. X-ray Photoelectron Spectroscopy (XPS) - Chemistry LibreTexts: https://chem.libretexts.org/Courses/Franklin_and_Marshall_College/Introduction_to_Materials_Characterization__CHM_412_Collaborative_Text/Spectroscopy/X-ray_Photoelectron_Spectroscopy_(XPS)

8 SYNTHESE DE FRANÇAIS

Le travail effectué dans ce projet de thèse s'est concentré sur l'ajout de nouvelles modalités thérapeutiques et diagnostiques aux nanoparticules ultra-petites de type bleu de Prusse (PB) tout en maintenant une voie de synthèse verte. Il peut être globalement divisé en trois sections principales. La première partie était consacrée à la création de nouveaux analogues du bleu de Prusse en remplaçant l'un ou les deux ions par un métal lourd. Cela a été fait pour incorporer une perspective de radiothérapie jamais explorée auparavant dans le PB. On sait que lorsqu'un rayonnement à haute énergie interagit avec des éléments à Z élevé, une cascade d'électrons Auger est générée. Ceux-ci sont responsables de la radiolyse de l'eau et aident à former des espèces réactives de l'oxygène (ROS) qui peuvent tuer les cellules cancéreuses à proximité. Trois nanoparticules de PBA individualisées et autoportantes contenant de l'or, du fer et du platine dans différentes combinaisons ont été produites dans l'eau. La synthèse et la caractérisation complète de ces nouveaux composés sont rapportées au chapitre II. Ces solutions appelées cyanosols ont été synthétisées de manière verte et facilement évolutive, en l'absence de tensioactifs et d'agents réducteurs, selon une méthode rentable. Les nanoparticules obtenues sont homogènes et restent stables dans l'eau sans agrégation ni dépôt, sur de longues périodes de temps.

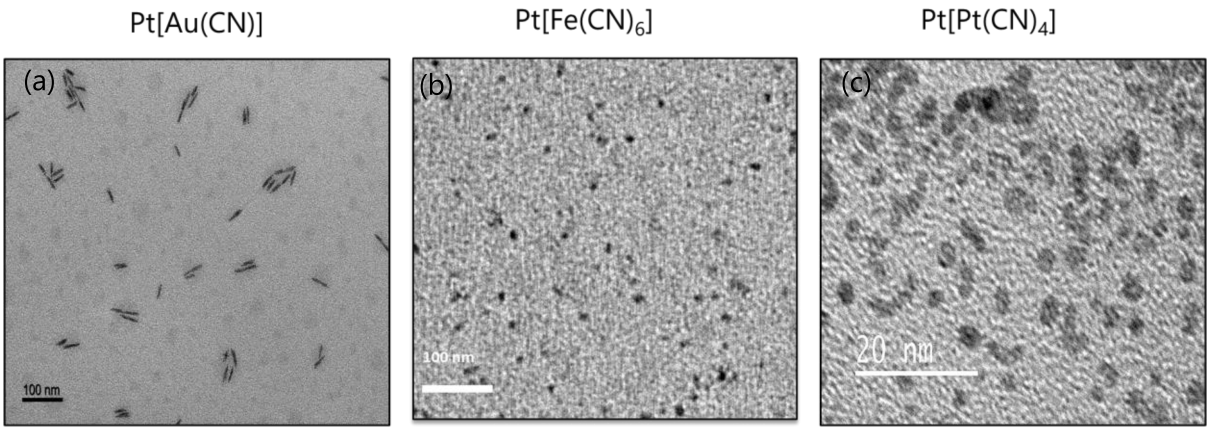

Figure 155. Images TEM de nanoparticules (a) AuPt (b) FePt et (c)PtPt

En optimisant les conditions expérimentales, des nanotiges d'or en forme de grain de riz d'environ 30 nm de long avec des extrémités effilées ont été obtenues. Cette nanostructure unique est composée de nanocristaux AuCN tandis que la surface a été décorée avec des nanoparticules sphériques de cyanosol contenant du Pt^{II} de 1 nm. De telles nanoparticules bimétalliques d'alliage or-platine avec Au^{I} et Pt^{II} n'ont jamais été décrites auparavant dans la littérature. La décoration périodique régulière de la nanostructure AuCN avec du Pt(II) doit être comprise. Des nanoparticules sphériques d'hexacyanoferrate de platine (FePt) et de 1-2 nm de tétracyanoplatinate de platine (PtPt) ont également été développées au cours de cette thèse. Ces nanoparticules poreuses contenant des ions Fe^{II} et Pt^{II} sont extrêmement stables dans l'eau ainsi que dans les milieux physiologiques. Il est important de noter qu'ils pourraient être post-revêtus de différents polymères en fonction des exigences. Ici, le polymère polyvinyl pyrrolidone a été utilisé pour recouvrir la surface de ces nanoparticules afin d'éviter toute extinction des radicaux formés sous irradiation, ce qui était précédemment observé avec le dextrane. Du sérum bovin fœtal et du liquide lysosomal artificiel ont été utilisés pour imiter les conditions biologiques et même avec l'introduction de tels milieux et l'exposition à 37 ° C pendant 6 à 15 heures, les signatures UV-Vis de FePt et PtPt restent intactes. Soumis à une dose de rayonnement γ de 4000 Gy, il y a eu apparition d'une bande SPR à 540 nm, dans le cas du cyanosol AuPt qui est caractéristique des nanoparticules d'or pur. Par conséquent, une petite proportion d' Au^{I} dans les nanoparticules a subi une réduction sous cette forte dose. Cependant, aucun changement significatif n'est apparu dans le cas des nanoparticules de FePt et de PtPt, fournissant une indication supplémentaire qu'elles pourraient être utilisées à des fins de radiothérapie.

L'effet de leur présence sur les biomolécules a été étudié en utilisant des plasmides comme nano-sonde. Sa structure double brin est considérée comme similaire à l'ADN et est généralement utilisée pour comprendre son comportement lors d'une exposition à des faisceaux de haute énergie. Une amélioration significative de l'incitation des DSB létaux et irréparables a été observée lors de la combinaison de ces nanoparticules poreuses contenant du Pt^{II} avec des plasmides avant l'irradiation gamma . Les expériences aident à comprendre les mécanismes moléculaires à l'origine des dommages induits par les radiations. Ensuite, des expériences *in cellulo* ont été menées. Les nanoparticules de cyanométallate FePt et PtPt semblent non toxiques pour les cellules fibroblastes primaires saines et biologiquement pertinentes. Ils sont également sans danger vis-à-vis des cellules cancéreuses du col de l'utérus (HeLa) jusqu'à une concentration totale en métal de $2{,}5\times10^{-4}$ $mol.L^{-1}$. Ces cellules incubées avec des nanoparticules ont été irradiées à l'aide d'une source de Cs-137, afin de vérifier si la réponse aux radiations obtenue avec les plasmides pouvait être traduite dans les cellules. Les fractions de survie obtenues en fonction de la dose fournie ont démontré que les deux nanoparticules amplifient significativement la mort des cellules cancéreuses par rapport à l'expérience témoin. Fait intéressant, on a pu voir que les lésions sublétales sont prédominantes et s'additionnent pour générer une conséquence létale globale. C'est un phénomène peu courant et peut-être le résultat de la porosité de nos nanoparticules. L'eau coordonnée à la surface ainsi que celles du réseau métallique ponté cyano sont disponibles pour la conversion en ROS. On suppose qu'ils pourraient se disperser et diffuser plus loin à travers le système poreux par rapport aux particules métalliques denses. Par conséquent, les dommages sont plus étendus et les lésions additives provoquent la mort cellulaire, améliorant l'index thérapeutique. La conception chimique de ces analogues du bleu de Prusse permet une modification facile de la structure grâce à des réseaux de coordination. Des études de contraste IRM avec des nanoparticules de FePt sont prévues. Des ions de gadolinium ou de manganèse pourraient également être dopés à la surface de ces nanoparticules pour améliorer la perspective diagnostique. De plus, les nanoparticules de PtPt sont constituées de feuillets 2D avec des distances inter-feuillets Pt-Pt proches qui expliquent la photoluminescence bleue observée. Il est très rare d'obtenir de la luminescence dans les analogues de PB et ce résultat semble très prometteur. Cela pourrait aider à suivre les nanoparticules ultra-petites *in vivo* et aider à suivre leur biodistribution.

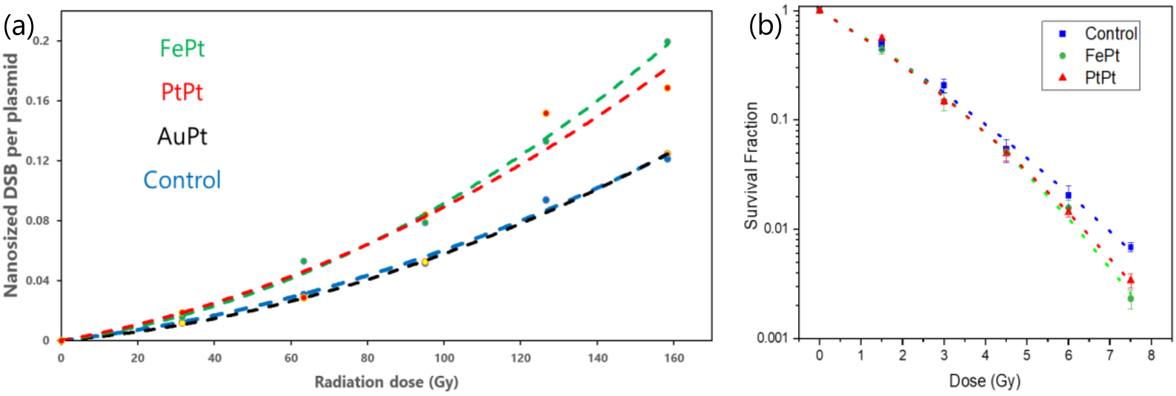

Figure 156. Graphiques illustrant (a) le nombre de DSB générés par plasmide en présence de Pt de type PB contenant des nanoparticules en fonction de la dose et (b) la fraction de survie des cellules HeLa lorsqu'elles sont soumises à un rayonnement après incubation avec 0,25 mM FePt et PtPt, par rapport à un échantillon témoin ne contenant pas de nanoparticules

Le deuxième axe de ce projet de thèse était la construction d'assemblages de nanoparticules théranostiques ultra-petites afin de surmonter un obstacle majeur à leur utilisation en médecine. Les grosses nanoparticules (> 10 nm) ne peuvent pas être éliminées par les reins, de sorte que l'accumulation et les effets secondaires possibles sont des préoccupations courantes, tandis que les particules inférieures à 10 nm sont prématurément éliminées du corps, ce qui réduit son activité thérapeutique. Afin d'obtenir un agent théranostique sûr, multifonctionnel et efficace , la formation d'assemblages activables de particules de PB d'environ 5 nm a été tentée. Il était difficile d'obtenir des assemblages homogènes tout en essayant de maintenir une voie de synthèse verte. Nous avons montré ici pour la première fois qu'un réseau phénolique métallique (MPN) construit à l'aide de fer et d'acide gallique peut auto-assembler des nanoparticules PB ultra-petites chargées en nanochaînes unidimensionnelles contrôlées. Cela pourrait être fait dans l'eau, sans l'utilisation de tensioactifs, à température ambiante. Les assemblages formés étaient stables et amélioraient les propriétés optiques par rapport aux nanoparticules individuelles. Les nanochaînes pourraient être post-revêtues de différents polymères comme le PVP, le dextran et le citrate de poly γ -cyclodextrine et sa caractérisation complète est rapportée au chapitre 3.

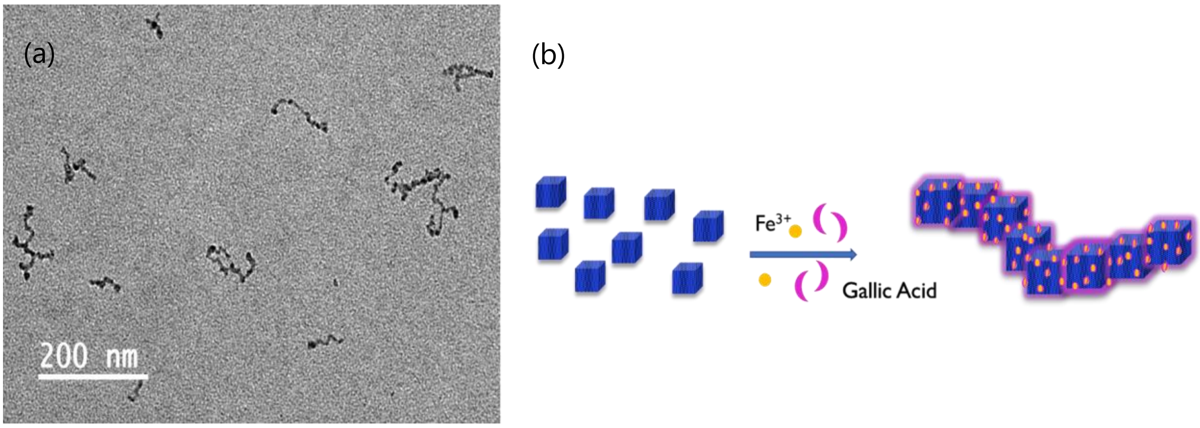

Figure 157. (a) Image TEM d'assemblages 1-D de nanoparticules ultra-petites de bleu de Prusse et son (b) illustration schématique

Le mécanisme de formation de ces assemblages a été étudié. Étant donné que le changement de l'ion introduit lors de la synthèse en sodium/calcium (Na$^+$ /Ca^{2+}) ne conduit pas à la formation d'assemblages similaires, on peut dire que l'espèce de réseau polymère Fe^{3+} -acide gallique pontée μ-oxo est nécessaire pour reliant les nanoparticules individuelles de PB riches en Fe. Il a été observé que la substitution par des ions gallium similaires (Ga^{3+}) pouvait conduire à la formation de nanochaînes, bien qu'elle soit moins contrôlée. Ce travail met en lumière la possibilité de caractéristiques intéressantes qui pourraient être développées en mettant l'accent sur les complexes Ga^{3+} -acide gallique et leur formation de réseaux phénoliques métalliques. On suppose que, de la même manière que pour les NP d'or chargés, une fois qu'un dimère de deux NP PB (liés par une coque FeGA) est formé, la double couche électrostatique se réorganise pour former une couche uniforme recouvrant la surface. Ensuite, les autres NP à proximité se fixent préférentiellement aux extrémités du dimère, afin de minimiser les répulsions électrostatiques entre les particules chargées négativement, ce qui pourrait être la raison de la formation de nanochaînes PB FeGA allongées. Des expériences in situ par DLS et spectroscopie UV-visible au cours de la formation sont nécessaires pour déterminer le mécanisme de formation. D'autres polyphénols pourraient également agir comme lieurs PB et aider à former des nanostructures similaires. La variation avec l'acide ellagique dans un mélange eau-éthanol avec des ions Fe^{3+} , Na$^+$ et Ca^{2+} conduisant à des assemblages dimensionnables a été décrite dans cette thèse. Des nanochaînes 1D pourraient également être formées à l'aide d'autres nanoparticules ultra-petites. Le PB dopé au Gd à 5 %, le PB lié au nitroprusside de sodium et le cyanosol FePt présentent des résultats intéressants qui ouvrent un large éventail de possibilités pour de études futures.

La dernière partie de cette thèse a été consacrée à l'évaluation de l'efficacité théranostique des nanochaînes à base de PB. Les expériences de chargement de médicaments ont révélé une augmentation marquée de la stabilité globale du nano-système lors de l'assemblage des nanoparticules. De plus, l'enrobage avec un polymère de citrate de poly-cyclodextrine (CD) améliore l'efficacité d'encapsulation (~ 85 % en 1 heure d'incubation) et stabilise le système

PB FeGA pour résister à une plus grande quantité de molécules anticancéreuses de charge opposée. C'est la première fois qu'une telle encapsulation aussi élevée de doxorubicine a été rapportée dans des systèmes PB ultra-petits.

Des expériences dans des milieux physiologiques ont clairement montré que près de 50 % du médicament encapsulé pouvait être libéré en une heure dans un environnement acide simulé de la tumeur, tandis que seule une petite quantité s'échappait du système, même lors d'une exposition prolongée à un pH cellulaire neutre et sain. On pouvait également voir qu'une élévation de la température locale augmenterait la quantité de médicament libérée dans la zone de concentration. Étant donné que les nanoparticules de PB ont une capacité de conversion photo-thermique, cette élévation de température pourrait facilement être atteinte. Les tests de rayonnement laser proche infrarouge ont révélé que les assemblages PB FeGA se comportent comme de meilleurs agents PTT par rapport aux particules ultra-petites PB de départ. Par conséquent, la photo thermie et la chimiothérapie synergiques pourraient conduire à une destruction efficace des cellules cancéreuses à l'aide de ces nouvelles nanochaînes PB chargées de médicaments. Les expériences in vitro menées ont montré la sécurité et la non-toxicité des nanochaînes envers les cellules, tandis que le PB FeGA chargé de doxorubicine était efficace pour tuer les cellules cancéreuses. L'internalisation du médicament a été visualisée par des études de microscopie confocale et a confirmé la capacité d'administration du médicament sous un pH acide une fois dans les lysosomes.

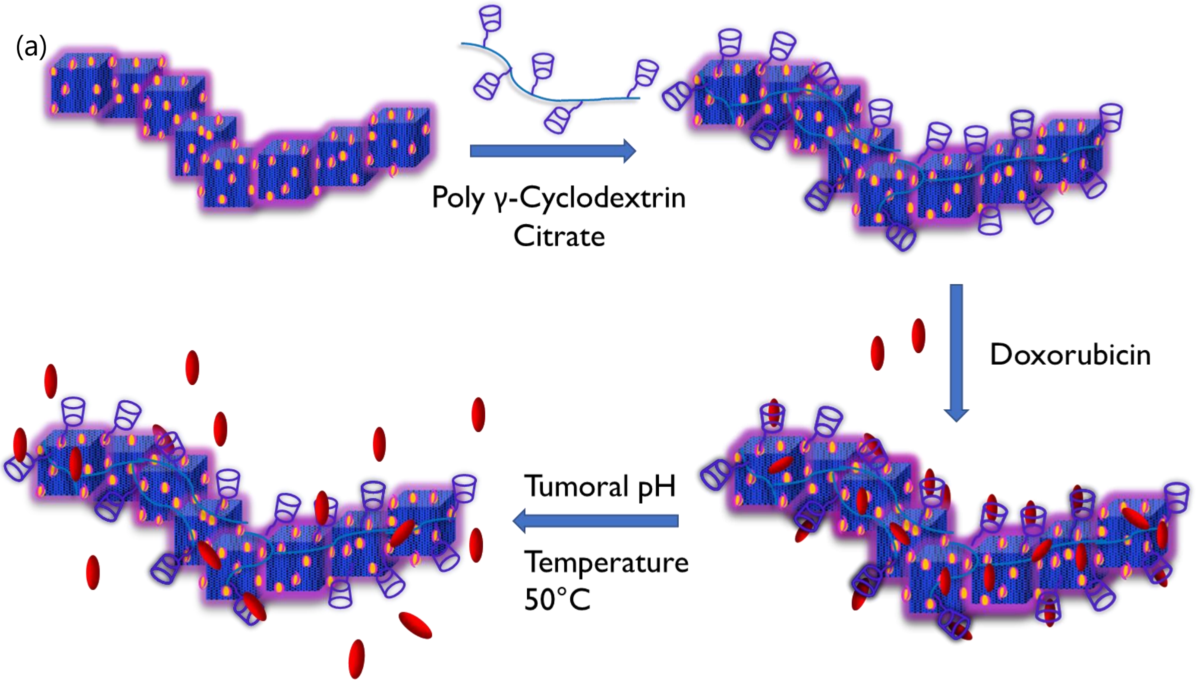

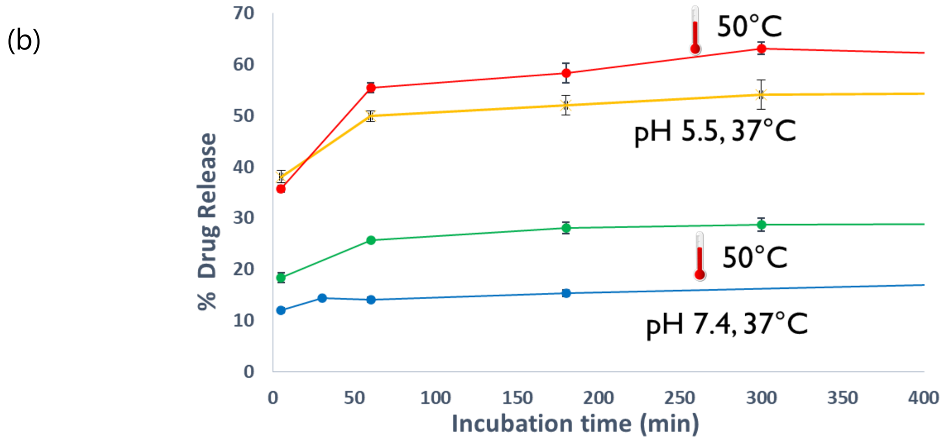

Figure 158. (a) Schéma représentant l'encapsulation de la doxorubicine dans des assemblages PB-FeGA enrobés de polymère CD citrate et sa libération dans l'environnement tumoral (b) Pourcentage de médicament libéré par les nano-assemblages dans différentes conditions de pH et de température.

La diversification des nanochaînes avec de l'oxyde nitrique (NO) contenant des nanoparticules ultra-petites a conduit à des résultats intéressants et à des fonctionnalités supplémentaires. NON, un inhibiteur de croissance tumorale et un gaz radio-sensibilisant pourraient être libérés des nanoparticules lors du chauffage. Ainsi, en plus d'être un véhicule d'administration de médicaments, cette nanostructure est également un transporteur de NO, qui peut être libéré avec un rayonnement NIR et fonctionner avec la thérapie photothermique. Les résultats de ces expérimentations préliminaires positives seraient reproduits dans les mois à venir avant de passer aux tests *in-vitro* .

Afin d'avoir une idée des capacités diagnostiques des nanochaînes, des études de relaxivité ont été réalisées à Mons, en Belgique. Des nanoparticules simples de PB pur et de Gd-PB et leurs assemblages respectifs ont été évalués. Étant donné que les complexes FeGA ont été utilisés pour créer l'assemblage PB, ils améliorent positivement le contraste IRM pondéré en T_1 des deux assemblages. Par conséquent, non seulement l'indice thérapeutique global des NP PB ultra-petits s'est amélioré, mais la formation de l'assemblage s'avère également bénéfique pour le diagnostic.

En conclusion, une nouvelle famille de nanochaînes auto-assemblées de particules ultrapetites a été créée au cours de cette thèse et elles semblent prometteuses pour plusieurs types d'applications théranostiques.